ABSTRACT

Title of Dissertation:	The Effect of CO_2 on Copper Partitioning in Sulfur-Free and Sulfur-Bearing Felsic Melt-Vapor-Brine Assemblages
	Brian C. Tattitch, Doctor of Philosophy, 2012
Dissertation Directed by:	Professor Philip Candela Department of Geology

ABSTRACT

Analysis of fluid inclusions from porphyry copper deposits (PCD) reveals that magmatic vapor and/or brine are vital for the removal of copper from arc magmas and its transport to the site of ore formation. Experiments in melt-vapor-brine systems allow for investigating the partitioning of copper between silicate melts and volatile phases under magmatic conditions. The presence of CO_2 affects both the pressure of vapor saturation and the composition of exsolving volatile phases. However, PCD are primarily sulfide ore deposits, and the role of sulfur must also be examined as part of magmatic-hydrothermal experiments. Therefore, the partitioning of copper in $CO_2 \pm$ S-bearing experiments was examined in an attempt to provide insights into copper partitioning and the generation of PCD.

I present the results from experiments performed at 800 ^{o}C and 100 MPa in CO_2-bearing melt-vapor-brine systems with $X_{CO2}^{v+b} = 0.10$ and 0.38. The compositions of vapor and brine inclusions and run-product glasses were used to determine the compositions of the magmatic phases. The partitioning of copper between brine and vapor ($D_{Cu}^{b/v} \pm 2\sigma$) increases from 25(±6) to 100 (±30) for sulfur-free experiments and increases from 11(±3) to 95(±23) for sulfur-bearing experiments as X_{CO2} is increased from 0.10 to 0.38. The partitioning of copper between vapor and melt ($D_{Cu}^{v/m} \pm 2\sigma$) decreases from 9.6(±3.3) (sulfur-free, HCl-bearing), 18(±8) (sulfur-bearing, HCl-free), and 30(±11) (sulfur-bearing, HCl-bearing) at $X_{CO2} = 0.10$, to 2(±0.8)(HCl-free) at $X_{CO2} = 0.38$, sulfur-free or sulfur-bearing. These data demonstrate that copper partitioning in sulfur-free, CO_2-bearing systems is controlled by the changes in the salinity of the vapor and brine corresponding to changes in X_{CO2}. Sulfur-bearing experiments demonstrate that magmatic vapors are enriched in copper in the presence of sulfur at low X_{CO2}. However,

the enrichment of copper in the magmatic vapor is suppressed for sulfur-bearing systems at high X_{CO2}.

The MVPart model presented by Candela and Piccoli (1998) was modified to incorporate CO_2 to predict trends in efficiency of removal of copper into exsolving CO_2-bearing magmatic volatile phases. The CO_2-MVPart model predicts two to three times lower efficiency for CO_2-rich ($X_{CO2} = 0.38$) magmatic volatile phases compared to low-CO_2 ($X_{CO2} \leq 0.10$) systems.

The Effect of CO_2 on Copper Partitioning in Sulfur-Free and Sulfur-Bearing
Felsic Melt-Vapor-Brine Assemblages

By

Brian C. Tattitch

Dissertation submitted to the Faculty of the Graduate School of the
University of Maryland, College Park in partial fulfillment
of the requirements for the degree of
Doctor of Philosophy
2012

Advisory Committee
      Professor Philip Candela, Chair
      Senior Research Scientist Philip Piccoli
      Professor William McDonough
      Professor James Farquhar
      Professor Martin Rabenhorst

Acknowledgments

I would like to first thank my wife Rebecca for her help well beyond what was required in both editing and completing the practical requirements of this project, as well as her tremendous support with the intangible demands of completing my PhD. I would not have completed this project without her. I would also like to thank my parents and family for their support throughout my education as I developed a love for the natural sciences. I would like to thank Jeannie Martin and Dr. Richard Walker who were so helpful in my application to the Geology Department at Maryland. Many of my fellow students helped me greatly during my program, but in particular Michael Mengason, Zoltan Zajacz, Nick Gava, and Brian Harms helped greatly in the completion of this project. I would also like to thank my collaborators at Virginia Tech, Dr. Robert Bodnar, Dr. Andras Fall and Dr. Luca Fedele for all their assistance in understanding and characterizing the complex fluid inclusions generated as part of my experiments. Finally, I would like to thank both my advisors, Dr. Phil Candela and Dr. Phil Piccoli, for their guidance and patience during the many trials of an experimental project involving new methods as well as their help in acquiring NSF funding for this project (NSF EAR 0738992, EAR 0911098, EAR 0842205) and the LMDR laboratory. Through this project they have provided me the unique opportunity to apply my training in laboratory chemistry, engineering, and thermodynamics to understanding the formation of vital natural resources.

TABLE OF CONTENTS

LIST OF TABLES

LIST OF FIGURES

Chapter 1:Introduction

1.1 Porphyry Copper Deposits

Nearly two thirds of the world's copper is mined from Porphyry Copper Deposits (PCD) (Sillitoe, 2010; Sinclair, 2007). In addition, PCD are an important source for a number of other ore metals (e.g. Mo, Au, Ag) enhancing the economic value of many deposits. Porphyry copper deposits are characterized by large hydrothermally altered volcanic and intrusive rock suites, ranging in size from tens to thousands of cubic kilometers of altered and mineralized rock, producing 10^{10} to 10^{12} metric tons of ore (Figure 1)(Sillitoe, 2010; Sinclair, 2007). Copper concentrations in the ore zone of PCD are on the order of thousands of ppm with particularly enriched regions of some deposits reaching >1 wt% copper (Sillitoe, 2010; Sinclair, 2007 and references therein).
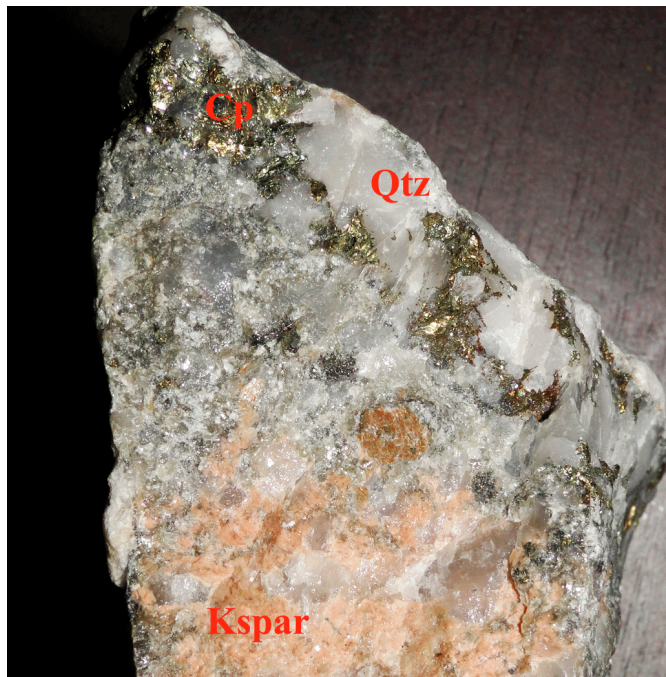
Figure 1: Sample of copper ore from the Highland Valley Porphyry Copper District, British Columbia (collected by Phil Candela). Sample is an altered porphyry containing K-feldspar (Kspar) and quartz veins (Qtz) with copper-iron sulfides, including chalcopyrite (Cp) and bornite (not-pictured)

Large historic PCD, such as the Bingham Porphyry Copper Deposit in Utah, have been mined for nearly 100 years. Mining at Bingham Canyon has exposed nearly two vertical kilometers of the ore zone over an area of four kilometers, and Kennecott Utah Copper reports that 19 Mt of copper has been produced at the Bingham Canyon mine, with a net value of ~ \$145 billion at January 5th, 2012 spot prices, and still produces ~300,000 tons of copper and 400,000 Oz of gold annually (\$2.6 billion). The concentration of copper in the ore zone of PCD ranges from several thousand ppm up to more than 1 wt%, representing copper anomalies ranging from nearly 200 to more than 400 times the average concentration of copper in the continental crust (~25 ppm : Rudnick and Gao, 2004). Understanding the wide range of processes that must operate together to generate a significant copper anomaly requires an understanding of evidence from the ore zone and causative igneous rock(s). Given that some evidence is destroyed as the system evolves, experiments are required to provide some constraints on the intensive and extensive variables required for ore formation.

The prevailing models for the formation of PCD all begin with the emplacement of shallow, felsic to intermediate, water-rich arc magmas at depths of 5-10 km (Audetat et al., 2008; Candela and Piccoli, 2005; Halter et al., 2005; John et al., 2010; Pettke et al., 2010; Sillitoe, 2010; Simon and Ripley, 2011; Sinclair, 2007). These melts are likely derived from a complex series of processes that begin with the formation of basaltic melts derived from partial melting in the mantle, and additional melts derived from partial melting of rocks in the lower crust. These deeper melts are generated by the interaction of the mantle and lower crust with volatile phases (e.g. $H_2O > CO_2 > SO_2$ components)

generated during metamorphic dehydration of subducting oceanic slabs and associated sediments. The addition of water reduces the solidus of the overlying rocks, and may result in partial melting in the mantle and/or lower crust, and the buoyant ascent of these melts into the overlying crust (John et al., 2010; Leeman et al., 1994). The mantle-derived basalts are emplaced primarily as sills (laterally extensive intrusions, structurally controlled by the host rock morphology) in the lower crust (~30 km) (Annen et al., 2006; John et al., 2010; Sillitoe, 2010; Sinclair, 2007). The emplacement of the basalts may also induce partial melting in the surrounding host rocks, which may mix with the basaltic melts. The melts formed in the mantle and lower crust can also assimilate wall rocks throughout ascent and differentiation, incorporating the host rock into the melt. At shallow levels of emplacement, magmas may also develop cupolas (anomalous domes of intrusive magma above the average magma chamber roof depth) and dikes, often near channels of earlier volcanic activity. The intrusion of partially crystallized magma from these shallow reservoirs along steeply dipping dike swarms results in more rapid crystallization and a porphyritic texture (large crystals in a fine grained matrix), giving the porphyry copper deposits their name.

Prior to emplacement, evolving arc magmas may lose water during adiabatic decompression ("first boiling") or fracturing of overlying rock. This process may play a role in the fluxing of volatile phases in evolving arc-magmatic systems. Upon emplacement at shallow levels, arc magmas will lose heat to cooler host rocks and crystallize dominantly anhydrous minerals after the temperature drops below the liquidus. The crystallization of these minerals reduces the melt fraction without removing water, enriching the remaining melt in water.

If a magma is unable to crystallize significant quantities of water-bearing phases (e.g. biotite), the remaining melt will become enriched in water as crystallization proceeds. As the decreasing melt fraction becomes enriched in water prior to complete crystallization, the melt may become saturated with respect to H_2O-CO_2-dominant volatile phase assemblages comprising a supercritical fluid or a low-salinity magmatic vapor ± high-salinity brine ("second boiling") (Audetat et al., 2008; Candela and Piccoli, 2005; Candela and Piccoli, 1998; John et al., 2010; Sillitoe, 2010; Sinclair, 2007). The degree of crystallization at volatile phases saturation is a function of the initial and saturation water concentration as well as the H_2O/CO_2 ratio of the melt. Once the sum of the vapor pressures of each volatile phase component reaches the total load pressure, either through decompression or enrichment in volatile components, first or second boiling will proceed. As the exsolution of volatile phases produces bubbles in the magma (first or second boiling) the bubbles produced will be buoyant, and may rise and coalesce in the cupolas and dikes at the top of the chamber.

Direct evidence of the melt-volatile phase equilibria vital to ore metal extraction is poorly preserved in natural systems and must often be inferred from analysis of fluids trapped at sub-solidus conditions. However, ore metals (e.g. Cu, Au, Mo, Ag) have been shown experimentally to partition strongly into magmatic volatile phases (MVPs) relative to coexisting magmas (Candela and Holland, 1984; Candela and Piccoli, 1995; Candela and Piccoli, 1998; Frank et al., 2011; Lerchbaumer and Audetat, 2009; Simon et al., 2005; Simon et al., 2008b; Simon et al., 2006; Williams et al., 1995; Zajacz et al., 2010b). During the exsolution of volatile phases in natural magma chambers, numerous intensive parameters (e.g. pressure, temperature, degree of crystallization, $f$$H_2O$, $f$$CO_2$)

will influence the efficiency with which these metals are removed from the melt by the MVPs relative to their initial concentrations in the parental magma. The affinity of these metals for the MVPs and the ability of the MVPs to separate from the parental magmas and coalesce along structural anomalies allows for focusing of these enriched "proto-ore fluids" (Candela et al. 2010) along the steeply dipping dikes and associated fractures.

As magmatic fluids ascend through the upper crust, a variety of processes (e.g. cooling, decompression, wall rock reactions) can lead to primary precipitation of copper-bearing minerals, which are dominantly magmatic-derived, "hypogene" sulfides. When abundant stress fracturing is associated with the porphyritic intrusions, hypogene mineralization is often confined to a broad matrix or "stockwork" of fine-grained quartz veins filling these fractures (Figure 2) (see Sinclair, 2007 for examples). Episodic magmatic intrusion is commonly associated with porphyry deposit formation, and in general the earliest porphyritic intrusions are associated with the highest degree of mineralization and minimal alteration. The stages of ore deposition are often complex and as an example, the large Bajo de la Alumbrera deposit is defined by seven independent porphyritic intrusions, each contributing to ore formation (Proffett, 2003).
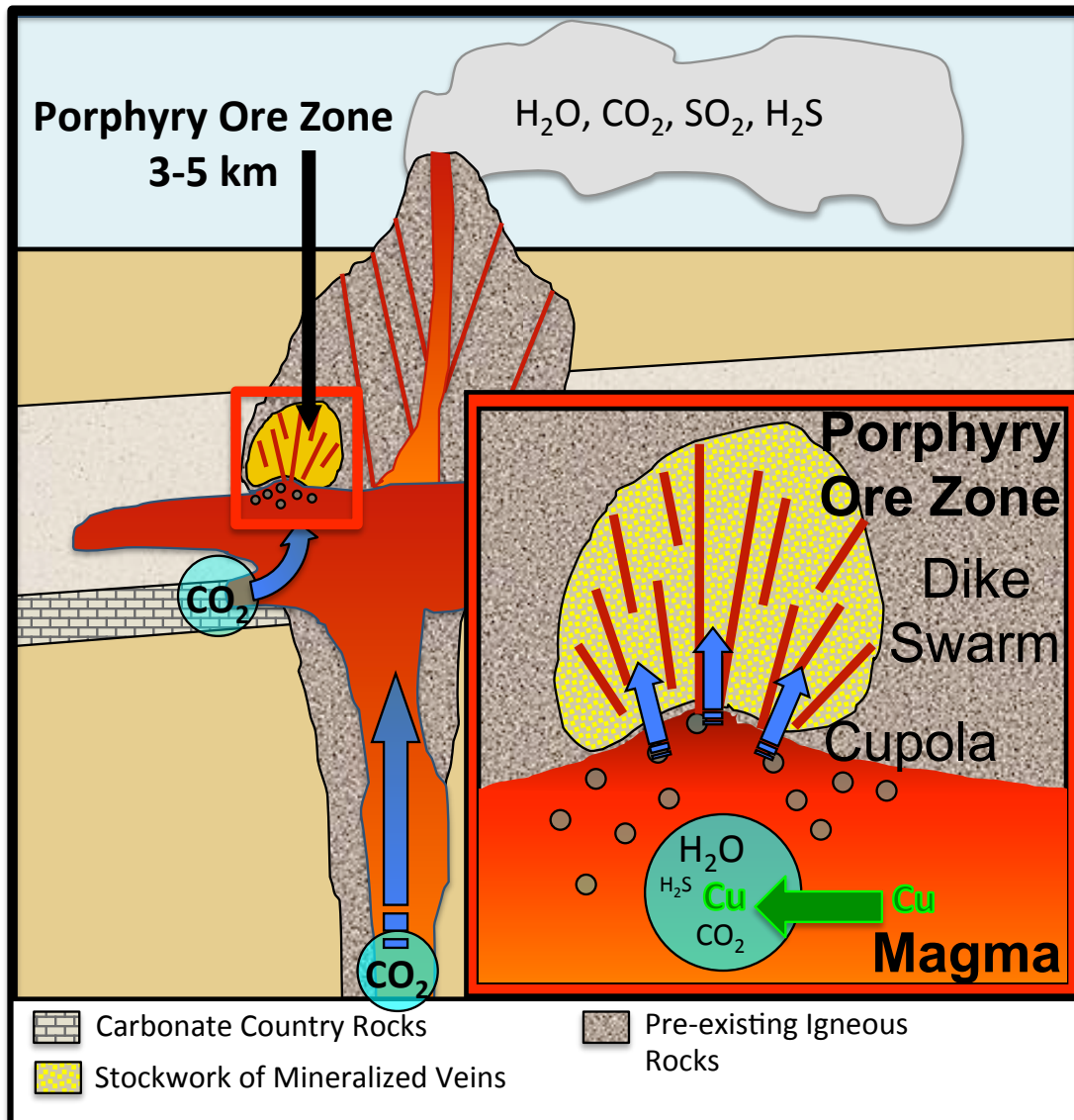
Figure 2: Schematic cross-section of an arc magma chamber with overlying volcanic and intrusive magma columns (modified from Shinohara, 1994; Sillitoe, 2010; Sinclair, 2007). CO_2 sourced from deeper mantle-derived melts or reaction/assimilation with country rocks is also shown. Inset: Porphyry ore zone with a raised, bubble-rich cupola and overlying dike swarm with associated stockwork of mineralizing ore veins. Efficiency of removal of copper into exsolving H_2O-CO_2 volatile phases (green arrow) exerts a strong control on ore grade or the potential for formation of an economic deposit. The subject of inquiry in this study is the role of CO_2 in melt-volatile phase equilibria that ultimately controls the efficiency of removal of copper into the MVPs.

The episodic fluxing of magmatic volatile phases through the overlying rock also produces a generally consistent alteration sequence throughout the majority of porphyry copper deposits. The core of PCD ore zones are dominated by a potassic alteration zone, with significant production of K-feldspar or biotite (± amphibole, ± anhydrite), and

6

deposition of copper dominantly as chalcopyrite (Cp) and bornite (Bn) (John et al., 2010; Proffett, 2003; Sillitoe, 2010; Sinclair, 2007). Sodic-calcic alteration zones occasionally underlie potassic alteration zones. The formation of sodic-calcic alteration is characterized by albite and magnetite and may result from alteration by sodium-rich brines formed either from fluid-host rock interactions and/or from primary exsolution of volatile phases (Sillitoe, 2010; Sinclair, 2007).

Laterally, the potassic zone is often surrounded by a propylitic alteration zone (e.g. albite, epidote ± chlorite), with sulfides grading from bornite to chalcopyrite to pyrite in potassic zones towards the propylitic zone. Few mineralized veins are observed in the propylitic zone and few to no copper-rich sulfides are present (Proffett, 2003; Sillitoe, 2010). These zones are generally inferred to be formed from the mixing of magmatic fluids, rich in sodium after potassic alteration, and convecting (thermally driven) meteoric waters (John et al., 2010 - and references therein; Sillitoe, 2010; Sinclair, 2007). Above the potassic alteration zone is generally a chlorite-sericite zone characterized by destruction of plagioclase to sericite (mica), magnetite to hematite and mafic minerals to chlorite. These zones are associated with later, more acidic, volatile phase fluxing and decreased hydrothermal temperatures (Sillitoe, 2010). The chlorite-sericite zones grade vertically into purely sericitic or "phyllic" alteration halos, (sericite + quartz) characterized by complete sericitization of feldspar, with both sericitic zones often overprinting previous potassic alteration. The broad phyllic zone may also extend down around the flanks of the potassic core (Sillitoe, 2010; Sinclair, 2007).

In the waning stages of magmatism and fluxing of MVPs in a porphyry copper deposit, the alteration zones that define the deposit often expand centrally downward,

producing a common "telescoping effect" (John et al., 2010; Sillitoe, 2010; Sinclair, 2007). However, the episodic nature of the fluxing of MVPs often results in complicated mixing between these zones with alteration overprinting by MVPs derived from the younger intrusions (Sillitoe, 2010). When copper grades are economic in the chlorite-sericite zone or phyllic zone, they are usually associated with coatings of chalcopyrite or bornite (or other high-sulfur copper bearing sulfides) on the pyrite, and likely results from later recharge of magmas and/or sulfur rich pulses of volatile phase fluxing. (Sillitoe, 2010).

Surrounding the phyllic zone is generally a complex, depleted "lithocap" defined by argillic alteration. Argillic alteration is typified by the formation of clay minerals (e.g. kaolinite, pyrophyllite) from primary igneous feldspar, sulfates (alunite) from oxidation of sulfide, and "vuggy" quartz filling pore spaces in the rock. The lithocap is generally barren of any mineralized veins, but in some deposits initial copper deposition may have dispersed copper removed from parental magmas over a large vertical range, into the shallow zones now occupied by the lithocap. Large-scale dissemination of copper mineralization hinders the formation copper-rich hypogene ore. However, late, down-flowing, oxidizing meteoric fluids that generate the lithocap can destroy shallow copper-rich sulfides by chemical weathering. Destruction of copper-bearing sulfides can remobilize copper, enriching the lower portions of the shallow intrusions in copper oxides. This process can produce different, "supergene" varieties of copper deposition (Sillitoe, 2010; Sinclair, 2007). These supergene-enriched zones are generally associated with "blankets" of ore minerals in the phyllic alteration zone, and contribute to high ore grades in some large PCD. The definition of these alteration zones is further complicated

by small-scale alteration of a similar nature around dikes and veins. These alteration halos are formed during the episodic magmatic and hydrothermal fluxing common to PCD.

Relatively impermeable host rocks may also improve the focused deposition of ore minerals from varied episodes of fluxing of magmatic volatile phases in large (e.g. marble at Grasberg, Sillitoe, 2010) and small (sandstone and limestone at Ridgeway, Wilson et al., 2003) porphyry copper deposits. Impermeable host rocks can mitigate the spread of ore fluids, improving high grade ore formation (Sillitoe, 2010). A number of other processes may affect ore-metal transport by magmatic-derived fluids and ore deposition in a variety of hydrothermal environments. These processes can lead to the formation of related skarn and epithermal deposits (Sillitoe, 2010). The common feature of all of these models for porphyry deposit formation is the hypothesis that the ore fluids were initially exsolved from, or were in chemical equilibrium with, the associated intrusive magmas.

The reduction in $f\mathrm{H_2O}$ associated with the release of magmatic volatile phases enhances the crystallization of the parental magma. The catastrophic nature of the release of volatile phases, and common occurrence of episodic magmatism, are often responsible for episodic exsolution of volatile phases. Dynamic magmatic processes often result in episodic fluxing of volatile phases consistent with textural and alteration evidence in PCD (Audetat et al., 2008; Candela and Piccoli, 2005; Halter et al., 2004; John et al., 2010; Sillitoe, 2010; Sinclair, 2007). Samples of these ore fluids, hypothesized to have extracted copper from the silicate melt and transported copper to sub-solidus ore zone conditions, are often trapped as fluid inclusions (Audetat et al., 2008; Heinrich et al.,

2004; Heinrich et al., 1999; Heinrich et al., 1992; Murakami et al., 2010; Pettke et al., 2010; Redmond et al., 2004; Seo et al., 2009; Sillitoe, 2010; Ulrich et al., 1999). Analyses of these natural fluid inclusions can provide direct measurements of the major and trace element composition of ore fluids at various stages of mineralization.

The composition of the evolved ore fluids at sub-solidus conditions is often determined by the analysis of these primary fluid inclusions, with focus on the largest and most economically productive deposits (Audetat et al., 1998; Heinrich et al., 2004; Heinrich et al., 1999; Pettke et al., 2010; Rusk et al., 2008; Rusk et al., 2004; Ulrich et al., 1999). These fluid inclusions from PCD display a wide range of salinities (1 wt% to > 50 wt%), bulk densities (0.25 to 1.25 g/cc yielding vapor ± liquid ± salt at room temperature), vapor bubble compositions (including $H_2O > CO_2 > CO + CH_4 + N_2$), and highly variable concentrations of ore metals (e.g. Cu, Ag, Au, Mo, W ranging from 10^1 to 10^5 ppm) and other trace elements. Small "daughter" minerals sometimes form upon cooling of fluid inclusions to ambient conditions. Analysis of the dissolution temperatures of these minerals or freezing point of the aqueous portion of inclusions (referred to as microthermometry) can yield information on the bulk composition of the inclusions. The development of Laser Ablation Inductively Coupled Plasma Mass Spectrometry (LA-ICPMS) techniques for analysis of fluid inclusions has also allowed for accurate characterization of multiple trace elements from a single inclusion down to concentrations in the 1-10 ppm range.

Significant portions of the recent studies of fluid inclusions in PCD were directed at characterizing the trace element concentrations of ore metals (e.g. Cu, Au, Mo, Ag). The partitioning of these trace elements, along with the major element composition (e.g.

$[Cl]^{MVP}$, $[S]^{MVP}$, Na/K/H ratio) of the varied ore fluids, is recorded by the natural fluid inclusions in the ore zone (Anderson et al., 1989; Audetat et al., 2008; Field et al., 2005; Halter et al., 2004; Heinrich et al., 2004; Heinrich et al., 1999; Imai, 2000; Pettke et al., 2010; Redmond et al., 2004; Rusk et al., 2008; Soloviev, 2011; Ulrich et al., 1999). One goal of characterizing the compositions of ore fluids is to identify the properties of the hydrothermal assemblage that might control the metal budget and deposition mechanisms required to form an economic deposit. However, identifying the causative ore fluids from a particular deposit can be difficult.

Variability in the composition of ore fluids trapped as fluid inclusions (e.g. salinity, homogenization temperature, daughter minerals) is indicative of the complexity of sources and transport processes involved in the formation of PCD. Audetat et al. (2008) note that a single quartz crystal from the Yankee Lode deposit (porphyry tin deposit similar to PCD) recorded multiple episodes of fluxing of MVPs over a wide P-T range (600 to 200 $^{\circ}$C and 90 to 30 MPa). Several of these studies of large porphyry copper deposits include mapping of fluid inclusion types. These maps connect the various episodes of fluxing of MVPs to variations in the composition of the magmatic volatile phases and the ore grade throughout the deposits. The summary of many of these large deposits and other barren intrusions presented by Audetat et al. (2008) demonstrates that the absolute copper concentration of the high temperature, sub-solidus, fluids trapped in fluid inclusions is a good predictor of formation of economic deposits and ore grade. Yet, the analysis of fluid inclusions from ore deposits generally only provides a record of fluids trapped at sub-solidus conditions.

The initial composition of proto-ore fluids *during the exsolution of volatile phases*, is not often recorded by natural fluid inclusions due to few phases present at magmatic conditions capable of trapping and maintaining recoverable fluid inclusions. Nonetheless, significant evidence exists for a magmatic source for ore fluids. Hydrogen isotopes in the fluids, trapped as fluid inclusions, and oxygen isotopes of hypogene alteration minerals are both consistent with a magmatic source for ore fluids in PCD (Dilles et al., 1992; Harris et al., 2005; Sillitoe, 2010). Homogenization temperatures of fluid inclusions imply trapping conditions near magmatic temperatures for some fluid inclusion assemblages, and allows for some degree of extrapolation to melt-volatile phase equilibrium conditions (Azbej et al., 2007; Bodnar, 1995; Halter et al., 2005; Hedenquist and Lowenstern, 1994; Heinrich et al., 2004; Heinrich et al., 1999; Roedder, 1971; Rusk et al., 2008; Rusk et al., 2004).

Audetat et al. (2008) summarizes evidence for high temperature magmatic fluids trapped as fluid inclusions in 4 barren and 13 mineralized magmatic-hydrothermal intrusions. In most of the intrusions they argue for exsolution of a low-salinity, single-phase fluid from the magma with later phase separation to coexisting vapors and brines occurring at sub-solidus temperatures. However, in several of the deposits, notably major PCD (Santa Rita, Bajo de la Alumbrera, and Grasberg), there is evidence for a two-phase volatile assemblage (low-salinity magmatic vapor and high-salinity magmatic brine) at or near magmatic conditions (Audetat et al., 2008; and references therin). This observation is consistent with exsolution of coexisting vapor and brine directly from the silicate melt in some PCD, noting the high mass fraction of vapor relative to brine at magmatic or sub-solidus conditions. Early experimental modeling of hydrothermal ore metal stability

confirms that certain transport paths, combined with wall rock interactions, can allow for transport of the majority of the ore metal budgets of magmatic derived fluids from >600 ^{o}C down to 250 ^{o}C, lending support for a magmatic origin for porphyry ore metals (Holland, 1965).

The partitioning of copper among the magmatic phases is affected by the composition of those phases, and the copper partitioning behavior will control the removal of copper from the magma. Variations in the efficiency of ore metal removal into MVPs are hypothesized to be vital in controlling the copper concentration of ore fluids and ultimately, the formation of porphyry copper deposits (Audetat et al., 2008; Candela and Piccoli, 1998). As a result, experiments designed to investigate melt-volatile phase equilibria or trace element solubility at magmatic conditions have been developed over several decades to fill in this gap in the observable data from natural systems.

1.2 Magmatic-Hydrothermal Experiments

The limited sampling of natural magmatic fluids in PCD highlights the importance of experiments in identifying the parameters of melt-volatile phase equilibria that control the removal of copper and other ore metals by exsolving MVPs. Early thermodynamic models of porphyry deposit formation were focused on identifying the conditions and reactions that control ore metal transport. These models are required to explain the transport of ore metals, such as copper, by volatile phases from magmatic conditions, through high-temperature sub-solidus conditions, to depositional conditions of 200 to 400 ^{o}C (Holland, 1965). These early models, along with studies of natural fluid inclusions, provided confirmation that the intrusive magmas associated with porphyry copper deposits were the likely source for ore-fluids and ore metals. Once sufficient

evidence existed for a magmatic source for natural ore fluids, experiments were conducted that were designed to characterize the composition of silicate melts in equilibrium with H_2O-dominated volatile phases at super-solidus and super-liquidus conditions. The dominant complexing ligand in those arc magmatic volatile phases is hypothesized to be chlorine (Holland, 1972; Roedder, 1971). Accordingly, the NaCl-H_2O system is commonly used in magmatic hydrothermal experiments as a simplified proxy for the more complex mixtures of chloride components in natural magmatic fluids.

Candela and Holland (1984) conducted experiments containing a magmatic assemblage comprising a felsic silicate melt and supercritical H_2O-NaCl-KCl fluid in platinum capsules. Quenched glasses formed from the silicate melt were characterized by electron microprobe (major elements) and ion microprobe (copper and molybdenum) analyses. The liquid formed from the supercritical fluid was extracted by using a syringe, diluted to a known volume, and was analyzed for copper and molybdenum using atomic absorption spectrophotometry. The study concluded that the partitioning of copper between the supercritical fluid and the silicate melt was correlated strongly with salinity, whereas the molybdenum concentration remained invariant. However, the possibility of coexisting magmatic vapor and brine required development of more complex copper partitioning experiments. Williams et al. (1995) used a similar design for copper partitioning experiments involving sampling condensate fluids along with mass balance calculations based on theoretical models for the NaCl-H_2O vapor-brine solvus presented by Bodnar et. al. (1985). They concluded that the partitioning of copper among coexisting vapor, brine and silicate melt was also strongly controlled by the salinity of the two magmatic volatile phases.

The advent of LA-ICPMS analysis techniques allowed for development of new methods for characterizing magmatic volatile phases from experiments by trapping synthetic fluid inclusions. Studies by Simon et al. (2005; 2008b; 2007; 2006) report values for the melt-volatile phase partition coefficients for copper, silver, gold, and arsenic by trapping samples of magmatic fluids and synthetic fluid inclusions and conducting quantitative analyses on their major and trace element concentration using LA-ICPMS. Several of these studies, along with more recent work on melt-volatile phase equilibria and copper solubility in magmatic fluids, not only characterized the role of chlorine in copper partitioning, but sulfur complexing as well (Frank et al., 2011; Zajacz et al., 2011).

The progress in experiment design has allowed for more accurate characterization of fluid compositions and identification of copper-bearing chlorine and sulfur complexes. These complexes likely control copper concentrations in volatile phases at magmatic conditions (Zajacz et al., 2011) and sub-solidus conditions prior to ore deposition (Pokrovski et al., 2008; Pokrovski et al., 2009a; Pokrovski et al., 2009b). However, the role of CO_2 (the second most abundant volatile phase component in arc magmas; Jarrard, 2003; Lowenstern, 2001) in copper partitioning among melt-volatile phase assemblages in natural systems has remained poorly constrained. The $f CO_2$ influences the salinity of coexisting magmatic volatile phases (Duan et al., 1995) and the timing of the exsolution of volatile phases from arc magmas (Botcharnikov et al., 2005; Lowenstern, 2001). Thus, significant changes to melt-volatile phase equilibria are expected with increasing mole fractions of CO_2 in the vapor ± brine (X_{CO2}^{v+b} simplified to X_{CO2}). Further experimentation

that includes CO_2 as a system component is required to progress towards more complete applicability of experimental data to the genesis of porphyry copper deposits.

1.3 Project Design

1.3.1 *Investigation of the Effect of CO_2 on Copper Partitioning*

The primary goal of this project is to evaluate the impact of CO_2, the second most abundant volatile phase component in arc magmas (Lowenstern, 2001), on the potential for the formation of porphyry copper deposits. The role of CO_2 in melt-volatile phase assemblages has remained relatively unconstrained in previous hydrothermal experiments, especially with respect to the behavior of copper partitioning at magmatic conditions. The prevailing models for copper partitioning address the importance of sulfur in at least copper transport, but little attention has been paid to CO_2. This project has been designed to evaluate the effect of CO_2, and any combined effect of CO_2 and sulfur, on copper partitioning. The complexity of melt-volatile phase equilibria, hypothesized to control copper removal from the silicate melt, required evaluating the effect of CO_2 without the presence of sulfur. The independent influence of CO_2 could then be separated from the results of experiments with CO_2 and sulfur as system components.

The experiments presented in this study examine copper partitioning in CO_2-bearing melt-vapor-brine assemblages. The experiments were performed in noble metal capsules at 800 ^{o}C and 100 MPa. Magmatic volatile phases were trapped as synthetic fluid inclusions and analyzed along with quench glasses formed from the silicate melt. A fundamental effect of the addition of CO_2 to the $NaCl$-H_2O system is a change in the salinities of vapor and brine that define the two-phase vapor + brine stability field. With

16

increasing X_{CO2} in the bulk volatile phase assemblage, the salinity of the vapor (brine-saturated) decreases and the salinity of the brine (vapor-saturated) increases (Figure 3). As discussed, CO_2-free magmatic-hydrothermal copper partitioning experiments ubiquitously include chlorides as components of the volatile phases, and many directly evaluate the contribution of chloride complexation to copper removal from the silicate melt (Candela and Holland, 1984; Candela and Piccoli, 1995; Frank et al., 2011; Lerchbaumer and Audetat, 2009; Simon et al., 2006; Zajacz et al., 2011).

The series of sulfur-free experiments presented in Chapter 2 were designed to investigate how CO_2 would affect copper partitioning given only chloride complexation of copper in the magmatic volatile phases. It was not hypothesized that CO_2 would act as a ligand for copper at magmatic conditions (Lowenstern, 2001) and should not directly contribute to copper complexation. However, I hypothesized that the strong influence of CO_2 on vapor and brine salinity should affect the concentration of chlorine-complexed copper in each magmatic volatile phase. By conducting experiments at low X_{CO2} and high X_{CO2} (Figure 3), I first confirmed the magnitude of the change in salinity predicted by theoretical models for coexisting vapor and brine in the $NaCl$-H_2O-CO_2 system at magmatic conditions.
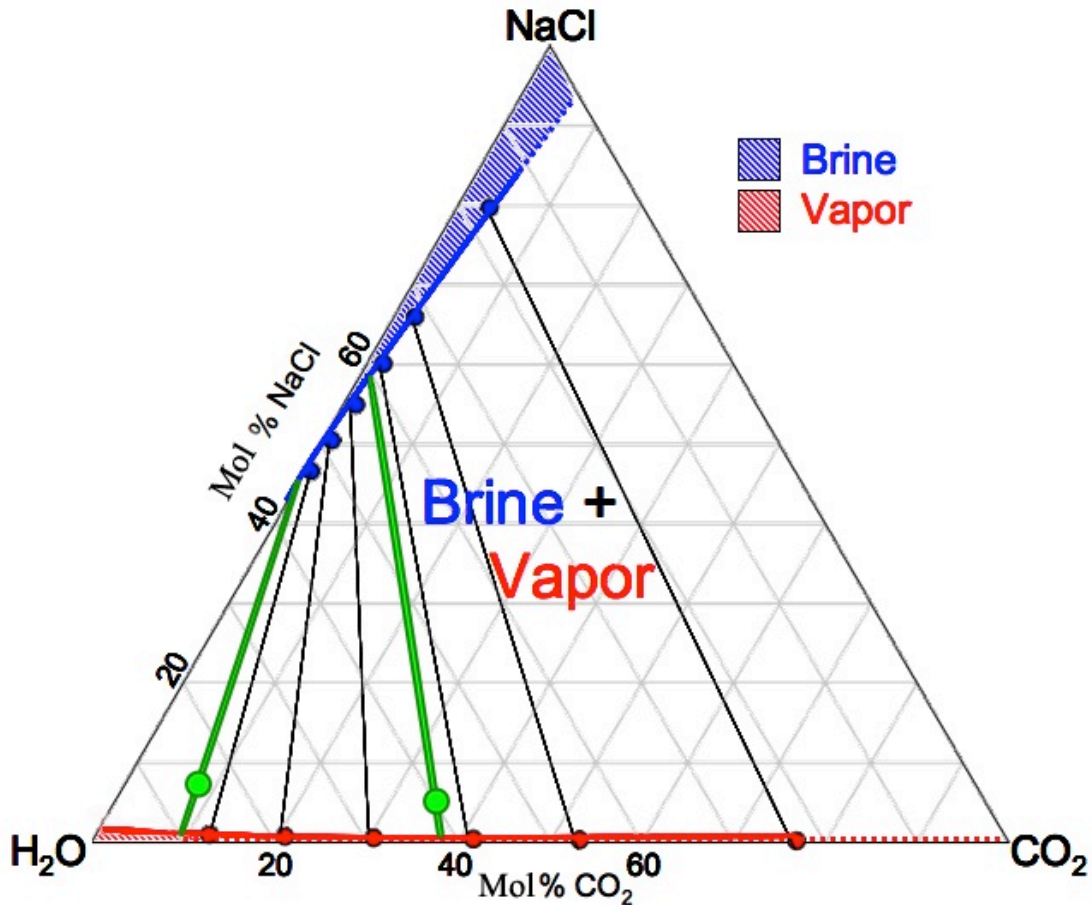
Figure 3: Schematic H₂O-CO₂-NaCl ternary shown in mol % at 800 °C and 100 MPa generated using the model presented in Duan et al. (1995). Green lines and dots represent the bulk volatile phase compositions of CO₂-bearing experiments presented in this study. Initial compositions fall within the two-phase field and were chosen to examine the range of compositions relevant to porphyry copper deposits.

The primary experimental challenges encountered in CO_2-bearing experiments lie in successful quantitative addition of CO_2 to the melt-vapor-brine assemblage and characterization of CO_2-rich, low-salinity magmatic vapor. Methods were developed for the addition of CO_2 using oxalic acid di-hydrate and evaluating its effect on experiment equilibrium (discussed in chapter 2). Methods are also discussed for the measurement of vapor inclusion salinity via Raman spectroscopic determination of fluid inclusion pressure, and measurement of the melting temperature of H_2O-CO_2 clathrate.

The copper partitioning data obtained from these experiments can then be evaluated for systematic variability as a function of the X_{CO2} of the bulk volatile phase.

18

These data are then compared to existing CO_2-free data from experiments and natural systems. In addition to interpretation of the static copper partitioning data, the effect of CO_2 on copper removal from a complex and evolving arc magma is also considered. Candela and Piccoli (1998) presented a model (MVPart) designed to predict the efficiency of removal of copper into $NaCl$-H_2O volatile phases during second boiling at varied magmatic conditions (pressure, temperature) and initial Cl/H_2O ratios in the melt. The reduced solubility of CO_2 in silicate melts, compared with H_2O, results in a strong influence of CO_2 on the evolving composition of magmatic volatile phases and the timing of the exsolution of volatile phases compared to CO_2-free systems (Botcharnikov et al., 2005; Lowenstern, 2001; Newman and Lowenstern, 2002). A modified version of the MVPart model has been formulated in order to incorporate the results of my CO_2-bearing melt-vapor-brine copper partitioning data for the limited conditions of 800 ^{o}C and 100 MPa (described in Chapter 2). This allows for an evaluation of secondary influences of CO_2 on the exsolution of volatile phases, as well as more complex influences of a variable vapor-brine solvus on copper removal from the silicate melt. Thus, the effect of CO_2 alone on the potential for the formation of PCD will be defined by the change in coexisting vapor-brine salinities, corresponding changes in static copper partitioning data, and model predictions for the efficiency of removal of copper into CO_2-bearing MVPs.

1.3.2   *The Combined Effect of CO_2 and Sulfur on Copper Partitioning*

Porphyry copper deposits are characterized by the presence of sulfide minerals as the dominant source of copper in the ore. Fluid inclusions that trap samples of ore fluid usually have high sulfur concentrations, and commonly sulfide daughter minerals are present (Audetat et al., 2008; Heinrich, 2005; Heinrich et al., 1999; Rusk et al., 2008;

Sillitoe, 2010; Simon and Ripley, 2011). Prior to accurate techniques for measurement of the sulfur concentration in fluid inclusions, several studies noted that the concentrations of other complexing ligands (e.g. chlorine) are insufficient to balance the solute load (Na, K, Fe, Ca, Cu, Au, etc.) of the vapor-rich fluid inclusions (Audetat et al., 2011; Heinrich et al., 2004). The ubiquity of sulfur in porphyry copper deposits, and its apparent role in copper transport and deposition, has led to a focus on the importance of sulfur in studies of deposits and magmatic-hydrothermal experiments (Audetat et al., 2008; Candela and Piccoli, 2005; Halter et al., 2005; Heinrich, 2005; Heinrich et al., 2004; Sillitoe, 2010; Simon and Ripley, 2011; Zajacz et al., 2011). In particular, experiments performed approaching magmatic conditions demonstrate that, over a wide range of conditions (800 ^{o}C to 1000 ^{o}C and 100 MPa to 150 MPa), the presence of sulfur increases the equilibrium concentration of copper in magmatic vapor relative to sulfur-free compositions (Frank et al., 2011; Simon et al., 2006; Zajacz et al., 2011). However, as discussed in the previous section, existing magmatic-hydrothermal experiments do not constrain the effect of CO_2 as a system component.

The experiments presented in Chapter 3 build upon the effect of CO_2 on chlorine complexed copper partitioning by adding sulfur (sourced from pyrrhotite) as a phase component of the magmatic phase assemblage. The pyrrhotite-saturated experiments provide direct measurement of the change in copper partitioning with the addition of sulfur, compared to sulfur-free experiments, as a function of X_{CO2}. Again, synthetic fluid inclusions were used to trap samples of the magmatic volatile phases. The addition of sulfur as a system component required several additional considerations in experiment design. Several adjustments were made to the capsule characteristic (e.g. length, starting

material mass, alloy) to ensure equilibrium at the time of trapping fluid inclusions and are discussed in detail in Section 3.2.2.

Vapor inclusions trapped as part of the pyrrhotite-saturated experiments contained H_2S in addition to CO_2. Characterization of CO_2-H_2S-bearing vapor inclusion salinity required developing a model for the complex mixed clathrate formed upon cooling. The mixed clathrate model and Raman Spectroscopic techniques (outlined in Chapter 3) are vital for accurate characterization of inclusion salinity and vapor inclusion copper concentrations. The results of the CO_2-MVPart model were then adjusted qualitatively based on the copper partition coefficients calculated for the melt-vapor-brine assemblages of the pyrrhotite-saturated experiments. The model results presented here provide constraints for how CO_2 adjusts the bulk properties of exsolving magmatic volatile phases. In addition, copper removal from the melt into sulfur-bearing MVPs is affected by changes in the stability of hypothesized chloride and bisulfide (HS^-) complexes in the exsolving magmatic vapor with increasing X_{CO2}.

1.3.3   Experimental Variables

The primary independent variables examined throughout the experiments presented in this study are the X_{CO2} of the bulk magmatic volatile phase, and the presence or absence of sulfur as a component of the silicate melt and volatile phases. However, several other changes were made to the experiment design to ensure capsule integrity, and to examine the role of melt composition on copper partitioning behavior. Variation in melt composition can affect intensive variables such as fHCl in the magmatic vapor. The effect of melt composition and the fHCl on copper partitioning is examined by using

either natural Bishop Tuff or synthetic haplogranite minimum melt glass (GR1) to generate the silicate melt at run conditions.

The capsule material was also changed from Pt to a Cu_6Au_{94} alloy synthesized using a technique developed by Zajacz et al. (2011). Two methods for trapping fluid inclusions are also presented using either pre-fractured quartz or in-situ fractured quartz. The development of consistent experimental methods for using in-situ fractured quartz help ensure that the synthetic fluid inclusions trap equilibrated fluids. The CO_2-bearing, sulfur-free experiments presented in Chapter 2 are labeled as the Cu300 series (X_{CO2} = 0.10) and the Cu500 series (X_{CO2} = 0.38). The pyrrhotite-saturated (sulfur-bearing) experiments presented in Chapter 3 are labeled as Cu400 series (X_{CO2} = 0.10) and Cu600 series (X_{CO2} = 0.38). The selection of starting glass, quartz fracture method, capsule material and presence or absence of magnetite and pyrrhotite are shown for each experiment in Table 1.

EXP NUMBER	10%CO$_2$	38%CO$_2$	PreFrac	In-Situ	B-Tuff	GR1	Mt	Po
	SULFUR-FREE EXPERIMENTS							
Cu320	X		X		X		X	
Cu321	X		X		X		X	
Cu326	X		X		X		X	
Cu351	X		X			X	X	
Cu330	X			X	X		X	
Cu332	X			X	X		X	
Cu500		X		X	X			
Cu502		X		X	X			
Cu503		X		X	X		X	
Cu504		X		X	X		X	
Cu505		X	X	X	X		X	
	SULFUR-BEARING EXPERIMENTS							
Cu402	X			X		X	X	X
Cu404	X		X	X		X	X	X
Cu405	X		X	X		X	X	X
Cu410	X		X	X	X		X	X
Cu411	X		X	X	X		X	X
Cu601		X	X	X		X	X	X
Cu606		X	X	X		X	X	X
Cu607		X	X	X		X	X	X

▢ (grey) – Platinum Capsule
▢ (yellow) – Cu$_6$Au$_{94}$ Capsule

Table 1: Attributes of CO$_2$-bearing melt-vapor-brine experiments. The use of pre-fractured quartz (PreFrac), in-situ fractured quartz (In-Situ) and either Bishop Tuff (B-Tuff) or synthetic granite minimum melt glass (GR1) is listed for each experiment. The presence of magnetite and pyrrhotite for the duration of an experimental run is also noted. Capsule material is also noted for either Pt (grey) or Cu$_6$Au$_{94}$ (yellow) experiments.

Chapter 2: The Effect of CO_2 on Magmatic Volatile Phase Salinity and Cu Partitioning

2.1 Introduction

The role of CO_2 in the formation of magmatic-hydrothermal deposits in arc environments has received little attention, despite the fact that CO_2 is an abundant component of fluxing of magmatic volatile phases in arc magma systems. This chapter focuses on a series of experiments designed to examine the role of CO_2 as a component of synthetic magmatic-hydrothermal assemblages also to and evaluate changes to chloride-dependent copper partitioning in a manner similar to previous experimental work on CO_2-free systems. I will first discuss previous work on CO_2-free, melt, volatile phase copper partitioning experiments and relevant natural analogs. I will also discuss the current state of knowledge on the role played by CO_2 in the formation of porphyry copper deposits and in magmatic arcs, in general. I will compare my results for the partitioning of copper among melt, vapor and brine with results from these CO_2-free experiments. I will also present a model for the efficiency of removal of copper from melts into CO_2-bearing MVPs and the implications of the model results on the formation of porphyry copper deposits.

2.1.1   Copper Partitioning in Porphyry Copper Deposits and Experiments

Measurement of homogenization temperatures in natural fluid inclusions provides strong support for the interpretation of a magmatic source for ore fluids in porphyry copper deposits. However, as discussed in the previous chapter, the trapping conditions of these inclusions are generally sub-solidus and significant adjustment to magmatic

volatile phase compositions is expected prior to ore deposition. Experimental work allows for the examination of melt-volatile phase equilibria with controlled variation of the magmatic volatile phase components to address the impact of MVP compositions on ore formation. The characterization of copper partitioning between magmatic phases at equilibrium, and models for the efficiency of removal of copper into exsolving volatile phases, can provide constraints on the magmatic conditions and compositions that are likely to result in the formation of porphyry copper deposits.

Experimental melt-vapor-brine partitioning studies have, to date, produced data indicating copper partitioning favors the brine phase relative to the coexisting vapor (Candela and Piccoli, 1995; Frank et al., 2011; Lerchbaumer and Audetat, 2009; Simon et al., 2006; Ulrich and Mavrogenes, 2008; Williams et al., 1995). Experimental efforts have identified aspects of magmatic volatile phase chemistry that affect melt-volatile phase copper partitioning, but many aspects of variability in magmatic volatile phases remain unconstrained. In addition, data from natural systems are quite varied in the bulk and trace element compositions of ore fluids, and produce complex and often conflicting results, requiring continued experimental research.

The silicic arc magmas emplaced at shallow depths (~ 5 to 10 km) associated with porphyry copper deposits are ultimately derived from deeper basaltic and andesitic melts. Fractional crystallization of the mantle or crustal melts can take place before or after ascent of these melts, generating andesitic magmas (~60% crystallization). The silicic magmas associated with porphyry copper deposits are produced, in part, by further magma differentiation at shallow levels (~ 90% crystallization from initial lower crustal melts and/or partial melting of intermediate rocks) (Annen et al., 2006). The mantle

derived basaltic melts that intrude into the lower crust are hypothesized to have H_2O

concentrations ranging from 2 to 6 wt% (Annen et al., 2006; and references therin).

Residual melts formed from crystallization of the mixed mantle and crustal melts stored

in the lower crust can have dissolved H_2O concentrations over short residence times up to

15 wt% (Annen et al., 2006). This is in contrast to the generally dry rocks inferred to be

present in the lower crust. Annen et al. (2006) discuss, in detail, arguments for the

generation of deep, super-liquidus, andesitic melts, which may rise nearly adiabatically

through the crust. The super-liquidus state of these melts can allow for resorption of

crystals entrained with the magma during ascent (Annen et al., 2006). Upon ascent, these

melts may rise from ~30 km to ~15 km before reaching the volatile phase saturation

pressure for a particular batch of melt. The first boiling of andesitic or primary basaltic

melts will then result in fluxing of H_2O (and possibly CO_2) though any overlying magma

chambers. Upon emplacement at shallow levels (5 to 10 km), these magmas will lose heat

and crystallize nearly isobarically and may become saturated with respect to a second

volatile phase assemblage (second boiling).

The volatile phases exsolved from crystallizing silicic magmas during first and

second boiling are dominated by H_2O and CO_2. However, dehydration of the subducting

slab also introduces chlorine and sulfur to arc magmas along with H_2O and CO_2. Fluid

and melt inclusions from PCD, barren intrusions and volcanic emissions, along with

models for the evolution of arc magmas, are consistent with Cl/H_2O ratios of shallow

felsic magmas that are initially influenced by the salinity seawater ($Cl/H_2O \sim 0.02$).

However, subducting slabs may also be enriched in chlorine relative to seawater, and/or

may exsolve fluid preferentially enriched in chlorine relative to water. As a result,

progressive fluid generation from the subducting slabs may release volatile phases with variable Cl/H_2O ratios.

Candela and Piccoli (2005) summarize data from volcanic arcs and model Cl/H_2O ratios suggesting that subducting slabs may initially generate fluids with high Cl/H_2O ratios (up to 0.1), five times that of seawater (0.02), for some arc environments. As the distance from the arc front increases, the Cl/H_2O ratio decreases. As a result, the Cl/H_2O ratios of arc magmas generated in the mantle and lower crust will be variable, and will depend on the chlorine enrichment of the slab, dynamics of fluid generation (e.g. slab angle, temperature, distance from the subduction front) and any crustal-derived chlorine or water component of the melts. The relatively low Cl/H_2O ratios (< 0.1) common for arc magmas generally leads to initial saturation with respect to a low-salinity vapor or supercritical fluid (Audetat et al., 2008; Candela and Piccoli, 2005; Heinrich et al., 2004; Jarrard, 2003; Lowenstern, 2000; Sillitoe, 2010; Sinclair, 2007). Chlorine can be modeled as a perfectly incompatible element in crystals relative to melt, and a moderately incompatible element in felsic melts relative to volatile phases ($D_{Cl}^{v/m} \sim 5$) for felsic magmas at shallow (~5km) emplacement depths (Candela and Piccoli, 1998). The Cl/H_2O ratio of the melt will therefore determine the salinity of the exsolved supercritical fluid, vapor, or the proportion of coexisting vapor and brine.

If brine saturation occurs at shallow magmatic conditions (< 130 MPa), evolving volatile phases will generally enter the two-phase field from the vapor limb and the vapor/brine mass ratio will remain high (Audetat et al., 2008; Bodnar, 1995; Candela and Piccoli, 1998; Sillitoe, 2010). Thermodynamics requires that at a given pressure and temperature, upon reaching vapor + brine saturation, the chlorine concentration of a melt

and both volatile phases becomes fixed, independent of the proportion of vapor and brine (Candela and Piccoli, 1998; Shinohara, 1994). The low variance required by the phase rule permits changing the phase proportion of a coexisting H_2O-NaCl vapor-brine pair to investigate partitioning behavior in a synthetic MVP assemblage without any effect on the Cl content of the melt.

The analysis of a quenched mixture of vapor and brine phases was used by Williams et al. (1995) to characterize copper partitioning between a melt and a magmatic vapor + brine assemblage at magmatic conditions (800 ^{o}C and 100MPa, and 850 ^{o}C and 50 MPa). Comparison of these data with the higher pressure experiments (140 MPa) presented by Candela and Holland (1984) suggest that a maximum exists for the apparent Cu-Na exchange constant ($K_{Cu,Na}^{(MVP)/m}$) between the aqueous volatile phases and the silicate melt at a pressure of 100 MPa. Williams et al. (1995) suggested that the maximum is a result of competition between changes in the density of the brine-saturated vapor and changes in melt polymerization. A decrease in melt polymerization, due to higher solubility of water in the melt with increasing pressure, causes $K_{Cu,Na}^{(v+b)/m}$ to decrease at pressures above 100 MPa. In contrast, the lower vapor density at pressures below 100 MPa reduces solute-solvent effects in the vapor, resulting in a decrease of $K_{Cu,Na}^{(v+b)/m}$ with decreasing pressure (Bodnar et al., 1985; Churakov and Gottschalk, 2003; Williams et al., 1995). The potential maximum of $K_{Cu,Na}^{(v+b)/m}$ also roughly correlates with observations of a maximum salinity for exsolved magmatic fluids at a pressure of ~130 MPa (Audetat et al., 2008). Nernst-type partition coefficients for brine-melt and brine-vapor of $D_{Cu}^{b/m} =$ 700 and $D_{Cu}^{b/v} = 120$ ($D_{Cu}^{v/b}$=0.008), respectively, were reported in Williams et al. (1995)

by modeling the proportion of vapor and brine using vapor and brine salinities estimated based on the data presented by Bodnar (1985).

The development of fluid inclusion analysis techniques has allowed for great improvements in the characterization of multiple elements in samples of magmatic and high temperature sub-solidus fluids. Fluid inclusion analyses can reveal a wide variety of information regarding the partitioning of ore metals in porphyry ore systems. Fluid inclusions can sample the magmatic-derived fluids (primary inclusions) involved in ore deposition, providing insight into the composition of those fluids. Some inclusion analysis techniques used in previous studies include Raman spectroscopy, used for gas species analysis, and Proton Induced X-Ray Emission (PIXE) for compositional analysis of fluid inclusions. Unfortunately, PIXE requires accurate measurement of the 3d geometry of inclusions, which are difficult to obtain (Gunther et al., 1998; Heinrich et al., 1992). The development of techniques for analysis of fluid inclusions by Laser Ablation Inductively Coupled Plasma Mass Spectrometry (LA-ICPMS) allows for quantification of fluid inclusion composition via simultaneous analysis of major elements (e.g Na, K) along with low concentration trace elements (e.g. Cu). Work by Gunther et al. (1998) demonstrates that LA-ICPMS allows for linear instrument response over 9 orders of magnitude in the concentrations for most elements of interest in the formation of porphyry copper deposits. The application of LA-ICPMS analytical techniques to the study of deposits and experiments has allowed for accurate quantitative measurement of the composition of magmatic hydrothermal fluids. The data from these studies have helped elucidate the partitioning behavior of copper among magmatic and hydrothermal phase assemblages from a wide variety of PCD and synthetic systems.

Some porphyry deposits (Bingham Cave Peak; Audetat et al. 2008) have vapor-brine fluid inclusion assemblages that show higher concentrations of copper in brine inclusions relative to vapor inclusions. This may indicate brine dominated copper transport from the magmatic regime to ore deposition, consistent with salinity dependent copper complexation. Yet, several deposits contain vapor-brine boiling assemblages (vapor and brine fluid inclusions from the same generation of quartz precipitation, implying coexisting phases) that have vapors enriched in copper relative to salinity-dependent copper partitioning. Grasberg, Bajo de Alumbrera (Ulrich et al., 1999), Yankee Load (Audetat et al., 1998), El Teniente and Santa Rita (Audetat et al., 2008), all have vapor inclusions with greater copper concentrations than the coexisting brine ($D_{Cu}^{b/v}$ values ≤ 1). In addition, several deposits with brines enriched in copper relative to the coexisting vapor ($D_{Cu}^{b/v}$ values > 1), such as Bingham Canyon (Redmond et al., 2004), are still consistent with copper partitioning that includes vapor-enrichment in copper relative to the critical vapor-brine salinity ratio.

Vapor inclusions enriched in copper relative to coexisting brine inclusions are often offered as evidence for vapor dominated copper transport from magmatic conditions to ore deposition. The expectation that copper is partitioning between vapor and brine only as Cu-Cl complexes should lead to brine dominance, rather than often observed vapor dominant copper partitioning behavior. Additional ligands (H_2S-Chapter 3) may account for some of the variability in apparent partitioning of copper between vapor and brine. However, changes to volatile phase compositions during transport from magmatic conditions to ore deposition will alter ore fluids trapped as fluid inclusions from their initial magmatic compositions. As discussed, this requires that the observation

of vapor dominated copper partitioning, observed in some coexisting vapor and brine inclusions, remain a measure of fluid compositions at sub-solidus condition or at the time of ore deposition. Direct evidence of metal partitioning at magmatic conditions is most readily derived from magmatic-hydrothermal experiments. Comparison of natural inclusions to magmatic conditions must include either complete characterization of the processes that occur during fluid ascent, or must be made based on mass balance considerations. Nonetheless, the high mass fraction of vapor relative to brine demonstrates the importance of vapor transport from the magma to the sites of ore deposition for many ore deposits (Audetat et al., 2008; Sillitoe, 2010).

The conditions under which fluids are trapped in natural fluid inclusions differ significantly from the magmatic conditions during exsolution of magmatic volatile phases. Experiments at magmatic conditions can investigate the melt-volatile phase equilibria that control the efficiency of removal of copper into exsolving MVPs. Yet this means that the fluids generated in melt-vapor-brine experiments are the product of magmatic melt-volatile phase equilibria, and at best, are representative of proto-ore fluids as they exsolve from a magma and extract ore metals. The processes of fluid ascent, decompression, cooling, mixing and reaction necessarily changes the properties of magmatic volatile phases. In order to characterize the magmatic volatile phases that control ore metal extraction from the magma and transport in the hydrothermal regime, more detailed experiments are required.

Experimental melt-vapor-brine data from LA-ICPMS analysis of fluid inclusions reported by Simon et al. (2006) indicate that copper partitions strongly into high-salinity magmatic brines relative to coexisting low-salinity vapors ($D_{Cu}^{b/v} = 3.7$ at 800 $^{\circ}$C and

140MPa) for S-free, CO_2-free experiments. Sulfur-bearing experiments at similar

conditions are consistent with an increase in the copper concentration of the magmatic

vapor, but the brine remains enriched in copper relative to the vapor ($D_{Cu}^{b/v}$ decreases but

remains > 1) (Frank et al., 2011; Simon et al., 2006). The data reported by Simon et al.

(2006) are also consistent with a maximum in the Cu-Na exchange $K_{Cu,Na}^{v/m}$ at 100 MPa.

This is consistent with Williams et al. (1995) and Candela and Holland (1984) given that

changes to the vapor salinity were hypothesized to control Cu-Na exchange in the

aqueous mixture analyzed. Some experimental data at sub-solidus conditions of 600 to

700 ^{o}C (Lerchbaumer and Audetat, 2009) and at hydrothermal conditions ranging from

350 to 450 ^{o}C (Pokrovski et al., 2005) also indicate that copper partitions strongly into

high-salinity brines compared to low-salinity vapors in the system NaCl-H_2O. This is in

contrast to some studies discussed previously that characterize apparent copper

partitioning into vapors relative to coexisting brines at sub-solidus conditions in porphyry

deposits. A small number of experimental studies have produced boiling assemblages

(coexisting vapor and brine) at lower temperatures and pressures (500 to 650 ^{o}C and 35 to

50 MPa) that are consistent with vapor dominated copper partitioning (Nagaseki and

Hayashi, 2008; Nagaseki et al., 2006). These experiments produced a small number of

sulfur-bearing vapor and brine fluid inclusion assemblages in which the copper

concentration of the vapor inclusions was greater than that of the brine inclusions. The

vapor-dominated behavior in these studies is confined to sulfur-rich fluid compositions

that may mimic ore fluids at conditions of ore deposition. However, it remains unclear

what properties of the vapor and brine change from magmatic conditions to produce this

different partitioning behavior. In addition, the budget of copper budget available for

transport from magmatic conditions to those of ore deposition must rely on the efficiency of removal of copper from the melt during exsolution of magmatic vapor and brine.

The results of recent experiments have also illuminated the need for diligence when evaluating copper, and other univalent cations, in natural settings that may have experienced multiple hydrothermal fluxing events; two examples are detailed below. Experimental work presented by Zajacz et al. (2009) identified the possibility of diffusive re-equilibration of fluid inclusions with respect to univalent cations, resetting the concentration of trapped fluid inclusions to that of later generations of magmatic fluids. Other researchers evaluating the alteration of previously trapped fluid inclusions from natural deposits have also begun to report experimental results that confirm the possibility for re-equilibration of vapor inclusions (Lerchbuamer and Audetat, 2011). These results may appear to be in conflict with the results presented for fluid inclusion analyses from ore zones in a number of porphyry copper deposits, but experiments at magmatic conditions are most useful in developing models for metal extraction by proto-ore fluids and are not directly comparable to natural fluids at sub-solidus conditions. The data from magmatic experiments should be used to fill gaps in our understanding of melt-volatile phase equilibria based on evidence recorded in natural systems.

The static copper partition coefficients reported for melt-vapor-brine assemblages consistently demonstrate a strong correlation between MVP salinity and copper concentration. However, initial chlorine concentration and Cl/H_2O ratios of silicate melts will exert a strong control on the efficiency of removal of copper into exsolving volatile phases during second boiling. The general efficiency of removal of copper into an MVP is usually defined by the concentration of copper in the accumulated magmatic volatile

phase ($[Cu]_{MVP}$), compared to the initial concentration in the silicate melt ($[Cu]^0_{melt}$), as

shown in Equation (1) below.

$$E = \frac{[Cu]_{MVP}}{[Cu]^0_{melt}}$$ (1)

The salinity of the exsolving vapor is determined by the melt/vapor partition coefficient

for chlorine, and the Cl/H$_2$O ratio of the melt. Copper is generally compatible in bulk

felsic igneous minerals ($D^{xtal/melt}_{Cu} \sim 2$)(Candela and Piccoli, 1998), and loss of copper from

the melt to small fractions (< 1wt%) of sulfide minerals (e.g. pyrrhotite) slowly depletes

the melt in copper during crystallization prior to volatile phase saturation (Jugo et al.,

1999; Mengason et al., 2010; Simon et al., 2008a). After volatile phase saturation, copper

becomes incompatible ($D^{xtal/melt}_{Cu} \sim 0.2$), partitioning strongly into the exsolving MVP(s) if

sulfides no longer crystallize from the magma (Candela and Piccoli, 1998; Jugo et al.,

1999; Simon and Ripley, 2011). In order to account for the evolution of exsolving MVPs,

models for magma crystallization and volatile phase exsolution have supplemented

copper partitioning experiments. These models investigate the role of various parameters

related to melt-volatile phase equilibria in determining the potential for ore deposit

formation.

Given the indications that MVP salinity has a strong influence on copper

partitioning, Candela and Piccoli (1998) presented a model for evaluating the efficiency

of removal of copper into magmatic volatile phases (MVPs) exsolved during second

boiling. The model involves a felsic magma, water under-saturated, cooling and/or

crystalizing before volatile phase saturation. Trace elements, including copper, are

partitioned between crystals and melt, reducing the efficiency of removal of copper from the melt into MVP(s) proportional to the fraction of the melt crystallized.

At some point in the crystallization of the melt, determined by the ratio of the water concentration in the melt relative to the water concentration at saturation, the melt saturates with respect to a vapor phase. Heat flow into cooler host rocks progressively crystallizes small fractions of melt, and for each aliquot of crystallization a known mass of vapor, or vapor + brine bubbles are formed. The buoyant bubbles of vapor and/or brine extract major elements and copper from the coexisting melts according to their chloride-dependent MVP/melt partition coefficients. Under certain conditions in natural systems these bubbles accumulate in the cupolas and dikes near the roof of a magma chamber. The budget of ore metals in the accumulated MVP bubbles is controlled by the integrated efficiency of removal of copper by successive aliquots of vapor and brine exsolved from the melt. Thus, the sum of the masses of each aliquot of magmatic vapor or brine represents an estimate of the total efficiency of removal of copper into the MVP(s) (E) during second boiling.

The MVPart model allows for varying the pressure, temperature, and initial water and chlorine concentrations of the melt to explore the variation in the efficiency of removal of copper from the melt into MVPs predicted for the range of conditions observed in natural arc magmas during exsolution of volatile phases. In addition to characterization of the partitioning of copper for melt-volatile phase equilibria in CO_2-beraring experiments, I also present a modified version of the MVPart model. The CO_2-MVPart model will incorporate the experimental data on the $NaCl$-H_2O-CO_2 system and

copper partitioning data presented in this study. I then present modified predictions for the efficiency of removal of copper from the melt into MVPs as a function of X_{CO_2}.

2.1.2 *CO_2 in Arcs and Porphyry Copper Deposits*

One important aspect in the formation of porphyry copper deposits, and other magmatic hydrothermal deposits, has not been included experimental work; the effect of the presence of CO_2 as the second most abundant magmatic volatile phase component in arc magmas remains poorly constrained in experimental partitioning studies (Anderson et al., 1989; Botcharnikov et al., 2005; de Leeuw et al., 2007; Fischer, 2008; Jarrard, 2003; Liu et al., 2005; Lowenstern, 1994; Lowenstern, 2001; Sano and Williams, 1996; Wallace, 2005). Volcanic emissions in active arcs range from nearly CO_2-free to close to 100% CO_2. This CO_2 can be derived from the mantle as part of the fluxing of volatile phases that generates arc magmas or via reaction and/or assimilation of carbon-bearing country rocks. Isotopic data suggest that the CO_2 flux from mantle depth is dominantly sourced from slab sediments (90%) with a small mantle input (10%) (de Leeuw et al., 2007). Models of slab fluxes presented by Jarrard (2003) indicate that the H_2O/CO_2 ratio of most slab derived volatile phases ranges from 5 to 10 (10 mol% to 20 mol% CO_2). As the magmas generated by the addition of slab derived fluxes of volatile phases ascend, they decompress, crystallize, change composition and may saturate with respect to volatile phases at various stages of ascent. Deeper mafic magmas can initially saturate with respect to a volatile phase with an H_2O/CO_2 ratio as low as 0.05 (~95 mol% CO_2) (Botcharnikov et al., 2005; Lowenstern, 2001). These volatile phases may ascend into, and mingle with, overlying, more evolved magmas (Botcharnikov et al., 2005; Lowenstern, 2001). Titrating CO_2 rich volatile phases through the overlying felsic

magmas can influence volatile phase compositions during exsolution and may impact the efficiency of removal of copper from the melt. Variability in the X_{CO2} of the MVPs is controlled by a variety of subduction characteristics including slab age, angle and rate of subduction, sediment composition, etc. (Jarrard, 2003) If CO_2 affects metal partitioning, then aspects of a particular slab which can influence the H_2O/CO_2 ratio and total mass of CO_2 evolved will affect the efficiency of removal of copper from the magma into volatile phases.

Whereas dissolved, mantle-derived CO_2 is controlled by the composition and P-T conditions of the silicate magma, the assimilation of carbon-bearing country rocks can not only add CO_2 to magmas, but can also affect magma composition; specifically melt composition or the relative oxidation of the magma (fO_2). The assimilation of reduced organic carbon by rising magma will generate both CO_2 (Equation **2**)

$$2C + 2H_2O = CO_2 + CH_4 \tag{2}$$

and CH_4 via reaction with H_2O. The CH_4 generated can then reduce iron-oxide and other magmatic system components (Equation **3**).

$$CH_4 + Fe_2O_3 \text{ (melt)} = 2FeO \text{ (melt)} + H_2O + CO_2 \tag{3}$$
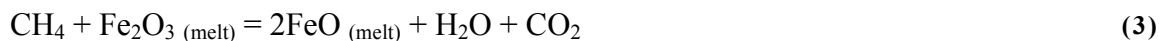
Magma oxygen fugacity has been shown to be a master variable for numerous magma evolution and metal partitioning processes. Changes in iron speciation, sulfur speciation and the stability of Fe-Cu-Au -bearing sulfides, associated with changes in fO_2, can exert a strong control on copper partitioning and efficiencies of removal of copper by the MVPs (Candela and Holland, 1984; Candela and Piccoli, 1995; Candela and Piccoli, 2005; Holland, 1965; Whitney, 1984).

Organic-rich shale units are generally more aluminum rich than arc magmas, and assimilation of shale host rocks into the silicate melt may induce crystallization and slightly increase the Al_2O_3 concentration of the melt in addition to affecting melt fO_2 and adding CO_2. A felsic magma comprising a melt saturated with feldspar, biotite and hornblende must further crystallize to raise the temperature (generating latent heat) and dissolve any shale host rock assimilated. The higher $Al_2O_3/(Na_2O+K_2O+CaO)$ ratio of the shale may also result in decomposition of hornblende to generate biotite. In contrast, the assimilation of limestone by the same melt would add dominantly CaO in addition to CO_2. This would result in decomposition of biotite to produce hornblende. However, the thermal cost (heating the country rock and dissolution in the melt) of assimilation of any host rocks equivalent to even 10% of the mass of the melt will usually result in nearly complete crystallization of a felsic magma.

Mafic and andesitic melts deeper in arc systems also assimilate host rocks during ascent and emplacement. The thermal cost of assimilation still remains, and may contribute to crystallization and differential of the arc magmas. Thus, assimilation of host rocks, and associated addition of CO_2, is limited by the excess heat of magmas (maintaining magmas at supra-solidus conditions). However, thermal dehydration and de-carbonation of host rocks may add CO_2 to shallow melts without significant incorporation of the host into the melt. These reactions can proceed with considerably lower heat flow out of the magma than complete assimilation. Addition of CO_2 via this form of contact metamorphism can occur throughout magmatic intrusion in arc systems.

The CO_2 concentration of arc magmas can increase from initial slab concentrations (10 mol% to 20 mol%) via enrichment of melts during differentiation

and/or interaction with host rocks. As a result, evolved magmas may initially saturate

with respect to a volatile phase with high CO_2 concentrations. Measurements of CO_2 in

melt inclusions from the Bishop Tuff suggest that the Bishop magma would have been in

equilibrium with a vapor phase containing as much as 45 mol% CO_2 (X_{CO2}=0.45)

(Anderson et al., 1989). However, where CO_2 data are available for porphyry deposits the

indication is that ore-fluids fall at the low end of the range seen in arc systems in general;

between 0 mol% to 10 mol % (Table 1) (Audetat et al., 2008; Lowenstern, 2001;

Redmond et al., 2004; Rusk et al., 2008).

Deposit/Experiment	Deposit Type	$D_{Cu}^{b/v}$		CO_2	Reference
Porphyry				(in V-rich FI)	
Bajo de la Alumbrera	Cu-Au	0.25		-	Ulrich et al. (1999)
Grasberg	Cu-Au	0.25-1		**Low**	Bakker et al. (2003)
Santa Rita	Cu-Mo-Au	0.25-1		**< 5mol%**	Audetat et al. (2008)
Bingham	Cu-Mo	2		**Low**	Redmond et al. (2004)
El Teniente	Cu-(Mo)	0.9		-	Audetat et al. (2008)
Butte	Cu-Mo-Au	-		**5 mol%**	Rusk et al. (2004)
Pine Grove	Mo-(Cu)	-		**Low**	Lowenstern (2001)
Yankee Lode	Sn-(Cu)	0.1		**Low**	Audetat et al. (1998)
Epithermal					
Tambo	Au	-		**up to 3 mol%**	Deyell et al. (2005)
Ohaaki	Au-Ag	-		**8-14 mol%**	Simmons et al. (2008)
Jinchang	Au	-		**CO_2-rich**	Zhang et al. (2008)
Experimental (800°C)	Element		MPa		
Condensed Fluid (MVB)	Cu	120	100	**N**	Williams et al. (1995)
Variable fS_2 FI (MVB)	Cu	7 to 17	100	**N**	Frank et al. (2011)
Fluid Inclusions (MVB)	Cu	3.7 ± 1.3	140	**N**	Simon et al. (2006)
Sulfur-Bearing FI (MVB)	Cu	1.4 ± 0.3	140	**N**	Simon et al. (2006)

Table 2: Copper partitioning behavior and CO_2 concentration of natural and experimental magmatic-hydrothermal systems. Natural deposits shown contain vapor inclusions with copper concentrations equal to or greater than brines, and often containing CO_2. Epithermal systems are observed with low, moderate and high concentrations of CO_2. Experiments do not commonly reproduce vapor dominant copper partitioning and do not contain CO_2. (MI) = melt inclusions; (-) = CO_2 concentration uncharacterized

Both high-salinity brines and low-salinity vapors have been trapped, at elevated

temperature and pressure, in inclusions found in porphyry and related ore deposits. If the

presence or absence of CO_2 does not play a role in ore genesis, then the same range of

CO_2 concentrations in fluid inclusions from deposits should be the same as that extrapolated for MVPs in equilibrium with arc magmas in general. However, several alternative explanations for this discrepancy must also be addressed. The mixing of magmatic fluids with other H_2O-rich fluids prior to trapping inclusions could dilute the concentration of CO_2 in the proto-ore fluids. However, even CO_2-free non-magmatic fluids would only dilute the X_{CO2} of the mixed fluid proportionally to the degree of contamination. Hydrogen isotopic analyses of the fluid inclusions from natural deposits and oxygen isotopic analyses of alteration minerals are consistent with, at minimum, a dominantly magmatic source for the trapped fluids (Dilles et al., 1992; Harris et al., 2005; Sillitoe, 2010). Given the limited range of CO_2 in PCD, the minimal dilution of magmatic CO_2 by fluid mixing is not a viable mechanism for explaining the discrepancy in X_{CO2}.

Another hypothesis might be that the fluids depositing copper in PCD are derived from a different stage of magmatism or exsolution of volatile phases. This argument requires that the CO_2-rich fluids that do or do not extract ore metals do not contribute to ore-deposition or are not sampled by fluid inclusions. The possibility of changes to metal partitioning or ore deposition as a function of X_{CO2} supports the need to investigate the effects of CO_2 on deposit formation. However, a complete account of the effects of CO_2 on fluid transport of metals in PCD will not be possible based solely on the results of the experiments described in this chapter. Nonetheless, the small range of X_{CO2} observed for natural deposits is an indication that CO_2-rich fluids play a negative role in the formation of porphyry deposits. In order to address this discrepancy, and the effect CO_2 may have on melt-volatile phase equilibria and copper partitioning, I present a series of experiments that evaluate copper partitioning in synthetic CO_2-bearing melt-vapor-brine assemblages.

The experiments reported in this study provide direct experimental measurements of copper partitioning between coexisting vapors, brines, and silicate melts at variable X_{CO_2} in the MVPs. Understanding $NaCl$-H_2O-CO_2 phase relationships is vital to understanding exsolution of CO_2-bearing volatile phases by arc magmas. The salinity data reported for the CO_2-bearing fluid inclusions from this study (determined by microthermometry) also provide experimental support for the model presented by Duan et al. (1995) for $NaCl$-H_2O-CO_2 at 800 ^{o}C and 100 MPa.

The experiments include an aqueous $NaCl$-KCl-$FeCl_2$-HCl magmatic volatile phase similar to that used in other experiments (Candela and Holland, 1984; Simon et al., 2006; Williams et al., 1995) as a proxy for the complex chloride component of volatile phases exsolved from magmas in arc systems. In order to quantify the composition of the MVPs, I present several variations on trapping synthetic fluid inclusions in quartz by pre-fracturing (Simon et al., 2006), or in-situ fracturing (Sterner and Bodnar, 1991) the quartz cores and trapping vapor and brine fluid inclusions. LA-ICPMS analyses of quenched glasses and fluid inclusions were then used to generate partition coefficients and equilibrium constants for copper partitioning at magmatic conditions. The sulfur-free copper partitioning data reported in this chapter are consistent with a decrease in the equilibrium efficiency of removal of copper into the vapor correlated with a decrease of the brine-saturated vapor salinity with increasing X_{CO_2}. The impact of this shift in copper partitioning can be extrapolated to conditions of dynamic exsolution of volatile phases using the CO_2-MVPart model presented in this chapter.

The common deposition of copper as sulfide in porphyry deposits also points to copper-sulfur complexes as another potentially important component to MVP-melt

partitioning behavior. Accordingly, the role of sulfur (including possible interactions with

CO_2) is at the forefront of ore deposit research (Alletti et al., 2009; Frank et al., 2011;

Jugo et al., 1999; Lerchbaumer and Audetat, 2009; Mengason et al., 2010; Mengason et

al., 2008; Pokrovski et al., 2008; Pokrovski and Dubrovinsky, 2011; Pokrovski et al.,

2009b; Simon et al., 2007; Simon et al., 2006; Zajacz et al., 2010a; Zajacz et al., 2011).

The combined effect of variable X_{CO2} on sulfur-bearing and chlorine-bearing copper

complexes was investigated by the CO_2-bearing and sulfur-bearing experiments

discussed in Chapter 3.

2.2 Experimental Methods

2.2.1   Starting Materials

Experiments with CO_2-bearing MVPs were run in Pt capsules or in Cu_6Au_{94}

capsules (OD/ID : 5.0/4.9 mm, 1.75 to 2.5 cm length). The Cu_6Au_{94} capsules were

fabricated using a technique presented by Zajacz et al. (2011). In that procedure, gold

tubes were electroplated with a known mass of copper on the external surface of the tube.

After cleaning the excess electroplating solution from the tube, along with any salts that

may have formed, the tube was dried and prepared for alloying. Fused silica tubes with

ID = 6 to 7 mm and wall thickness 0.5 mm were then sealed at one end and the copper

plated gold tubes were placed inside the silica tube. The silica tube was then sealed under

vacuum. The proto-capsule was then heated to ~850 $^{\circ}$C for one day to begin the alloying

process and prevent any eutectic melting at the Cu/Au interface. The temperature was

then raised to 930 $^{\circ}$C for 3 days to allow for a homogeneous alloy to form over the length

of the capsule before cooling to room temperature. Each proto-capsule was then

inspected for signs of contamination or copper oxidation.

Prior to running the experiments, the capsule material was cleaned and anealed at temperatures > 1200 $^{\circ}$C for Pt and > 900 $^{\circ}$C for Cu_6Au_{94}. The welding of Pt and Cu_6Au_{94} capsules was performed in a bath of cold CO_2 vapor (formed from sublimation of dry ice) to mitigate capsule oxidation due to heat generated by the carbon arc welder. At the pressure and temperature conditions of the experiments (800 $^{\circ}$C and 100 MPa) felsic silicate melts were generated from either powdered Bishop Tuff or powdered Corning Glass, a 100 MPa haplogranite minimum melt (GR1). The Bishop Tuff was formed from ash fall deposits mixed with varying amounts of associated ignimbrites (clasts of dominantly biotite, plagioclase, quartz, and sanidine as well as small amounts of apatite and magnetite) occasionally visible as grains within crushed samples (Hildreth and Wilson, 2007; Wilson and Hildreth, 1997). To determine the composition of the hydrous starting melt, Bishop Tuff was melted in a separate experiment at the same run conditions and in the presence of excess H_2O (See Table 3). The hydrous starting melt was allowed to form a glass upon cooling. The hydrated melt generated from the powdered Bishop Tuff was peraluminous, with an ASI = 1.21 calculated according to Equation (4)

$$ASI = \frac{[Al_2O_3]}{[Na_2O + K_2O + CaO]} \tag{4}$$

presented by Shand (1949).

The ASI or "Aluminum Saturation Index" compares the aluminum and alkali components of the melt, and provides a comparison to feldspar stoichiometry. The powdered Corning Glass (haplogranite) has a composition close to the 100 MPa water-saturated granite minimum melt (Table 3). The use of a haplogranite melt was particularly important for CO_2-bearing experiments (X_{CO2} = 0.38) as it allowed for maintaining a low degree of crystallization (crystals are dominantly alkali feldspar and

plagioclase) and thus, minimal change to melt composition compared to low-CO_2

experiments. In contrast, experiments attempted at high X_{CO2} with Bishop Tuff magmas

were almost entirely crystalline by the end of the run. This would make measurements of

the glass composition, and melt-volatile phase copper partitioning data, difficult of

obtain. The absence of iron in the synthetic haplogranite glass required the addition of

magnetite in order to ensure accurate comparison of MVPs at low and high X_{CO2}.

Bishop Tuff (wt%)		GR1 (Starting Glass-wt%)	
Na_2O	2.7%	Na_2O	3.7%
MgO	0.02%	MgO	0.1%
Al_2O_3	14.1%	Al_2O_3	11.1%
SiO_2	72.4%	SiO_2	75.2%
K_2O	6.6%	K_2O	4.4%
CaO	0.03%	CaO	0.17%
TiO_2	0.08%	TiO_2	0.03%
MnO	< 0.01%	MnO	0.01%
FeO	0.03%	FeO	0.04%
ASI	1.2	ASI	0.99

Table 3: Starting glass compositions for hydrated Bishop Tuff and GR1. Analyses of glass formed from Bishop Tuff melt performed using EPMA methods described in section (3.4). Composition of Corning starting glass (GR1), was determined by Frank et al. (2001) using XRF. ASI values are shown for comparison to run product glasses.

Natural magnetite collected from Essex City, New York was added to some

experiments, to ensure sufficient iron was available for maintaining magnetite-saturated

conditions regardless of whether magnetite is created or destroyed during the run. The

natural magnetite contains small impurities of titanium (0.3 wt%), manganese (0.08 wt%)

and less than 100 ppm vanadium and cobalt (Mengason, 2007). Acid tests conducted on

crusted samples of magnetite were consistent with little to no carbonate contamination.

Thus, no effect on the major element composition or X_{CO2} of the magmatic phases is

expected due to the addition of magnetite. Oxalic acid dihydrate (99.5% oxalic acid,

purchased from Alfa Aesar) was used to generate CO_2 in all experiments. Other

experiments have utilized silver oxalate to add CO_2 to noble metal capsules (Sterner and

44

Bodnar, 1991). However, Kruger and Diamond (2001) reported evidence that silver oxalate may react with NaCl-bearing solutions and may change homogenization behavior of fluid inclusions synthesized in experiments utilizing silver oxalate. Copper oxalate could be used in its place, but it remains unclear if the same reaction problem exists for other salts of oxalic acid. Regardless, the high concentration of CO_2 required for the experiments in this project prevents the use of these CO_2 sources because the concentration of silver or copper in the experiments would become > 10 wt% for high-CO_2 runs. High silver or copper concentrations will change the bulk chemistry of the vapor and brine, adding undesired variance between low-CO_2 and high-CO_2 experiments. The use of oxalic acid allows for precise control of the concentration of CO_2 while mitigating undesired reactions and variable concentrations of silver or copper at the start of an experiment.

Natural, inclusion-free Brazilian quartz was cored to create 4 mm diameter cylinders for trapping fluid inclusions. Water was used to lubricate during cutting. Cores were cleaned in ethanol and dried in an oven for 12-24 hours to ensure that no additional water or contaminants were added to the experimental charge. Starting solutions were created by using oven dried NaCl, KCl, standardized 1M HCl, and anhydrous $CuCl_2$.

2.2.2 Experiment Design

Experiments with $X_{CO2} = 0.10$ and 0.38 (the maximum value possible given the experiment design) were conducted to evaluate the effect of CO_2 on copper partitioning within the X_{CO2} range observed in natural arc systems. Experiments were run in noble metal capsules inside René alloy vessels at magmatic conditions for five days. The René vessels, used in combination with noble metal capsules that are permeable to H_2 at

45

temperatures in excess of 500 °C (Chou, 1987), buffer the oxygen fugacity of the experiments to near Ni-NiO. At elevated run temperatures (800 ^{0}C), the vessel material allows for control of the oxygen fugacity via H_2 diffusion across the walls of the Pt or CuAu capsule, and the resulting equilibrium with the internal aqueous solution and external water pressure medium. The final oxygen fugacities of the CO_2-bearing experiments are log fO_2 = NNO and log fO_2 = NNO – 0.2 for experiments at X_{CO2} = 0.10 and 0.38, respectively (Appendix II).

When osmotic H_2 equilibrium has been established between the capsule contents and the external pressure fluid, the fO_2 inside the capsule will still not match the vessel fugacity because of the difference between the fH_2O inside and outside the capsule. The equivalence of fH_2 between two reservoirs of different fH_2O, yields different oxygen fugacities by virtue of the equilibrium constant, as shown in Equation (5) below.

$$K_w = \frac{[fH_2]^2[fO_2]}{[fH_2O]}$$
(5)

The value of the equilibrium constant (K_w = 4.4x10^{-19}) was calculated by SUPCRT92 for 800 °C (Johnson et al., 1992). On average, an internal capsule fO_2 ~ 0.1 to 0.4 log units below that of the vessel is expected for the compositional range in my CO_2-bearing experiments. This intrinsic fO_2 of the René vessels used in our experiments has been measured to NNO + 0.1 to 0.2 log units via CoPd alloy-CoO sensor, and consideration of the equilibria described by Chou (1987) and Taylor et al. (1992) (Appendix I).

During the initial increase of pressure and temperature, oxalic acid decomposes, ultimately yielding CO_2, H_2O (from hydrate) and H_2 gas. The decomposition produces CO_2, rather than CO or CH_4, given that the decomposition proceeds quickly at temperatures above 400 °C (Higgins et al., 1997). The CO_2 generated has a volume less

46

that the internal capsule volume at experimental conditions. Other experiments confirm

that upon decomposition, silver oxalate (salt of oxalic acid) (Schmidt and Bodnar, 2000;

Sterner and Bodnar, 1991) and oxalic acid (Azbej et al., 2007; Fall et al., 2011) can be

used to accurately generate the desired quantity of CO_2. The formation of H_2 gas requires

more careful consideration as it causes temporary disequilibrium between the experiment

and the intrinsic vessel fO_2.

Oxalic acid decomposition is accompanied by the generation of H_2. The increase

in the fH_2 lowers the initial fO_2 of the experiments (< NNO -3 log units) (Appendix II).

Using the method described by Chou (1987), I calculated the time required for the system

to reach equilibrium. This requires removal of H_2 from an experiment capsule by

diffusion. Numerically, this was accomplished by recursively calculating the internal

hydrogen fugacity using estimates of the volatile phase proportions, and simplified

fugacity calculations. The activity coefficient for H_2, at experimental conditions and a

low proportion of H_2 as a MVP component, varies ~ 5%. Assuming one value for the

activity coefficient of the H_2 component of the MVP simplified the calculation, resulting

is a slight underestimate of the initial fH_2 and slight overestimate of time required for

equilibration. Based on this model, experiments performed in Cu_6Au_{94} capsules required

~ 4 to 40 hours to reach equilibrium with respect to H_2. Experiments performed in Pt

capsules required only 0.5 to 5 hours for fH_2 equilibration (See Appendix II for details).

The starting aqueous solution for the experiments was also varied as changes were

made to the X_{CO2}. As discussed, the oxalic acid used to generate CO_2 in the experiments

is hydrated. Thus, changing the amount of oxalic acid added to the experiment changes

the amount of chloride-free water added as well. The chemistry of the starting aqueous

solution must be adjusted accordingly to account for the water added along with CO_2

from the oxalic acid hydrate. This also ensures that a Cl/H_2O ratio similar to that of vapor

+ brine mixtures exsolved from felsic magmatic systems ($Cl/H_2O \sim 0.06$) was maintained

in all experiments. The starting solution in all experiments was an equal mixture of NaCl

(1.75M) and KCl (1.75M) with roughly 0.1M HCl. Additionally, all the solutions

contained $\sim$5000 ppm copper added as $CuCl_2$.

The starting ratios of water, carbon dioxide and salts were designed to generate

coexisting vapor and brine phases at the experiment conditions (800 ^{o}C, 100 MPa). A

ternary plot for the $NaCl-H_2O-CO_2$ system generated by using software based on the

model presented by Duan et al. (1995), shows the two-phase field of interest in the CO_2-

bearing MVP experiments (Figure 4). The NaCl component of the ternary system was

used as a proxy for the $NaCl-KCl-HCl\pm CaCl_2\pm FeCl_2$ MVP chloride component of the

experiments, and for the more complex chloride components in natural systems. The

formation of a two-phase field with the addition of chlorides to the H_2O-CO_2 binary is a

colligative property, and the "salinity" of the coexisting phases is controlled by the effect

of the number of particles present. The presence of divalent cations (Ca^{2+} and Fe^{2+}) will

yield 3 particles instead of 2 and the low concentration of these species can be treated as

1.5 $NaCl_{eq}$ to ensure accurate estimation of the appropriate phase relations.
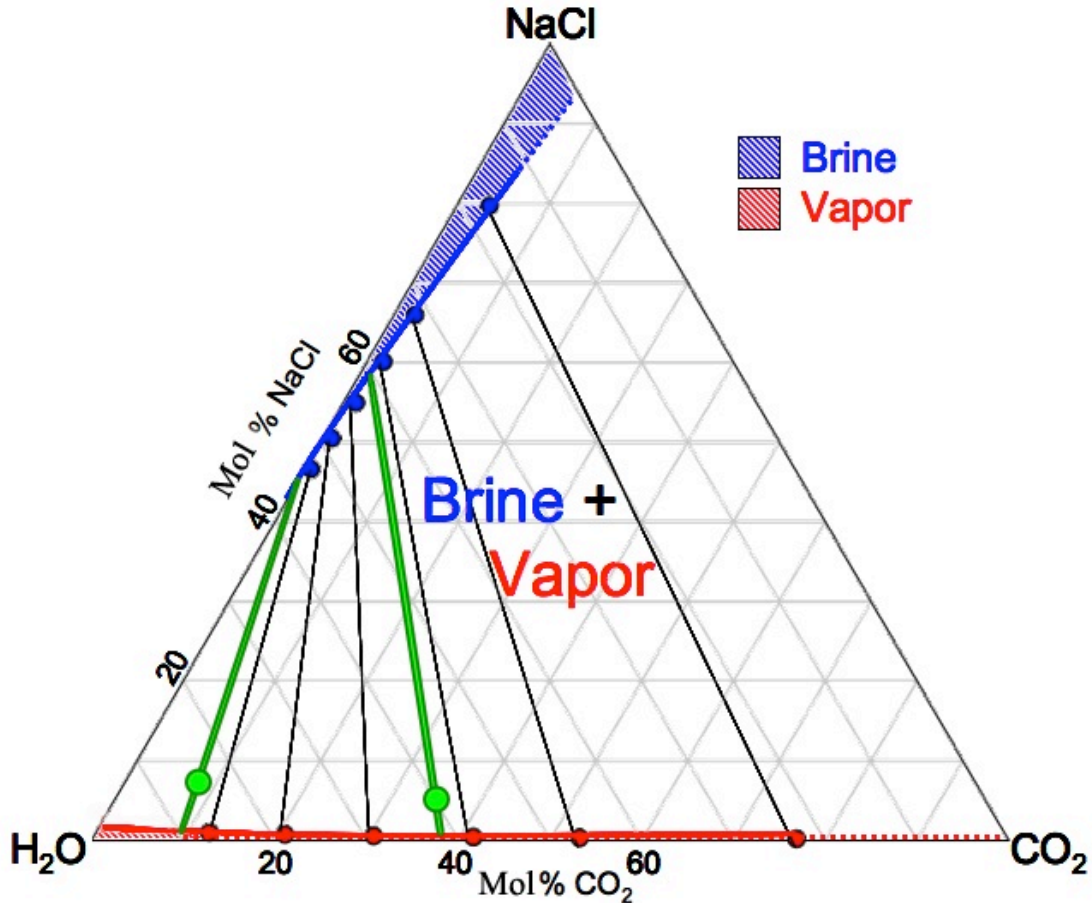
Figure 4: Schematic H$_2$O-CO$_2$-NaCl ternary shown in mole % for 800 °C and 100 MPa generated using the model presented in Duan et al. 1995. Green lines and dots represent the compositions of the bulk MVP and the individual vapor and brine components. Initial compositions within the two-phase field will exsolve coexisting vapor and brine.

An inclusion-free natural quartz core was added to each charge to allow for

trapping of synthetic vapor and brine fluid inclusions at run conditions. Early

experiments utilized pre-fractured quartz cores (fractured prior to the start of the run),

employing a method similar to that described by Simon (2007). An in-situ fracturing

technique (fractured during the run at magmatic conditions) described in Sterner and

Bodnar (1991) was used for later experiments. This technique requires that an un-

fractured quartz core is placed inside the capsule. After allowing for equilibration of the

run at high temperature, the vessel is then inverted and the capsule falls the cold end of

the vessel. This results in a drop in the temperature surrounding the capsule from 800 °C

to ~ 400-450 $^{\circ}$C. The drop in temperature shock fractures the quartz core and the vessel is then quickly inverted again, returning the capsule to the hot end with little time for formation of any low temperatures phases. This technique ensures equilibration between volatile phases, silicate melt, and capsule at the desired oxygen fugacity prior to trapping inclusions (see Discussion section for details). In all in-situ fractured experiments, the quartz was fractured on day three of the experiment to ensure fO_2 equilibration prior to fracturing while still leaving two days for inclusion formation. A schematic diagram of the experiment design is shown in Figure 5.

Once a capsule was prepared and welded, it was loaded into a René 41 alloy cold seal pressure vessel. The vessel was inclined at an angle of ~12° from horizontal, cold end down, to minimize convection (Figure 5). At shallower angles, horizontal convection of the pressure fluid results in larger thermal gradients across the capsule. At steeper angles the capsule may easily fall to the cold end of the vessel. Internal thermocouples were used to record thermal gradients of approximately 4^{0}C across the length of a sample capsule and record temperatures within 1 to 2 ^{0}C to an external thermocouple.
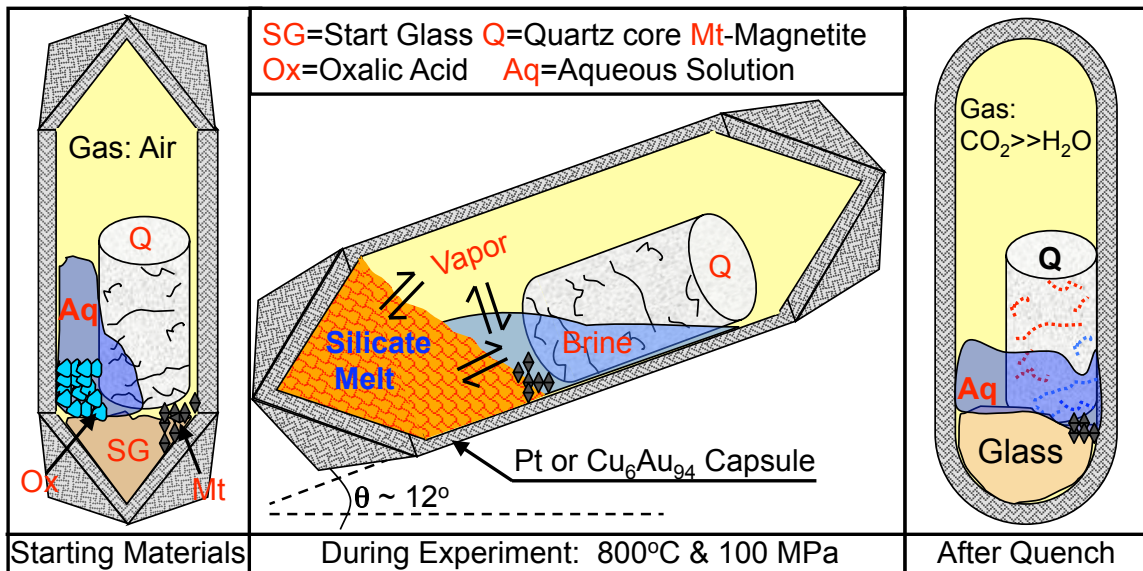
Figure 5: Schematic diagrams showing the Pt capsule phase assemblage throughout an experiment. The angle θ shows the vessel angle above horizontal during the experiment. Arrows indicate the equilibration of the melt-vapor-brine assemblage during 3 to 5 days at conditions shown. Red and blue dots shown inside quartz core after quench represent vapor and brine fluid inclusions.

After the vessel is fitted with a thermocouple and placed in the furnace an initial pressurization is performed. Generally, the system is pressurized to ~20 to 50 MPa to test the vessel seal, force aqueous solution into the fractured quartz inside the capsule and prevent capsule rupturing during vigorous oxalic decomposition (Schmidt and Bodnar, 2000). The temperature and pressure are then raised to 800 ^{o}C and 100 MPa over ~ 30 minutes. Once a stable temperature was obtained, a constant pressure and temperature (± 2 ^{o}C) was maintained for five days, except during in-situ fracturing, to ensure equilibration. A small drop in pressure and temperature occurs during fracturing. However, the temperature and pressure were never allowed to drop more than 10% from their equilibrium values ensuring that the capsule returns to 800 ^{o}C and 100 MPa within 10 minutes of fracturing. After five days the vessel was removed from the furnace, and compressed air was blown across the vessel until the vessel reached room temperature, which takes roughly 1 to 2 minutes. After the whole vessel-assembly was cooled the remaining system pressure was released and the capsule was extracted.

2.2.3 Run Products

In order to compare the composition of the magmatic phases and associated copper partitioning, the composition of the silicate melt and magmatic vapor and brine were determined from run products which preserve the magmatic phase compositions down to ambient P-T conditions. The silicate melt composition was preserved from 800 ^{o}C down to the ambient conditions through rapid cooling down to temperatures below ~500 ^{o}C in less than 1 minute (5 ^{o}C/sec), producing homogeneous glass from the small mass (15 to 30 mg) of silicate melt. Water speciation experiments presented by Nowak and Behrens (1995) demonstrate that similar hydrous (4.14 wt%) metaluminous (ASI = 0.98) haplogranite melts at similar conditions (800 ^{o}C and 1500 MPa), and slower cooling rates (5 ^{o}C/min), had glass transition temperatures of ~ 600 ^{o}C. Other rapid quench experiments (5 ^{o}C/sec) presented by Deubener et al. (2003) are consistent with somewhat lower glass transition temperatures of ~ 500 ^{o}C for hydrous granitic melts at the 800 ^{o}C and 100 MPa and 4 wt% water, and with minimal water loss from the melt. The lower glass transition temperature has been assumed to be valid to ensure that quench time was not underestimated.

Testing of compressed air quench methods to cool the René vessels at the end of a run confirms that the experimental capsules consistently reached the glass transition temperature in ~1 minute. The short cooling time helps to ensure that the composition of the silicate melt is well preserved by the run product glass, and that trace elements (e.g. copper) are not lost during protracted dehydration of the melt. Care was also taken to maintain pseudo-isobaric conditions upon cooling until the glass transition temperature was reached. This minimizes inclusion formation due to the exsolution of bubbles of

vapor and brine expected during decompression. Decreasing the number and size of fluid inclusions formed upon quench resulted in large regions of inclusion-poor glass (>20 μm), which were selected for analysis, and improves retention of as much of the H_2O + CO_2 dissolved in the melt as possible.

Samples of the vapor and brine were trapped as synthetic fluid inclusions during "healing" of the fractures in the quartz cores at high temperature during the run. The use of synthetic fluid inclusions allowed for trapping the homogeneous magmatic volatile phases. Any mineral precipitation that occurred during quench from a single aliquot of a MVP occurred entirely within the volume of the inclusions. Given that an inclusion has "healed" completely closed, analysis of the entire inclusion volume, including these precipitated phases, provides a complete picture of the composition of the trapped MVP. Quartz cores were sectioned parallel to fluid inclusion trails and doubly polished until inclusions were 10-40 μm beneath the surface of the quartz.

Within the quartz-hosted fluid inclusion assemblages, inclusions were chosen that were associated with large regions of similar inclusions to minimize analysis of inclusions formed from a mixture of vapor + brine. Only inclusions > 10 μm and < 60 μm were selected for analysis to ensure a strong sample signal and to minimize the chances of decrepitation (exploding during ablation) or incomplete inclusion capture (see Section 2.3.5 for details). As discussed in detail in Section 2.3, the salinity of quartz-hosted fluid inclusions was first characterized to confirm a low degree of two-phase mixing, and to use as an internal standard for LA-ICPMS. The LA-ICPMS analysis of the fluid inclusions allowed for simultaneous quantification of major and trace element

concentrations, which were then averaged to yield the composition of the magmatic

vapor and brine for a given experiment.

2.2.4   Demonstration of Equilibrium

Bishop Tuff or synthetic haplogranite melt cool from 800 ^{o}C through their

assumed glass transition temperature (~ 500 ^{o}C) (Deubener et al., 2003) in ~1 minute

during quench. Significant diffusive re-equilibration of copper in the melt during quench

would result in spatially variable copper concentrations in the run product glass, which

would prevent accurate estimation of the melt copper concentrations. However, trace

elements such as chlorine, and copper have characteristic diffusion distances (L_d) of, at

most, 5μm to 20μm over this time interval (Zhang et al., 2010). The L_d is defined by the

diffusion coefficient (K_d) and time (t) according to Equation (6) below.

$$L_d = 2\sqrt{K_d t}$$
(6)

Given that the glass bead formed upon quench is on the order of 1 mm in maximum

dimension, the [Cu]$_{melt}$ should be homogeneous across the sample. Small heterogeneities

may exist near the edges of the grains or near large inclusions. However, any gradients in

copper or chlorine will occur over smaller distances than the analytical volume of the

glass analyses. To confirm this hypothesis, the copper concentration throughout the run

product glass was examined for heterogeneity.

Early experiments utilizing pre-fractured quartz cores were susceptible to some

disequilibrium if the concentration of copper in the MVPs was variable throughout the

experiment. Some fluid inclusions may represent early MVPs whereas the glass formed

from the silicate melt was in equilibrium with the final MVP composition. As discussed,

the use of in-situ quartz fracturing helps ensure that fluid inclusions sample equilibrated

fluids and prevents transient disequilibrium features from affecting the apparent equilibrium between the MVPs and silicate melt. The pre-fractured quartz cores from our experiments usually sampled fluids close to equilibrium, but significantly more scatter and somewhat elevated MVP copper concentrations are observed in the data from pre-fractured experiments.

In addition, glass-hosted brine inclusions have been analyzed from a subset of the CO_2-bearing experiments in order to compare their composition to the quartz-hosted brine inclusions used to characterize MVP compositions. Glass-hosted brine inclusions were formed upon quench, trapping the brine *inside* the glass formed from the final silicate melt. Consistency between the composition of glass-hosted and quartz-hosted brines confirms that the quartz-hosted brine-vapor assemblages also represent equilibrium compositions. The composition of the run product glass was also measured close (<50 µm) to Cu-rich brine inclusions during their ablation to make a host correction. These glass analyses were then compared to analyses from the inclusion-poor glass used to quantify the composition of the silicate melt to check for any exchange of copper between melt and large fluid inclusions. Thus, equilibrium was assessed based on two factors; homogeneity of the copper concentration of the silicate melt, and consistency between the copper concentration of quartz-hosted and glass-hosted inclusions. Consistency in glass and fluid inclusion compositions confirm that partition coefficients and equilibrium constants calculated from these analyses represent equilibrium magmatic conditions.

2.3 Analytical Techniques

2.3.1   Fluid Inclusion Microthermometry

Fluid inclusion microthermometry is the determination of the major element chemistry of fluid inclusions by observations of phase changes that occur during the heating or freezing of inclusions. The goal of microthermometry conducted on the synthetic fluid inclusions from this study was to determine the salinity of the inclusions, or more accurately the NaCl concentration. The sodium concentration was then used as an internal standard for LAICPMS analyses. The salinities of both vapor and brine fluid inclusions from CO_2-bearing experiments were measured using microthermometry. The technique for analyzing each type of inclusion is detailed below.

The quartz core containing vapor and brine inclusions was mounted in Crystal Bond and cut into 400-1000 μm thick slices. The slices were doubly polished yielding the inclusion trails of interest sub-parallel to the polished surface at depths between 10-40 μm. Petrographic observation of fluid inclusion assemblages was used to discriminate brine-dominant or vapor-dominant zones of an inclusion assemblage. Inclusions were discriminated via consistency in precipitated salt content or vapor-bubble volume in brine and vapor inclusions, respectively. Inclusions that show significant deviation from the norms for each experiment were identified as mixed inclusions (vapor + brine) and were usually observed at or near a vapor-brine interface within the healed fracture(s). Inclusions identified as mixed inclusions were avoided for analysis, though microthermometric measurements were also used to identify some mixed inclusions missed by visual observations. Inclusions that deviate from the 2σ standard deviation of

the remaining vapor or brine inclusions from a single experiment were also labeled as mixed inclusions and not analyzed by LA-ICPMS.

Inclusions that are obviously "necked" or interconnected were not used as they also usually represent mixed or uncertain compositions. Small groups of vapor and brine inclusions were observed during heating and cooling cycles using the USGS microthermometry stage. Nitrogen gas was heated (via a heating coil) or cooled (via a liquid N_2 bath) and then flowed through the chambers to heat or cool the sample chip. The sample was held in place by a thermocouple, which was also used to monitor the temperature during the analysis, and was standardized to the freezing point of distilled water at $0\ ^oC$ and 0.1 MPa. Measurements made on a USGS stage with the thermocouple tip within 1 mm of the inclusions have temperature uncertainties of $< 0.2\ ^oC$.

2.3.2 Brine Inclusions

The brine inclusions from my experiments were identified at room temperature by the presence of two or more crystalline phases, a vapor bubble, and aqueous solution filling the remainder of the inclusion (Figure 6 A). The dominant crystalline phases are halite (NaCl) and sylvite (KCl) crystals that precipitated from the brine upon quench. Inclusions used range in size (diameter) from 30 microns down to ~10 microns.
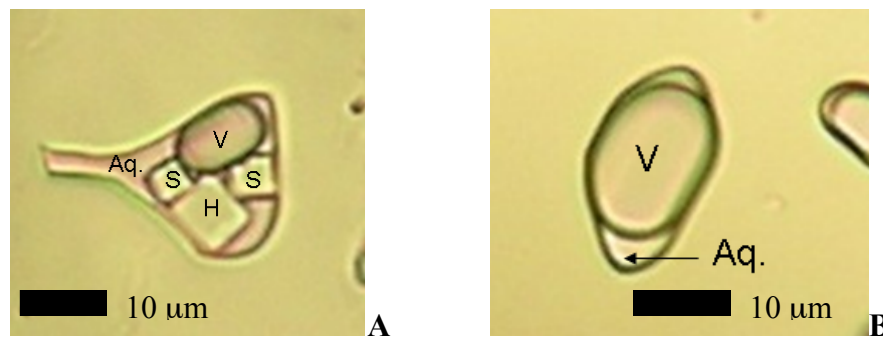
Figure 6: Photomicrographs of brine (A) and vapor (B) inclusions from experiment Cu#320. Phases identified are: (H) Halite, (S) Sylvite, (Aq.) Aqueous Solution, and (V) Vapor (CO_2 dominant)

57

Once an inclusion (or several proximal inclusions) is selected, a voltage is applied to the

heating coil while 30 cfs (cubic feet per second) of N_2 flows across the coil into the stage.

As the temperature rises, the sylvite begins to dissolve into the aqueous solution first,

followed by the halite. The dissolution temperature of the two crystalline phases is then

used to calculate both the Na/K ratio of the inclusion as well as its bulk salinity using the

Fortran program SALTY outlined in Bodnar et al. (1989) (Figure 7).

Phase Equilibrium for H₂O-NaCl-KCl-Vapor-saturated Brine Inclusions
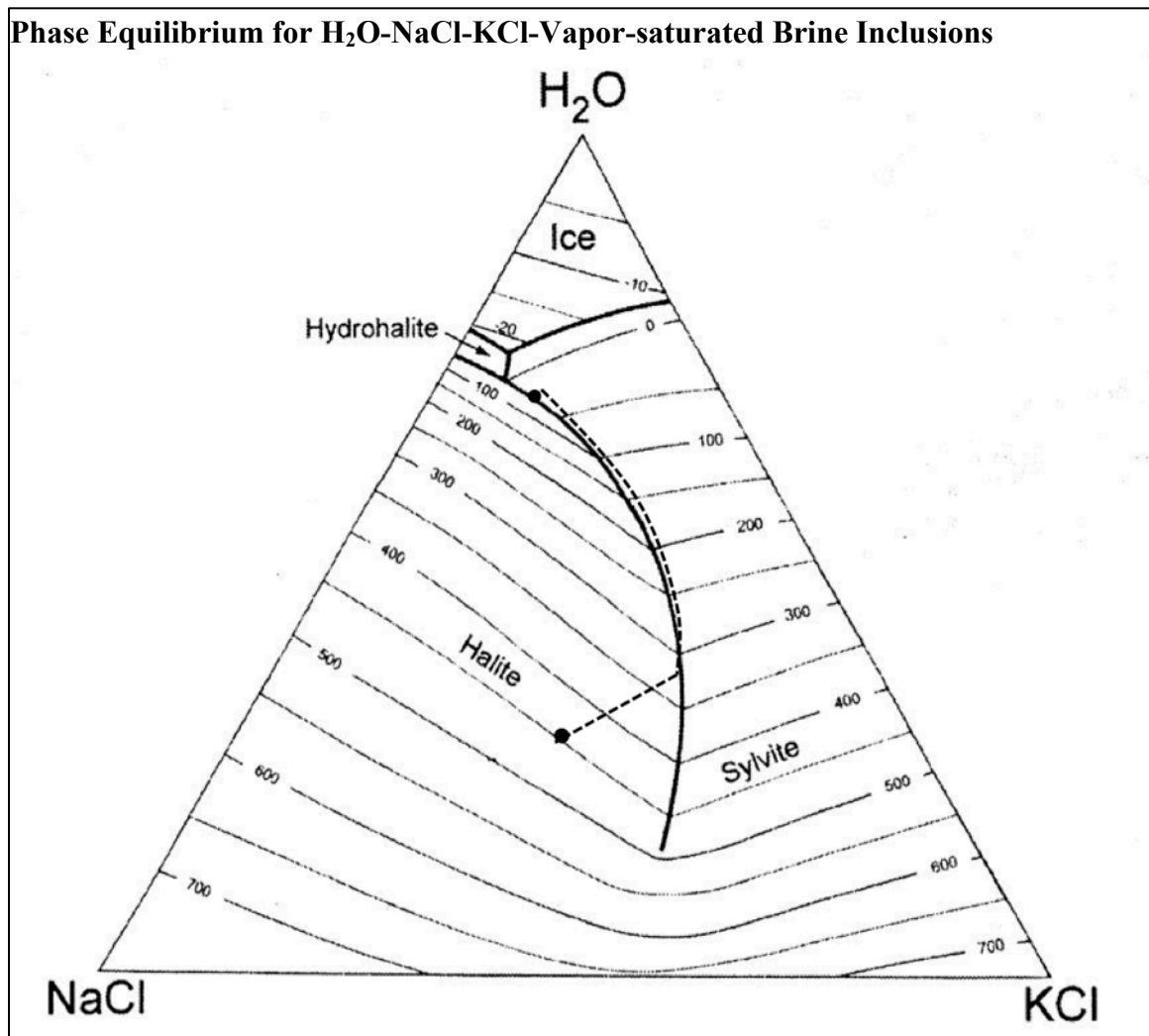
Figure 7: Polybaric phase diagram in wt% (presented in Bodnar 2003) demonstrating the composition of a vapor-saturated aqueous solution in equilibrium with halite, sylvite or both at a given temperature. The composition of a given inclusion can be determined by following the equilibrium path of the system upon heating until both sylvite and halite dissolve (Example path shown as the dashed line above - Calculation uses FORTRAN program SALTY).

2.3.3   Vapor Inclusions

The vapor inclusion microthermometry is significantly more complicated than that of brine inclusions. Vapor inclusions were identified at room temperature by a large vapor bubble (~80% of the inclusion volume) and condensed aqueous liquid (Figure 6 B). The inclusions used were similar in size to the brine inclusions. Freezing of inclusions to -100 ^{o}C resulted in the formation of three or more new phases. The phases of interest are clathrate, ice, and a solid CO_2-rich phase formed by the vapor bubble. The clathrate is a solid phase composed of a mixture of CO_2 and H_2O. The ice phase is H_2O-ice with a small amount of the NaCl and KCl incorporated. Upon heating the vapor inclusions, the CO_2-rich phase disappears first at ~ -56 ^{o}C. Second, the ice will melt to form aqueous liquid at temperatures from -6 to -1 ^{o}C. Lastly, the clathrate melts at ~ +4 to +10 ^{o}C and was the most difficult to observe.

The hydration of CO_2 produces structure I clathrates with the formula 6X-2Y-46H_2O where "X" is a gas "cage" made of 24 water molecules and "Y" is a cage made from 20 water molecules (Diamond, 1994; Sloan and Koh, 2008). The more simplified formula is 8H_2O•(CO_2, H_2S), and thus the nucleation of clathrate removes salt-free water equal to eight times the quantity of gas enclathrated. This will artificially enrich the remaining water in salt, resulting in erroneously high salinities calculated using ice melting temperatures. Only clathrate melting temperatures provide an accurate measure of the vapor inclusion salinities for vapor inclusions that nucleate clathrate upon cooling.

To determine clathrate melting temperatures (T_m^{clath}) the inclusions were heated slowly to a predetermined temperature (e.g. +1 ^{o}C) and then the heating coil was turned

off and cold air quickly re-cools the inclusions. If clathrate was still present in the inclusion, crystal growth was observed at the vapor-liquid interface. The inclusion was then heated to 0.1-0.5 ^{o}C higher than before (1.1-1.5 ^{o}C) and then rapidly cooled. The melting point has been reached when no clathrate grows immediately upon cooling. Clathrate is very slow to melt or nucleate upon heating or cooling and cyclical heating is necessary to ensure accurate determination of T_m^{clath}.

Often, the observation of the freezing point depression of both clathrate and ice are used along with a volume estimate of the vapor bubble to determine the composition of vapor inclusions in CO_2-bearing vapor inclusions. Several computer programs outlined by Bakker and Brown (2003) use the phase change and volume observations to evaluate the composition of the inclusions yielding mole proportions of H_2O, CO_2, Na, K, and Cl. However, this method results in very large uncertainties and imprecision in the low fluid inclusion pressure (P_{FI}) range of interest. Other accurate methods for salinity determination exist, but rely upon the observation of both CO_2 vapor and CO_2 liquid during heating/freezing experiments (Bakker and Diamond, 2000). In order to characterize vapor inclusions containing CO_2 vapor only at room temperature, the salinity of CO_2-bearing vapor inclusions was determined using only the T_m^{clath} and an accurate direct measurement of CO_2 density, or pressure of the inclusion, when only one CO_2 phase was observable. The clathrate stability field is depressed to lower temperatures by the addition of increasing concentrations of chlorides (Bakker and Brown, 2003; Diamond, 2003; Fall et al., 2011; Sloan and Koh, 2008). As with water, the freezing point depression of clathrate is a colligative property, and the mixture of NaCl, KCl, HCl, and minimal $CaCl_2$ and $FeCl_2$ in vapor inclusions from CO_2-bearing experiments will behave

almost identically to pure NaCl. Only $CaCl_2$ and $FeCl_2$ produce three solvated particles rather than two, increasing the effect of these chlorides by 50%, which can be accounted for when calculating total salinity. Accurate modeling of the clathrate stability boundary (Sun and Duan 2006) allows for determination of the salinity required for the T_m^{clath} to intersect the CO_2 isochore for the inclusion at the clathrate stability boundary.

Previous studies have shown that Raman spectroscopy can be used to determine the density of CO_2-bearing inclusions (Kawakami et al., 2003) albeit at higher pressures in metamorphic environments. Work by Fall et al. (2011) utilized a custom pressure cell to investigate CO_2 Raman peak splitting in the region from 1-10 MPa in 0.5 MPa increments and fit an empirical 3rd order polynomial to the data, shown below in Equation (7).

$$\rho CO_2 = -0.03031 \cdot \Delta^3 + 9.432 x 10^9 \cdot \Delta^2 - 977.9 \cdot \Delta + 33780 \tag{7}$$

The density of the inclusion (ρCO_2) can then be converted to a pressure using NIST empirical equation of state calculations for CO_2 (Lemmon et al., 2012). By identifying the density of the inclusion, the CO_2 isochore can be then used to find the fluid inclusion pressure (P_{FI}) at T_m^{clath}. More detailed information on Raman CO_2 measurements is available in Appendix V.

Raman analyses were conducted at Virginia Tech using a JY Horiba LabRam HR (800 mm) spectrometer and a 514.53 nm Laser Physics 100S-514 Ar^+ Laser with assistance of technician Charles Farley. Raman spectroscopy was first used to characterize the carbon species present in vapor inclusions, specifically ruling out the formation of CO or CH_4 during the decomposition of oxalic acid. Values of P_{FI} were calculated by application of the model presented by Fall et al. (2011) to the peak splitting

measured Raman analyses of run product vapor-rich inclusions from the CO_2-bearing experiments of this study. Pressure measurements match both the observed phase assemblage (CO_2 vapor only), as well as simplistic isochoric quench calculations. Isochoric quench calculations for vapor-rich inclusions model the phase transformations of sealed inclusions from 800 ^{o}C and 100 MPa trapping conditions to 25 ^{o}C using NIST empirical EOS calculations (Lemmon et al., 2012). Condensation of the H_2O-rich component of an inclusion will results in a corresponding pressure drop in the dominantly CO_2 vapor phase, which was estimated by incorporating the X_{CO2} and estimates of salinity.

The Raman density calculation model (Fall et al., 2011) cites a ± 0.2 MPa analytical uncertainty cited, which is combined with the variance observed between three measurements of the same inclusion to obtain the uncertainty for the pressure of a given inclusion assemblage (variance between inclusions was less than the instrument uncertainty). The pressure calculated using the Raman CO_2 density calculation (P_{FI}), and T_m^{clath} must intersect on the salinity dependent clathrate stability boundary. The model of the salinity dependence of clathrate stability presented by Duan and Sun (2006) was then used to find the salinity at which the clathrate stability boundary passes through the intersection of P_{FI} and T_m^{clath} for a vapor-rich inclusion (Figure 8).
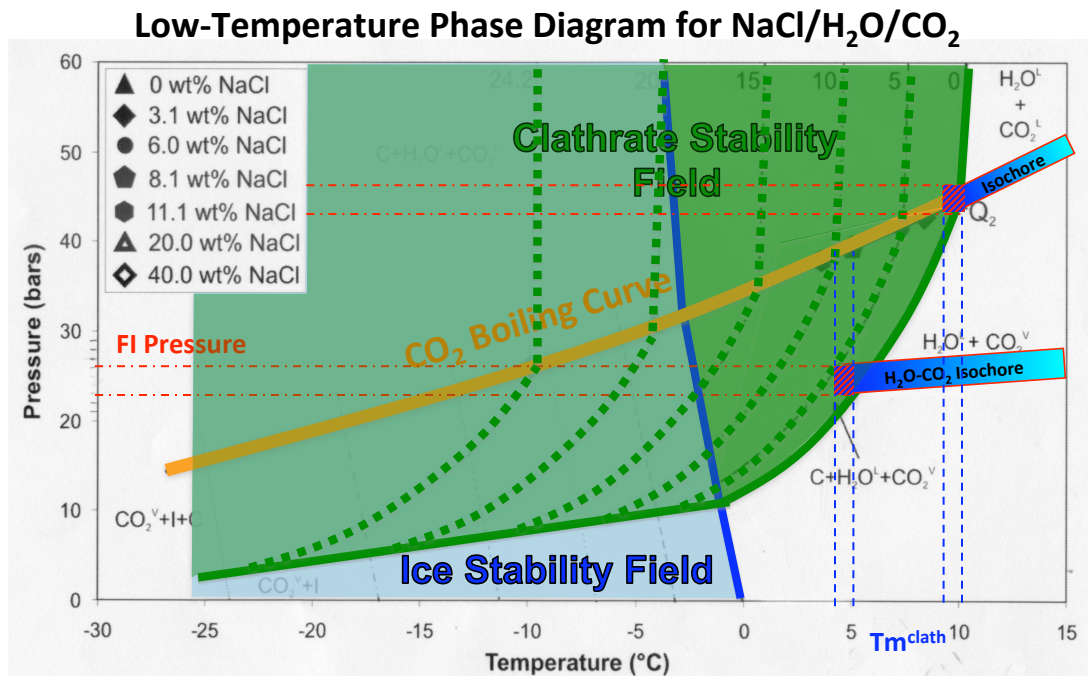
Figure 8: Clathrate stability diagram for low-pressure H₂O-CO₂ clathrates, modified from (Diamond, 2003). Clathrate is stable to higher temperatures than ice for the composition of all CO2-bearing experiments of this study. The isochore for low X_{CO2} fluid inclusions (lower) falls in the liquid water (H₂O^L) + vapor carbon dioxide (CO₂^V) field, and intersects the clathrate stability boundary in a point defined by the clathrate melting temperature (blue dashed lines) and the fluid inclusion pressure at that temperature (red dashed lines). The isochore for high X_{CO2} fluid inclusions (upper) intersects the CO₂ boiling curve (orange) at temperatures above clathrate stability. Once immiscible liquid CO₂ forms in the inclusion the isochore will follow the boiling curve and clathrate will form from the liquid-liquid-vapor H₂O-CO₂ mixture. The clathrate melting temperature (determined by microthermometry) and pressure of the fluid inclusion (determined by Raman) are input into the model for clathrate stability (Duan and Sun, 2006) to calculate inclusion salinity. The dashed green boundary lines show the decrease in the melting temperature of clathrate with increasing salinity.

2.3.4   EPMA Analysis of Run Product Glasses

The major element chemistry of run product glasses from sulfur-free, CO₂-bearing experiments was determined using a JEOL 8900 Superprobe Elecron Probe Microanalyzer (EPMA). The glasses were mounted in 1" epoxy mounts, polished, and mapped for inclusion free zones and large brine inclusions. The degree of crystallization was also estimated using transmitted and reflected light microscopy. Regions of silicate glasses observed (transmitted light microscopy) to have minimal fluid inclusions near the

surface were chosen for EPMA spots to minimize contamination by incorporation of fluid inclusions in the analytical volume. A qualitative assessment was also made of the degree of heterogeneity and crystallization present in the glass by assessing the average composition of the glass across the sample surface using backscatter electron imaging (BSE).

Quantitative Wavelength Dispersion Spectroscopy (WDS) was used to characterization the major element composition (Na_2O, K_2O, CaO, FeO, Al_2O_3, SiO_2) and trace element composition (Cl) of each run product glass sample. External standards for glass analyses included Yellowstone rhyolite (Na_2O, K_2O, Al_2O_3, SiO_2), hornblende (FeO, CaO), and scapolite (Cl). Several spots (~10-30 μm diameter) within one or more glass sample from each experiment were selected, and an accelerating voltage of 15 kV, and a beam current of ~ 5 nA were used for major element analysis of all glasses. A low beam current was necessary to minimize the diffusion of Na away from the analysis spot and ensure an accurate glass analysis. The use of a larger beam diameter also promotes analysis of a representative glass volume. Between 8 and 20 glass analyses were collected for each experiment, discarding some analyses for low totals (< 90%) and element ratios consistent with erroneous analysis of feldspar or quartz. Totals for major element glass analyses fall slightly below 100% owing to 2 to 4 wt% water content. WDS analyses were also used to calculate values of melt ASI and as and were used as an additional standard for LA-ICPMS analyses of melt copper concentrations.

2.3.5   LA-ICPMS Analysis of Fluid Inclusions

Quantification of the composition of fluid inclusions was achieved by LA-ICPMS analyses allowing for simultaneous, quantitative analysis of most elements present in the

inclusions (Na, K, Fe, Si, Al, Cu, ± Au, ± Ca). The use of LA-ICPMS on fluid inclusions was rigorously described by Gunther et al. (1998) and has since undergone numerous improvements. Quadropole mass spectrometers allow for limits of detection (LOD) in the ppm range for most "trace" elements analyzed along with major elements (Heinrich et al., 2003; Mutchler et al., 2008). Assuming complete inclusion signal capture, Heinrich et al. (2003) demonstrated that 10 to 15 sampling cycles for each element are necessary for fluid inclusion LA-ICPMS to avoid systematic errors. Complete signal capture requires that all the phases present in an inclusion are completely sampled and are included in the sample signal integration. This is especially important for inclusions containing precipitates (halite, sylvite, etc.) to ensure accurate element ratios and bulk chemistry. Additionally, the use of a He carrier gas maximizes the fraction of material reaching the plasma by maximizing aerosol formation in the low-density gas and minimizing deposition outside the ablation crater which can also distort element abundances.

LA-ICPMS analyses were conducted at the Virginia Tech Fluids Research Group facility using an Agilent 7500ce ICPMS and a GeoLas 193nm eximer laser with the assistance of technician Luca Fedele. The LA-ICPMS analysis requires that all inclusions are ~ 20 to 50 μm below the surface of the quartz, which maximizes the signal intensity and minimizes explosive fracturing (decrepitation) of the quartz due to laser heating of the inclusions. Each analysis session started and ended with the collection of two NIST 610 glass standard analyses to use as an external standard and to correct for instrument drift. During each fluid inclusion analysis session, several other sets of standard analyses were also collected to monitor for changes in element ratios due to high concentrations of certain elements in the inclusions. An inclusion and appropriate beam diameter were

selected to insure complete ablation based on the size and depth of each inclusion. A background signal was collected for 60 seconds (He carrier gas flow only) prior to firing the laser. The laser is focused on the sample surface, centered above the inclusion, and ablation begins with a 10-16 μm laser spot to prevent cracking or decrepitation. The laser spot is stepped up in size until reaching the desired diameter before ablating the inclusion at depth. Once the signal for all elements drops to nearly background levels the ablation is stopped and the signal captured.

Run product glass analyses were also conducted using the LA-ICPMS facility at Virginia Tech. Analyses of glass required the selection of regions of that appeared to have minimal inclusion density. A 24 μm laser spot was used for all glass analysis along with lower laser power (~7 J/cm^2) owing to the better laser coupling characteristics of the glass compared to quartz. Approximately 50% of the glass analyses were discarded because they contained large signal spikes due to ablating large glass-hosted fluid inclusions.

AMS (Analysis Management System) is software developed at Virginia Tech for the reduction of data collected by LA-ICPMS with specific considerations for analysis of fluid inclusions. The software is based on similar methodology to that laid out in Gunther et al. (1998) and Heinrich et al. (2003). NIST 610 glass analyses are used as an external standard for each element along with sodium concentrations in both NIST610 and the fluid inclusion as an internal standard according to Equation (8).

$$\frac{C_i^{FI}}{C_{Na}^{FI}} = \frac{C_i^{STD}}{C_{Na}^{STD}} \cdot \frac{I_i^{FI} I_{Na}^{STD}}{I_{Na}^{FI} I_i^{STD}} \qquad\qquad (8)$$

The Na concentration is obtained from the inclusion salinity (NaCl wt%) through microthermometry and/or iterative calculation based on the characterization of bulk salinity according to Equation (9).

$$NaCl_{eq}(wt\%) = C_{NaCl}^{FI} + C_{KCl}^{FI} + C_{CaCl_2}^{FI} + C_{FeCl_2}^{FI} \tag{9}$$

Data from microthermometry is used calculate inclusion salinity and NaCl concentration for use as the internal standard according to Equation (9). The NaCl concentration is determined by subtracting the contribution of KCl. A correction is then made for the contribution of $FeCl_2$ and any $CaCl_2$ present based upon element ratios determined by LAICPMS. The background is selected from ablation of the quartz host and the "peak" is selected to include all of the signal contributions from ablation of all phases in the inclusion.

The combined sample set from each inclusion trail is then averaged to produce a single representative composition for a fluid inclusion assemblage (FIA). Inclusions may be rejected based on quartz fracturing, overall signal strength (no signal above 3σ of the background for major elements), and other mechanical failures during ablation. A small number of brine inclusions were discarded based on deviation in the NaCl/KCl ratio, measured by LA-ICPMS, from the 2σ uncertainty of the ratio among the other inclusions. Microthermometric halite and sylvite dissolution temperatures allow for determining the ratio independent of the LAICPMS analyses. The ratio determined via microthermometry (1 ± 0.2) matches the measured ratio for the bulk of the brine inclusions, excluding a small number with a ratio very different from the microthermometric ratio. These deviations indicate a non-homogeneous inclusion or incomplete signal capture during ablation and thus, an unrepresentative composition. This likely results from the failed

ablation of either the halite or sylvite daughter minerals in the inclusion. The 1σ

deviation in the NaCl concentration from microthermometry is then applied to each

element to account for small variability and imprecision in salinity estimation between

inclusions.

2.3.6 *LA-ICPMS Analysis of Run Product Glasses and Glass-Hosted Brines*

Run product glass analyses were also conducted using the LA-ICPMS facility at

Virginia Tech. Analyses of glass required the selection of regions that had a low

inclusion density. A 24-90 µm diameter laser spot was used for all glass analysis along

with lower laser power (~7 J/cm^2) owing to the better laser coupling characteristics of the

glass compared to quartz. Spots were chosen using transmitted light microscopy to

minimize the number of fluid inclusions included in the analytical volume. Spots were

also chosen at or near the same locations as those chosen for EPMA analysis. Raw data

were produced using a routine of summing all signals to a 100% oxide composition using

AMS software. This composition was corrected for an estimate of glass water

concentration and then the Na_2O from the LAICPMS was compared the Na_2O

concentration from EPMA analyses. The concentration of all major elements determined

by ICPMS was within 10% of the same element in the EMPA analyses. The LAICPMS

analysis of the run-product glass was only used to determine the concentration of copper

in the melt, and the deviation in the concentration of copper in a single run-product glass

sample was always greater than the deviation in major element concentrations.

Glass-hosted brine fluid inclusion analyses were conducted by selecting large (>

30 µm) fluid inclusions at depths of 20 to 60 µm below the surface, with proportions of

daughter chloride minerals similar to that observed in quartz-hosted brine inclusions. A

background glass analysis was collected while ablating down to the fluid inclusions, and again after complete inclusion ablation. Glass-hosted brine signals were reduced using the same method described for quartz-hosted brines with the addition of a correction factor for the contribution of the host glass signal. The composition of the glass surrounding the glass-hosted brine inclusions was first characterized by reducing the portion of the sample signal obtained prior to ablation of the brine inclusions, using the same methods described for other glass analyses. This glass compositions and ICPMS signals were then used to subtract the contribution of the glass from the signal derived from ablation of the fluid inclusion for each element. The final signal was then reduced using the same methods described for quartz-hosted brine inclusions. The glass analyses collected before and after the inclusion signal, as well as glass analyses collected away from inclusions, were used for host corrections, for a sub-set of glass-hosted brine analyses. No deviation in glass composition was observed within analytical uncertainty when comparing either host correction method. The data reduction including host correction is also completed using AMS software (Mutchler et al., 2008).

2.4 Results

2.4.1   Silicate Melt Composition: Major Elements

Major element compositions and ASI for quench glasses were determined by EMPA analysis, and are listed in Table 4. The ASI for each run product glass is calculated using the formula shown in Equation (4). The ASI of starting melt compositions is 0.99 and 1.2 for haplogranite (GR1) and Bishop Tuff starting materials, respectively. The change in ASI reported for quenched glasses compared to starting material compositions is due to equilibration between the silicate melt and the initial fluid

69

composition via HCl, NaCl and KCl exchange. The ASI of the melts also gives an indication of the concentration of HCl in the MVPs. This relationship, discussed by Williams et al. (1997), indicates that an increase in the ASI of the silicate melt is correlated with a decrease in the $(Na+K)/H$ ratio of the MVPs with HCl partitioning strongly into the magmatic vapor relative to brine.

Melt Composition		Na_2O wt%(2σ)	K_2O wt%(2σ)	CaO wt%(2σ)	FeO wt%(2σ)	Al_2O_3 wt%(2σ)	SiO_2 wt%(2σ)	Cl ppm(2σ)	Total wt% (2σ)	ASI
Pre-Fractured	Cu320	2.7 (0.3)	6.4 (0.2)	0.03 (0.02)	0.03 (0.05)	12.4 (0.6)	73 (0.8)	ND (-)	94.7 (1.4)	1.1
	Cu321	2.4 (0.2)	7 (0.7)	0.02 (0.01)	0.02 (0.04)	12.1 (0.9)	72.7 (1)	ND (-)	94.2 (1.4)	1.0
	Cu326	2.3 (0.3)	7.1 (1.1)	0.01 (0.02)	0.03 (0.05)	12.1 (0.9)	72.7 (1.3)	ND (-)	94.3 (1.1)	1.0
	Cu351	2.2 (0.4)	5.2 (0.6)	ND (-)	2.14 (0.47)	9.6 (1.1)	73.3 (1.5)	2800 (380)	92.6 (1)	1.0
In-Situ Fractured	Cu330	2.7 (0.2)	6.4 (0.7)	0.02 (0.02)	0.02 (0.05)	11.8 (0.8)	73.6 (1.3)	2000 (500)	94.8 (1.2)	1.0
	Cu332	2.7 (0.2)	6.4 (0.5)	0.02 (0.03)	0.01 (0.02)	11.7 (0.5)	73 (1)	2200 (840)	94.1 (1.2)	1.0
High CO_2 Fe-Poor	Cu500	2.9 (0.7)	6 (0.8)	NA (-)	ND (-)°	10.7 (1.9)	74 (2.9)	1700 (370)	93.8 (1.8)	0.9
	Cu502	2.2 (0.5)	5.7 (0.8)	NA (-)	ND (-)°	8.9 (0.6)	74.5 (1.8)	3100 (420)	94.5 (2.9)	0.9
High CO_2 Magnetite Sat'd	Cu503	2.4 (0.2)	6.4 (1.3)	NA (-)	2.5 (0.3)°	10.3 (1.5)	73.7 (1.9)	2500 (390)	94.8 (1)	0.9
	Cu504	2.8 (0.5)	6.4 (0.6)	NA (-)	2.6 (0.6)°	10.6 (1.8)	72.2 (2.3)	3200 (460)	94.9 (0.8)	0.9
	Cu505	2.4 (0.2)	5.9 (0.3)	NA (-)	1.6 (0.8)°	9.7 (0.7)	75.1 (1)	2400 (410)	95 (1.2)	0.9

Table 4: EPMA analyses of run product glasses from CO_2-bearing MVP experiments. Low-CO_2 experiments were all run with Bishop Tuff melt (except for Cu351-GR1) and have ASI~1, indicating a metaluminous melt. GR1 melt contains no appreciable Ca and no other Ca source exists in the experiments. High-CO_2 experiments using GR1 produced synthetic magmas with high crystallinity (~50%). A higher FeO solubility in peralkaline melts is observed for high-CO_2 magnetite-saturated runs.

The lower starting ASI of the synthetic haplogranite yields a lower final melt ASI and higher $(Na+K)/H$ for runs (Cu#330, Cu#332, Cu#351). The decrease in the ASI of the Bishop Tuff runs (#320, #321, #326) does not lower the final ASI enough to match GR1 runs, however, the lower $(Na+K)/H$ of these runs will not affect the total salinity of the magmatic vapor and brine. Some adjustment must be made to the cation ratios, when using the sodium concentration as an internal standard for fluid inclusion analysis, due to HCl making up a significant portion of the vapor salinity. Thus, $(Na+K)/H$ ratios for the vapor inclusions, calculated using equations presented by Williams et al. (1997) based on melt ASI, are used to adjust the sodium concentration used as an internal standard for reducing the LA-ICPMS data.

The melt ASI for the Bishop Tuff experiments falls between 1.0 and 1.1 corresponding to log (Na+K)/H = +0.4 to -0.3, resulting in a significant vapor HCl concentration (>1.5 wt%) for experiments with an ASI of 1.01 or higher. HCl concentrations in the brine are small (< 10 mol% for all run-product melt compositions) but brine salinity is corrected in a similar manner before using brine sodium concentration as an internal standard. High-CO_2 experiments (Cu#500 through Cu#504) required the use of the haplogranite (100 MPa minimum melt) starting glass to ensure a stable melt at lower fH$_2$O. Equilibrium between the melt and MVPs of the high-CO_2 experiments (X_{CO2}=0.38) resulted in a shift in the ASI of the melt towards slightly peralkaline compositions, rather than the metaluminous to peraluminous melt compositions observed in low-CO_2 (X_{CO2} = 0.10) experiments. Rough estimates of the degree of crystallization of the synthetic magmatic assemblage are consistent with the change in X_{CO2} across all experiments (<10% crystals to ~50% crystals in going from X_{CO2} = 0.10 to 0.38). The concentration of copper in the run product glass ranges from ~10 to 40 ppm (Section 2.4.2) and are too low for accurate quantification by EMPA. As a result, LA-ICPMS analyses were used to quantify the copper concentration of quenched glasses.

2.4.2   Silicate Melt Composition: Copper

LA-ICPMS analyses of run product glasses were used to quantify the copper concentrations of the silicate melts at magmatic conditions. Copper concentrations for all experiments range from 10 to 60 ppm (Table 5). Low-CO_2, sulfur-free experiments (Cu320 through Cu332) generally have copper concentrations at the low end of the range (10 to 15 ppm Cu) with the exception of Cu351 (Cu_6Au_{94} capsule), which has am

elevated melt copper concentration (~30 ppm). Melts from high-CO_2 experiments with the same proportion of starting materials (Cu503 through Cu505) are more enriched in copper (50 to 60 ppm Cu) than melts from low-CO_2 experiments. Cu505 was run with higher but proportional masses of initial starting materials than other CO_2 experiments. As a result, more copper was lost from the capsule and the melt has a lower final melt copper concentration (10 to 20 ppm; Table 5). In addition, I compare the copper concentration from glass analyses away from fluid inclusions to glass analyses collected during ablation of large glass-hosted brine inclusions.

The large size of the fluid inclusions in the glass indicates that they are likely "bubbles" of MVP mixtures present in the silicate melt during the experiment, and not quench phenomena. There is often significant overlap in the glass analyses, but the data are consistent with a slightly higher copper concentration in the glass near the large fluid inclusions. These data suggest a slight heterogeneity in the synthetic melt, indicating copper enrichment of the melt may occur near these large volatile phase bubbles. However, the difference may simply be due to increased incorporation of sub-micron inclusions (often observed near larger inclusions) in the analytical volume. Variation of the host composition between these glass analyses did not affect the signal reduction of the associated glass-hosted brine inclusions. Given that the difference in copper concentration between the two types of glass analyses is quite small, and usually overlaps within uncertainty, this heterogeneity will not affect any extrapolation to magmatic melt-volatile phase equilibria.

LA-ICPMS Glass Analyses: Copper

	Run	N	Type	Cu (±2σ)	ASI
Pre-Fractured	Cu320	6	Glass	12 (4)	1.1
	Cu320	-	FI-Glass	NA	
	Cu326	7	Glass	15 (4)	1.0
	Cu326	6	FI-Glass	18 (6)	
	Cu351	5	Glass	30 (8)	1.0
	Cu351	7	FI-Glass	32 (9)	
In-Situ Fractured	Cu330	5	Glass	13 (2)	1.0
	Cu330	-	FI-Glass	NA	
	Cu332	6	Glass	12 (8)	1.0
	Cu332	6	FI-Glass	14 (10)	
High CO$_2$ Magnetite Saturated	Cu503	5	Glass	48 (23)	0.9
	Cu503		FI-Glass	NA	
	Cu504	6	Glass	53 (11)	0.9
	Cu504	5	FI-Glass	55 (8)	
	Cu505	16	Glass	11 (4)	0.9
	Cu505	6	FI-Glass	16 (3)	

Table 5: Copper concentrations of CO$_2$-bearing run product glasses. Analyses away from fluid inclusions (Glass) and collected during glass-hosted brine analyses (FI-Glass) are shown (±2σ). Melt ASI shown at right for reference. NA=Not Analyzed

2.4.3   *Vapor-Brine Salinity and Vapor Inclusion Pressure Determination*

Microthermometric measurements of halite and sylvite dissolution temperatures

(~300-350 ^{o}C for sylvite and ~420-480 ^{o}C for halite) for brine inclusions yielded average

calculated salinities of 69 to 71 wt% NaCl$_{eq}$ and 78 to 80 wt% NaCl$_{eq}$ for the experiments

at X_{CO2} = 0.10 and 0.38, respectively. Raman Spectroscopic measurements of vapor

inclusions from experiments with X_{CO2} = 0.10 and 0.38 yielded Fermi-diad splitting

values (Δ) of ~ 102.8 and 103.3 cm^{-1}, respectively. Using Equation (4) (Fall et al., 2011)

and a CO$_2$ equation of state (Lemmon et al., 2012) these Δ values were correlated to

pressures at T$_m$^{clath} of 2.6 MPa and 5 MPa, respectively. The T$_m$^{clath} and inclusion pressure

were input into the model presented by Sun and Duan (2006) to calculate the salinity of

vapor-rich inclusions. Vapor inclusions from the experiments at X_{CO2} = 0.10 have T$_m$^{clath}

values between 4 and 5 ^{0}C, yielding salinities between 3.5 and 4 wt% NaCl$_{eq}$, adjusting

for HCl. Experiments at $X_{CO2} = 0.38$ have T_m^{clath} values between 9 and 9.5 ^{o}C yielding a salinity of ~1 wt% NaCl$_{eq}$. Often clathrate melting was difficult to observe for vapor inclusions in experiments at $X_{CO2} = 0.38$. For these inclusions, ice melting temperatures of -1°C to -2 ^{o}C were used to confirm a ~1 wt% salinity. Vapor inclusions occasionally have T_m^{clath} temperatures several ^{0}C below the ranges listed above. These inclusions were not analyzed because they likely represent significant brine contamination of the high temperature vapor. The difficulty in evaluating vapor salinity in the CO_2-bearing experiments is the dominant source of uncertainty in quantifying the partitioning of copper between the high temperature vapor and brine.

2.4.4   Fluid Inclusion Compositions

The sodium, iron and copper concentrations of the fluid inclusion assemblages analyzed from each experiment are shown below in Table 6, along with number of inclusions analyzed, average salinity, fracture method and X_{CO2}. Each experiment includes both vapor and brine inclusions from at least two separate fluid inclusion assemblages from different parts of the quartz core.

LA-ICPMS Analysis of Fluid Inclusions from CO_2-bearing Experiments

	Run	Inclusion Type	# of FI	X_{CO2} (Bulk	Salinity (Wt% NaCl$_{eq}$)	Na (±2σ) FIAs	Fe (±2σ) FIAs	Cu (±2σ) FIAs	Melt ASI
Pre-Fractured	320	Brine	23	0.092	71-72	120000 (600)	11500 (4600)	3200 (500)	1.1
	‡321	*Brine*	*8*	*0.092*	*69-72*	*140000 (10000)*	*3300 (5300)*	*54000 (14000)*	*1.1*
	326	Brine	8	0.096	69-72	140000 (44000)	7000 (2200)	2600 (700)	1.0
	351	Brine	15	0.098	69-71	120000 (16000)	45000 (10000)	9200 (1800)	1.0
	320	Vapor	6	0.092	2.5-3.5	4600 (20)	180 (230)	120 (70)	
	‡321	*Vapor*	*11*	*0.092*	*2.5-3.5*	*6500 (0)*	*240 (170)*	*2500 (800)*	
	326	Vapor	3	0.096	2-4	5600 (2200)	310 (110)	120 (90)	
	351	Vapor	11	0.098	2.5-3.5	4800 (970)	1200 (330)	290 (100)	
In-Situ Fractured	330	Brine	11	0.097	70-72	140000 (17000)	2700 (1300)	2500 (600)	1.0
	332	Brine	7	0.095	70-72	130000 (37000)	1200 (300)	2500 (500)	1.0
	330	Vapor	9	0.097	2.5-3.5	4800 (970)	60 (40)	100 (40)	
	332	Vapor	8	0.095	2.5-3.5	5200 (1000)	30 (30)	90 (50)	
High CO_2 — Fe-Poor	500	Brine	11	0.39	79-81	160000 (5600)	ND	1700 (200)	0.9
	502	Brine	10	0.39	79-81	140000 (54000)	600 (300)	4700 (2200)	0.9
	500	Vapor	8	0.39	1	2300 (340)	ND	30 (18)	
	502	Vapor	7	0.39	1	2100 (320)	22 (17)	99 (23)	
Mt-Sat'D	503	Brine	9	0.38	78-80	130000 (34000)	36000 (42000)	9300 (1800)	0.9
	504	Brine	9	0.37	78-80	150000 (17000)	17000 (2000)	8900 (800)	0.9
	505	Brine	21	0.38	78-80	150000 (20000)	23000 (5500)	2600 (500)	0.9
	503	Vapor	11	0.38	1	1600 (430)	700 (400)	90 (50)	
	504	Vapor	9	0.37	1	1600 (510)	600 (500)	90 (50)	
	505	Vapor	16	0.38	1	1900 (630)	400 (400)	30 (10)	

Table 6: Fluid inclusion characteristics for vapor and brine fluid inclusions from experiments with X_{CO2}~ 0.10 and 0.38. X_{CO2} calculated based upon mass balance of starting materials. Salinities calculated using microthermometry and models presented by Bodnar (1989). Na, Fe, and Cu concentrations determined by LAICPMS. Melt ASI calculated based on EMPA analysis of quench glasses and equations presented by Williams et al. (1997). (ND) = No Detection. ‡*Experiment #321 produced inclusions with Cu concentrations ~ 5-10x greater than all other experiments and was not reproducible.*

The major element composition of the fluid inclusions was fixed by the composition of the bulk volatile phase chosen for each experiment. The Na/K/H molar ratio of 10/10/1 utilized in all experiments resulted in final bulk compositions slightly enriched in sodium relative to potassium due to corresponding exchange and compositional adjustment of these cations with the silicate melt. Variability in the iron content of the vapor and brine is a result of the addition of iron to each system either through the use of a natural magnetite-bearing starting glass or via the addition of magnetite to the experimental charge. Early experiments utilizing pre-fractured quartz (#320, #321, #326, #351) show higher variability in copper concentrations than those with the same bulk composition utilizing the in-situ quartz fracturing method (#330, #332). Experiments with $X_{CO2} = 0.38$ conducted with iron-poor bulk compositions

showed significant deviations in copper partitioning behavior from those conducted under

magnetite-saturated (Mt-Sat'd) conditions, yielding significantly less enrichment of

copper in the brines relative to the coexisting vapor.

Glass-hosted brine inclusions analyzed from a subset of CO_2-bearing experiments

(Cu505 and Cu332) had the same copper compositions as quartz-hosted inclusions within

analytical uncertainty. The large potassium and sodium host signal prevents analysis of

glass-hosted vapor inclusions. The consistency between glass-hosted brine and quartz-

hosted brines indicates that the quartz-hosted fluid inclusion assemblages represent the

equilibrium compositions of the respective magmatic phases.

2.4.5 Partition Coefficients and Equilibrium Constants

Nernst-type partition coefficients reported in Table 7 were calculated using fluid

inclusion and quenched glass compositions and are calculated using the copper

concentration of any two of the magmatic MVPs present at run conditions. The

relationship between D_{Cu} and the concentration of copper is defined by Equation (10)

below.

$$D_{Cu}^{x,y} = \frac{C_{Cu}^x}{C_{Cu}^y} \quad \{x,y = v,b,m\} \tag{10}$$

Average calculated partition coefficients ($\pm 2\sigma$) for $D_{Cu}^{b/v} = 25(\pm 7)$ at $X_{CO2} = 0.10$ (pre-

fractured), $25(\pm 5)$ at $X_{CO2} = 0.10$ (in-situ fractured), and $53(\pm 22)$ and $100(\pm 30)$ for

experiments at $X_{CO2} = 0.38$ (Fe-poor and magnetite-saturated, respectively). These

partition coefficients demonstrate a significant enrichment of copper in the dense high-

salinity magmatic brine relative to the coexisting low-salinity vapor. This is in general

agreement with other CO_2-free experimental studies of copper partitioning between vapor

and brine at magmatic conditions ($D_{Cu}^{b/v} > 1$, Williams et al. 1997 and Simon et al. 2006). Additionally, data from the experiments at $X_{CO2} = 0.38$ indicate that iron may exert some control on copper partitioning, whereas experiments at $X_{CO2} = 0.10$ show, at best, only a correlation between iron and copper absolute concentrations.

D_{Cu} & $K_{Cu,Na}$		X_{CO2}	$K_{Cu,Na}^{b/v}$	$D_{Cu}^{b/v}$	$K_{Cu,Na}^{b/m}$	$D_{Cu}^{b/m}$	$D_{Cu}^{v/m}$
	Cu320	0.092	1.03 (0.6)	28 (17)	44 (14)	300 (100)	9 (6)
Pre-Fractured	◆Cu321	0.092	0.98 (0.3)	21 (7)	840 (230)	5600 (1500)	260 (100)
	Cu326	0.096	0.88 (0.8)	22 (17)	26 (11)	180 (50)	8 (6.3)
	Cu351	0.098	1.3 (0.6)	32 (13)	59 (20)	310 (110)	10 (4)
In-Situ Fractured	Cu330	0.097	0.8 (0.4)	24 (12)	27 (7)	190 (50)	8 (3)
	Cu332	0.095	1.1 (0.7)	29 (17)	31 (17)	210 (120)	7.2 (5.5)
High CO$_2$ Fe-Poor	Cu500	0.38	0.8 (0.6)	59 (40)	20 (7)	150 (106)	2.5 (1.7)
	Cu502	0.38	0.7 (0.4)	47 (20)	29 (24)	130 (110)	2.8 (1.9)
High CO$_2$ Magnetite Saturated	Cu503	0.38	1.3 (0.8)	110 (60)	35 (18)	190 (100)	1.7 (1.2)
	Cu504	0.37	1.1 (0.7)	110 (60)	25 (8)	170 (60)	1.6 (1)
	Cu505	0.38	1.2 (0.4)	90 (30)	31 (15)	230 (100)	2.5 (1.1)

Table 7: Nernst-type partition coefficients (D) and equilibrium exchange constants (K) for CO$_2$-bearing experiments (±2σ). ◆*Experiment #321 produced inclusions with Cu concentrations ~ 5-10x greater than all other experiments and was not reproducible.*

Evaluating copper partitioning between the silicate melt and vapor or brine is also vital to modeling the effect of CO_2 on the potential for extraction of copper by MVPs. Average calculated partition coefficients (±2σ) for $D_{Cu}^{b/m} = 195(\pm60)$ and $195(\pm56)$ and $D_{Cu}^{v/m} = 9.6(\pm3.3)$ and $1.9(\pm0.6)$ at $X_{CO2} = 0.10$ and 0.38, respectively (in-situ fractured-Table 7). No significant deviation is observed for the D$^{brine/melt}$ partition coefficients. However, the shift in the D$^{vapor/melt}$ indicates a significant decrease in the copper concentration of the magmatic vapor relative to the silicate melt with increasing X_{CO2}. Pre-fractured experiments match closely the results of in-situ fractured experiments, with the exception of an outlier replicate (#321), which shows dramatically elevated $D_{Cu}^{b/m}$ and $D_{Cu}^{v/m}$ relative to the other experiments. This difference is associated with higher copper concentrations in the fluid inclusions, which approximate the expected initial copper concentration of the experiment prior to any copper loss to the silicate melt and capsule.

Although equilibration should occur quickly, these early experiments included Pt capsules that were under-saturated (no initial copper) with respect to the copper concentration of the vapor and brine. This resulted in a decrease in copper concentration throughout the run duration. I believe that the outlier, and greater spread in the copper data for the pre-fractured experiments, is a result of variable early trapping of fluid inclusions, which trapped MVP with disequilibrium compositions. This concern was the impetus behind changing to an in-situ fractured experiment design.

The equilibrium exchange of copper and sodium between the vapor and brine also provides insight into the partitioning and complexation of these cations in the volatile phases The apparent equilibrium constant for Cu-Na exchange between magmatic phases ($K_{Cu,Na}^{b/v}$) has previously been used in experiments with chloride complexed copper and sodium (Simon et al., 2006; Williams et al., 1997). The relevant equilibrium constant for Cu and Na exchange in CO_2-free systems is defined by Equation (11) below (Williams et al., 1997).

$$K_{Cu,Na}^{b/v} = \frac{C_{Cu}^b \bullet C_{Na}^v}{C_{Cu}^v \bullet C_{Na}^b} \qquad\qquad (11)$$

If CO_2 is unable to complex either copper or sodium at magmatic conditions then chloride complexation will control the concentration of both copper and sodium in the magmatic vapor and brine. Thus, comparison of partition coefficients and apparent equilibrium constants can confirm that the influence of CO_2 is, or is not, salinity dependent. The average calculated $K_{Cu,Na}^{b/v}$ are 1.0 (±0.3) ($X_{CO2} = 0.10$ pre-fractured), 1.0 (±0.4) ($X_{CO2} = 0.10$ in-situ fractured), 0.8 (±0.3) ($X_{CO2} = 0.38$ Fe-poor), and 1.2 (±0.5) ($X_{CO2} = 0.38$ magnetite-saturated), respectively. The overlap between these equilibrium

exchange constants is consistent with my hypothesis that higher X_{CO2} does not affect Cu-Na exchange between magmatic vapor and brine. No change in Cu-Na equilibrium is observed because the shifts in salinity associated with variable X_{CO2} adjust the chloride-complexed copper and sodium concentrations equally. A simple chloride equilibrium expression is then applicable to the exchange of copper and sodium as chlorides between the magmatic vapor and brine, defined by Equation (12) below.

$$CuCl^{vapor} + NaCl^{brine} = CuCl^{brine} + NaCl^{vapor} \tag{12}$$

Additionally, Cu and Na are hypothesized to exchange between the volatile phases and silicate melt via the equilibrium shown by Equation (13) below.

$$CuO_{0.5}^{melt} + NaCl^{brine} = CuCl^{brine} + NaO_{0.5}^{melt} \tag{13}$$

This equilibrium defines Cu-Na exchange according to equilibrium between copper and sodium present in the MVP as chlorides and copper and sodium oxide components of the melt. Both reactions are based upon the dominance of Cu^{+1} in both the melt and volatile phases. Candela and Holland (1984) discussed that Cu^{+2} should only be present in silicate melts at a much higher oxygen fugacity ($\sim +6$ log units) than that of the Ni-NiO buffer for which both Fe^{+2} and Fe^{+3} are sub-equal. Thermodynamic modeling of the Cu-Cu$_2$O and Cu$_2$O-CuO equilibria demonstrates that Cu$_2$O (not Cu or CuO) is stable in the presence of magnetite, without wustite (FeO) or hematite (Fe$_2$O$_3$), at 800 ^{o}C (Chou, 1987; Oneill, 1988). The presence of equilibrium magnetite at 800 ^{o}C suggests that the relative oxidation state of a system is too low to allow for appreciable Cu^{+2}. In addition, Zajacz et al. (2011) discuss in detail thermodynamic evidence for the presence of copper complexes with a Cu^{+1} ion and two -1 ligands balanced by H^+, Na^+, or K^+, supporting the presence of dominantly Cu^{+1} in the volatile phase(s). Based on this evidence I have

chosen to model copper as Cu^{+1} in all magmatic phases. The average calculated $K_{Cu,Na}^{b/m} =$ 27 ($\pm$8) and 30 ($\pm$10) for experiments at $X_{CO2} = 0.10$ and 0.38, respectively. Again, this lack of adjustment to $K_{Cu,Na}^{b/m}$ at elevated X_{CO2} indicates that CO_2 does not play a role in Cu or Na complexation, and that the reported changes in $D_{Cu}^{b/v}$ and $D_{Cu}^{v/m}$ result from the effect of CO_2 on vapor and brine salinity.

2.5 Discussion

2.5.1   Effect of CO_2 on Salinity of Volatile Phases

The results reported for fluid inclusion salinity from this study place additional experimental constraints on $NaCl$-H_2O-CO_2 model predictions (Duan et al., 1995). The measured salinity of the brine increased from ~62 wt% to ~71 wt% $NaCl_{eq}$ at X_{CO2} (vapor) = 0.10 and to ~ 80 wt% $NaCl_{eq}$ at X_{CO2} (vapor) = 0.38, consistent with the model presented by Duan et al. (1995) at 800 ^{o}C and 100 MPa. The model of Duan et al. (1995) predicts a shift in the salinity of brine-saturated vapor (800 ^{o}C, 100 MPa) from 3.5 wt% at $X_{CO2} = 0.10$ to 0.9 wt% at $X_{CO2} = 0.38$. The microthermometric measurements of fluid inclusion salinity reported in this study conform closely to these model predictions. The microthermometric measurements from the CO_2-bearing experiments are consistent with the Duan et al. (1995) to within $\pm$ 10%. The consistency between measured salinity and model predictions allows for extrapolation of copper partitioning data to MVP compositions at X_{CO2} values other than those explicitly examined. The extrapolation of partition coefficients to any concentration of CO_2 relies on the salinity-dependent behavior of copper partitioning with variable X_{CO2} in the MVPs.

2.5.2 Copper Partitioning in the CO₂-Bearing Melt-Vapor-Brine Assemblages

The D_{Cu} values reported in this study provide new tools to evaluate copper

partitioning between silicate melts and exsolved, CO_2-bearing volatile phases. These

results are applicable to volatile phases formed as dissolved H_2O and CO_2 exsolve during

magmatic evolution in natural arc environments. Variable CO_2 can also be added to

shallow magmas through reaction with, or assimilation of, carbon-bearing country rocks

or during intrusion of new batches of basaltic or andesitic magmas. The partitioning of

copper between coexisting vapor and brine is strongly affected by the X_{CO2} of the MVP.

The brine/vapor partition coefficients ($\pm 2\sigma$) for $D_{Cu}^{b/v} = 25(\pm 7)$ (pre-fractured), and $26(\pm 9)$

(in-situ fractured) at $X_{CO2} = 0.10$ and $100(\pm 30)$ (in-situ fractured) for experiments at X_{CO2}

$= 0.38$ are consistent with a salinity-dependent model for copper partitioning. Given that

the ratio of the vapor and brine salinities is proportional to the $D_{Cu}^{b/v}$, I present a salinity-

dependent extrapolation of the measured $D_{Cu}^{b/v} = 25\ (\pm 7)$ at $X_{CO2} = 0.10$ to higher X_{CO2} as

a function of the measured brine/vapor salinity ratio (Figure 9).
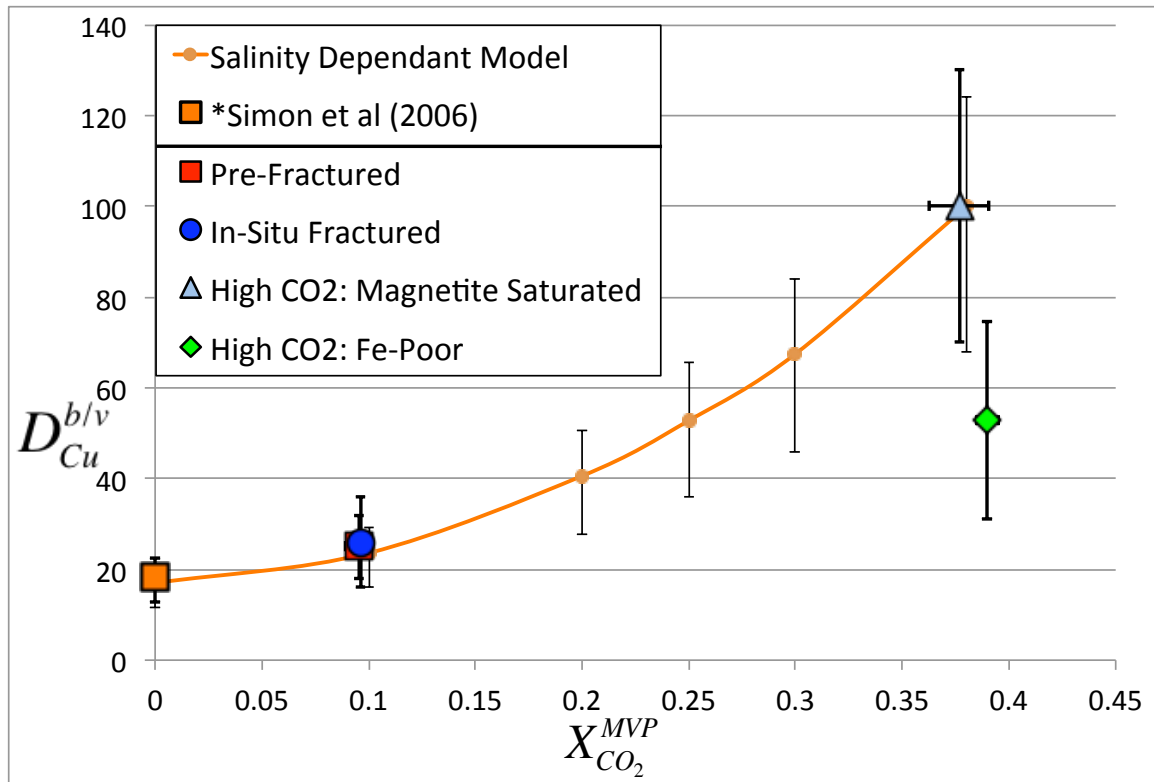
Figure 9: Copper partition coefficient between brine and vapor as a function of X_{CO2}. The $D_{Cu}^{b/v}$ **is higher at higher X_{CO2}, and the change is a function of the change in salinity of the vapor and brine and corresponding chlorine-complexed copper concentrations. Data presented by Simon et al. (2006) is shown, adjusted for differences in salinity due to different run P-T conditions. A salinity dependent extrapolation of $D_{Cu}^{b/v}$ at X_{CO2} = 0.10 to higher and lower CO_2 concentrations is consistent with both the CO_2-free data presented by Simon et al. (2006) and high-CO_2 (X_{CO2} = 0.38) data from this study (orange line). Error bars represent 2σ uncertainties between at least 3 experiments. Error bars on model based on extrapolation of minimum and maximum for D value and salinity.**

The measured value for $D_{Cu}^{b/v}$ = 100(±30) at X_{CO2} = 0.38 is consistent with the

extrapolation of $D_{Cu}^{b/v}$ from X_{CO2} = 0.1; in the limit of X_{CO2} = 0, this salinity dependent

extrapolation is also consistent with the existing CO_2-free experimental data presented by

Simon et al. (2006) (Figure 9). The consistency of this salinity-dependent model for

copper partitioning from low to high X_{CO2} is a strong indication that the primary effect of

CO_2 on the partitioning of chlorine-complexed copper is a shift in the copper

concentrations of the vapor and brine correlated with the shift in salinity. Furthermore,

the consistency with CO_2-free experiments indicates that the addition of CO_2 to the melt-

vapor-brine experiments does not directly affect the copper exchange equilibria. However, there remains the question of explaining the drop in $D_{Cu}^{b/v}$ for iron-poor, CO_2-rich MVPs indicated by experiments #500 and #502. The $K_{Cu,Na}^{b/v}$ for the iron-poor (0.8 ± 0.3) and magnetite-saturated (1.2 ± 0.5) experiments with X_{CO2} = 0.38 overlap within uncertainty. However, the spread between the $K_{Cu,Na}^{b/v}$ for iron-poor and magnetite-saturated high-CO_2 experiments may indicate that a change to chloride exchange equilibria between the melt and MVPs occurs in melt-vapor-brine assemblages without significant iron present.

The average brine-melt partition coefficients (±2σ) are $D_{Cu}^{b/m}$ = 190(±50) and 180(±56), respectively (in-situ fractured). The consistency between $D_{Cu}^{b/m}$ in sulfur-free experiments indicates that the magmatic brine shows consistently high concentrations of copper, independent of X_{CO2}. In contrast, the magmatic vapor shows lower potential for efficient removal of copper with increasing X_{CO2} ($D_{Cu}^{v/m}$ = 9.2(±4.2) and 1.6(±0.8) at X_{CO2} = 0.10 and 0.38), and approaches compatible behavior for copper in the melt with respect to partitioning into the vapor ($D_{Cu}^{v/m}$ <1) at X_{CO2} > 0.38. As discussed, the mass fraction of brine also decreases at fixed Cl/H_2O as X_{CO2} increases. Thus, high X_{CO2} melt-vapor-brine assemblages will have a low brine/vapor mass ratios and lower potential for efficient removal of copper from the melt into the MVPs at equilibrium conditions relative to CO_2-poor systems. Ultimately, the deposit potential of magmas that exsolve or equilibrate with a CO_2-rich volatile phase assemblage also relies on the total H_2O-CO_2 budget. Any input of additional volatile phases from more mafic parts of the arc system, and the fate of the small proportion of any copper-rich magmatic brine will also affect the potential for

formation of PCD. Furthermore, predictions based solely on partition coefficients and equilibrium constants are static representations of evolving systems in natural arc environments. To fully address the implications of the salinity dependent variation in copper partitioning as a function of X_{CO2}, the partitioning data presented from the CO_2-bearing experiments has been applied to evolving exsolution of volatile phases via a modified MVPart model.

To the extent to which models can predict the change in salinity of magmatic vapors due to variable X_{CO2}, the partitioning data presented in this study can be extrapolated to any X_{CO2} value between 0 and 0.38. In principle, this allows for modeling the efficiency of removal of copper from the melt into CO_2-bearing volatile phases and the implications of CO_2 on deposit formation. The CO_2-MVPart model presented in Section 2.5.3 examines variable conditions of the exsolution of volatile phases and implications for efficiencies of removal of copper from arc magmas into similar proto-ore fluids. However, several issues arise from extrapolating to other P-T-X conditions that must be addressed before discussing implications for ore deposition at sub-solidus conditions.

First, the correlation between shifts in copper partitioning and X_{CO2} dependent MVP salinity is only applicable at magmatic conditions for which CO_2 behaves as a hard gas species in the volatile phase assemblage. At lower temperatures and pressures, down to 350 $^{\circ}$C and 30 MPa, a two-phase field still exists in the $NaCl$-H_2O-CO_2 system given at least $X_{CO2} > 0.04$ (Duan et al. 1995). However, this study cannot account for the possible effect of CO_2 hydration on metal complexation at these low temperatures. Thus,

effects on the efficiency by which copper is removed from the melt by the MVPs will be used to address the effect of X_{CO2} on ore-formation.

Second, numerous studies have been conducted to evaluate the relative magmatic solubilities and phase relations in the $NaCl-H_2O-CO_2$ system to much higher P-T conditions and into intermediate to mafic melt compositions (Alletti et al., 2009; Behrens et al., 2004; Botcharnikov et al., 2005; Duan et al., 1995; Duan and Sun, 2003; Liu et al., 2005; Lowenstern, 2000; Lowenstern, 2001; Newman and Lowenstern, 2002; Webster et al., 2011). The exsolution of CO_2-bearing volatile phases from more mafic magmas deep in the arc environment can generate CO_2-rich volatile phases that are out of equilibrium with shallow felsic magmas. The addition of CO_2 through fluxing of volatile phases from a reservoir of deep mafic magma within a complex arc system can sustain the presence of CO_2-rich volatile bubbles throughout long periods of cooling and crystallization in shallow felsic magmas. Reaction between silicate melts and carbon-bearing country rocks can also result in the addition of CO_2, generating CO_2-buffered melt-volatile phase assemblages. This is in contrast to the short time frame for exsolution of CO_2-rich MVPs directly from felsic magmas owing to the low solubility of CO_2 in these magmas. The CO_2-MVPart model presented in Section 2.5.3 evaluates the efficiency of removal of copper into CO_2-bearing MVPs based upon the partitioning data presented in this study. The model is relevant to both of these possibilities by utilizing a fixed X_{CO2} for CO_2 to approximate buffered, or to generate predictions representing boundary conditions for melt-volatile phase equilibria in systems with variable X_{CO2} during volatile phase exsolution.

The addition of CO_2 to arc magmas through reaction or assimilation of carbon-bearing country rocks can cause the magmas to become reduced, potentially several log units below NNO (Audetat et al., 2008; John et al., 2010). The experimental data reported in this study do not include any consideration for lower fO_2, but the general trends for the efficiency of removal of copper into CO_2-bearing volatile phases should apply to reduced systems. The phase relations in the $NaCl$-H_2O-CO_2 systems and hard ligand properties of CO_2, are not significantly affected by lower fO_2. Thus, the salinity dependent trends of copper partitioning at variable X_{CO2} will likewise not be affected. However, the decrease in $D_{Cu}^{b/v}$ observed for iron-free experiments at $X_{CO2} = 0.38$ does indicate some adjustment to MVP copper partitioning may occur to the extent that lower fO_2 affects iron oxidation and speciation. As a result, I can extrapolate the effect of CO_2 on the efficiency of removal of copper into CO_2-bearing MVPs via chloride-complexation to model the behavior of felsic magmas over a wide range of X_{CO2}. The copper partitioning data reported herein were incorporated into the CO_2-MVPart model to predict trends for the efficiency of removal of copper from the melt into CO_2-bearing volatile phases in evolving arc systems.

It must be noted that the models and interpretations discussed in this chapter are for chloride-complexed copper only, and do not take into account other important complexing ligands (e.g. H_2S). Investigations into possible interaction between CO_2 and sulfur ligands will be discussed as part of pyrrhotite-saturated experiments presented in Chapter 3.

2.5.3 *Efficiency of Removal of Copper into MVPs: A CO_2-MVPart Model*

Partition coefficients and equilibrium constants can provide information on the potential for exchange of copper between silicate melts and MVPs for a static set of conditions. However, the extraction of copper from natural arc magmas is a dynamic process. As discussed in Section 2.1.1, the MVPart model presented by Candela et al. (1998) provides an estimate of the efficiency of removal of copper into magmatic volatile phases as a magma chamber loses heat and crystallizes isothermally and isobarically. The model requires that upon reaching volatile phase saturation, the melt exsolves magmatic vapor only. As crystallization proceeds, and the melt and exsolving vapor become enriched in chlorine, brine saturation may occur. The model then evaluates the fraction of copper removed from the initial melt by the MVP mixture, allowing for calculation of efficiencies of copper removal into the vapor, or vapor + brine mixture. The X_{CO2} affects the degree of crystallization at volatile phase saturation, coexisting vapor and brine salinities, and vapor-melt chlorine concentrations. Each of these parameters can be varied in the MVPart model and thus, play a role in predictions for the efficiency of copper removal into the vapor or vapor + brine mixtures.

Given that the MVPart model is designed for chloride-complexed copper partitioning, I have developed a modification of this model (CO_2-MVPart), which incorporates some of the effects of CO_2 on melt-volatile phase equilibria. The modified model is designed to evaluate the efficiency of removal of copper into vapor, or vapor + brine mixtures as a function of the X_{CO2} of magmatic vapors at volatile phase saturation. The model can evaluate the efficiency of removal of copper into CO_2-bearing volatile phase exsolution at conditions of 800 ^{o}C and 100 MPa. In the following sections I will

describe the how certain parameters have been changed within the model to achieve this goal, and how to evaluate the efficiency of removal of copper into vapor + brine mixtures or vapor only. I will then present results that describe how the efficiency varies from $X_{CO2} = 0$ to $X_{CO2} = 0.38$, based upon the salinity dependent partitioning data previously presented.

2.5.3.1 Modifications to MVPart

One of the most important effects of CO_2 on melt-volatile phase equilibria is a change in the concentration of water in the melt that results in exsolution of volatile phases. At higher concentrations of CO_2, the saturation water concentration of silicate melts decreases at a fixed temperature and pressure (Botcharnikov et al., 2005; Lowenstern, 2001). This feature is vital in modeling an evolving magma, because second boiling will occur at smaller degrees of crystallization at higher concentrations of CO_2. In the original MVPart model, the concentration of water at vapor saturation is set to a fixed value of 4.24 wt% at 800 $^\circ$C and 100 MPa (Holtz et al., 1995). In the CO_2-MVPart model this fixed value has been replaced by the function

$$[H_2O]_{Wt\%}^{Saturated\,melt} = -3.27 * (X_{CO_2}) + 4.13 \qquad \textbf{(14)}$$

based on VolatileCalc data presented by Newman and Lowenstern (2002) (see Appendix VI for details). The "X_{CO2}" variable in Equation (14) represents the mole fraction of CO_2 in the magmatic vapor in equilibrium with the silicate melt at volatile phase saturation. In addition, the $f H_2O$ at 800 $^\circ$C and 100 MPa is adjusted for the presence of CO_2 using the theoretical model for fluid mixtures presented by Churakov and Gottschalk (2003). The

88

$f\mathrm{H_2O}$ is primarily used in the model for equilibrium calculations to estimate the $\mathrm{FeCl_2}$ concentration in the magmatic vapor and brine.

The previous MVPart model also utilized the model presented by Bodnar et al. (1985) to calculate the salinities of the vapor (brine-saturated) and brine (vapor-saturated) at magmatic conditions. The temperature of 800 $^{\mathrm{o}}$C and 100 MPa represents a single slice through the $\mathrm{NaCl}\text{-}\mathrm{H_2O}$ solvus described by this model, and the two salinities remain fixed at these conditions for a $\mathrm{CO_2}$-free system. However, the salinity of the coexisting vapor and brine change significantly with increasing X_{CO2}. Accurate modeling of the saturation of a melt first with vapor, then subsequently vapor + brine, requires an accurate model for this variation in salinity. The reported vapor and brine salinities from the microthermometry data presented in Section 2.4.3 and the model presented by Duan et al. (1995) have been used to generate equations for the vapor and brine salinity as a function of X_{CO2} at 800 $^{\mathrm{o}}$C and 100 MPa (Appendix VI).

Each of the changes to the MVPart model is designed to characterize the melt-volatile phase equilibrium for a volatile phase assemblage at a fixed $\mathrm{H_2O/CO_2}$ ratio. Upon progressive devolatilization, the melt and the associated vapor will both evolve toward higher $\mathrm{H_2O/CO_2}$ ratios in natural systems, because the solubility of $\mathrm{CO_2}$ in silicate melts is much lower than $\mathrm{H_2O}$ (Botcharnikov et al., 2005; Lowenstern, 2000; Lowenstern, 2001; Morizet et al., 2002; Newman and Lowenstern, 2002). However, the addition of mafic magmas, or the titration of deeply sourced, $\mathrm{CO_2}$-rich volatile phases, into shallow felsic magmas, may allow for exsolution of MVPs at sustained, moderate to high X_{CO2}. I propose that the results of the $\mathrm{CO_2}$-MVPart model may be used at a fixed value for $\mathrm{CO_2}$-buffered MVPs, or by using any two values of X_{CO2} as boundary conditions with an

evolving magma moving from a high X_{CO2} towards low X_{CO2} MVP compositions. With this in mind, I present data on the efficiency of removal of copper into CO_2-bearing MVPs at 800 $^{\circ}$C and 100 MPa.

2.5.3.2 Efficiency of Removal of Copper from Melt into CO₂-Bearing MVPs

In order to evaluate the effect of varying magmatic conditions, the modified CO_2-MVPart model was run for multiple fixed vapor compositions with X_{CO2} = [0, 5, 10, 24, 38] at 800 $^{\circ}$C and 100 MPa. These vapor compositions were combined with two different initial water concentrations in the melt equal to 2.8 wt% and 1.5 wt%. The initial chlorine concentration in the melt was varied between 200 ppm, 400 ppm and 800 ppm to generate a matrix of initial model conditions (Figure 10). Results from the model focus on changes in the efficiency of removal of copper into CO_2-bearing vapor, or vapor + brine mixtures, within a matrix of magmatic conditions. The CO_2-free conditions produced the same general results as the data presented using the MVPart model (Candela and Piccoli, 1998). Trends in "peak efficiency" of removal of copper from the silicate melt into exsolving CO_2-bearing vapors, or vapor + brine mixtures are also reported as a function of X_{CO2}.

The matrix of initial water and chlorine concentrations in the melt includes six groups (Figure 10), representing combinations of 2.8 wt% or 1.5 wt% water and 200 ppm, 400 ppm, or 800 ppm chlorine. One group, 1.5 wt% water and 800 ppm, is omitted because under these conditions the melt would initially saturate with respect to a two-phase vapor + brine mixture, which is beyond the modeling capabilities of the CO_2-MVPart model.
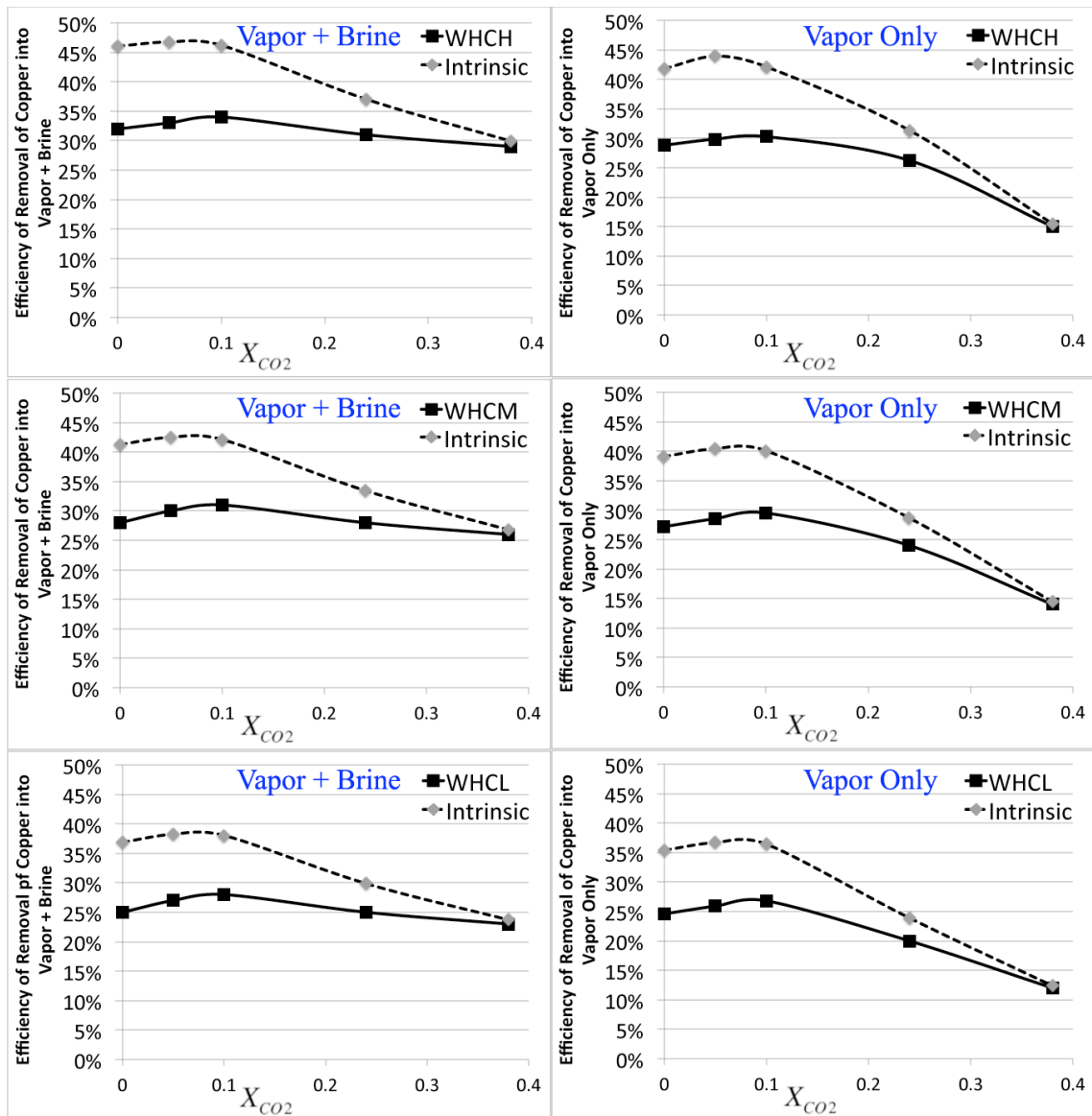
Model Conditions	Initial H$_2$O (Wt%)	Initial Cl (ppm)	Peak eff. (V+B)	Peak eff. (vapor)	Peak eff. (X_{CO2})
WHCH (.028)	**2.8**	**800**	**34%**	**30%**	**0.05 – 0.1**
WLCM (.028)	1.5	400	11.0%	8.8%	0.05 – 0.1
WHCH-ASI	2.8	800	27%	23%	0.05
WHCM (.013)	**2.8**	**400**	**31%**	**30%**	**0.1**
WLCL (.013)	1.5	200	11.0%	8.7%	0.05 – 0.1
WHCM-V/B	2.8	400	24%	23%	0.05 – 0.1
WHCL (.007)	**2.8**	**200**	**28%**	**27%**	**0.1**

Figure 10: CO$_2$-MVPart model results: Model conditions are divided into groups base on water concentration and chlorine concentration; high (H), moderate (M), and low (L) with Cl/H$_2$O ratios shown in parentheses. Efficiency of removal of copper (solid lines) into vapor + brine (left), and vapor only (right) is shown as a function of X$_{CO2}$. Dashed curves represent the intrinsic efficiency of removal of copper, defined by Equation (15), which is standardized to the same copper concentration in the melt at vapor saturation. $D_{Cl}^{v/m}$ was decreased from 6 at low X$_{CO2}$ to 1 at high X$_{CO2}$, based on measured chlorine partitioning data and observations of Webster et al. (1988). Peak efficiencies (table) represent the maxima in the trends for efficiency with increasing X$_{CO2}$ (shown above). Results for sensitivity tests for ƒHCl (ASI = 1.04 vs. 1.01), and reduction of brine-saturated vapor salinity (V/B: Vapor NaCl$_{eq}$ = 1/2) for modified model conditions are also shown.

The exsolution of magmatic vapor from a silicate melt occurs at increasingly lower water concentrations with increasing X_{CO2}. Given a fixed total pressure of 100 MPa, the exsolution of volatile phases during second boiling occurs at progressively lower degrees of crystallization in the magma with increasing X_{CO2}. If the exsolution of MVPs occurs at a lower degree of crystallization, more copper remains available for extraction from the melt, given that copper is behaving as a crystal compatible element prior to vapor saturation. The decrease in the copper concentration of the melt at higher degrees of crystallization results from the partitioning of copper into crystallizing phases. The crystallization decreases the copper concentration in successive aliquots of silicate melt as crystallization proceeds. After volatile phase saturation copper will partition into the exsolving vapor ± brine proportionally to the partitioning of chlorine among the melt, vapor, and brine.

Webster et al. (1988) observed a significant decrease in the partitioning of chlorine between magmatic vapor and a topaz-rhyolite melt ($D_{Cl}^{v/m}$ decreases from 2 down to 0.4) as the X_{H2O} in the vapor decreased from 1.0 to 0.6 at 800 ^{o}C and 2kbar. Measurements of chlorine partitioning between the vapor and melt ($D_{Cl}^{v/m}$) from the CO_2-bearing experiments of this study are consistent with a similar decrease from ~6 to ~1 as X_{H2O} decreases from 0.90 to 0.62 with increasing X_{CO2}. The decrease in chlorine partitioning will result in a decrease in the efficiency of removal of copper into exsolving vapor and brine with increasing X_{CO2}. Thus, the predictions of the CO_2-MVPart model for the efficiency of removal of copper into vapor + brine mixtures rely upon the competition between more copper available for extraction, due to early volatile exsolution, and less copper removed, due to lower chlorine partitioning.

If both the magmatic vapor and any later brine are included in the efficiency calculations, then the efficiency of removal of copper into the vapor + brine mixtures is remains relatively constant with changes in X_{CO2}, with only a small increase at low X_{CO2} (Figure 10). This is due to exsolution of vapor, and later brine, at smaller degrees of crystallization with increasing X_{CO2} and thus, less copper is lost to crystallization. As the X_{CO2} in the vapor increases, the effect of lower chlorine partitioning becomes more pronounced. Despite early vapor phase saturation, each aliquot of vapor and brine does not remove copper from the crystallizing melt as efficiently and the overall efficiency of removal of copper again remains roughly the same with only a small decrease predicted at high X_{CO2} (Figure 10). However, this efficiency calculation cannot evaluate the contribution of the magmatic vapor independent of any brine present.

Several studies of the exsolution of two-phase MVPs from shallow magmas demonstrate that abundant, low-density magmatic vapor may separate from low proportions of high-salinity brine (Audetat et al., 2008; Sillitoe, 2010). Later fluids may erode this reservoir of copper-rich brine, but the deposit forming potential of the separated phases may remain independent. Thus, the efficiencies of removal of copper into the vapor and brine should also be evaluated independently. Furthermore, some deposits may form almost exclusively from a single-phase magmatic vapor or supercritical fluid. The efficiency of removal of copper into supercritical fluids can be approximated by exsolution of vapor without brine saturation.

Prior to brine saturation, the efficiency of removal of copper into the vapor alone increases with progressive crystallization due to enrichment of chlorine in the melt and vapor. Upon reaching brine saturation, the efficiency of removal of copper into the

magmatic vapor decreases rapidly due to strong partitioning of copper into the high-salinity magmatic brine. Three factors affect how the efficiency of removal of copper into the vapor as a function of X_{CO2}: early volatile phase saturation, lower chlorine partitioning, and the degree of crystallization at brine saturation during second boiling. The salinity of brine-saturated vapor varies only a small amount at $X_{CO2} \leq 0.10$. At these conditions, the benefit of early volatile phase saturation outweighs the formation of a late brine phase, and no change is observed for $D_{Cl}^{v/m}$. As a result, the "peak efficiency" of removal of copper from the melt into the vapor will occur at low, but non-zero, values of X_{CO2} (Figure 10). In contrast, the benefit of CO_2-rich ($X_{CO2} \geq 0.24$) volatile phase exsolution at low degrees of crystallization is greatly outweighed by a low $D_{Cl}^{v/m}$ and the concomitant low salinity of the brine-saturated vapor. Accordingly, lower efficiencies of removal of copper are predicted for high-CO_2 magmatic vapors compared to CO_2-free or low-CO_2 vapor exsolution.

The CO_2-MVPart model also allows for the calculation of the "intrinsic" efficiency of removal of copper (E^I) into magmatic vapor. The intrinsic efficiency is determined by the concentration of copper in the vapor compared to the concentration of copper in the melt at volatile phase saturation ($[Cu]_{melt}^S$), rather than the initial concentration of copper in the silicate melt ($[Cu]_{melt}^0$). The intrinsic efficiency is calculated using the raw efficiency (E^0), the initial concentration of the copper in the melt, and the copper concentration at volatile phase saturation according to the function:

$$E^I = E^0 \cdot \frac{[Cu]_{melt}^0}{[Cu]_{melt}^S} \qquad (15)$$

The intrinsic efficiency does not include any specific modeling of the timing of volatile saturation but instead evaluates the intrinsic ability of the vapor or vapor + brine to extract copper from a melt.

In all cases, the intrinsic efficiency of removal of copper into the magmatic vapor decreases with increasing X_{CO_2} (Figure 10). The intrinsic efficiency is a measure of the quantity of copper removed from the melt relative to the quantity of copper present in the melt at the time it first saturated with a volatile phase, as opposed to the overall efficiency, which is relative to the initial concentration of copper in melt before any crystallization occurred. Thus, the intrinsic efficiency of removal of copper into MVPs decreases more significantly with increasing X_{CO_2}. In order to highlight the CO_2-MVPart predictions for the efficiency of removal of copper into exsolving magmatic volatile phases a bulleted list of model results is shown below in Table 8.

Efficiency of removal of copper from melt into vapor + brine mixtures:

- Is relatively constant, increasing *slightly* (~3%) as a function of increasing X_{CO2} for $X_{CO2} < 0.10$, then decreasing *slightly* (~5%) for $X_{CO2} > 0.38$.

- is enhanced at low X_{CO2} due to vapor saturation at lower degrees of crystallization

- is limited at high X_{CO2} because of the decrease in vapor/melt chlorine partitioning with increasing X_{CO2}

Efficiency of removal of copper by the vapor only:

- increases *slightly* (~3%) as a function of increasing X_{CO2}, for $X_{CO2} < 0.10$, then decreases *strongly* (~15%) for $X_{CO2} > 0.38$ where vapor efficiency can be reduced by as much as a factor of 2

- is enhanced at low X_{CO2} due to vapor saturation at lower degrees of crystallization

- decreases at high X_{CO2}, due to earlier brine saturation and lower vapor/melt chlorine partitioning

Intrinsic efficiency of removal of copper into vapor or vapor + brine:

- decreases with increasing X_{CO2} as the calculation of the intrinsic efficiency removes the effect of any crystallization prior to MVP saturation

Table 8: Bulleted summary of CO_2-MVPart model predictions: see text for discussion

2.5.3.3 Effects of Changes to Model Variables

Several key magmatic parameters of melt-volatile phase equilibrium must be set for the model. These parameters are discussed in either the original model presented by Candela at al. (1998), or in the changes designed to account for the presence of CO_2 in the MVPs (Section 2.5.3.1). Changes to many of these parameters will affect both the

absolute magnitude of efficiencies of removal of copper, and concentration of CO_2 at "peak vapor efficiency". Several sensitivity tests were run in order to evaluate the strength of the trends in the efficiency of removal of copper into MVPs presented in the previous section. The sensitivity tests examined the influence of changes to the Cl/H_2O ratio in the melt, melt ASI and associated fHCl, and the model for coexisting vapor-brine salinities.

The "peak vapor efficiency" for removal of copper from the melt into the vapor only is predicted to occur at the same X_{CO2} for a fixed Cl/H_2O ratio in the melt. Changes in initial chlorine and water concentrations in the melt will result in changes in the absolute efficiency, but proportionally the same decrease in efficiency with increasing X_{CO2} (Figure 10). This is due to low crystal-melt partition coefficients for both chlorine and water, and similar progression of volatile phase exsolution towards brine saturation at a fixed Cl/H_2O ratio. Changes to the Cl/H_2O ratio will influence the efficiency of removal of copper into MVPs. Melts with higher Cl/H_2O ratios exsolve volatile phases with higher efficiency of copper removal and thus, have higher intrinsic deposit potential. A small shift in peak vapor efficiency is also observed due to changes in the degree of crystallization at vapor and brine saturation, both of which are functions of the Cl/H_2O ratio. As a result, the trend of lower efficiency of removal of copper into CO_2-rich magmatic vapors, and lower potential for deposit formation, will be increasingly pronounced for magmas with high Cl/H_2O ratios, which otherwise have a high potential for formation of PCD.

I also evaluated the impact of changing the aluminum saturation index of the melt (which also affects the fHCl) between 1.01 and 1.04, which is within the range expected

for natural magmas associated with PCD (Audetat et al., 2008; Sillitoe, 2010; Simon and Ripley, 2011; Williams et al., 1997). The primary impact of this change on the model is an increase in the available magmatic chlorine, but a decrease in the solubility of FeO in the melt and corresponding increase in $FeCl_2$ in the magmatic vapor (Eugster and Baumgartner, 1987). The decrease in chlorine available for copper complexing results in a decrease in the magnitude of the predicted efficiency of removal of copper into the vapor (30% down to 23%), and a shift towards lower values of X_{CO2} at peak vapor efficiency (Figure 10).

The vapor salinity measurements presented for fluid inclusions from this study and that predicted by Duan et al. (1995) are slightly elevated compared to the range presented by Bodnar et al. (1985) for the $NaCl$-H_2O system. A sensitivity test designed to evaluate the importance of the brine saturated vapor salinity was conducted to investigate the effect of this discrepancy on efficiency of removal of copper into MVPs. The brine-saturated vapor limb of the $NaCl$-H_2O-CO_2 solvus was reduced to 50% of the previous value for the sensitivity test. This lower salinity results in a reduction of the efficiency of removal of copper into the vapor at peak vapor efficiency (30% down to 23%), and a shift in the X_{CO2} value at peak vapor efficiency (0.10 down to ~ 0.05) due to earlier brine saturation (Figure 10). All sensitivity tests confirm that the observations from the general CO_2-MVPart model are robust. A strong decrease in efficiency is still predicted at all model conditions for the magmatic vapor with increasing X_{CO2}. Additionally the efficiency of removal of copper into vapor + brine mixtures is predicted to decrease slightly, even assuming that all magmatic brine contributes to the total efficiency of the magmatic volatile phases. The peak vapor efficiency is predicted to occur at low

concentrations of CO_2 in the magmatic vapor (X_{CO2} = 0.05 to 0.10) for all model
conditions.

2.5.4   *Geologic Implications for Copper Removal by CO_2-Bearing MVPs*

The goal of magmatic copper partitioning experiments is to develop better genetic
models of the conditions that maximize the potential for deposit formation. Modeling of
the variability in the efficiency of removal of copper into MVPs as a function of X_{CO2}
provides a tool for evaluating the effect of CO_2 on the potential for the formation of PCD.
These models can then be used to account for the influence of slab characteristics,
magma evolution, fluxing of MVPs, and emplacement geology on the potential for
deposit formation. Each of these aspects of an intrusion will influence the budget and
evolution of CO_2 concentrations throughout the lifetime of an intrusion, in particular
during exsolution of MVPs and extraction of copper from the silicate melt.

The dominant source of the H_2O-CO_2-Cl component of arc magmas is the
seawater incorporated into subducting slabs, and/or associated with ocean sediments. The
exsolution of H_2O-CO_2-Cl-bearing volatile phases from slabs is causative in the
formation of melts within a mantle wedge and lower crust (Baker and Balcone-Boissard,
2009; Candela and Piccoli, 2005; de Leeuw et al., 2007; Fischer, 2008; Geiger et al.,
2005; Jarrard, 2003; Lowenstern, 1994; Wallace, 2005). Therefore, the Cl/H_2O of ratio of
arc magmas is initially controlled by seawater (Cl/H_2O ~ 0.02). The Cl/OH ratios in
magmatic amphibole (Burnham 1997) and Cl/H_2O fluxes from arc volcanoes (Hedenquist
and Lowenstern, 1994; Jarrard, 2003) support a similar Cl/H_2O ratio.

Given an intrinsic Cl/H_2O ratio similar to seawater, shallow arc magmas with an
initial water concentration of ~ 1 to 4 wt% should have chlorine concentrations on the

order of 200 to 800 ppm. The generally incompatible behavior of both chlorine and water in crystals formed from evolving arc magmas mitigates significantly changing the Cl/H_2O ratio of the evolving melts. However, enrichment of chlorine in subducting slabs is possible, and can generate Cl/H_2O ratios higher than 0.02 in some arc magmas (Candela and Piccoli, 2005). As discussed, melts that are generated with a Cl/H_2O ratio greater than that of seawater will have a higher potential for PCD formation, but are more susceptible to poisoning by high X_{CO2}.

Numerous studies of magmatic volatile phases note that the expected range of Cl/H_2O ratios would result in exsolution of volatile phases with bulk salinities ranging from 1 to 2 wt% $NaCl_{eq}$ at initial saturation, up to 5 to 10 wt% $NaCl_{eq}$ near the end of volatile phase exsolution (Baker and Balcone-Boissard, 2009; Bodnar, 1995; Candela and Piccoli, 1995; Candela and Piccoli, 2005; Hedenquist and Lowenstern, 1994; Heinrich et al., 2004; Simon et al., 2006). The volatile phases assemblages exsolved from shallow arc magmas usually comprise either a single low-density phase, or a two-phase coexisting low-density vapor and high-density brine. The conditions for my CO_2-bearing melt-vapor brine experiments and the CO_2-MVPart model are designed to be consistent with these melt-volatile phase assemblages. This consistency allows for the results to be representative of copper removal during exsolution of MVPs from natural arc magmas. However, interpretation of the data from the CO_2-MVPart model requires considering the variability in the volatile phase(s) during exsolution and physical phase separation at magmatic conditions as the magma crystallizes.

The exsolution of volatile phases from a shallow magma is generally hypothesized to begin with exsolution of a single low-salinity fluid, which may intersect

the vapor-brine solvus as the salinity of the exsolving fluid increases (Audetat et al., 2008; Candela and Piccoli, 2005; Candela and Piccoli, 1998; Heinrich et al., 2004; Sillitoe, 2010). As discussed, a number of porphyry deposits contain fluid inclusions with signatures of magmatic proto-ore fluids that exsolved as two-phase vapor-brine mixtures directly from the causative magma. The results of the CO_2-MVPart model are the most applicable to the exsolution of a low salinity vapor, followed by brine saturation. The efficiency of removal of copper into CO_2-rich ($X_{CO2} > 0.24$) vapor and brine will be roughly 5% lower than similar vapor + brine mixtures at low concentrations of CO_2 ($X_{CO2} \leq 0.10$). The lower efficiency will, at a minimum, lower the copper budget of any copper anomaly formed by CO_2-rich vapor + brine mixtures. In addition, as the contribution of the exsolved brine to ore deposit formation decreases, the poisoning effect of CO_2 becomes more pronounced.

In the limit wherin brine makes no contribution to ore formation, the efficiency of removal of copper into the vapor alone will control the potential for formation of a PCD. The results presented in Figure 10 demonstrate that the efficiency of removal of copper into the magmatic vapor at high X_{CO2} can decrease by as much as a factor of 2 compared to vapors exsolved at low X_{CO2}. Furthermore, the degree of crystallization, and pressure, at volatile saturation in a natural system will be controlled by numerous factors including the H_2O/CO_2 ratio in the melt. The CO_2-MVPart model is only designed to evaluate exsolution of volatile phases at a fixed pressure, and cannot incorporate the dynamic range of volatile phase saturation conditions that likely obtains in shallow arc magmas. As discussed, the trends in the intrinsic efficiency (E^I) are independent of any

crystallization prior to volatile phase saturation. Yet, the results of the CO_2-MVPart model are only snapshots of volatile exsolution at a fixed H_2O/CO_2 ratio.

The solubility of CO_2 in silicate melts is much lower H_2O. If the CO_2 is derived solely from within the primary shallow felsic magma, the exsolution of CO_2-rich volatile phases will quickly deplete the magma in CO_2, or result in exsolution of MVPs at a higher pressure (Alletti et al., 2009; Behrens et al., 2004; Botcharnikov et al., 2005; Liu et al., 2005; Lowenstern, 2001; Newman and Lowenstern, 2002). Although our model does not account for variability in volatile phase saturation pressure, the evolution of magmas under these conditions will proceed towards CO_2-poor compositions. If the shallow (< 5 km) felsic magma is the only source for CO_2, then only MVPs exsolved early during second boiling will have lower efficiencies at high concentrations of CO_2. However, the concentration of CO_2 in the magma may also be buffered by additional CO_2 reservoirs. The episodic injection of mafic or andesitic melts into the upper crust from deeper within an complex arc system can contribute higher concentrations of CO_2 to shallow arc magmas (Annen et al., 2006; Behrens et al., 2004; Botcharnikov et al., 2005; Hattori and Keith, 2001; Lowenstern, 2001; Proffett, 2003). Alternatively, these magmas may titrate bubbles of CO_2-rich volatile phases into the shallower magma from a deeper CO_2-rich reservoir (Annen et al., 2006; John et al., 2010). In addition, the shallow felsic magma, and/or the deeper ascending magmas, can incorporate CO_2 through assimilation or contact metamorphism of carbon-bearing host rocks.

Magmas with a large source reservoir of CO_2 might maintain moderate to high CO_2 concentrations in the exsolving volatile phases much longer than magmas with CO_2 dissolved in the shallow magma as the only CO_2 source. To the extent to which chlorine

complexation and/or salinity control copper removal from the melt into MVPs, these systems can maintain a dramatically lower potential for formation of PCD. The CO_2-MVPart model predicts a maximum decrease from nearly 50% removal of copper into magmatic vapors exsolved at low X_{CO2}, down to below 15% efficiency for exsolution of vapor at high X_{CO2}. The lower efficiency of removal of copper into the vapor at high X_{CO2} is associated with early brine saturation of the magma. The high salinity and small mass fractions of brine exsolved at high X_{CO2} increase the possibility that the low-density vapor will physically separate from the brine, which may result in textural evidence for the exsolution of only a low-salinity vapor (Audetat et al., 2008). Later magmatic fluids, or convecting meteoric fluids, may erode the pooled brine phase as the intrusion cools and may still transport its dissolved ore metals, ultimately contributing to an ore deposit (Audetat et al., 2008; John et al., 2010). The poisoning effect of CO_2 is lessened with increasing influence of the brine on PCD formation.

Volatile exsolution of a single-phase fluid may occur at high-pressure conditions, but equilibrium at shallow levels requires the formation of brine except for low Cl/H_2O ratios. The CO_2-MVPart model demonstrates that the formation of even small amounts of brine at high X_{CO2} may alter the potential for deposit formation. In natural intrusions with protracted brine exsolution, a significant decrease in the efficiency of removal of copper into the vapor is predicted at high X_{CO2}.

Audetat et al. (2008) notes that exsolution of supercritical fluids or low-salinity vapor exsolution can occur in both intrusions associated with, and not associated with PCD. The CO_2-MVPart model predicts that the efficiency of removal of copper into only a single, low salinity volatile phase will increase slightly, or stay nearly constant at low

X_{CO_2} due to initial volatile saturation slightly earlier in the crystallization sequence of a given intrusion. If the magma exsolves only a single volatile phase at high X_{CO_2}, the lower chlorine partitioning will still result in lower efficiency of removal of copper into the volatile phase. In that study, those systems in which volatile phases were determined to have exsolved from magmas that gave rise to mineralized systems, and those that did not, were only characterized for the presence or absence of CO_2. Thus, the conclusion that volatile exsolution produced only a single volatile phase does not account for CO_2.

Fluid inclusions from the ore zone trap fluids that are thought to be sourced from volatile phases exsolved from causative magmas associated with PCD. However, few observations are made regarding the presence or absence of CO_2 in the fluid inclusions (Audetat et al., 2008; Heinrich, 2005; Heinrich et al., 2004). Without Raman spectroscopic measurements, or other similar direct tests for CO_2, detection relies upon microthermometric observations of clathrate. Even when microthermometry is used to characterize fluid salinity, the small amount of clathrate present melts at temperatures well above 0 ^{o}C, and is often difficult to detect. Accurate detection is also made more complicated by the presence of other volatile phase components (e.g. H_2S-Chapter 3). The result is that clathrate melting might often be overlooked or poorly constrained in the characterization of fluid inclusions from many deposits. Nonetheless, the range of X_{CO_2} in the magmatic vapor at peak vapor efficiency predicted by the CO_2-MVPart model is also remarkably consistent with the range of CO_2 concentrations observed for natural PCD. Section 2.1.2 notes that analyses of some natural fluid inclusion assemblages include observation of "low concentrations of CO_2" in vapor-rich inclusions, and where quantitative measurements are made, 5 to 10 mol% CO_2 is reported (Audetat et al., 1998;

Audetat et al., 2008; Lowenstern, 2001; Rusk et al., 2008; Webster et al., 2011). For the wide range of melt-volatile conditions tested by the CO_2-MVPart model, the peak vapor efficiency for copper removal by the vapor or vapor + brine also falls in the 5 to 10 mol% CO_2 range. The mechanisms behind this consistency are worth more fully investigating in the future, considering that the CO_2-MVPart model was not specifically designed to match the peak vapor efficiency with any natural conditions or observations.

The CO_2-MVPart model only considers the loss of copper during crystallization of phases in which copper is not an essential structural constituent. The longer magma crystallization proceeds before exsolution of volatile phases, the more the formation of copper-rich minerals in the magma, such a sulfides, can reduce the copper available for extraction by the MVPs (Candela and Piccoli, 2005; Clemente et al., 2004; Halter et al., 2005; Jugo et al., 1999; Mengason et al., 2008; Seo et al., 2009; Sillitoe, 2010; Simon et al., 2008a; Simon and Ripley, 2011). However, the equilibrium between the silicate melt and exsolved volatile phases in a CO_2 and sulfur-bearing magmatic assemblage will likely have additional features not predicted by modeling and partitioning data based upon chlorine complexation alone. Any CO_2-sulfur interactions that affect copper partitioning may reinforce or mitigate the trends in efficiency of copper removal into MVPs predicted by the CO_2-MVPart model. In order to fully evaluate the variation in efficiency as a function of X_{CO2}, with and without brine contribution, additional experiments including sulfur as component of the MVPs and silicate melt are presented in Chapter 3.

2.5.5   Conclusions and Progression to Sulfur-Bearing Experiments

Microthermometry conducted on fluid inclusions presented in this study is consistent with model predictions for the $NaCl$-H_2O-CO_2 system at magmatic conditions. The combination of clathrate melting temperature measurements and micro-Raman measurements, to calculate inclusion pressure, allow for accurately quantifying CO_2-bearing vapor inclusion salinity. These techniques provide a new tool for analysis of inclusions with only one CO_2 phase at room temperature. This method can be utilized to characterize fluid inclusions that trap low-salinity fluids from shallow magmatic and sub-solidus hydrothermal environments or their experimental analogs. However, the extension of this experiment design to include sulfur requires expanding the method to determine vapor inclusion salinity to account for inclusions that also contain a mixture of clathrate-forming volatile phase components (e.g. CO_2 + H_2S)

Copper partitioning data reported in this chapter provide direct experimental constraints on the effect of CO_2 on the potential for chloride-complexed copper removal by a MVP that contains significant X_{CO2}. The increase in $D_{Cu}^{b/v}$ from 21($\pm$8) to 110($\pm$40) and decrease in $D_{Cu}^{v/m}$ from 9.2($\pm$4.2) to 1.6($\pm$0.8) at X_{CO2} = 0.10 and 0.38, respectively (in-situ fractured) indicate that at higher X_{CO2}, there is an enrichment of copper in magmatic brines and a depletion of copper in magmatic vapors relative to melt-vapor-brine assemblages with lower X_{CO2}. The clear picture emerges that, to the extent that Cl controls copper complexation, the decrease in the brine/vapor mass proportion and shift in copper partitioning at higher X_{CO2}, requires that CO_2-rich vapors have a lower potential for efficient removal of copper from the melt. Furthermore, the CO_2-MVPart model predicts that the exsolution of volatile phases at X_{CO2} > 0.24 will produce large

mass proportions of low-salinity vapor that will remove half of the copper from the silicate melt compared to low-CO_2 systems. Copper-rich brines may or may not contribute to formation of PCD, depending upon entrainment with the magmatic vapor or erosion and incorporation by later magmatic or meteoric fluids. If the brine does contribute to the potential for deposit formation, then the poisoning effect of CO_2 on the efficiency of removal of copper from the melt into the vapor + brine mixture will be mitigated. Nonetheless, the peak efficiency of removal of copper into vapor, or vapor + brine, predicted by the CO_2-MVPart model is consistent with the range of CO_2 observed in natural PCD (5 mol% to 10 mol% CO_2), suggesting that low CO_2 concentrations may have a positive influence on deposit formation. In contrast, volatile phases at the upper end of the range for arcs in general ($X_{CO2} > 0.25$) will have a reduced potential for the formation of ore deposits, particularly for brine-free ascending vapors.

The partitioning of chloride-complexed copper has long been shown to be important in porphyry deposit formation. However, the role of sulfur needs to be determined. MVP copper partitioning experiments presented in Chapter 3, using a similar design to that presented in this chapter, incorporate sulfur as a component of the MVPs and silicate melt. These experiments will more fully address the role of CO_2 in the generation of proto-ore fluids. The results for these experiments allow for quantifying the effects of any interactions that may occur between CO_2 and sulfur-complexing ligands such as HS^- and any corresponding effect on copper partitioning. Results from the CO_2-MVPart model, and their implications for ore formation, will then be reviewed in light of variability in copper partitioning among sulfur-bearing magmatic phases as a function of X_{CO2}.

Chapter 3: Copper Partitioning in CO_2 and Sulfur-Bearing Magmatic Volatile Phases

3.1 Introduction

The prevailing hypothesis for the formation of porphyry copper deposits, and related magmatic hydrothermal deposits, relies upon extraction of copper and other ore metals from magma into exsolved magmatic volatile phases (Holland 1972, Candela and Piccoli 1995, Simon et al. 2006). These "proto-ore fluids" (Candela et al. 2010) extract metals from magmas (arc magmas in the case of porphyry copper deposits) with varying efficiencies according to their bulk composition (salinity, K/Na/Fe ratio, fH$_2$O, fO$_2$, fHCl, fS$_2$, etc.), physical properties (e.g., density), conditions of volatile phase exsolution (e.g. temperature and pressure), and can ultimately become saturated with respect to copper-bearing phases (e.g. Cp, Bn) as they evolve towards the ore-fluids that likely deposit ore in porphyry or epithermal deposits. Chapter 2 provides new constraints on the role of CO_2 in controlling MVP salinities and copper removal from melts via chlorine complexation. However, porphyry copper deposits are primarily sulfide deposits, and, increasingly, experimental research is focused on investigating how sulfur interacts with chlorine to complex copper in MVPs, and how this affects the efficiency of removal of copper into exsolving magmatic volatile phases. This chapter focuses on a series of experiments designed to investigate the effect of variable concentrations of CO_2 on the partitioning of copper among sulfur-bearing, melt, vapor and brine, and the implications for the efficiency of copper removal from the melt into sulfur-bearing MVPs.

3.1.1 Sulfur in Porphyry Copper Deposits

Observations from porphyry copper deposits show that copper in the ore is hosted almost exclusively in sulfide minerals. The precipitation of sulfide from the ore-fluid points to possibility that sulfur ligands (e.g. HS^-) play an important role in, at minimum, metal transport and deposition under hydrothermal conditions (Audetat et al., 1998; Heinrich, 2005; Heinrich et al., 2004; Heinrich et al., 1999; Pettke et al., 2010; Pokrovski et al., 2008; Rusk et al., 2004; Ulrich et al., 1999). Early thermodynamic analysis of hydrothermal fluids revealed that ascending volatile phases could be cooled from at least 600 °C down through 250 °C and retain significant amounts of sulfur and ore metals through interactions with wall rock (Holland, 1965). Numerous methods have been employed to determine directly the source of the sulfur associated with porphyry mineralization. Primary fluid inclusions (formed with initial quartz/sulfide/sulfate vein precipitation) from the ore-zone of porphyry deposits often contain opaque daughter phases inferred to be sulfides. Studies of fluid inclusions from the ore zone often note that the chloride content of the fluid inclusions is insufficient to balance the solute load, implying the presence of other ligands such as HS^- (Audetat et al., 2008; Heinrich et al., 1999). Recent ability to quantify sulfur concentrations in fluid inclusions demonstrates that sulfur can range from thousands of ppm up to ~ 5 wt% (Audetat et al., 2008; Halter et al., 2005; Hattori and Keith, 2001; Rusk et al., 2004; Seo et al., 2009; Sillitoe, 2010; Simon and Ripley, 2011). Some fluid inclusions assemblages in porphyry deposits also have homogenization temperatures approaching the solidus temperatures of felsic magmas, consistent with a magmatic origin for the sulfur content of high-temperature proto-ore fluids (Azbej et al., 2007; Bodnar, 1995; Halter et al., 2005; Hedenquist and

Lowenstern, 1994; Heinrich et al., 2004; Heinrich et al., 1999; Roedder, 1971; Rusk et al., 2008; Rusk et al., 2004).

Sulfur isotopic data from porphyry deposits also support a magmatic source for mineralizing sulfur. Several recent studies of δ^{34}S systematics of sulfides from porphyry deposits including Bingham, Butte, and Lepanto Far Southeast, are consistent with a magmatic origin for the sulfur (Field et al., 2005; Hattori and Keith, 2001; Imai, 2000; Simon and Ripley, 2011). Hattori and Keith (2001) discuss that sulfides from porphyry copper deposits consistently show magmatic sulfur isotopic signatures despite sources of sulfur within host rocks and, when combined with mass balance considerations, suggest a large sulfur reservoir sourced from deep mafic magma input. The intrusion of sulfur-bearing, CO_2-rich mafic melts into shallower felsic melts may add CO_2 and sulfur during periods of resurgent magmatism (Alletti et al., 2009; Audetat et al., 1998; Audetat et al., 2008; Botcharnikov et al., 2005; Halter et al., 2005; Halter et al., 2004; Hattori and Keith, 2001; Lowenstern, 2001; Simon and Ripley, 2011). Simon et al. (2011) note that significant scatter is observed in δ^{34}S, especially for smaller deposits, but that this is likely due to post mineralization alteration and interaction with surrounding sedimentary rocks and meteoric water. It remains unclear what proportion of deep sulfur flux is added to shallow magmas via injection of mafic magmas versus through fluxing of volatile phases within a complex arc system.

The presence of significant magmatic sulfide may sequester ore metals due to large $D_{Cu}^{Sulfide/melt}$ at magmatic conditions. If the sulfides are removed from the magma prior to exsolution of MVPs, will greatly reduce the potential for deposit formation (Jugo et al., 1999; Lynton et al., 1993; Mengason et al., 2010; Mengason et al., 2008; Sillitoe,

2010; Simon et al., 2008a; Simon and Ripley, 2011). In addition, reduced silicate melts have a much higher sulfur solubility at a given $f\mathrm{S}_2$, resulting in less sulfur available for MVP ore metal complexing in reduced arc magmas (Clemente et al., 2004). Magmas associated with PCD are generally relatively oxidized (>NNO) and this feature helps increase the fugacity of sulfur species in the exsolved MVPs (Sinclair, 2007; Whitney, 1984). However, assuming that that prevailing hypothesis of a magmatic source for porphyry ore fluids is correct, many arc environments are evidently characterized by appropriate $f\mathrm{S}_2$, $f\mathrm{H}_2\mathrm{O}$ and a high enough $f\mathrm{O}_2$ to allow for exsolution of volatile phases with significant partitioning of sulfur into the exsolved MVPs. These MVPs can then ascend into overlying fractures and dikes and deposit the magmatic sulfur along with copper as, dominantly, copper-iron-sulfides (e.g. Bn, Cp).

Analyses of fluid inclusions from natural deposits, and experiments at magmatic conditions, also provide evidence for sulfur-complexing of copper. These studies demonstrate that if chlorine alone is available for metal complexing, the partitioning of copper among the silicate melt, vapor and brine or silicate melt and supercritical fluid will follow the salinity of the MVPs and chlorine concentration of the melt (Candela and Holland, 1984; Candela and Piccoli, 1995; Candela and Piccoli, 2005; Frank et al., 2003; Simon et al., 2006; Williams et al., 1995). The presence of CO_2 as a phase component of the magmatic phase assemblage will not disrupt the salinity-dependent partitioning of copper, beyond altering the salinity of the coexisting vapor and brine, if CO_2 does not act as a ligand at magmatic conditions (Lowenstern, 2001). Heinrich et al. (1999; 1992) note that charge balance, and the high concentration of sulfur in ore zone inclusions, imply the presence of complexing ligands other than Cl⁻. Fluid inclusions from natural deposits

show deviations from the behavior predicted for chlorine-complexation at magmatic

conditions. Grasberg, Bajo de Alumbrera (Ulrich et al., 1999), Yankee Load (Audetat et

al., 1998), El Teniente, and Santa Rita (Audetat et al., 2008) all have $D_{Cu}^{b/v}$ values ≤ 1,

whereas others, such as Bingham Canyon (Redmond et al., 2004), fall below the critical

vapor-brine salinity ratio. These data from natural deposits provide strong evidence that

natural ore metal transport from magmatic conditions to those at ore deposition requires

significant complexation by ligands other that Cl$^-$. The high concentration of sulfur in ore

minerals and fluid inclusions demonstrates that sulfur ligands (e.g. HS$^-$) may play a role

in complexing a significant portion of ore metals that ultimately form PCD. In order to

understand the role of sulfur in removal of copper from the melt by the magmatic volatile

phases, recent experiments at magmatic conditions have included sulfur as part of the

melt-volatile phase assemblage.

3.1.2 Sulfur in Copper Partitioning Experiments

Recent experimental work has incorporated sulfur into the Cl-H$_2$O systems

previously used to simulate natural magmatic volatile phases. The results indicate that

sulfur complexing may also play an important role in the magmatic regime of copper

partitioning (Frank et al., 2011; Jugo et al., 1999; Pokrovski et al., 2008; Simon et al.,

2006; Simon and Ripley, 2011; Zajacz et al., 2011). Simon et al. (2006) reports a

significant increase in the partitioning of copper into magmatic vapor relative to

coexisting brine at 800 ^{o}C and 140 MPa ($D_{Cu}^{v/b}$ increases from 0.27 ± 0.10 to 0.69 ± 0.16

with the addition of sulfur) near the critical point for NaCl-H$_2$O volatile phases. When

compared to the silicate melt there is an increase in the copper partitioning into both

vapor and brine ($D_{Cu}^{b/m}$ and $D_{Cu}^{v/m}$ increase from 240 ± 80 and 63 ± 31 to 443 ± 68 and 316

± 22, respectively) relative to the melt, consistent with the presence of sulfur complexing at magmatic conditions. Frank et al. (2011) demonstrate that the magnitude of the concentration of copper in the MVPs and efficiency of removal of copper into the MVPs are functions of the fS$_2$ ($D_{Cu}^{v/m}$ = 3.1 ± 0.7 and 12 ± 7 for log fS$_2$ = -1 to -3, respectively). However, the mechanism for copper removal from the melt into MVPs at magmatic conditions has remained poorly understood.

Numerous studies have been conducted to investigate copper complexing by sulfur-bearing ligands at sub-solidus temperatures. These studies hope to explain the observation of copper enrichment of low-salinity vapors, and volatile phases in general, with the addition of sulfur. Zajacz et al. (2011) reports new thermodynamic models for Cu-HS ± Cl complexes, stabilized by the presence of Na$^+$, K$^+$, H$^+$ ions along with solubility data for CuAu alloys in H$_2$O-dominated vapor at 1000 ^{o}C and 150 MPa consistent with the thermodynamic models. Those data help to explain how the fS$_2$, fHCl, and the Na/K/H ratios of the MVPs may influence the partitioning of copper between silicate melts and volatile phases or between coexisting vapor and brine. However, none of the existing sulfur-bearing magmatic copper partitioning experiments includes CO$_2$ as a component of the system and thus there is no constraint on how CO$_2$ affects the partitioning of copper in such systems.

This chapter focuses on a series of experiments at 800 ^{o}C and 100 MPa that evaluate copper partitioning in synthetic, CO$_2$-bearing, pyrrhotite-saturate melt-vapor-brine assemblages. The copper partitioning data reported from these experiments shed light on the influence of CO$_2$ and sulfur on metal complexing, copper removal by magmatic volatile phases, and the formation of porphyry copper deposits, The data

reported herein provide direct experimental measurements of copper partitioning between coexisting vapors, brines, and silicate melts as a function of X_{CO2} and in equilibrium with magmatic sulfide (pyrrhotite). In addition, new methods (Raman spectroscopy and microthermometry to characterize the salinity of low-salinity vapors via melting temperatures of CO_2-H_2S clathrates) are presented, which are necessary to characterize fluid inclusions from CO_2-S-bearing MVP assemblages. Pyrrhotite-saturated experiments include a $NaCl$-KCl-$FeCl_2$-HCl component similar to that presented by Candela and Holland (1984) and Williams et al. (1995) as a proxy for the complex chloride-bearing phases generated during exsolution of volatile phases from arc magmas. Synthetic pyrrhotite was generated with a composition close to equilibrium with magnetite at experimental conditions and was added to experiments to add sulfur to the MVPs and silicate melt. Welded Cu_6Au_{94} alloy gold capsules (Zajacz et al., 2011) were used to ensure copper equilibrium and accurate characterization of copper partitioning.

The equilibrium composition of the CO_2 and sulfur-bearing MVPs, was quantified via analysis of magmatic volatile phases trapped as vapor and brine fluid inclusions assemblages using in-situ fracturing (Sterner and Bodnar, 1991). LA-ICPMS analysis of fluid inclusions and quenched glasses were then used to calculate partition coefficients and equilibrium constants for copper. The data reported show that the addition of sulfur to MVPs results in a pronounced increase in the copper partitioning into the magmatic vapor at low X_{CO2}. However, the enrichment of copper in the vapor due to the addition of sulfur is suppressed at high X_{CO2}. The suppression of sulfur-bearing copper complexation and reduction of vapor salinity at high X_{CO2} will affect the efficiency of removal of copper into magmatic volatile phases as a function of X_{CO2}. Qualitative modifications to

the predictions of the CO_2-MVPart model are also presented to evaluate the influence of X_{CO2} on the efficiency of removal of copper into sulfur-bearing MVPs, which are hypothesized to be vital in the formation of PCD.

3.2 Experimental Methods

3.2.1 Starting Materials

All pyrrhotite-saturated experiments were run in Cu_6Au_{94} capsules alloyed using the technique of Zajacz et al. (2011). Felsic silicate melts were generated at run temperatures from melting either powdered Bishop Tuff or powdered Corning Glass haplogranite minimum melt (GR1). The natural magnetite collected from Essex City, New York was added to all experiments, to ensure sufficient Fe was available for maintaining magnetite-saturated conditions regardless of whether magnetite was created or destroyed during equilibration with magmatic sulfides. Synthetic pyrrhotite was used for all experiments to allow for initial pyrrhotite compositions close to that expected for pyrrhotite-magnetite equilibrium at 800 ^{o}C, 100 MPa, and $fO_2 \sim$ NNO ($\sim Fe_{1-0.2}S$) (Mengason et al., 2010; Whitney, 1988). The synthetic pyrrhotite was generated via high-temperature heating of powdered iron metal with elemental sulfur. The masses of iron and sulfur were mixed and added to a fused silica tube with a small excess of sulfur relative to the desired composition. Once the tube was sealed under vacuum and heated, some sulfur must vaporize to generate the equilibrium P_{Sulfur} at the higher temperatures used for growing pyrrhotite. The synthetic pyrrhotite from a single experiment was used for all pyrrhotite-saturated experiments, ensuring homogeneous starting composition across all experiments.

Natural, inclusion-free Brazilian quartz was cored to create 4 mm diameter cylinders for trapping fluid inclusions. Water was used for lubrication and cooling during cutting, and cores are cleaned and oven dried for 12-24 hours to ensure that no additional water or contaminants are added to the experimental charge. Starting solutions were created using NaCl, KCl, HCl, and anhydrous $CuCl_2$.

3.2.2   Experiment Design

Sulfur-bearing copper partitioning experiments were performed in Cu_6Au_{94} (Zajacz et al., 2011) capsules (ID/OD : 4.9/5.0 mm) with $X_{CO2} = 0.10$ and 0.38 with methods similar to the design presented in Chapter 2. The experiments were run for five days at 800 ^{o}C and 100 MPa. The primary independent variable in these experiments remains the mole fraction of CO_2 (X_{CO2}). However, addition of pyrrhotite to experiments Cu402 through Cu411 and Cu601 through Cu607 added sulfur to the melt and MVP's in order to evaluate the effect of CO_2 on the coupled complexation of copper via chlorine and sulfur. The partitioning of copper will then be compared to the CO_2-bearing sulfur-free experiments and CO_2-MVPart model presented in Chapter 2, as well as to CO_2-free, pyrrhotite-saturated experiments from the literature (Frank et al., 2011; Lerchbaumer and Audetat, 2009; Simon et al., 2006; Zajacz et al., 2011).

René 41 vessels, used in combination with H_2 permeable noble metal capsules, were used to buffer the oxygen fugacity of the experiments to near the nickel-nickel oxide buffer (NNO ~ $1x10^{-15}$ MPa at 800 ^{o}C and 100 MPa)(Chou, 1987). The presence of sulfur as a phase component of the synthetic magmatic phase assemblage will not affect the establishment of H_2 equilibrium via osmotic equilibrium across the capsule walls, or the $f$$H_2O$ in the experiments. Thus, sulfur-bearing experiments will have the same $f$$O_2$ as

sulfur-free experiments. Sulfur-bearing experiments at $X_{CO2} = 0.10$ had an $fO_2 \sim$ NNO, whereas experiments at $X_{CO2} = 0.38$ had an $fO_2 \sim$ NNO – 0.1 to NNO – 0.2 log units. However, the H_2 gas generated by oxalic decomposition initially lowered the oxygen fugacity to NNO – 2 to NNO – 3 log units, well below FMQ.

Unlike the sulfur-free experiments, pyrrhotite-saturated experiments are much more vulnerable to the formation of additional phases, such as fayalite, at low oxygen fugacity, which may persist metastably at higher fO_2. Previous unsuccessful experiments showed that where pyrrhotite was in contact with large quantities of starting material glass and oxalic acid, macroscopic fayalite crystals grew (Figure 11). The formation of fayalite is particularly troublesome for high-CO_2 experiments where oxygen fugacity may remain below FMQ, because of the elevated transient hydrogen fugacity, for nearly 12-24 hours.
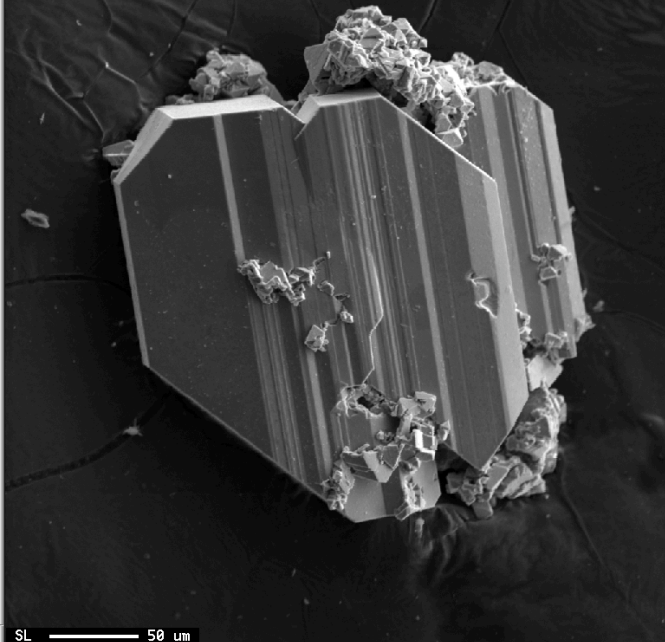
Figure 11: SEI image of fayalite crystals formed during the transient low oxygen fugacity environment predicted for pyrrhotite-saturated, CO_2-bearing experiments. Fayaltite crystal growth was observed in a previous experiment design, which allowed for physical contact between pyrrhotite (Po), starting glass and oxalic acid.

The Cu_6Au_{94} capsules used for pyrrhotite-saturated, high-CO_2 experiments (X_{CO2}=0.38) included half the mass of starting materials but had lengths of ~1.8 cm rather than the 2.5

cm used in the sulfur-free experiments. Thus, the pyrrhotite-saturated experiments required ~ 4 and ~ 24 hours to remove excess H_2 and ensure fO_2 equilibrium for experiments with $X_{CO2} = 0.10$ and 0.38, respectively, somewhat less than that predicted for the sulfur-free experiments. The change in the ratio of starting materials to capsule surface area, and resulting shorter equilibration time was the first change made to mitigate the formation of meta-stable phases.

To further mitigate the formation of fayalite, or other metastable phases, the starting pyrrhotite and magnetite were kept physically separate from the silicate melt by placing them inside an inner Cu_6Au_{94} capsule that is crimped closed but not welded (Figure 12). The physical separation of the pyrrhotite and magnetite also ensures that the silicate melt remains low in sulfide and helps ensure homogeneous analyses of the glass formed upon quench.
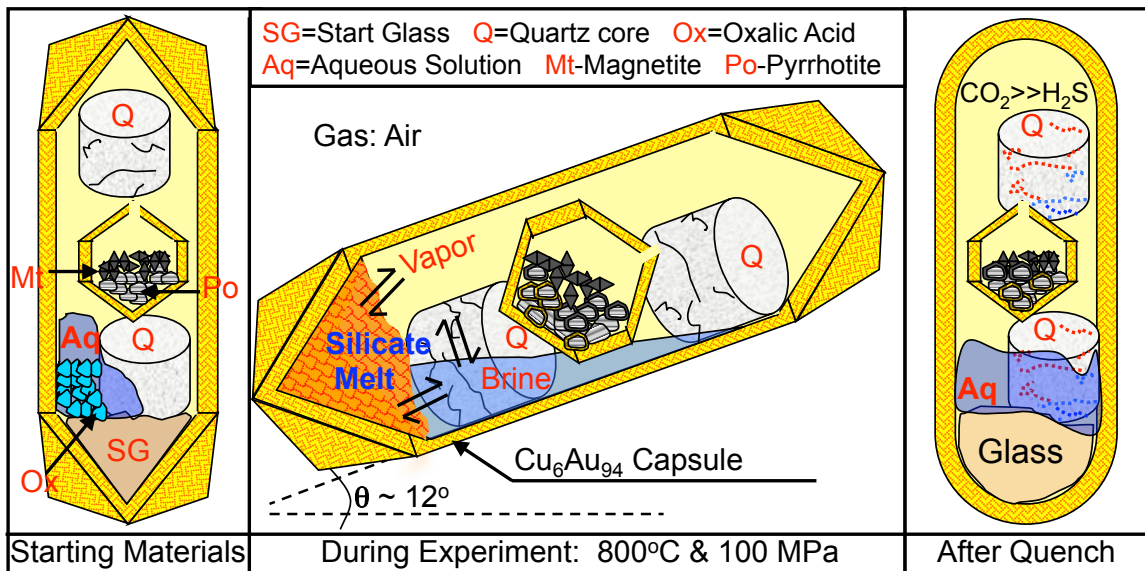
Figure 12: Cross-section of pyrrhotite-saturated MVP experiments in 5mm ID Cu_6Au_{94} capsules before, during, and after magmatic conditions of the run. Magnetite and pyrrhotite are contained inside 4mm ID inner capsules of the same alloy. Pyrrhotite converts to magnetite to liberate the sulfur required for equilibrium with all other magmatic phases and is also often rimmed in other Cu-Fe-sulfides due to the high a_{Cu} in the experiments. All experiments remain pyrrhotite and magnetite-saturated throughout their duration.

Gibbs phase rule defines the variance of an equilibrium assemblage by the equation F=C-P+2. For the 4-component (Fe-S_2-O_2-H_2) hydrothermal system at magnetite-pyrrhotite equilibrium (3 phases) there are 9 possible intensive variables but only 3 degrees of freedom. Thus at a fixed temperature, pressure and fO_2 (800 ^{o}C 100 MPa, and 1×10^{-15} MPa, respectively) there are no remaining degrees of freedom in an equilibrium system, and the composition of the pyrrhotite becomes fixed (Whitney, 1984). This equilibrium also fixed the fH_2O, fS_2, fSO_2, and fH_2S in the pyrrhotite-saturated experiments. However, the addition of copper as a component of pyrrhotite allows for an additional degree of freedom and small variability in fS_2 and at fixed fO_2 as a function of the $a_{Cu}^{CuAu\ Alloy}$ for copper-poor metal alloys (See Section 3.4.2). Small amounts of pyrrhotite are consumed by dissolution in the silicate melt, vapor, and brine, but all experiments remain pyrrhotite-saturated for the duration of the experiment.

The NaCl, KCl, and HCl concentration of the aqueous solution used as a starting material was also varied in the experiments as changes were made to the X_{CO2}. The starting solution in all experiments after oxalic acid dehydration still remains an equimolar mixture of NaCl and KCl (NaCl+KCl ~ 1.75 M) with roughly 0.09 M HCl resulting in a 10/10/1 initial Na/K/H molar ratio. As in the sulfur-free experiments, copper is added to the starting solution as $CuCl_2$ (~5000 ppm copper) to promote faster equilibration between the MVP's and the Cu_6Au_{94} capsule. The bulk volatile phase composition is designed to generate coexisting vapor and brine phases at the experiment conditions (800 ^{o}C, 100 MPa). The ternary plot for the $NaCl$-H_2O-CO_2 system based on work by Duan et al. (1995) shows the two-phase field of interest in these experiments and is reproduced below for reference (Figure 13).
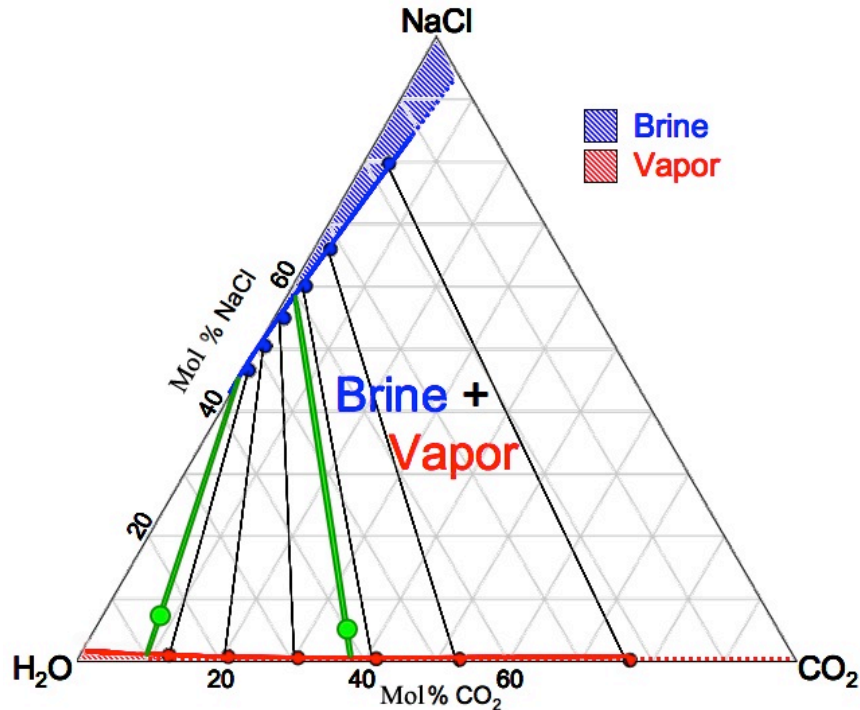
Figure 13: Ternary phase diagram for the NaCl-H₂O-CO₂ system: Low salinity vapor (red) and high-salinity brine (blue) fields are defined according to Duan et al. (1995). Bulk MVP compositions and tie-lines for pyrrhotite-saturated experiments are shown in green.

The NaCl component in this simple system, which is used as a general guide only, is used to represent the NaCl-KCl-FeCl₂-HCl±CaCl₂ chloride component of the volatile phases, and their natural analogues. The effects of sulfur species such as H_2S, or S_3^- on the MVP phase equilibria should be minor (see section 3.2.3) and no correction to the MVP phase relations was made relative to the sulfur-free conditions. The total salinity of the starting solution has been adjusted for all other starting materials to ensure that all experiments maintain a Cl/H_2O ratio similar to that of fluids exsolved from felsic magmatic systems, fixed at the same value used for the sulfur-free experiments (Cl/H_2O ~ 0.06) (Candela and Piccoli, 1995; Candela and Piccoli, 2005).

An inclusion-free core of Brazilian quartz was added to each charge to allow for trapping of synthetic vapor and brine fluid inclusions at run conditions. All pyrrhotite-saturated experiments utilized both in-situ and pre-fractured quartz cores. The in-situ

120

fracturing technique described in Sterner and Bodnar (1991) allows for additional time for equilibration between volatile phases and silicate melt prior to fluid entrapment. The use of in-situ fracturing was particularly vital in the pyrrhotite-saturated CO_2-bearing experiment design. The sulfur speciation (and any sulfur-bearing metal complexation) of the MVP's in these experiments is dependent upon oxygen fugacity, which is significantly out of equilibrium in CO_2-bearing experiments early in run duration. Thus, concerns regarding early trapping in pre-fractured quartz are even more troublesome. As a result, analyses of pre-fractured, quartz-hosted inclusions from these experiments are treated as supplementary data to analyses from in-situ fractured quartz, and were not accepted as equilibrium MVP compositions on their own. Glass-hosted fluid inclusions are also formed as bubbles of vapor-brine mixtures are trapped during quench. These inclusions must, by definition, be in equilibrium with the silicate melt at the glass transition temperature. However, only glass-hosted brine inclusions can be quantified by LA-ICPMS due to the strong host (glass) signal. In addition, quartz-hosted vapor and brine inclusions both provide more consistent data than glass-hosted inclusions because microthermometry can be used to discriminate between mixed inclusions and nearly pure-phase inclusions.

3.2.3   *MVP's: Composition and Fugacities*

The volatile phase assemblage presented for experiments with $X_{CO2} = 0.10$ and 0.38 was calculated based on the mass of starting materials, accounting for the mass of H_2O and CO_2 that enter the melt. As discussed above, the Cl/H_2O ratio of the bulk MVP is fixed (~ 0.06) across all experiments, and at a temperature of 800 ^{o}C always lies in the two-phase vapor + brine field. However, in going from $X_{CO2} = 0.10$ to $X_{CO2} = 0.38$, the

121

bulk volatile phase composition moves along a line which intersects the pure CO_2 corner of the $NaCl$-H_2O-CO_2 ternary. Thus, as the solvus expands with increasing CO_2 (Duan et al., 1995), and the bulk composition moves towards the H_2O-CO_2 limb, the vapor + brine mixture continually moves towards increasingly vapor dominant phase proportions at a fixed Cl/H_2O ratio. At the same time, the $NaCl$-H_2O-CO_2 solvus is characterized by an increase in the brine salinity (vapor-saturated) and decrease in the vapor salinity (brine-saturated).

The reduction in the fH_2O due to the addition of CO_2 to the MVPs results in a lower fO_2 for experiments at high X_{CO2}. In addition, several equilibria that are dependent upon fH_2O will also be affected. The most important is the equilibrium between magnetite and pyrrhotite at magmatic temperatures, which controls the fH_2S in the MVPs according to Equation (16) below,

$$3FeS^{Po} + 4H_2O = Fe_3O_4 + 3H_2S + H_2 \qquad \textbf{(16)}$$

and changes in the fH_2S are defined by the equilibrium constant for this expression, defined by (17) below:

$$K = \frac{(fH_2S)^3(fH_2)}{(aFeS)_{Po}^3(fH_2O)^4} \qquad \textbf{(17)}$$

As the X_{CO2} was increased from 0.10 to 0.38 the fH_2O in the experiments decreased from ~76 MPa to 54 MPa and there was a concomitant 27% decrease in fH_2S (0.2 log units lower) compared to the low-CO_2 equilibrium value.

Whitney et al. (1984) quantified the various equilibria between magnetite, hematite, fayalite, pyrrhotite, and pyrite as a function of fO_2 and fS_2. As discussed, the René 41 alloy vessels used in the pyrrhotite-saturated experiments buffer fO_2 to near

NNO (800 $^{\circ}$C = log fO$_2$ ~ -14). Pyrrhotite-magnetite equilibrium at these conditions corresponds to a log fS$_2$ = -3 (Whitney, 1984). Given that the experiments remain saturated with pyrrhotite and magnetite, the fH$_2$S and fSO$_2$ will be fixed at run conditions. Whitney et al. (1984), Ohmoto and Kerrick (1977), and Zajacz et al. (2011) predict fH$_2$S/fSO$_2$ ratios in the range of ~10^2 to >10^3 at these conditions, stressing the dominance of reduced sulfur in the MVPs. Recent modeling of sulfur speciation at magmatic conditions maintains that H$_2$S is dominant, but also discusses the importance of other ligands in metal complexation such as Cu-HS-Cl complexes (See Section 3.5.3), and possibly more obscure species such as trigonal S$_3^-$ (Pokrovski and Dubrovinsky, 2011; Zajacz et al., 2011). Interaction between CO$_2$ and these sulfur ligands, stabilizing ions, and the associated copper complexes, is hypothesized to affect the copper partitioning behavior in the experiments described in this chapter.

3.2.4   Run Products

The compositions of the silicate melt, pyrrhotite, and magmatic vapor and brine must be inferred from run products which preserve the magmatic phase compositions down to ambient conditions. Pyrrhotite is the simplest to evaluate, as numerous studies have shown that the composition of pyrrhotite can be preserved upon quench (Jugo et al., 1999; Lynton et al., 1993; Mengason et al., 2010; Mengason et al., 2008) given that the sulfide composition is stable down to ambient temperature. Thus, provided that no signs of quench exsolution textures are observed, analysis of the run product pyrrhotite can be taken as the composition of the pyrrhotite phase at magmatic conditions. Pyrrhotite-saturated experiments used the same rapid quench method as the CO$_2$-free experiments discussed in Chapter 2. The capsule temperature decreases from 800 $^{\circ}$C down to the glass

transition temperature ~500 $^{\circ}$C in ~ 1 minute. The run product glasses produced are also low in sulfide inclusions due to the physical separation of pyrrhotite from silicate melt via an inner capsule (Figure 12).

The use of in-situ quartz fracturing helps promotes sampling equilibrated fluids and prevents erroneous conclusions based on transient disequilibrium features of the MVPs early in an experimental run. Fluid inclusion assemblages chosen were associated within large regions of similar inclusions to minimize analysis of inclusions formed from a mixture of vapor + brine. Only inclusions > 10 μm and < 60 μm are selected for analysis to ensure a strong sample signal and to minimize the chances of decrepitation or incomplete inclusion capture. The salinity of quartz-hosted fluid inclusions is first characterized to confirm a low degree of two-phase mixing, and to use as an internal standard for complete MVP characterization (see Section 3.3 for details). The LA-ICPMS analyses of the fluid inclusions were then averaged to yield the composition of the magmatic vapor and brine for a given experiment.

3.2.5   Demonstration of Equilibrium

The run product glass that forms from the Bishop Tuff or synthetic haplogranite melt drops from the 800 $^{\circ}$C run temperature to its glass transition temperature of ~500 $^{\circ}$C in ~1 minute during quench. There is little evidence of any change to copper diffusion in silicate melts with the addition of sulfur. Thus, the characteristic diffusion distance for copper should remain small (~ 5 μm) over the quench time. However, to confirm this hypothesis, analyses of glass composition have been made close to the edges of large glass beads and small glass beads, and compared to other analyses within the glass

124

volume. The variable sampling allows for identification of any significant heterogeneity in the copper concentration within the run-product glass.

In addition, glass-hosted brine inclusions have been measured for a subset of the pyrrhotite saturated experiments (Cu404, Cu411, Cu601, Cu607) in order to compare their composition to the quartz-hosted brine inclusions used to characterize MVP compositions. Glass-hosted brine inclusions are trapped upon quench and therefore, sample the final composition of the brine. Despite the lower precision of glass-hosted inclusions, due to the host signal, consistency with the quartz-hosted inclusions demonstrates that the more precise quartz-hosted analyses represent final equilibrium compositions. Glass-hosted inclusion analyses also allow for measuring the composition of the run product glass very close to Cu-rich brine inclusions. These glass compositions are used in order to make a host correction. The glass analyses near inclusions were then compared to analyses from inclusion-poor regions, to check for any diffusive re-equilibration between fluid inclusions and the melt during quench. A significant difference in copper concentration across a single glass bleb would indicate copper disequilibrium still existed during quench. Homogeneity of analyses across all three of these measures provides evidence that quartz-hosted fluid inclusions and glass analyses represent the final, equilibrium composition of their respective magmatic phases.

3.3 Analytical Methods

3.3.1 Fluid Inclusion Microthermometry

Fluid inclusion microthermometry, using a USGS microthermometry stage, was used to determine the bulk salinity of sulfur-bearing fluid inclusions by observations of phase changes that occur during the heating and/or freezing of inclusions. The quartz core

containing vapor and brine inclusions was mounted in Crystalbond^{Tm} and cut into 200-1000 μm thick slices and doubly polished, exposing the inclusion trails of interest sub-parallel to the polished surface at depths between 10-40 μm. Petrographic observation of fluid inclusions was initially used to discriminate brine-dominant or vapor-dominant zones of an inclusion assemblage. Inclusions identified as mixed inclusions are avoided for analysis. Microthermometric measurements were also used to identify some mixed inclusions missed by visual observations. Inclusions that deviate from the 2σ standard deviation of the remaining vapor or brine inclusions from a single experiment are also labeled as mixed inclusions and not analyzed by LA-ICPMS.

3.3.2   Brine Inclusions

The brine inclusions from sulfur-bearing experiments were identified at room temperature by the presence of three or more crystalline phases (NaCl, KCl, Cu/Fe-S), a vapor bubble, and aqueous solution filling the remainder of the inclusion (Figure 14A). The dominant crystalline phases were still halite (NaCl) and sylvite (KCl) crystals that precipitated from the brine upon quench due to high magmatic brine salinity.
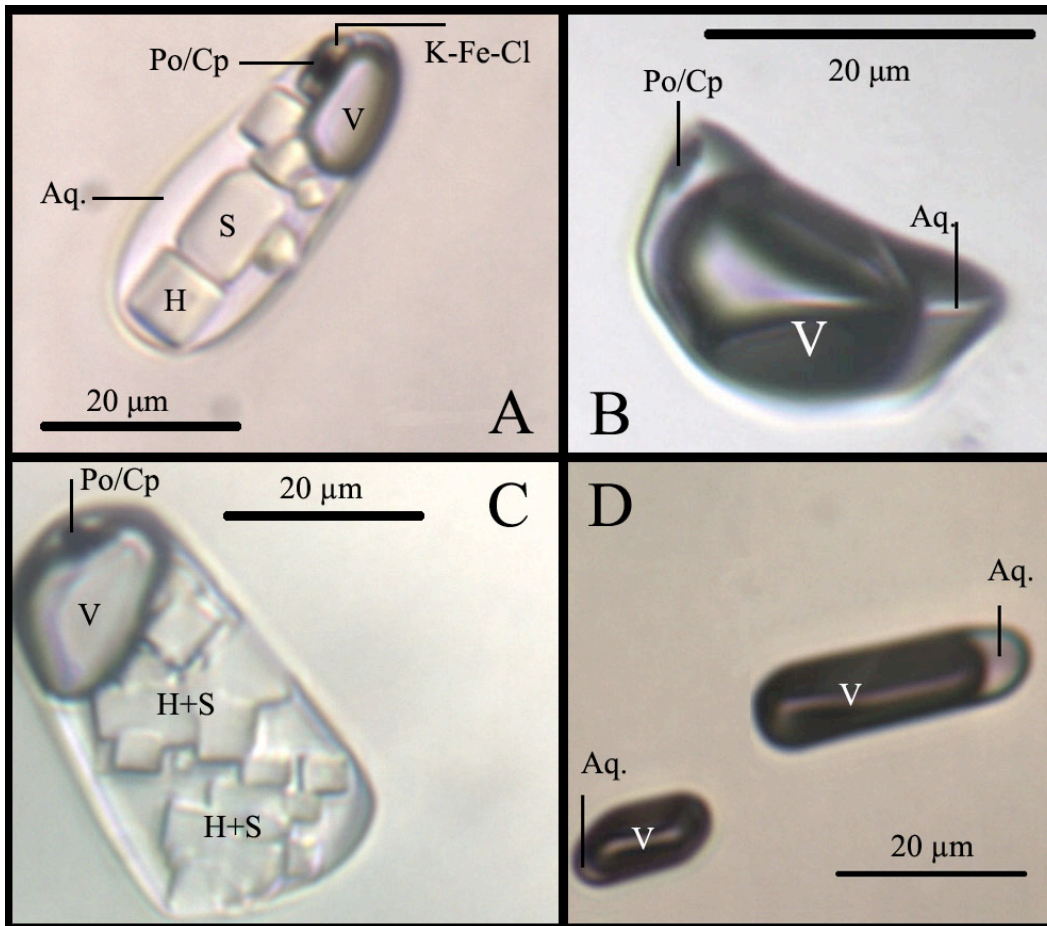
Figure 14: Photomicrographs of fluid inclusions from CO$_2$-bearing, pyrrhotite-saturated melt-vapor-brine experiments. [A] Brine inclusion (MVP X$_{CO2}$=0.1) with halite (H), sylvite (S), pyrrhotite/chalcopyrite (Po/Cp), and orange/red (K-Fe-Cl) daughter minerals similar in appearance to daughter minerals in natural deposits. An aqueous solution (Aq.) with a vapor bubble (V) is also present. [B] Vapor inclusion (MVP X$_{CO2}$=0.1) with a CO$_2$-rich vapor bubble (V-white) and an aqueous solution (Aq.) and a sulfide daughter crystal (Po/Cp). [C] Brine inclusion from experiments with MVP X$_{CO2}$=0.38 showing an increase in proportion of daughter minerals (H+S) due to higher salinity and [D] vapor inclusions from the same experiment with a larger vapor bubble (V) and no observable daughter minerals.

Brine inclusions from high-CO$_2$ experiments (X$_{CO2}$ = 0.38) produce both halite and

sylvite, albeit with a higher relative proportion of crystals to aqueous liquid due to the

higher salinity (Figure 14C). The brine inclusions from pyrrhotite-saturated experiments

also ubiquitously contained small opaque phases that are likely a mixture of pyrrhotite

and chalcopyrite. In addition, many of the brine inclusions are large enough to observe

small red-orange crystals, which are similar in appearance to hydrated iron ± potassium

chlorides observed in natural fluid inclusions, usually associated spatially with the sulfides within the inclusion volume (Kodera et al., 2003). Measurements of halite and sylvite dissolution temperatures in sulfur-bearing brine inclusions were conducted using the same technique as that described in in Section 2.3.2 for sulfur-free brines.

3.3.3   Vapor Inclusions

Vapor inclusion microthermometry in pyrrhotite-saturated CO_2-bearing experiments required several additional calculation and modeling steps. Vapor inclusions from CO_2-bearing experiments were first identified at room temperature by a large vapor bubble (>80% of the inclusion volume) and condensed aqueous liquid. Occasionally the vapor inclusions were large enough to identify an opaque daughter crystal(s) inferred to be a mixture of pyrrhotite and chalcopyrite (Figure 14B). Vapor inclusions from high-CO_2 experiments ($X_{CO2} = 0.38$) have an increased bubble volume and are often smaller in size if not necked. The inclusions used are similar in size to the brine inclusions and inclusions smaller than 10 μm are avoided, as the signal is often too weak for complete signal capture and quantification. Freezing of inclusions to -100 ^{o}C results in the formation of the three phases observed in sulfur-free vapor inclusions; clathrate, ice, and a solid CO_2-rich phase formed by the vapor bubble. The clathrate is a solid phase composed of a mixture of CO_2, H_2S and H_2O that excludes chloride salts. Upon heating the vapor inclusions, the CO_2-rich phase melts at ~ -56 ^{o}C and forms a CO_2-H_2S vapor (low magmatic X_{CO2}) or CO_2-H_2S liquid + vapor mixture (high magmatic X_{CO2}). Second, the ice will melt and disappear to form aqueous liquid at temperatures ranging from -6 to -1 ^{o}C. Finally, the clathrate melts at ~ +6 to 11 ^{o}C depending upon the density of the CO_2/H_2S mixture and the salinity of the quenched aqueous liquid. Measured clathrate

melting temperatures of mixed CO_2-H_2S clathrates were obtained using the same cyclical freezing technique described in Section 2.3.3 for sulfur-free clathrates.

However, unlike sulfur-free, CO_2-bearing fluid inclusions described in Chapter 2, the clathrate formed in vapor inclusions from pyrrhotite-saturated experiments forms from a mixture of CO_2 and H_2S. The stability of the mixed gas clathrate is dependent upon the stability of the two end-member clathrates and the partial pressure of CO_2 and H_2S at the conditions of clathrate formation (Avlonitis, 2005; Diamond, 1994; Diamond, 2003; Herri et al., 2011). Furthermore, the presence CO_2 and H_2S as components of the magmatic vapor will affect the density and phase stability of the vapor. The liquid-vapor phase equilibria and the stability of the mixed gas clathrate must both be considered before the T_m^{Clath} can be used to characterize vapor inclusion salinity. Yet, given an appropriate model of the clathrate stability, the salinity of CO_2-bearing vapor inclusions can still be determined using only the T_m^{Clath} and an accurate direct measurement of CO_2 density, via a similar Raman spectroscopy method to that used for sulfur-free CO_2-bearing vapor inclusions.

The process of calculating vapor inclusion compositions involves several more steps than for brine inclusions. The adjustments required to compensate for the effects of H_2S further complicate this process. In order to guide the reader, a flow chart for vapor and brine fluid inclusion analysis methods is presented below (Figure 15), including the section headings for each relevant step.
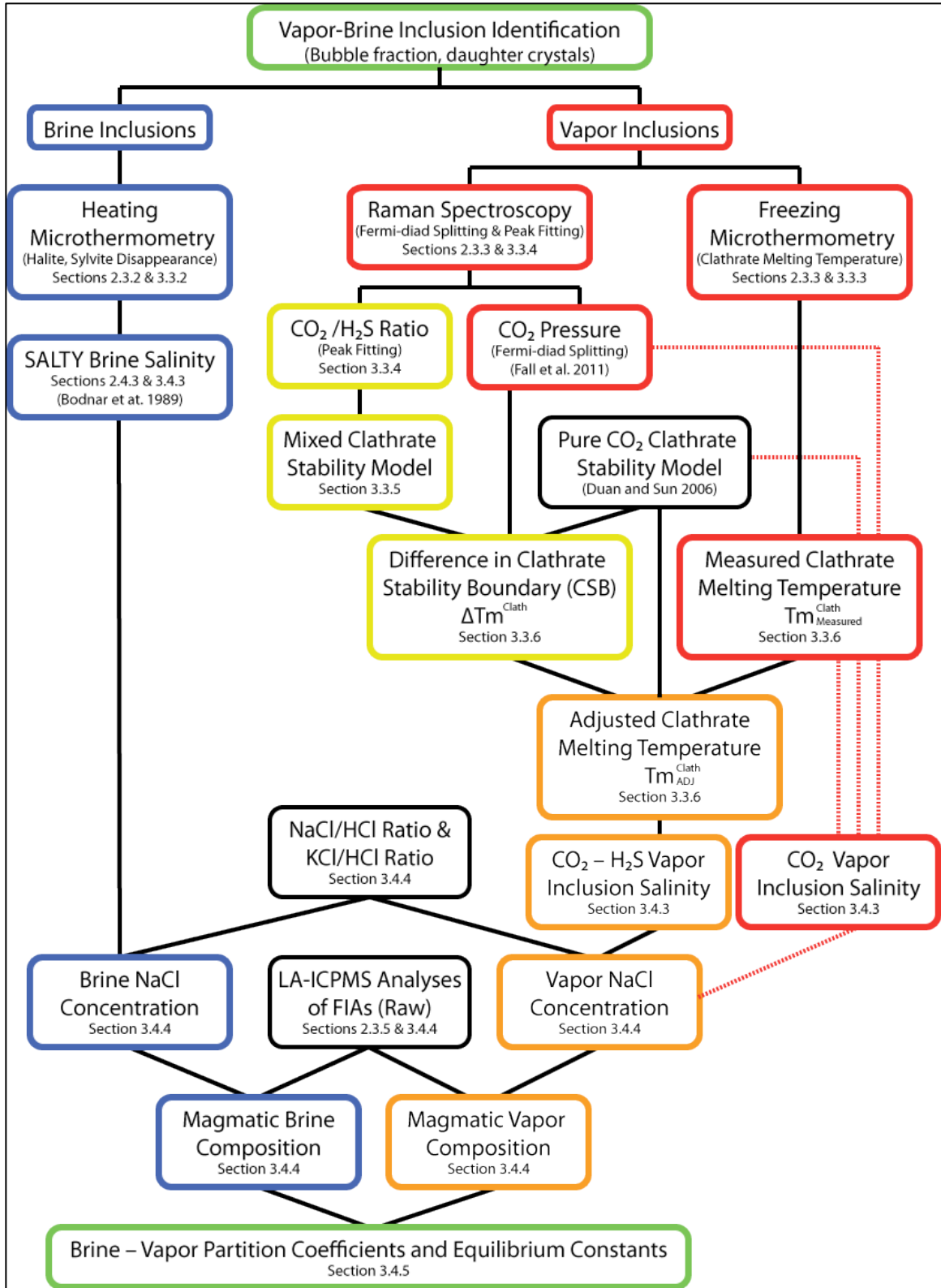
Figure 15: Flow chart (top to bottom) for characterization of fluid inclusion compositions. Blue boxes are brine characterization steps. Red boxes and dashed lines are the original, sulfur-free vapor characterization steps. Yellow are the additional steps to adjust for H₂S. Black boxes are steps based on models presented by other authors.

3.3.4   *Raman CO_2 Pressure Determination and CO_2/H_2S ratio*

The work by Fall et al. (2011), in which I participated, allows for direct measurement of CO_2 density via the Raman Fermi-diad peak splitting for CO_2. There is no indication that the peak splitting will be affected by the presence of an additional gas species, as it is a function of the vibrational modes of the CO_2 molecule and the density of the bulk gas (See Appendix V). Raman analyses of CO_2-H_2S vapor bubbles were conducted at Virginia Tech using a JY Horiba LabRam HR (800 mm) spectrometer and a 514.53 nm Laser Physics 100S-514 Ar^+ Laser with the assistance of technician Charles Farley. Raman spectra of vapor inclusions from pyrrhotite-saturated experiments include two strong CO_2 peaks at ~1286 cm^{-1} and ~1389 cm^{-1} and a weak H_2S peak at ~2611 cm^{-1} (Fall et al., 2011; Pasteris et al., 1986). No evidence for CO or CH_4 gas was detected via Raman spectroscopy, similar to observations for sulfur-free CO_2-bearing vapor inclusions. Application of the model presented by Fall et al. (2011) to the peak splitting measured in vapor-rich inclusions from the pyrrhotite-saturated CO_2-bearing experiments of this study, results in pressure determinations that match the observed phase assemblage for low-CO_2 (CO_2 +H_2S vapor only at $X_{CO2} = 0.1$) and high-CO_2 (CO_2 +H_2S vapor + liquid at $X_{CO2} = 0.38$) compositions. However, the CO_2 density of vapor inclusions is slightly higher at low-CO_2 and slightly lower at high-CO_2 for pyrrhotite-saturated experiments relative to sulfur-free experiments with the same MVP bulk composition (see Section 3.3.2 for details).

In addition to Raman characterization of CO_2 density, the Raman H_2S peak was characterized for a subset of vapor inclusions to estimate CO_2/H_2S ratios. The peak areas for both CO_2 and H_2S were calculated numerically from the Raman intensities after a

simple background subtraction. The relative signal strength of CO_2 and H_2S was then

estimated by correcting these peak areas using the Raman scattering efficiencies of one of

the CO_2 vibrational modes ($2V_2 = 1.5$) and the H_2S mode ($V_1=6.4$) relative to N_2

(Appendix V). The ratio of CO_2/H_2S at room temperature is then calculated from the

corrected signal strengths for each vapor inclusion. The experiments with a magmatic

$X_{CO2} = 0.1$ produced vapor inclusions with ~ 5 to 6 mol% H_2S at room temperature

(CO_2/H_2S ~19), whereas experiments with a magmatic $X_{CO2} = 0.38$ produced vapor

inclusions with ~ 2 mol% H_2S at room temperature. Model predictions of the fCO_2 and

fH_2S for pyrrhotite-saturated experiments predict CO_2/H_2S ratios approximately one fifth

of those observed in vapor-rich inclusions (see Section 2.3). However, the formation of

smaller daughter sulfides from the magmatic vapor (pyrrhotite + chalcopyrite) removes

the majority of the H_2S from the vapor inclusions upon quench.

The density of the inclusion is then converted to a pressure at T_m^{Clath} using a

density model for $CO_2 + H_2S$ mixtures presented by Stouffer et al. (2001) and following

the appropriate isochore for the desired CO_2/H_2S ratio from room temperature down to

T_m^{Clath}. This fluid inclusion pressure (P_{FI}) is then critical in correlating the T_m^{Clath} with the

inclusion salinity. However, for the pyrrhotite-saturated experiments the clathrate

stability boundary must be corrected for the presence of H_2S.

3.3.5   *Mixed CO$_2$-H$_2$S Volatile Phases and Mixed Clathrate Stability Model*

Modeling the formation of mixed $CO_2 + H_2S$ clathrates relies upon understanding

the liquid-vapor equilibria as well as the clathrate stability of the two end-member

clathrate compositions. The mixing of CO_2 and H_2S forms a complete solution in both the

vapor-only and liquid-only phase stability fields. However, early experimental results

indicate that the vapor-liquid equilibrium deviates significantly from ideal mixing for a wide range of compositions in the pressure-temperature region of interest for vapor-rich inclusion clathrate formation (Bierlein and Kay, 1953; Sobocinski and Kurata, 1959). Yet, experimental data and theoretical models predict pseudo-azeotropic behavior of CO_2-H_2S mixtures for CO_2-rich ($CO_2/H_2S > 9$) vapor compositions (Li et al., 2011). This is due to a minimum in the binary vaporus curve and upper liquidus curve at $CO_2/H_2S \sim 9$ and very small gap between the curves for more CO_2-rich compositions. Thus, the vapor-liquid equilibrium for vapor inclusions with $CO_2/H_2S > 9$ can be treated as azeotropic.

This point is vital in predicting clathrate stability upon cooling of fluid inclusions because, as Diamond (2003) notes, many clathrate forming volatile phase mixtures enter a liquid-liquid immiscibility field in the region close to the boiling curve but before clathrate formation. For these mixtures, and for more H_2S-rich CO_2 + H_2S mixtures, clathrate will form from multiple phases. The resulting heterogeneous clathrate melting behavior would prevent accurate determination of clathrate stability boundary and inclusion salinity from T_m^{Clath} and P_{FI}. However, azeotropic behavior is observed for the vapor-liquid equilibrium for the CO_2-H_2S mixtures present in the vapor inclusions from this study. Thus, a well-defined clathrate melting temperature should be expected if no liquid immiscibility is predicted for H_2S-poor mixtures ($CO_2/H_2S > 9$). Although the vapor-liquid equilibrium for the vapor inclusions can be treated as azeotropic, and accurate clathrate melting temperatures obtained, the challenge of predicting the pressure and salinity dependent clathrate stability boundary of the mixed clathrate still remains.

Numerous studies exist to predict the stability of clathrates formed from mixtures of CO_2 and species other than H_2S, such as CH_4, N_2, etc., (Diamond, 1994; Diamond,

2003; Herri et al., 2011; Sloan and Koh, 2008). The formation of clathrate often deviates from ideal mixing of the two end-members for binary systems. However, the behavior of clathrate forming volatile phase mixtures with compositions close to an end-member component are much closer to ideal, even for gas mixtures whose end members form structurally distinct clathrates (Diamond, 1994; Sloan and Koh, 2008). Herri et al. (2011) discuss that although N_2 and CH_4 form structure II clathrates and CO_2 forms structure I clathrates, CO_2-rich mixtures with either gas yield clathrate stabilities very close to ideal mixing of the two end-member clathrates. However, as noted by Sloan and Koh (2008), little data exists on CO_2-H_2S binary clathrates. As a result, I present a model for CO_2-H_2S clathrate formation based upon ideal mixing of the pure CO_2 and H_2S clathrates.

Both CO_2 and H_2S form structure I clathrates and both have similar phase relationships including Q_1 and Q_2 invariant points along the clathrate stability boundary (Diamond, 2003; Herri et al., 2011; Sloan and Koh, 2008). The Q_1, or lower invariant point, in the pure CO_2-H_2O system is the point at which V_{CO2}, L_{H2O}, ice, and clathrate coexist. The Q_2, or upper invariant point, in the pure CO_2-H_2O system is the point at which V_{CO2}, L_{CO2}, L_{H2O}, and c=lathrate coexist (Figure 16). Both Q_1 and Q_2 invariant points also exist for the pure H_2S system with liquid and vapor H_2S replacing CO_2 in the phase equilibria (Figure 16). In addition, mixtures of CO_2+H_2S will have a continuous loci of Q_1 and Q_2 points defining a line between the pure CO_2 and H_2S clathrate stability boundaries (Diamond, 1994; Sloan and Koh, 2008). By defining these invariant points, any mixture with a CO_2/H_2S ratio > 9 will have a clathrate stability boundary defined by ideal mixing of the CO_2 and H_2S end-member clathrates, with invariant points lying along the previously described lines defined by the loci of Q_1 and Q_2 points (Figure 16).

The P_{FI} can then be used to follow the isochore for the given CO_2+H_2S mixture (Stouffer et al., 2001) until intersecting this model clathrate stability boundary at the T_m^{Clath} in the same manner as for pure CO_2 clathrates.
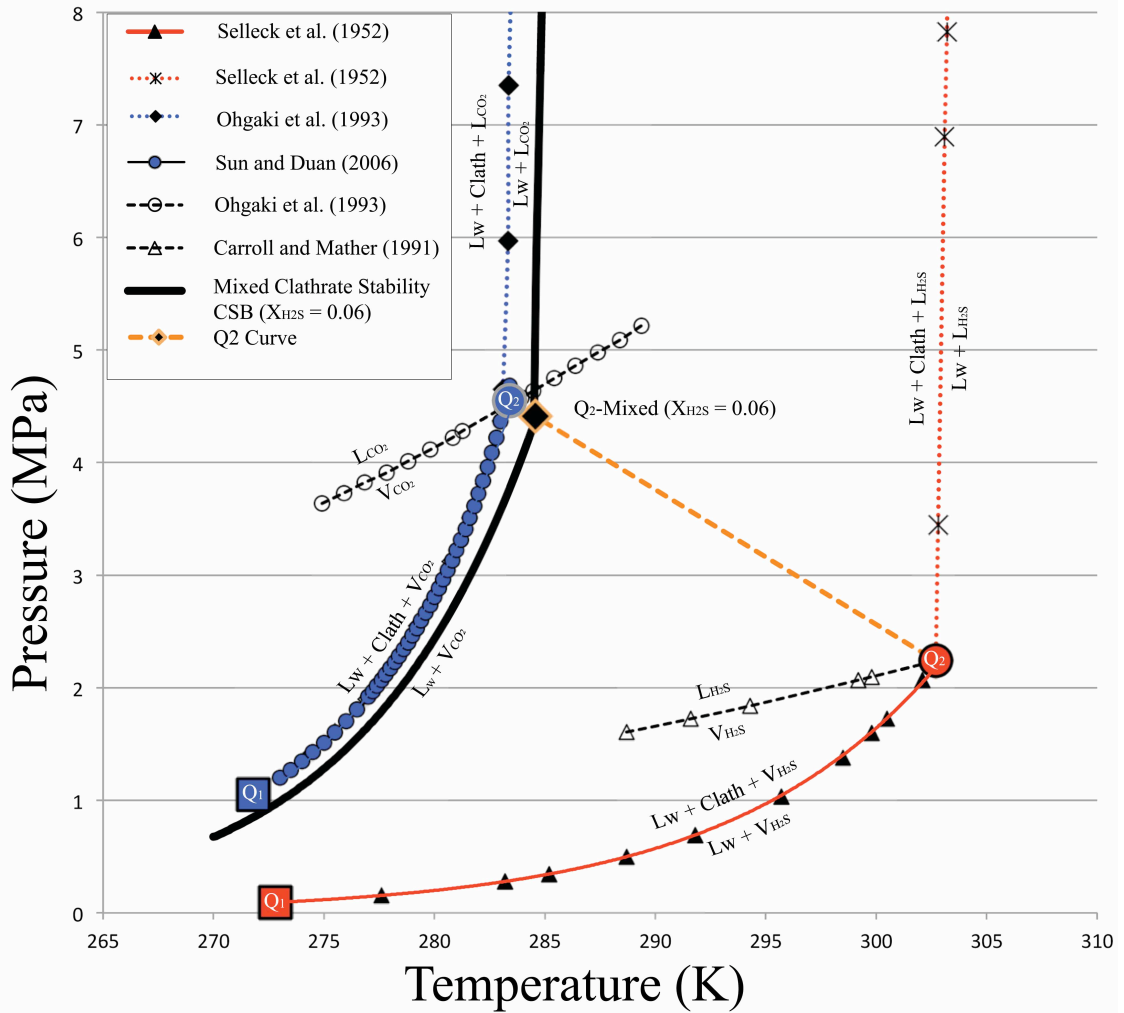
Figure 16: Clathrate Stability Boundary (CSB) diagram for CO_2 (blue), H_2S (red) and mixed CO_2/H_2S clathrates (black). Clathrate (Clath) forms from liquid water (Lw), and CO_2 vapor (V_{CO2}), CO_2 liquid (L_{CO2}), H_2S vapor (V_{H2S}), or H_2S liquid (L_{H2S}). Boiling curves for both pure phases are shown with open circles and triangles. Q_2 invariant points for pure CO_2 and pure H_2S are defined by coexistence of Lw, Clath, $V_{CO2/H2S}$, and $L_{CO2/H2S}$ at the intersection of the CSB and boiling curve for the pure phases. The loci of Q2 points for any mixture of $CO_2 + H_2S$ defines the Q2-curve which must fall along the CSB model for ideal mixing between the pure end-member clathrates ($CO_2/H_2S = 9$ shown).

3.3.6   Adjusted Clathrate Melting Temperatures and Salinity

The intersection between the P_{FI} and the model clathrate stability boundary yields the clathrate melting temperature for the salt-free clathrate formed from any defined mixture of CO_2+ H_2S (Tm^{Clath}_{Mixed}). The Tm^{Clath}_{Mixed} is then compared to the clathrate melting temperature for the pure CO_2 clathrate stability boundary at the same pressure (Tm^{Clath}_{CO2}), defined by the model presented by Sun and Duan (2006). The difference between the two clathrate melting temperatures was then used as a correction factor to the measured clathrate melting temperatures ($Tm^{Clath}_{Measured}$) yielding adjusted clathrate melting temperatures ($Tm^{Clath}_{Adjusted}$) according to the equations:

$$\Delta Tm^{Clath} \equiv Tm^{Clath}_{Mixed} - Tm^{Clath}_{CO2}$$

(18)

$$Tm^{Clath}_{Adjusted} \equiv Tm^{Clath}_{Measured} - \Delta Tm^{Clath}$$

(19)

The clathrate stability field of pure CO_2 clathrates is depressed to lower temperatures by the addition of increasing concentrations of chlorides and the magnitude of change is well constrained as a function of salinity (Diamond, 2003; Duan and Sun, 2006; Fall et al., 2011; Tohidi et al., 1997). Limited experimental data on the effect of chlorides on pure H_2S clathrates suggests that the magnitude of the change on the clathrate stability boundary is similar to that of pure CO_2 clathrates (Bond and Russell 1949). Accordingly, the mixed CO_2-H_2S model assumes that the clathrate stability boundary of mixed CO_2-H_2S clathrates will shift to lower temperatures in the same manner. The salinity of vapor inclusions is then calculated by finding the intersection of the clathrate melting temperature, adjusted for the presence of H_2S ($Tm^{Clath}_{Adjusted}$), and the pressure of the fluid inclusion P_{FI}, which must fall along the salinity dependent clathrate

stability boundary. The model of Duan and Sun (2006) for clathrate salinity dependence is then used to calculate the salinity required for the CO_2 clathrate stability boundary to pass through the intersection of P_{FI} and T_m^{clath} for a particular fluid inclusion.

3.3.7 EPMA Analysis of Run Product Glasses and Sulfides

The major element chemistry of run product pyrrhotite and silicate glasses was determined by using a JEOL 8900 Superprobe Elecron Probe Microanalyzer (EPMA). The solid run products were first mounted in epoxy and polished and mapped for inclusions using transmitted and reflected light microscopy. Run product sulfides were then characterized via energy dispersive spectroscopy (EDS) to identify individual phases and check for any exsolution textures or inclusion heterogeneities. Regions of silicate glasses observed (transmitted light microscopy) to have minimal fluid inclusions near the surface were chosen for EPMA spots to minimize contamination by incorporation of fluid inclusions in the analytical volume. A qualitative assessment was also made of the degree of heterogeneity and crystallization present in the glass by assessing the average composition of the glass across the sample surface using backscatter electron imaging (BSE). Quantitative analyses of pyrrhotite and glass phase compositions were obtained using standardizations based upon analysis of similar, well-characterized minerals.

Quantitative wavelength dispersive spectroscopy (WDS) was used to characterize the major element composition (Na_2O, K_2O, CaO, FeO, Al_2O_3, SiO_2) and trace element composition (Cl, SO_3) of each run product glass sample. External standards for glass analyses included Yellowstone rhyolite (Na_2O, K_2O, Al_2O_3, SiO_2), hornblende (FeO, CaO), and scapolite (Cl, SO_3). An accelerating voltage of 15 kV and beam diameters between 10 to 30 μm were used for all glass analyses, and a beam current of ~ 5 nA was

used for major element analysis. A low beam current was used to minimize the diffusion of Na away from the analytical volume. Given the low concentration of sulfur and chlorine in the run product glasses, all glasses from pyrrhotite-saturated experiments were subsequently analyzed a second time at a much higher beam current of ~50 nA, and with longer counting times for chlorine and sulfur. Between 10 and 20 glass analyses were collected for each experiment, discarding some analyses for low totals (< 90%) and element ratios consistent with erroneous analysis of feldspar or quartz. Totals for major element glass analyses should fall slightly below 100%, owing to 2 to 4 wt% water concentrations in the glass based on solubility data for H_2O and CO_2 (Botcharnikov et al., 2005; Lowenstern, 2001). Chlorine and sulfur concentrations for pyrrhotite-saturated experiments quantified using separate analyses at a higher beam current were externally standardized separately and internally standardized based on aluminum and potassium from major element EPMA analyses.

Quantitative WDS was also used to determine the Fe, Cu and S concentration of run product pyrrhotite. A pyrrhotite standard was used to quantify the composition of iron and sulfur in run product pyrrhotite, whereas a chalcopyrite standard was used to characterize the copper concentration in the run product pyrrhotite. Sulfide analyses were conducted using an accelerating voltage of 20 kV, beam diameters between 1 to 3 μm, and a beam current of ~ 50 nA. The higher beam current and smaller spot sizes can be used because of the high thermal conductivity of sulfides. This is crucial as run product sulfide grains can often be small and difficult to polish, and pyrrhotite grains were often observed to have copper-rich sulfide rims, which must be avoided to ensure accurate quantitative pyrrhotite analyses.

3.3.8   LA-ICPMS Analysis of Fluid Inclusions

Quantification of the composition of pyrrhotite-saturated CO_2-bearing fluid inclusions was achieved by LA-ICPMS analysis using the same technique described for the sulfur-free experiments. LA-ICPMS analyses were conducted at the Virginia Tech Fluids Research Group facility using an Agilent 7500ce ICPMS and a GeoLas 193nm eximer laser with the assistance of technician Luca Fedele. As with sulfur-free inclusions, LA-ICPMS analysis requires that all inclusions are ~10-40 µm below the surface of the quartz, which maximizes the signal intensity and minimizes explosive fracturing of the quartz due to laser heating of the inclusions. The quadrupole mass spectrometer allows for limits of detection (LOD) in the ppm range for most "trace" elements along with major elements (Heinrich et al., 2003; Mutchler et al., 2008). However, sulfur concentrations could not be quantified in fluid inclusions due to a high instrument background for sulfur.

Complete signal capture is vital to accurate characterization of volatile phase compositions and requires that all the phases present in an inclusion are completely sampled and are included in the sample signal integration. This is especially important for sulfur-bearing brine inclusions, which contain precipitates (halite, sylvite, pyrrhotite, chalcopyrite, etc.), to ensure accurate element ratios and bulk chemistry. Monitoring of the LA-ICPMS signal during ablation showed that the copper signal in brine inclusions is separate from the sodium and potassium signals. This is likely because copper is dominantly hosted in the daughter sulfide(s), which ablate over a slightly different, overlapping interval from the halite and sylvite. Additionally, the use of He carrier gas maximizes the fraction of material reaching the plasma by maximizing aerosol formation

in the low-density gas. This minimizes deposition outside the ablation crater, which can also distort element abundances. The process of analyzing each inclusion then proceeds following the same routine as the analytical method described in Section 2.3.5.

3.3.9   *LA-ICPMS Analysis of Run Product Glasses and Glass-Hosted Brines*

Run product glass analyses were also conducted using the LA-ICPMS facility at Virginia Tech. Analyses of glass required the selection of regions that had a low inclusion density. A 24-90 μm diameter laser spot was used for all glass analysis along with lower laser power (~7 J/cm^2) owing to the better laser coupling characteristics of the glass compared to quartz. Spots are chosen using transmitted light microscopy to minimize the number of fluid inclusions included in the analytical volume. Spots are also chosen at or near the same locations as those chosen for EPMA analysis. Raw data were produced using a routine of summing all signals to a 100% oxide composition using AMS software. This signal is then corrected for an estimate of glass water concentration and then using Na from EPMA analyses as correction factor of absolute elemental abundances.

Glass-hosted brine fluid inclusion analyses were conducted by selecting large fluid inclusions at depths of 20 to 60 μm below the surface, with proportions of daughter chloride minerals similar to that observed in quartz-hosted brine inclusions. A background glass analysis was collected while ablating down to the fluid inclusions, and again after complete inclusion ablation. Glass-hosted brine signals are reduced using the same method described for quartz-hosted brines with the addition of a correction factor for the contribution of the host glass signal. The composition of the glass surrounding the glass-hosted brine inclusions is first characterized by reducing the portion of the sample

signal obtained prior to ablation of the brine inclusions, using the same methods described for other glass analyses. This composition and signal are then used to subtract the contribution of the glass from the signal derived from ablation of the fluid inclusion for each element. The final signal is then reduced using the same methods described for quartz-hosted brine inclusions. The glass analyses collected before and after the inclusion signal as well as glass analyses collected away from inclusions were used for host corrections, for a sub-set of glass-hosted brine analyses. No deviation in glass composition is observed within analytical uncertainty when comparing either host correction method. The data reduction including host correction is also completed using AMS software (Mutchler et al., 2008).

3.4 Results

3.4.1 Silicate Melt Composition: Major Elements

Run product glasses were characterized by EPMA to estimate high-temperature melt compositions. Major element compositions determined by EMPA analyses, with adjusted Al_2O_3, FeO, and chlorine concentrations as well as ASI, are listed in Table 9.

Melt Composition		Na_2O wt%(2σ)	K_2O wt%(2σ)	CaO wt%(2σ)	FeO wt%(Low)°	Al_2O_3 wt%(High)*	SiO_2 wt%(2σ)	SO_3 ppm(2σ)	Cl ppm(Low)°	Total wt% (2σ)	ASI
Bishop	Cu410	2.8 (0.2)	6.6 (0.3)	0.1 (0.03)	1 (0.6)°	11.6 (11.8)*	72.2 (0.9)	100 (140)	2500 (0.7)°	94.2 (0.7)	1.0
Tuff	Cu411	2.9 (0.3)	6.6 (0.4)	0.1 (0.03)	1.7 (1.3)°	11 (12)*	71.8 (1.4)	70 (110)	3500 (1)°	94 (1)	1.0
Granite	Cu402	2.1 (0.6)	4.8 (1.4)	NA (-)	3.1 (2.8)°	8.4 (9.8)*	73.7 (1.5)	80 (210)	3600 (2.6)°	92.5 (2.6)	1.0
Min-Melt	Cu404	2.1 (0.2)	4.8 (5.1)	NA (-)	5.1 (4.2)°	7.9 (8.8)*	72.4 (0.9)	NA (-)	4200 (1)°	92.7 (1)	1.0
(GR1)	Cu405	2.4 (0.2)	5.3 (5.6)	NA (-)	4.8 (4.7)°	8.5 (9.8)*	72.3 (1)	NA (-)	4700 (0.9)°	93.7 (0.9)	1.0
High CO_2	Cu601	2.6 (0.5)	6.3 (0.6)	NA (-)	0.8 (1.2)°	9.8 (10.5)*	73.4 (3.7)	90 (110)	2100 (1.1)°	93.1 (1.1)	0.9
Po/Mt	Cu606	2.5 (0.3)	5.9 (0.3)	NA (-)	2 (1.1)°	9.2 (9.7)*	74 (1.7)	140 (200)	2900 (1.2)°	93.4 (1.2)	0.9
Sat'd	Cu607	2.6 (0.4)	6.3 (0.3)	NA (-)	3.1 (0.8)°	9 (10.4)*	71.9 (2.1)	200 (200)	3400 (1.3)°	93.1 (1.3)	0.9

Table 9: Glass compositions for pyrrhotite-saturated experiments determined by EPMA. Abundance of Fe-Cl-rich Al-poor fluid inclusions in run product glasses results in systematic errors in FeO (increased), chlorine (increased) and Al_2O_3 (decreased) concentrations with increasing mass of inclusions included in the analytical volume. *Data for Al_2O_3 are shown with the average value followed by the high value (high), which is inferred to represent the closest approximation of the uncontaminated glass concentration (referred to as the corrected Al_2O_3). Similarly, the FeO and Cl data are shown with the average value followed by the lowest value (low). ASI is calculated using the corrected Al_2O_3 concentration.

ASI or aluminum saturation index is calculated using the corrected value for Al$_2$O$_3$ and average values for Na$_2$O, K$_2$O, and CaO. The ASI of starting glass compositions is 0.99 and 1.21 for GR1 and Bishop Tuff starting materials. The change in ASI reported for quenched glasses compared to starting material compositions is due to equilibration between the silicate melt and the initial fluid composition via HCl, NaCl and KCl exchange. The Na-K-H exchange between the silicate melt and MVPs shifts the melt toward peralkaline compositions. Bishop Tuff remains at or above ASI = 1 in equilibrium with the MVP and thus final ASI values for Bishop Tuff experiments remain metaluminous to peraluminous (Table 9). The haplogranite melt become slightly peralkaline in equilibrium with the MVPs. Low-CO$_2$ experiments (X$_{CO2}$ = 0.1) show a low degree of crystallization and, as a result, haplogranite melt compositions remain close to ASI = 1. However, the low fH$_2$O in high-CO$_2$ experiments (X$_{CO2}$ = 0.38) results in significant crystallization. The lower fraction of melt remaining is more affected by cation exchange, and thus the melt from high-CO$_2$ experiments have moderately peralkaline final melt compositions (Table 9).

The ASI of the melts also gives an indication of the relative ratio of HCl to NaCl and KCl in the MVPs. This relationship, discussed by Williams et al. (1997), indicates that an increase in the ASI of the silicate melt is correlated with an increase in the HCl/(Na+K)Cl ratio of the MVPs for ASI > 1, with HCl partitioning strongly in the magmatic vapor. The lower starting ASI of the synthetic haplogranite glass yields a lower final melt ASI and no significant HCl in the MVP's for most sulfur-bearing experiments (Cu402, Cu404, Cu405, Cu601, Cu606, Cu607). The higher ASI of the Bishop Tuff runs (Cu410 and Cu411) indicates significant HCl was present in the high-temperature vapor

of these runs. Although the total salinity should not be affected, some adjustment must be made to the cation ratios when using the sodium concentration as an internal standard for fluid inclusion analyses due to HCl making up a significant portion of the vapor salinity (Simon et al., 2006; Williams et al., 1997). Thus H/(Na+K) ratios for the vapor inclusions calculated using Williams et al. (1997) and melt ASI are used to adjust the sodium concentration used as an internal standard for reducing the LA-ICPMS data (see Section 3.4.3). The melt ASI for the pyrrhotite-saturated Bishop Tuff experiments (~ 1.0) corresponds to a log (Na+K)/H ratio ~ +0.4 in the magmatic vapor (Williams et al., 1997). The concentrations of HCl in the brine are low (< 1 mol% for all run-product melt compositions) but brine salinity is corrected in a similar manner before using brine sodium concentration as an internal standard.

Quench techniques designed to maintain capsule integrity also generate abundant fluid inclusions in many of the glasses. Considerable effort was made to choose analysis spots that avoid fluid inclusions, but heterogeneous incorporation of fluid inclusions in glass analyses still occurs. In order to evaluate the extent of inclusion sampling I compared the concentrations of Al_2O_3, Cl, Na_2O, and K_2O to FeO in the run product glass analyses across all pyrrhotite-saturated experiments (Figure 17). A significant negative correlation between Al_2O_3 and FeO is observed for most glasses. This correlation is likely due to the small concentration of aluminum and high concentration of iron in glass-hosted brine inclusions with iron-sulfide daughter minerals. Thus, variable amounts of Fe-rich, Al-poor inclusions incorporated into the analytical volume would result in the observed negative correlation. The positive correlation between Cl and FeO also supports this interpretation. Fluid inclusions, especially high-salinity brines, have significantly

higher Cl concentrations than the coexisting silicate melt, resulting is elevated Cl

concentrations correlated with increasing FeO as more fluid inclusions are sampled.

Na_2O and K_2O show much weaker correlations with FeO. This is likely due to the

presence of sodium and potassium in fluid inclusions at a similar ratio to iron as that of

the silicate melt. As more fluid inclusions are sampled, FeO will increase and the Na_2O

and K_2O should decrease. However, the minimal aluminum concentration in the fluid

inclusions compared to higher iron, sodium and potassium concentrations would result in

a smaller apparent increase in sodium and potassium in the melt with increasing

inclusions in the analytical volume. The net result is a minimal shift in sodium and

potassium concentrations due to fluid inclusions, consistent with the observation of little

correlation between Na_2O and K_2O with FeO in the glass.
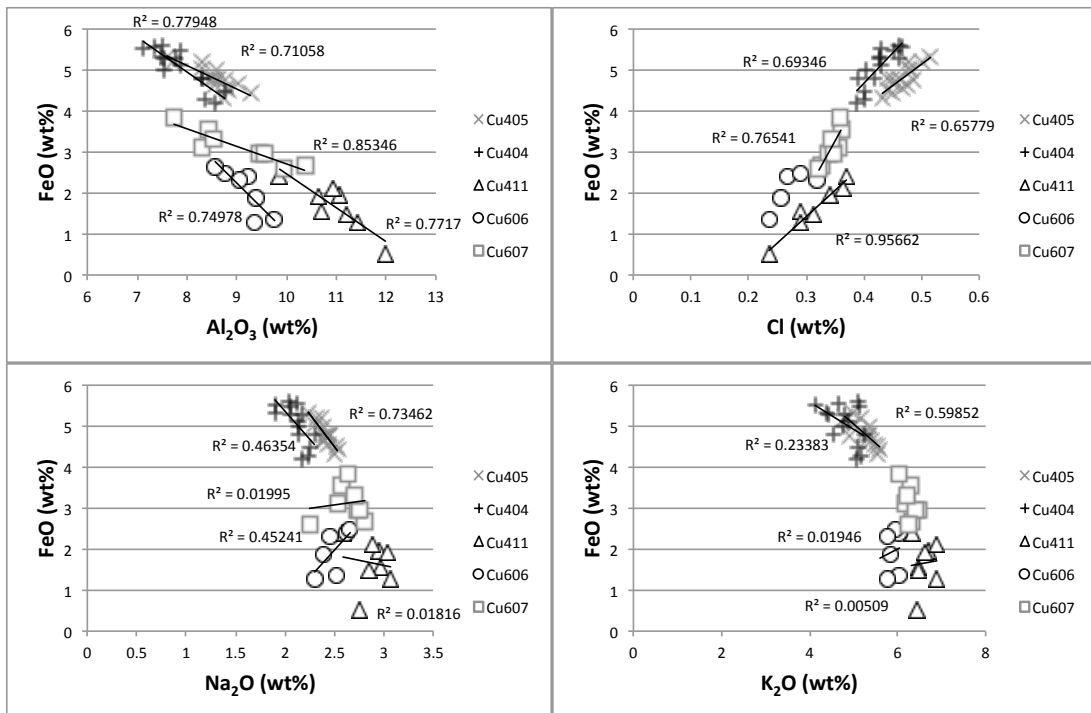
Figure 17: Plots of Al_2O_3, Cl, Na_2O and K_2O vs. FeO in run product glasses by EPMA. Al_2O_3 decreases significantly with increasing FeO due to small amounts Al in fluid inclusions. Conversely, Cl increases with increasing FeO as high-salinity inclusions have much higher Cl concentrations than the glass. Na_2O and K_2O have much weaker correlations with FeO, if any, due to the presence of Na and K in fluid inclusions at similar ratios with Fe as in the silicate melt.

144

The incorporation of fluid inclusions in the analytical volume of run product glass analyses requires correcting the glass analyses to obtain an accurate melt composition. Given that the decrease in Al_2O_3, with increasing FeO and Cl is a function of increasing incorporation of fluid inclusions, the upper limit for Al_2O_3 and lower limit for FeO and Cl have been taken as the best estimate of their respective glass concentrations. The adjusted value for the Al_2O_3 concentration has also been used in the ASI calculation to better represent the influence of the melt on vapor and brine compositions. The melt chlorine concentration (2000-4500 ppm) is at the upper end of the range predicted for shallow arc magmas during second boiling. The bulk chlorine concentration in the experiments is set slightly higher than for natural systems to ensure the formation of sufficient brine to trap fluid inclusions. The total chlorine concentration will not affect copper partitioning between the vapor and brine because both the vapor and brine have fixed salinities at a given X_{CO2} of the bulk volatile phase composition. The concentration of copper in the melt is controlled by a copper oxide component of the melt (Candela and Holland, 1984) and thus, the chlorine concentration in the silicate melt will not affect the partitioning of copper between the MVPs and the silicate melt. Sulfur concentration in the melt is variable, but the values are consistent with other studies involving silicate melts in equilibrium with magmatic sulfide (See section 3.5.1).

3.4.2   Silicate Melt Composition: Copper

LA-ICPMS analyses of run product glasses were used to quantify the copper concentrations of the silicate melts from the pyrrhotite-saturated runs. Copper concentrations in run product glasses range from 10 to 25 ppm. Low-CO_2 experiments (Cu402 through Cu411) produced melts at the lower end of the range (10 to 15 ppm Cu).

Melts from high-CO_2 experiments (Cu601 through Cu607) were more enriched in copper (18 to 25 ppm Cu). In addition, I compare the copper concentration from glass analyses away from large inclusions to glass analyses collected during ablation of large glass-hosted brine inclusions (Table 10).

LA-ICPMS Glass Analyses: Copper

	Run	N	Type	Cu (±2σ)	ASI
Bishop Tuff	Cu410	6	Glass	13 (1)	1.0
	Cu410	7	FI-Glass	16 (5)	
	Cu411	7	Glass	10 (1)	1.0
	Cu411	7	FI-Glass	12 (1)	
Haplo-Granite Min-Melt(GR1)	Cu402	7	Glass	12 (1)	1.0
	Cu402	-	FI-Glass	NA	
	Cu404	9	Glass	10 (2)	1.0
	Cu404	5	FI-Glass	13 (4)	
	Cu405	10	Glass	13 (1)	1.0
	Cu405	6	FI-Glass	14 (1)	
High CO₂ Po/Mt Sat'd	Cu601	6	Glass	22 (3)	0.9
	Cu601	5	FI-Glass	27 (6)	
	Cu606	6	Glass	18 (3)	0.9
	Cu606	4	FI-Glass	22 (4)	
	Cu607	6	Glass	17 (2)	0.9
	Cu607	5	FI-Glass	20 (2)	

Table 10: Copper concentration in run product glasses. Glass spots far from large (>25 µm) fluid inclusions (Glass) have an average copper concentration slightly lower that of glass analyses collected during ablation of glass-hosted fluid inclusions (FI-Glass). Although many experiments show overlap between these two populations, the data is consistent with a slight enrichment of copper in the melt copper near large brine bubbles, which likely form the large fluid inclusions present in run product glasses.

Although there is often significant overlap of both types of glass spots, the data are consistent with a slightly higher copper concentration in the glass near large fluid inclusions. However, the large fluid inclusions in the glass are likely "bubbles" of MVP mixtures present in the silicate melt, not quench phenomena. Thus, it is possible that there is a slight heterogeneity in the synthetic melt with copper enrichment near these large volatile phase bubbles. However, the difference in copper was not sufficient to affect the signal reduction of the associated glass-hosted brine inclusions, which were analyzed to demonstrate equilibrium. Given that the difference in copper concentration is

generally the same as the uncertainty in copper concentration, it is unlikely that this heterogeneity will affect any extrapolation to magmatic melt-volatile phase equilibria.

3.4.2   *Pyrrhotite Composition and fS$_2$*

Crystals of run product pyrrhotite were collected from all sulfur-bearing experiments. Most crystals were anhedral, showing signs of dissolution during the run. Sustained high copper concentrations, due to use of Cu_6Au_{94} capsules, resulted in the formation of other Cu-rich copper-iron-sulfide(s). The formation of additional sulfides may contribute to apparent pyrrhotite dissolution and variability in copper concentration. These sulfides also show significant exsolution of at least two copper-bearing sulfide phases (Figure 18).
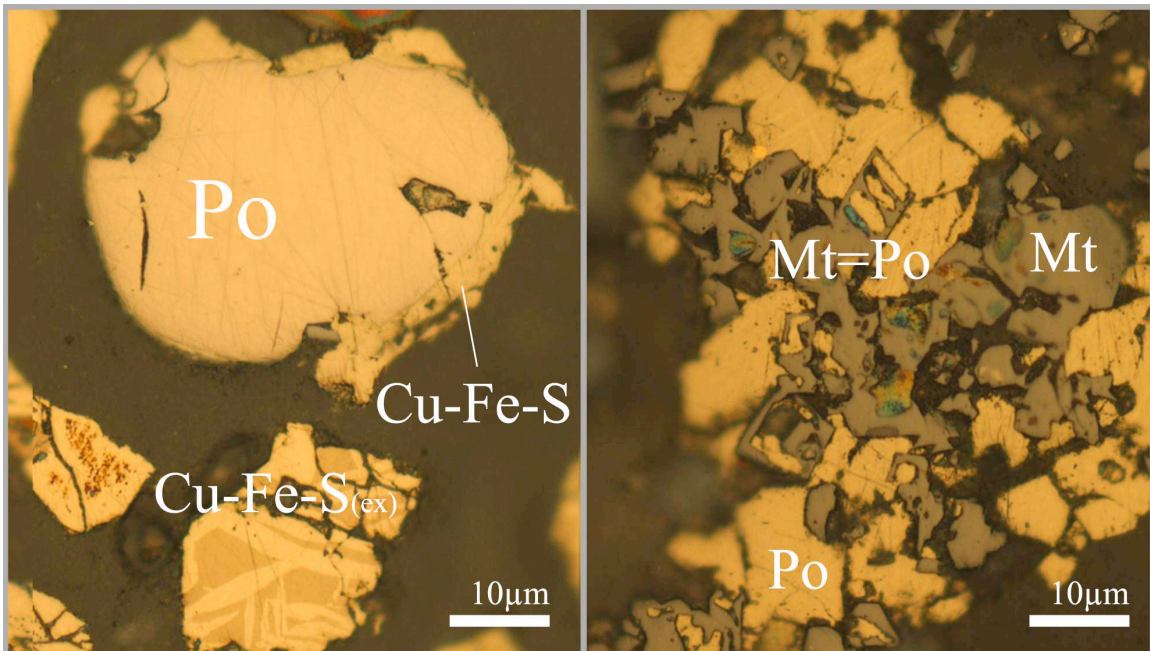

Figure 18: Photomicrographs of run product sulfides and magnetite in reflected light. Magnetite (Mt) and pyrrhotite (Po) were recovered from all sulfur-bearing experiments. Large pyrrhotite grains were commonly observed with rims of more copper-rich copper iron sulfide (Cu-Fe-S), qualitatively determined by EDS. Grains of copper iron sulfides were also occasionally observed with exsolution textures (Cu-Fe-S$_{(ex)}$). Grains of magnetite with pyrrhotite cores and pyrrhotite grains with magnetite cores Mt=Po) are consistent with the magnetite-pyrrhotite exchange required to buffer the sulfur speciation in the magmatic volatile phases and silicate melt.

147

Individual crystals occasionally include anomalous, heterogeneous gold-rich trails

visible by using backscatter electron imaging combined with EDS analysis. The vein-like

character of the gold-rich trails suggests the formation of a gold and sulfur-bearing phase,

which precedes the formation of the other Cu-Fe sulfides. Gold data are not reported in

detail in this study but gold does not affect the pyrrhotite composition as EPMA

analytical volumes do not intersected gold-rich sulfides. Run product pyrrhotite

compositions are shown in Table 11. Analyses were obtained from a minimum of three

individual crystals (30 to 100 μm in diameter) and ten separate spot analyses.

EPMA Analysis of Pyrrhotite (wt%) and Cu-Adjusted fS_2

	Run	S ($\pm2\sigma$)	Fe ($\pm2\sigma$)	Cu ($\pm2\sigma$)	Au (ppm)	log fS_2 ($\pm2\sigma$)
Bishop Tuff	Cu410	38.1 (0.3)	59.2 (0.8)	3.2 (0.9)	< 140	-2.6 (0.3)
	Cu411	38 (0.3)	59.2 (0.7)	3.3 (0.8)	< 140	-2.8 (0.3)
Granite Min-Melt (GR1)	Cu402	38.2 (0.4)	59.5 (0.7)	3.2 (0.9)	< 140	-2.7 (0.5)
	Cu404	38.4 (0.2)	59.3 (0.6)	3.1 (0.6)	< 140	-2.3 (0.2)
	Cu405	38.3 (0.3)	59.1 (0.6)	3.2 (0.6)	< 140	-2.4 (0.3)
High CO$_2$ Po/Mt Sat'd	Cu601	38.4 (0.2)	60.2 (0.3)	2.3 (0.3)	< 140	-2.7 (0.3)
	Cu606	38.6 (0.3)	59.8 (0.4)	2.5 (0.4)	< 140	-2.4 (0.3)
	Cu607	38.1 (0.2)	59.5 (0.9)	2.7 (0.9)	< 140	-2.7 (0.3)

Table 11: EPMA analysis of run product pyrrhotite and chalcopyrite. Average compositions from at least 3 pyrrhotite crystals (N>5 for each) from each experiment are shown (2σ). LogfS_2 calculated using $CuS_{0.5}$ model presented by Mengason et al. (2011).

The copper concentration of the run product pyrrhotite remains relatively constant

across low-CO$_2$ experiments (3.1 to 3.3 wt% Cu) and high-CO$_2$ experiments (2.3 to 2.7

wt% Cu) and is similar to the copper concentration in pyrrhotite from other experiments

at magmatic conditions (Jugo et al., 1999; Lynton et al., 1993). The consistency in copper

concentration for each series of experiments is a direct result of all experiments using

Cu_6Au_{94} capsules. The large mass of the capsule compared to all other starting materials

148

results in very little adjustment to the composition of the metal and consistent a_{Cu}^{Metal} for

the duration of the experiment.

The composition of pyrrhotite can be used to calculate the $f\mathrm{S}_2$ given equilibrium

with magnetite and a fixed oxygen fugacity at 800 $^\circ$C and 100 MPa (Section 3.2.2).

Toulmin and Barton (1964) present an equation relating the composition of pyrrhotite

with $f\mathrm{S}_2$, as a function of temperature (K) and the X_{Fe}^{Po} in the FeS-S$_2$ system. The X_{Fe}^{Po}

defines the variable N according to the expression:

$$N \equiv 2\left(\frac{nFe}{nFe+nS}\right) \tag{20}$$

The $f\mathrm{S}_2$ can then be calculated using the temperature (T) and N according to the

expression:

$$\log f S_2 = (70.03 - 85.83N)\left(\tfrac{1000}{T}-1\right) + 39.30\sqrt{1-0.9981N} - 11.91 \tag{21}$$

Mengason et al. (2010) note that $f\mathrm{S}_2$ calculations based upon pyrrhotite compositions

with 2 to 3 wt% copper will overestimate $f\mathrm{S}_2$ by an order of magnitude without

correcting the original Toulmin and Barton (1964) equation for copper. Thus, the copper

concentrations of run product pyrrhotite from the Cu$_6$Au$_{94}$ capsule experiments of this

study require correction to avoid overestimating $f\mathrm{S}_2$ during the run. Mengason et al.

(2010) present a corrected equation for calculating (N), in the equation presented by

Toulmin and Barton (1964), that includes the effect of a CuS$_{0.5}$ component to pyrrhotite

shown below.

$$N \equiv 2\left(\frac{nFe+nCu}{nFe+1.5nCu+nS}\right) \tag{22}$$

After correcting for copper according to these equations, the run product pyrrhotite

compositions were used to calculate the equilibrium fS$_2$ in each experiment (Table 11).

Calculated values for fS$_2$ are consistent with the value predicted by Whitney et al. (1984)

for magnetite-pyrrhotite equilibrium at fO$_2 \sim$ NNO and 800 ^{o}C (log fS$_2 \sim$ -3).

3.4.3   Fluid Inclusion Salinity and Vapor Inclusion Pressure

Microthermometric heating measurements of halite and sylvite dissolution

temperatures (~280 to 340 ^{o}C for sylvite and ~ 430 to 490 ^{o}C for halite) for brine

inclusions yielded calculated salinities of 69 to 72 wt% NaCl$_{eq}$ and 79 to 81 wt% NaCl$_{eq}$

for the experiments at X$_{CO2}$ of 0.10 and 0.38, respectively (Table 12).

LA-ICPMS Analysis of Fluid Inclusions from CO_2-bearing Mt/Po Saturated Experiments

	Run	Inclusion Type	# of FI	X$_{CO2}$ (Bulk Comp)	Salinity (Wt% NaCl$_{eq}$)	Na (±2σ) FIA's	Fe (±2σ) FIA's	Cu (±2σ) FIA's	ASI
Bishop Tuff	Cu410	Brine	14	0.098	70-72	98000 (14000)	65000 (19000)	5000 (400)	1.0
	Cu411	Brine	10	0.098	70-72	100000 (4200)	66000 (5200)	4500 (500)	1.0
	Cu410	Vapor	7	0.098	3.5-4.5	7800 (1100)	4200 (2800)	400 (90)	
	Cu411	Vapor	14	0.098	3.5-4.5	7700 (1100)	5100 (2100)	400 (80)	
Haplo-Granite Min-Melt (GR1)	Cu402	Brine	13	0.097	69-71	122000 (24000)	38100 (16000)	1900 (300)	1.0
	Cu404	Brine	16	0.098	70-72	126000 (20000)	32100 (32000)	1600 (400)	1.0
	Cu405	Brine	25	0.098	70-72	119000 (17000)	49300 (18000)	3000 (800)	1.0
	Cu402	Vapor	9	0.097	3-4	9700 (1400)	6700 (8600)	180 (100)	
	Cu404	Vapor	10	0.098	3.5-4.5	9200 (1300)	4700 (7200)	160 (100)	
	Cu405	Vapor	13	0.098	3.5-4.5	8900 (1300)	5100 (4500)	280 (130)	
High CO$_2$ (GR1)	Cu601	Brine	10	0.38	79-81	145000 (12000)	28700 (5100)	4100 (800)	0.9
	Cu606	Brine	13	0.37	79-81	162000 (5000)	35200 (3400)	4700 (700)	0.9
	Cu607	Brine	21	0.38	79-81	140000 (7000)	32400 (7300)	3400 (700)	0.9
	Cu601	Vapor	14	0.38	0.9-1	1600 (300)	390 (420)	40 (10)	
	Cu606	Vapor	7	0.37	0.9-1	1700 (100)	320 (140)	50 (10)	
	Cu607	Vapor	16	0.38	0.9-1	1500 (300)	840 (210)	40 (10)	

Table 12: Fluid inclusion characteristics for vapor and brine fluid inclusions from experiments with X$_{CO2}$~ 0.10 and 0.38. X$_{CO2}$ calculated based upon mass balance of starting materials. Salinities calculated using microthermometry and models presented by Bodnar (1989) and Duan et al. (1995). Na, Fe, and Cu concentrations determined by LAICPMS. Melt ASI calculated based on EMPA analysis of quench glasses and equations presented by Shand (1949).

Raman spectroscopic measurements of vapor inclusions from experiments with

X$_{CO2}$ of 0.10 and 0.38 yielded Fermi-diad splitting values (Δ) of 102.9 and 103.1 cm^{-1},

respectively. As predicted, these splitting values correspond to pressures slightly higher

at X_{CO2} = 0.10 and slightly lower at X_{CO2} = 0.38 compared to sulfur-free experiments

described in Chapter 2. Peak fitting of Raman analyses yields H_2S concentrations of 5 to

6 mol% and 2 to 3 mol% of the quenched vapor bubble for vapor inclusions from

experiments with magmatic X_{CO2} = 0.10 and 0.38, respectively. These H_2S

concentrations fall significantly below the predicted CO_2/H_2S ratio at high temperature.

As discussed, the small opaque daughter crystals formed upon quench in vapor inclusions

consume most of the available sulfur. However, the concentration of H_2S at room

temperature was used to correct clathrate equilibria, and pyrrhotite compositions were

used to estimate magmatic fH_2S. The Fermi-diad splitting values (Δ) correlated with

pressures at $Tm_{Adjusted}^{Clath}$ of 3 MPa and 4.5 MPa, respectively, using Equation (4) presented

by Fall et al. (2011) to calculate density at room temperature, and the CO_2-H_2S equation

of state presented by (Stouffer et al., 2001) to determine the appropriate ischore. The

model for mixed CO_2-H_2S clathrates discussed in Section 3.3 was used to calculate a

ΔTm^{Clath} = 1 ^0C and 0.5 ^0C for experiments at X_{CO2} = 0.10 and 0.38, respectively.

The $Tm_{Adjusted}^{Clath}$ and the inclusion pressure were then input into the model presented

by Sun and Duan (2006) to calculate the salinity of each inclusion. Vapor inclusions from

experiments at X_{CO2} = 0.10 have $Tm_{Measured}^{Clath}$ values between 6.5 and 7 ^0C and $Tm_{Adjusted}^{Clath}$ =

5.5 to 6 ^0C yielding salinities between 3.5 wt% and 4 wt% $NaCl_{eq}$, adjusting for HCl as

needed. Experiments at X_{CO2} = 0.38 have $Tm_{Measured}^{Clath}$ values between 9.5 and 10 ^oC and

$Tm_{Adjusted}^{Clath}$ = 9 to 9.5 ^0C yielding a salinities between 0.9 and 1 wt% $NaCl_{eq}$. Often

clathrate melting was difficult to observe for vapor inclusions in experiments at X_{CO2} =

0.38 and ice melting temperatures of -1^oC to -2 ^oC were used to confirm a ~1 wt%

salinity. Vapor inclusions occasionally have $Tm^{Clath}_{Measured}$ temperatures several ^0C below the ranges listed above, and are not analyzed as they represent significant brine contamination of the high-temperature vapor. The difficulty in evaluating vapor salinity in the CO_2-bearing experiments is the dominant source of uncertainty in quantifying the partitioning of copper between the high-temperature vapor and brine.

3.4.4   Fluid Inclusion Compositions

The sodium, iron and copper concentrations of the fluid inclusion assemblages analyzed from each experiment along with the number of inclusions analyzed, average salinity, and X_{CO2} are shown below in Table 12. Each experiment includes both vapor and brine inclusions from at least two separate fluid inclusion assemblages from different parts of the quartz core.

The initial major element composition of the fluid inclusions is controlled by the bulk composition of the starting solution for each experiment. The Na/K/H molar ratio of 10/10/1 utilized in all experiments results in final bulk compositions slightly enriched in sodium relative to potassium due to corresponding exchange and compositional adjustment of these cations with the silicate melt. Variability in the iron content of the vapor and brine is primarily the result of variable concentrations of HCl in the MVPs. Variability in the fHCl resulted in changes in the concentration of $FeCl_2$ according to magnetite and pyrrhotite decomposition equilibria show in Equation (23) and (24) below.

$$Fe_3O_4 + 6HCl^{MVP} = 3FeCl_2^{MVP} + 4H_2O^{MVP} \tag{23}$$

$$FeS^{Po} + 2HCl^{MVP} = FeCl_2^{MVP} + H_2S^{MVP} \tag{24}$$

In an equilibrium experiment, the formation of FeCl$_2$ will affect the MVP compositions but has little impact on copper partitioning. The formation of additional FeCl$_2$ could have a greater impact on copper partitioning in evolving melt-volatile phase equilibria in natural arc environments owing to budgets of total chlorine. In contrast, the presence of H$^+$ in place of Na$^+$ and K$^+$ ions could affect copper complexation and thus copper partitioning in the equilibrium melt-volatile phase experiments presented in this chapter.

The increase in fHCl in the metaluminous experiments (Cu410 and Cu411) is correlated with higher copper concentrations in the vapor and brine relative to slightly peralkaline experiments (Cu402 through Cu405). This increase in copper partitioning into MVP's with increasing fHCl is consistent with observations and predictions of the impact of HCl on metal partitioning from other CO$_2$-free experimental studies in the literature (Frank et al., 2003; Zajacz et al., 2010b; Zajacz et al., 2011). As noted by Zajacz et al. (2011), copper may be present in the vapor at high temperature (1000 ^{o}C) as mixed chloride-hydrogen sulfide complexes, many of which are stabilized by Na$^+$, K$^+$, or H$^+$. There is not sufficient sampling of variable HCl concentrations within the described experiments to make a complete comparison to Zajacz et al. (2011), but they predict that copper solubility reaches a maximum near a Na/H ratio ~ 1. This maximum is close to the (Na+K)/H ratio of the pyrrhotite-saturated experiments presented in this chapter, and I hypothesize that the small change in the observed copper partitioning is due to a similar availability of multiple stable complexes at 800 ^{o}C. However, the primary focus of the experiments is the comparison of copper partitioning among the vapor, brine and silicate melt in low-CO$_2$ and high-CO$_2$ experiments. This is best accomplished by evaluating partition coefficients and equilibrium constants (Section 3.4.6).

3.4.5 *Quartz-Hosted Brines and Glass-Hosted Brines: Equilibrium*

The copper concentration of glass-hosted brine inclusions was determined by LA-ICPMS for 4 sulfur-bearing experiments. Determinations of copper concentrations in glass-hosted brine inclusions were complicated by several factors. First, the high-salinity of the brine inclusions (>70 wt%) results in final halite disappearance temperatures between 400 and 500 $^{\circ}$C. These temperatures are close to the glass transition temperature and thus no direct measurement of salinity is possible for glass-hosted brine inclusions. As a result, the average salinity of the quartz-hosted brine inclusions is used to characterize salinity and the sodium concentration for use as the internal standard. As discussed, the inclusions chosen are those that appear to have a similar proportion of halite + sylvite to quartz-hosted brine inclusions. Second, as noted by Simon et al. (2006), the high concentration of potassium in the run product glass and glass-hosted brine inclusions requires a significant host correction to quantify the brine composition, resulting in scatter in the potassium concentration of the glass-hosted inclusions. Yet, the copper concentrations in the glass-hosted brine inclusions are consistent with the copper concentration of the quartz-hosted brine inclusions (Figure 19).
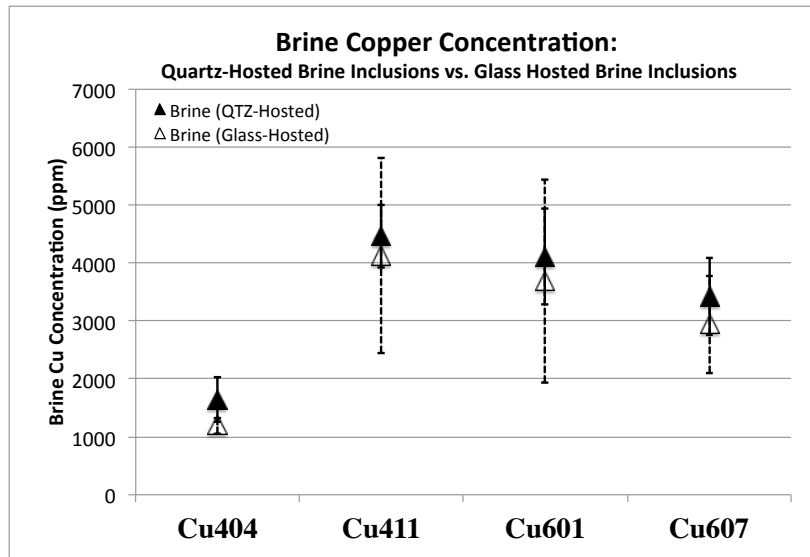
Figure 19: Copper concentrations in quartz and glass-hosted brine inclusions. The copper concentration in the glass-hosted inclusions is always below that of the quartz-hosted inclusions, but they are the same within uncertainty. Exsolution of water from the quenching melt and entrapment of small amounts of vapor dilute the Cu-rich brine in the glass. Experiments: Cu404 (GR1, $X_{CO2}=0.1$), Cu411 (Bishop Tuff, $X_{CO2}=0.1$), Cu601 & Cu607 (GR1, $X_{CO2}=0.38$).

As expected, there is significantly more scatter in the copper concentration of the glass-hosted brine inclusions owing to the large host correction and lack of individual salinity values. The average copper concentration of the glass-hosted brines is always below that of the quartz-hosted inclusions. It is likely the case that small amounts of vapor are trapped along with brine during initial entrapment of MVPs within the newly formed silicate melt as an experiment reaches run conditions. These vapor + brine mixtures may persist throughout the experiment and thus, analyses of glass-hosted brines may include variable amounts of vapor with lower concentrations of copper. Analysis of brine inclusions from brine-dominated regions of glass-hosted fluid inclusions should mitigate vapor contamination, although without salinity measurements, quantifying the extent of dilution is not possible. The process of exsolution of water from the melt into large fluid inclusions during quench would also tend to dilute the copper concentration

and may also contribute to the slightly lower copper concentration of glass-hosted brine

inclusions and higher concentrations in the surround melt.

3.4.6   Partition Coefficients and Equilibrium Constants

Nernst-type partition coefficients are reported for copper partitioning between the

vapor and brine as well as the vapor and brine relative to the silicate melt (Table 13). The

partition coefficients are defined by the copper concentration of any two of the magmatic

phases (vapor, brine and melt) present at run conditions as shown in Equation (25) below.

$$D_{Cu}^{x/y} \equiv \frac{C_{Cu}^{x}}{C_{Cu}^{y}} \quad \{x, y = vapor, brine, melt\} \tag{25}$$

Average calculated partition coefficients ($\pm 2\sigma$) for $D_{Cu}^{b/v}$ = 12($\pm$1) at X_{CO2} = 0.10 (Bishop

Tuff), 10.5($\pm$5) at X_{CO2} = 0.10 (GR1), and 95($\pm$23) for experiments at X_{CO2} =0.38 (GR1)

(Table 13). These partition coefficients demonstrate a significant enrichment of copper in

the dense high-salinity magmatic brine relative to the coexisting low-salinity vapor for all

melt and MVP compositions. These data are consistent with the general trend of brine

dominance observed by other experimental studies of copper partitioning between silicate

melts and MVPs ($D_{Cu}^{b/v}$ > 1) (Frank et al., 2011; Lerchbaumer and Audetat, 2009; Simon

et al., 2006; Williams et al., 1995).

D_{Cu} & $K_{Cu,Na}$		X_{CO2}	$K_{Cu,Na}^{b/v}$	$D_{Cu}^{b/v}$	$K_{Cu,Na}^{b/m}$	$D_{Cu}^{b/m}$	$K_{Cu,Na}^{v/m}$	$D_{Cu}^{v/m}$
Bishop Tuff	Cu410	0.098	0.9 (0.3)	11 (2)	83 (30)	340 (100)	92 (40)	30 (10)
	Cu411	0.098	0.97 (0.3)	13 (3)	93 (24)	380 (90)	97 (37)	30 (10)
Haplo- Granite Min-Melt	Cu402	0.097	0.81 (0.3)	10 (3)	33 (5)	160 (20)	41 (17)	16 (5)
	Cu404	0.098	0.77 (0.6)	10 (7)	25 (14)	170 (90)	33 (28)	16 (13)
	Cu405	0.098	0.81 (0.5)	11 (6)	46 (13)	220 (60)	57 (29)	20 (9)
High CO$_2$ Po/Mt (GR1)	Cu601	0.38	1.04 (0.4)	92 (28)	25 (13)	160 (90)	24 (13)	1.8 (0.9)
	Cu606	0.38	1.02 (0.4)	97 (27)	30 (15)	230 (120)	29 (17)	2.4 (1.3)
	Cu607	0.38	1.03 (0.3)	97 (23)	28 (11)	180 (60)	27 (11)	1.9 (0.6)

Table 13: Nernst-type partition coefficients (D) and apparent equilibrium exchange constants (K) for CO₂-bearing experiments (±2σ).

Comparison of these $D_{Cu}^{b/v}$ values with sulfur-free experiments ($D_{Cu}^{b/v} = 25\pm7$) demonstrates the thiophilic character of copper and corresponding enrichment of copper into magmatic vapor in the presence of H_2S, which partitions strongly into the vapor relative to the brine (Behrens and Gaillard, 2006; Clemente et al., 2004; Heinrich et al., 2004; Seo et al., 2009; Sillitoe, 2010; Simon and Ripley, 2011; Zajacz et al., 2011). Recent modeling presented by Zajacz et al. (2011) points to a number of ligands and ligand pairs that incorporate a mixture of Na^+, K^+, H^+ and Cl^- along with H_2S or HS^-, which they demonstrate are important for copper complexing at magmatic conditions.

The enrichment of copper into pyrrhotite-saturated magmatic vapor at $X_{CO2} = 0.10$ relative to similar sulfur-free experiments indicates that the formation of sulfur-bearing copper complexes is not inhibited by small concentrations of CO_2. In contrast, the partitioning of copper between brine and vapor in pyrrhotite-saturated experiments at $X_{CO2} = 0.38$ ($D_{Cu}^{b/v} = 95\pm23$) is the same as sulfur-free experiments (110 ± 40) within analytical uncertainty. One explanation is that at high X_{CO2}, copper enrichment of magmatic vapors via sulfur-bearing complexation is absent due to suppression of the copper complexation in the low-salinity CO_2-rich vapor. The low-salinity of the high-temperature vapor reduces the amount of sodium and potassium available for stabilization of the ion pair copper complexes predicted by Zajacz et al. (2011). The high-CO_2 vapor may also have different physical properties (e.g. polar character and dielectric potential), which may also affect the stability of the copper complexes (Lowenstern, 2001; Pokrovski et al., 2008; Zajacz et al., 2011).

Evaluating copper partitioning between the silicate melt and magmatic vapor and brine is also vital to modeling the effect of CO_2 on the potential for extraction of copper

by sulfur-bearing MVPs. Average calculated partition coefficients for partitioning of copper between brine and melt ($\pm 2\sigma$) for $D_{Cu}^{b/m}$ = 360($\pm$110) (Bishop Tuff, X_{CO2} = 0.10), 180($\pm$60) (GR1, X_{CO2} = 0.10), and 190($\pm$80) (GR1, X_{CO2} = 0.38). The average calculated partition coefficients for copper partitioning between vapor and melt are $D_{Cu}^{v/m}$ = 30($\pm$11) (Bishop Tuff, X_{CO2} = 0.10), 18($\pm$8) (GR1, X_{CO2} = 0.10) and 2($\pm$0.8) (GR1, X_{CO2} = 0.38). Copper partitioning between brine and melt for most pyrrhotite-saturated experiments falls in the same range as sulfur-free CO_2-bearing experiments ($D_{Cu}^{b/m}$ = 200 $\pm$ 60). However, the presence of HCl in brines from metaluminous experiments is correlated with an increase in iron and copper relative to HCl-free brines. Accordingly, the $D_{Cu}^{b/m}$ partition coefficient is slightly higher for metaluminous melts with at X_{CO2} = 0.10, owing to an increase in the copper concentration of the brine, relative to the silicate melt. Experiments at X_{CO2} = 0.38 have a similar $D_{Cu}^{b/m}$ (190 $\pm$ 80) to low-CO_2 experiments and high-CO_2, sulfur-free experiments (190 $\pm$ 50), but have dramatically lower $D_{Cu}^{v/m}$ values.

All pyrrhotite-saturated experiments at low X_{CO2} show an enrichment of the vapor in copper with the addition of sulfur. This is confirmed by the increase in the vapor-melt copper partition coefficients compared to sulfur-free experiments. The magmatic vapor phase from metaluminous experiments also show enrichment in copper, relative to slightly peralkaline experiments. However, the pyrrhotite-saturated experiments at X_{CO2} = 0.38 indicate that vapor-melt copper partition coefficients ($D_{Cu}^{v/m}$ = 2 $\pm$ 0.8) are an order of magnitude lower than for melt-vapor equilibrium at low concentrations of CO_2 ($D_{Cu}^{v/m}$ = 18 to 30). Copper retention by the silicate melt is increased (~20 ppm vs. ~10 ppm at X_{CO2} = 0.38 and 0.10, respectively) in addition to the marked decrease in the copper

158

concentration of the magmatic vapor (~50 ppm vs. ~200-400 ppm at X_{CO2} = 0.38 and

0.10, respectively). I hypothesize that this change in copper partitioning behavior is due

to the suppression chloride-hydrogen sulfide copper complexes with increasing X_{CO2}. As

a result, CO_2-rich, sulfur-bearing magmatic vapors will have lower efficiencies of

removal of copper into the MVPs, compared to low-CO_2 sulfur-bearing vapors, than the

difference in the sulfur-free systems ($D_{Cu}^{v/m}$ decreases from 8.5 ± 3 to 1.9 ± 0.6).

Evaluating the equilibrium exchange of copper and sodium between the vapor and

brine also provides insight into the partitioning and complexation of these cations in the

volatile phases (Williams et al. 1997; Simon et al. 2006). The relevant equilibrium

constant for Cu-Na exchange in chloride-complexed CO_2-free systems is defined by

Equation (26) below (Williams et al. 1997).

$$K_{Cu,Na}^{b/x} \equiv \frac{C_{Cu}^{b} \bullet C_{Na}^{x}}{C_{Cu}^{x} \bullet C_{Na}^{b}} \quad \{b = brine; \, x = vapor, melt\} \tag{26}$$

Theoretical and experimental data are consistent with sodium playing an important role in

stabilizing some of these complexes (Simon et al., 2006; Zajacz et al., 2011). CO_2 is

unable to complex either copper or sodium under the magmatic conditions of this study

and thus, chlorine and sulfur-bearing copper complexation will control the concentration

of both copper and sodium in the magmatic vapor and brine. The pyrrhotite-saturated

experiments of this study vary the H/Na ratio and the salinity, density, and polar character

of the MVPs due to variable X_{CO2}, and thus copper complexation may also be variable.

Thus, Cu-Na exchange will produce different apparent equilibrium constants if copper

and sodium complexation are affected differently by the presence of CO_2.

The average calculated $K_{Cu,Na}^{b/v}$ are 0.93 (±0.1) (Bishop Tuff, X_{CO2} = 0.10), 0.80

(±0.4) (GR1, X_{CO2} = 0.10) and 1.03 (±0.3) (GR1, X_{CO2} = 0.38). The values for pyrrhotite-

saturated experiments overlap with each other and the sulfur-free experiments within

analytical uncertainty, but there is some indication that the mechanism for Cu/Na

exchange varies from low to high X_{CO2}. The average $K_{Cu,Na}^{b/v}$ value for GR1 experiments

(0.80 ± 0.4) at X_{CO2} = 0.10 is below the value of ~1 observed for similar sulfur-free

experiments. A drop in the equilibrium constant is likely associated with the increase in

the concentration of copper in the magmatic vapor due to lower sulfur-bearing copper

complexation in the magmatic brine. The suppression of sulfur-bearing copper

complexation at high X_{CO2} results in a higher $K_{Cu,Na}^{b/v}$ (1.03 ± 0.3), as the copper

complexation returns to dominantly chlorine based ligands and a value close to unity. The

$K_{Cu,Na}^{b/v}$ value for Bishop Tuff experiments (0.93 ± 0.1) at X_{CO2} = 0.10 is slightly elevated

on average compared to GR1 experiments, and is primarily due to a decrease in sodium

concentration in the magmatic vapor relative to the brine due to the fHCl.

Additionally, copper and sodium are exchanged between the brine and silicate

melt via the equilibrium between sodium and copper present in the brine as chloride

complexes and sodium and copper oxide components of the melt, as shown below in

Equation (27) below.

$$CuO_{0.5}^{melt} + NaCl^{brine} = CuCl^{brine} + \tfrac{1}{2} Na_2O^{melt} \qquad\qquad (27)$$

Similar equilibria to that shown in Equation (27) above must exist for the exchange of

potassium and hydrogen ions (H^+- derived from HCl) between the brine and silicate melt.

The average calculated $K_{Cu,Na}^{b/m}$ = 90 (±30) (Bishop Tuff, X_{CO2} = 0.10), 35 (±10) (GR1,

$X_{CO2} = 0.10$), and 28 (±11) (GR1, $X_{CO2} = 0.38$) for experiments at $X_{CO2} = 0.10$ (Bishop

Tuff), 0.10 (GR1), and 0.38, respectively. The variability observed in $K_{Cu,Na}^{b/m}$ for

experiments at $X_{CO2} = 0.1$, is linked to a change in the concentration of HCl in the brine,

and a corresponding change in the complexation copper. An increase in any of the three

chlorides (NaCl, KCl, HCl) will increase copper complexation, although the $K_{Cu,Na}^{b/m}$ must

decrease with increasing HCl or KCl in the magmatic brine, or a decrease in the Na_2O

component of the melt. The solubility study and thermodynamic models presented by

Zajacz et al. (2011) do not include considerations for copper complexing in magmatic

brines and thus, no sulfur complexes are proposed for the brine-melt equilibria.

Copper and sodium exchange between the vapor and silicate melt is modeled as

the exchange of copper and sodium chloride complexes, along with ion pair complexes

formed from mixtures of chloride and bisulfide ligands (Zajacz et al., 2011), with the

copper and sodium oxide components of the melt, as shown in Equation (28) through

(30) below.

$$2CuO_{0.5}^{melt} + 4NaCl^{vapor} + 4H_2S^{vapor} = 2(Na)^+[Cu(HS)_2^-]^{vapor} + 4HCl^{vapor} + Na_2O^{melt} \qquad \textbf{(28)}$$

$$2CuO_{0.5}^{melt} + 4NaCl^{vapor} + 2H_2S^{vapor} = 2(Na)^+[CuHSCl^-]^{vapor} + 2HCl^{vapor} + Na_2O^{melt} \qquad \textbf{(29)}$$

$$2CuO_{0.5}^{melt} + 4NaCl^{vapor} = 2(Na)^+[CuCl_2^-]^{vapor} + Na_2O^{melt} \qquad \textbf{(30)}$$
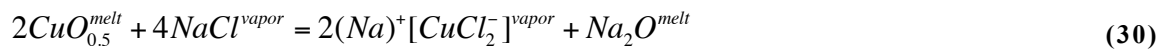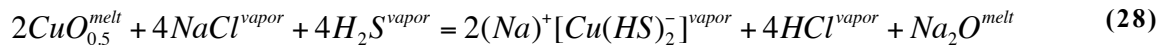
Zajacz et. al (2011) discusses that similar copper complexes should exist with potassium

or hydrogen ions (H^+-derived from HCl) replacing sodium. Thus, similar K-H-Cu-HS-Cl

equilibria to that shown in Equation (28), should be considered when discussing copper

complexing and apparent equilibrium constants for copper-sodium exchange between the

vapor and silicate melt.

The average calculated $K_{Cu,Na}^{v/m}$ = 95 (±40) (Bishop Tuff, X_{CO2} = 0.10), 45 (±21)

(GR1, X_{CO2} = 0.10), and 25 (±12) (GR1, X_{CO2} = 0.38). The increase in the $K_{Cu,Na}^{v/m}$ for low-

CO_2 Bishop Tuff experiments compared to low-CO_2 GR1 experiments is a result of an

increases H/(Na+K) ratio and corresponding increase in copper complexation in the

vapor, without an increase in the sodium concentration of the vapor. The Cu-Na

exchange equilibria and partition coefficients for sulfur-bearing systems also suggests

that sulfur-bearing complexation remains present in melt-vapor-brine systems at low

X_{CO2}. As a result, changes in copper partitioning observed in other experiments with

changes in fS_2 (Frank et al., 2011) and changes in cation ratios (H/Na/K : Zajacz et al.,

2011) will likely still affect the efficiency of removal of copper into MVPs at low X_{CO2}.

In contrast, the decrease in $K_{Cu,Na}^{v/m}$ observed for high-CO_2 experiments, relative to low-

CO_2 experiments, is consistent with a lack of appreciable sulfur-bearing copper

complexes present in the vapor. This conclusion is supported by the return of the

apparent equilibrium constant for Cu-Na exchange to that of sulfur-free systems. The

apparent equilibrium constants for sulfur-free experiments at X_{CO2} = 0.10 ($K_{Cu,Na}^{v/m}$ = 30 ±

19) and X_{CO2} = 0.38 ($K_{Cu,Na}^{v/m}$ =25 ± 17) are all consistent with the high-CO_2, sulfur-bearing

experiments.

3.5 Discussion

3.5.1 *Calculating MVP Bulk Composition at Magmatic Conditions*

Unfortunately, direct measurement of magmatic CO_2/H_2S ratios is not possible

via characterization of the gas component of fluid inclusions at ambient conditions. The

observation of opaque daughter minerals, inferred to be sulfides (Figure 14),

demonstrates that a large portion of sulfur in the vapor phase at magmatic conditions is crystallized as sulfide during quench. However, measurement of the CO_2/H_2S ratio at ambient conditions is vital to quantifying the other properties of vapor inclusions. Calculating the vapor composition at magmatic conditions requires estimating the degree of sulfide formation or the use of thermodynamic models for sulfur speciation.

Assuming that the sulfide component of vapor inclusions is a mixture of copper-iron-sulfide(s), the fluid inclusion data could be combined with $FeCl_2$ solubility equilibria to estimate the concentration of $f H_2S$ in the magmatic vapor. The exchange of iron between magnetite and the magmatic vapor can occur as a function of the $f HCl$ according to Equation (31) below.

$$FeS^{Po} + 2HCl^{vapor} = FeCl_2^{vapor} + H_2S^{vapor} \tag{31}$$

However, the majority of the pyrrhotite-saturated experiments are slightly peralkaline, and have no appreciable concentration of HCl in the magmatic vapor. Thus it is not appropriate to consider equilibria that include HCl. For peralkaline systems it is necessary to evaluate the equilibrium between $FeCl_2$ in the MVPs and the FeO component of the silicate melt.

$$FeO^{melt} + 2NaCl^{vapor} = FeCl_2^{vapor} + Na_2O^{melt} \tag{32}$$
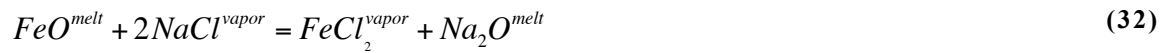
The crux of either calculation is the modeling or calculation of relevant equilibrium constants for the conditions of magmatic-MVP experiments. However, direct modeling of sulfur equilibria based on pyrrhotite composition is well established (Clemente et al., 2004; Jugo et al., 1999; Lynton et al., 1993; Toulmin and Barton, 1964; Whitney, 1988). In addition, the same method can be used for all experiments, because all sulfur-bearing

experiments were pyrrhotite and magnetite saturated. Thus, pyrrhotite-magnetite equilibrium was used to characterize the $f\text{H}_2\text{S}$ at magmatic conditions.

Other experimental studies involving magmatic sulfur (Clemente et al., 2004; Jugo et al., 1999; Simon et al., 2006; Whitney, 1984) have estimated the $f\text{S}_2$, $f\text{H}_2\text{S}$, and $f\text{SO}_2$ based upon the $f\text{H}_2/f\text{O}_2$ at magmatic conditions according to the simplified equilibrium expressions shown below in Equations (33) and (34)

$$H_2 + \tfrac{1}{2}S_2 = H_2S \tag{33}$$

$$O_2 + \tfrac{1}{2}S_2 = SO_2 \tag{34}$$
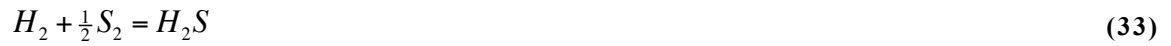
and using a thermodynamic model for calculating equilibrium constants. Equilibrium constants were calculated using SUPCRIT2 (Johnson et al., 1992), consistent with those presented by both (Ohmoto and Kerrick, 1977) and Zajacz et al. (2011) which are similar for 800 $^{\circ}$C and 100 MPa and the compositions of the MVPs.

Although the $f\text{O}_2$ and $f\text{H}_2$ are well characterized, the $f\text{S}_2$ must be established before using these equilibria to estimate the fugacities of sulfur species at magmatic conditions. At 800 $^{\circ}$C, 100 MPa and $f\text{O}_2 = $ NNO the $f\text{S}_2$ predicted by Whitney (1984) will be log $f\text{S}_2 = $ -3. However according to the model presented by Mengason et al. (2010) the $[\text{Cu}]^{\text{Po}} \sim 3.2$ wt% and 2.5 wt% for run product pyrrhotite from my experiments would result in a decrease in the equilibrium $f\text{S}_2$ of ~ 0.1 log units. The equilibrium log $f\text{S}_2$ of -3.1 is equivalent to a ΔFFS (iron-troilite equilibrium) value of 6.25, according to the expression

$$\Delta FFS = \log f\,S_2 - \log\left[e^{\frac{2}{RT}(-0.2655(P-1)-35910+12.56T)} \right] \tag{35}$$

which was derived based on the work of Clemente et al. (2004) where R = 1.986 cal/mol-K, P in bars, and T is in K.

The value predicted by Mengason et al. (2010)for pyrrhotite-magnetite equilibrium at 800 °C, 100 MPa, and fO_2 = NNO (log fS_2 = -3.1, ΔFFS = 6.25) is similar to the fS_2 calculated based upon the composition of run product pyrrhotite from this study (log fS_2 = -2.4 to -2.8 and ΔFFS = 6.75 to 6.35). Clemente et al. (2004) quantifies the equilibrium between fS_2 and the concentration of sulfur dissolved in the silicate melt ($[S]_{ppm}^{melt}$) as a function of temperature and fO_2.

$$\frac{\log[S]_{ppm}^{melt} - 0.001(T) + 0.2567\Delta NNO}{0.1713 + .0034\Delta NNO} = \Delta FFS \tag{36}$$

The pyrrhotite-saturated experiments from this study have sulfur concentrations between 80 to 140 ppm, resulting in ΔFFS values between 5.5 to 6, which are equivalent to a log fS_2 = -3 to -3.1, within 0.5 log units of the value calculated using pyrrhotite compositions. However, these values are near the LOD for WDS analysis by EPMA and the high degree of scatter in the data for the sulfur concentration in run product glass indicates that the fS_2 calculated from pyrrhotite compositions is the most accurate estimate of the fS_2 at run conditions. The fS_2, fH_2O and fO_2 correspond with an equilibrium fH_2S = 10 to 13 MPa and fSO_2 < 0.003 MPa, calculated using Equation (33) and (34) at the magmatic conditions of our pyrrhotite-saturated experiments. This value of fH_2S is consistent with a CO_2/H_2S ratio of ~ 10 and ~ 40 at X_{CO2} = 0.10 and 0.38, respectively.

Calculation of the CO_2/H_2S ratio at ambient conditions in vapor inclusions is based on the Raman peak fitting described in Section 3.4.3, with values of ~15 and 40 at

X_{CO2} = 0.10 and 0.38, respectively. The decrease in the relative concentration of H_2S in low-CO_2 vapors upon quench is consistent with the observation of opaque sulfide daughter minerals in the majority of vapor inclusions from these experiments.

3.5.2   *Modeling to Calculate Vapor Inclusion Salinity*

In the pursuit of characterizing the composition of magmatic vapor inclusions I have developed a method of combining microthermometry and Raman spectroscopy to overcome the challenges associated the presence of both CO_2 and H_2S in vapor-rich fluid inclusions. The characterization of the gas composition (CO_2/H_2S ratio) of mixed gas vapor inclusions at ambient conditions must be the first step in the characterization of all other inclusions properties. The method for analysis of vapor inclusions by micro-Raman spectroscopy described in Sections 3.3.4 allows for the simultaneous collection of CO_2 and H_2S peaks in single analysis. The peak fitting measurements characterize the gas compositions of individual fluid inclusions after the precipitation of opaque daughter minerals. The Fermi-diad splitting of the Raman CO_2 peaks is used to accurately characterize the P_{FI}, regardless of the presence of H_2S.

These individual measurements are also crucial to accurate characterization of gas composition because, the proportion of sulfur converted to sulfide upon quench is likely variable. Replicate experiments at X_{CO2} = 0.10 have a range of X_{H2S} in the ambient gas in vapor inclusions from 5 to 7 mol%. This may be due to variability in the quench phenomena as a function of the physical characteristics of individual vapor inclusions (size, shape, distance from core boundary, etc.) and small variability in the cooling rate during quench.

Only given an accurate measure of CO_2 and H_2S in each vapor inclusion is it possible to model the salinity dependent stability of mixed gas clathrates that will form upon cooling vapor inclusions. Furthermore, the formation of clathrate in a vapor inclusion precludes the accurate measurement of salinity using microthermometry measurements of ice melting temperatures (Diamond, 1994; Diamond, 2003). Both CO_2 and H_2S form structure I clathrates. The formula for CO_2 and H_2S clathrates is 6X-2Y-46H$_2$O where "X" is a gas "cage" made of 24 water molecules and "Y" is a cage made from 20 water molecules (Diamond, 1994; Sloan and Koh, 2008). The similarity in clathrate formation by CO_2 and H_2S contributes to the validity of an idealized model for the stability of mixed CO_2-H_2S clathrates. As discussed, the model presented for ideal mixing and of CO_2 and H_2S in the gas phase and clathrate is only valid for low concentrations of H_2S. However, the H_2S concentration of vapor inclusions from all pyrrhotite-saturated experiments is within the pseudo-azeotropic region of gas mixing, which promotes the formation of clathrate from a gas, or gas + liquid of a single composition.

Some models for mixed gas clathrate formation account for non-ideal mixing in clathrate stability by evaluating the preference of each gas component for the clathrate relative to the gas mixture and the degree of "cage" filling. Sloan and Koh (2008) discuss one such method in which clathrate forming gasses are assigned K_{vsi} values representing the effective gas/clathrate partition coefficient for each gas component. However, the K_{vsi} values and mixing procedure are designed for dominantly natural gas clathrates and do not account for the similarity in clathrate structure and gas mixing properties of CO_2-rich CO_2/H_2S mixtures. Although statistical thermodynamic models also exist, their

167

applicability to CO_2-H_2S mixtures is limited and no experimental studies of the CO_2-H_2S binary have been conducted. Given that numerous studies of clathrate suggest that volatile phase compositions near one of the end-member components produce clathrates that closely approximate the properties of the end-member clathrate (Diamond, 1994; Sloan and Koh, 2008), I chose to model the clathrate mixing in our pyrrhotite-saturated experiments with an ideal mixing model.

The model reported in Section 3.3.5 allows for calculating the salt-free clathrate stability boundary as a function of the CO_2/H_2S ratio of vapor inclusions. The equations used for calculating the mixed clathrate stability boundary at any ratio of CO_2 to H_2S are discussed in more detail in Appendix IV, although the model remains most useful at values CO_2/H_2S > 9. Sun and Duan (2006) present the most recent thermodynamic model for the effect of salinity on the clathrate stability boundary in the pure CO_2-H_2O-NaCl system. Although the chloride mixture in the pyrrhotite-saturated experiments in this study is a combination of NaCl, KCl, HCl, and $FeCl_2$, the freezing point depression of clathrate is a colligative property and thus only $FeCl_2$ behaves slightly differently, contributing 3 particles instead of the 2 particles contributed by the other chlorides (Diamond, 2003; Sloan and Koh, 2008). This is because, similar to water, clathrate excludes most of the solvated chlorides, and thus the behavior of both pure CO_2 and pure H_2S clathrate should behave similarly. The limited experimental data constraining the effect of NaCl on the pure H_2S clathrate stability boundary reports approximately the same magnitude of freezing point depression for 10 wt% NaCl solutions (Bond and Russell, 1949).

In light of the similar salinity dependence for CO_2 and H_2S clathrates, I chose to apply a correction factor to clathrate melting temperatures equal to the magnitude of the difference between the pure-CO_2 clathrate stability boundary and the boundary for the CO_2-H_2S mixture of individual inclusions. This allows for inputting the values of $Tm_{Adjusted}^{Clath}$ into the model for the salinity dependent pure-CO_2 clathrate stability presented by Sun and Duan (2006) to calculate the molarity of the chloride solution required for intersection of the $Tm_{Adjusted}^{Clath}$ and P_{FI} at the clathrate stability boundary. Once adjustments were made for the actual chloride mixture, including the presence of HCl, this model represents the best available method for estimating the salinity of CO_2 and H_2S bearing vapor inclusions. Although many natural fluid inclusions have undergone significant readjustment to sulfur speciation, if H_2S remains the dominant species, a similar method could be employed for characterizing clathrate nucleating inclusions in natural systems.

3.5.3   *Enrichment of Copper in MVPs with the Addition of Sulfur.*

The method for characterizing fluid inclusion salinity using microthermometry, Raman spectroscopy, and modeling of mixed CO_2-H_2S clathrate stability provides an accurate internal standard for LA-ICPMS analysis similar to that used in other experiments characterizing fluid inclusions. Given the strong evidence of equilibrium, the compositions of quartz-hosted fluid inclusions and run product glass samples are inferred to yield accurate partition coefficients for copper at magmatic conditions. The data presented are in agreement with the general trends reported by other experimental studies of copper partitioning in sulfur-bearing MVPs, at least at low X_{CO2}. First, the preference of sulfur species for the magmatic vapor is hypothesized to correspond to a preference of sulfur-bearing copper complexes for the magmatic vapor (Zajacz et al., 2011). The

reported decrease in $D_{Cu}^{b/v}$ from (25±7) to (11±3) for sulfur-free and pyrrhotite-saturated

experiments at X_{CO2} = 0.10 is in general agreement with the $D_{Cu}^{b/v}$ values reported by

Simon et al. (2006) (5 ± 1; salinity adjusted) and Frank et al. (2011) (7 ± 3) for CO_2-free

experiments at similar fS_2 and magmatic conditions, correcting for salinity (Figure 20).

In all three sets of experiments the Na/K ratio is ~ 1, supporting the consistency in

reported partition coefficients. Frank et al. (2011) reports additional experiments at log

fS_2 = -1.5 with a Na/K ratio ~ 2 which produced a higher $D_{Cu}^{b/v}$ = 17 ± 11. Zajacz et al.

(2011) demonstrated that the solubility of sulfur-bearing copper complexes at 1000 ^{o}C is

affected by the stabilizing cation, with K^{+} having a stronger stabilizing effect than Na^{+}.

This difference in stability of sulfur-bearing copper complexes may explain the change in

$D_{Cu}^{b/v}$ observed at a different Na/K ratio. Frank et al. (2011) also reports a $D_{Cu}^{b/v}$ = 95±5 at

log fS_2 = -4, significantly higher than is observed in the sulfur-free experiments

described in Chapter 2. It remains unclear why such strong preference for brine/vapor

was observed in these experiments compared to sulfur-free experiments of Simon et al.

(2006) and this study.
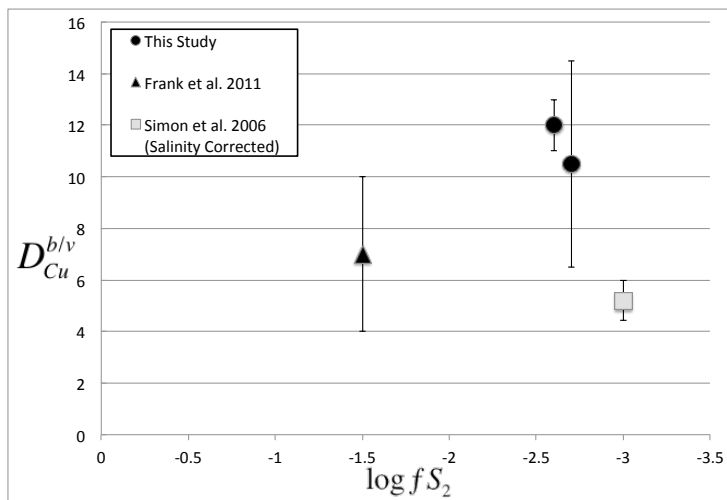
Figure 20: $D_{Cu}^{b/v}$ partition coefficients for pyrrhotite-saturated experiments at magmatic conditions (800 ^{o}C and 100MPa-This study and Frank et al. 2011; 140 MPa, Simon et al. 2006). Data from Simon et al. (2006) was adjusted for the difference in the NaCl-H_2O solvus at 100 and 140 MPa (Noted as *salinity corrected* on diagram). Frank et al. (2011) also reports $D_{Cu}^{b/v}$ = 95±5 at log fS_2=-4, significantly higher than experiments in this study.

The magnitude of enrichment of magmatic vapor in copper is consistent with the solubility observations and thermodynamic models presented by Zajacz et al. (2011). They report an increase in copper concentration with the addition of sulfur (fH$_2$S ~ 10 MPa) from ~175 ppm to 300±50 ppm copper and ~125 ppm to 636±100 ppm copper for NaCl-bearing and KCl-bearing volatile phases, respectively. Although measured at 1000 ^{o}C rather than 800 ^{o}C, these data show that an increase of two to five times the copper concentration of similar sulfur-free vapors can be expected with the addition of H$_2$S to the magmatic vapor. The lower temperatures of my experiments and some enrichment of the brine in copper with the addition of sulfur will slightly increase $D_{Cu}^{b/v}$. However, a decrease by factor of 2 to 3 observed in experiments at X$_{CO2}$ = 0.10 and the CO$_2$-free experiments of Simon et al. (2006) are consistent in the magnitude of vapor enrichment predicted. Yet the crux of the pyrrhotite-saturated, variable X$_{CO2}$ experiments lies in the observation of magmatic vapor less enriched in copper at high X$_{CO2}$, pointing to a suppression of sulfur-bearing copper complexes in the magmatic vapor.

3.5.4   Suppression of Sulfur-Bearing Copper Complexing in High-CO$_2$ MVPs

The salinity of magmatic vapor and brine change as the solvus expands with increasing X$_{CO2}$. This effect alone can significantly alter copper partitioning between the vapor, brine and silicate melt. As discussed, the addition of sulfur to experiments at X$_{CO2}$ = 0.10 yields more copper enriched vapors, lower $D_{Cu}^{b/v}$, and higher $D_{Cu}^{v/m}$. Comparison of $D_{Cu}^{b/v}$ at X$_{CO2}$ = 0.10 to CO$_2$-free experiments presented by Simon et al. (2006) is consistent with salinity dependent vapor-brine copper partitioning, adjusting for pyrrhotite-saturated vapor enrichment in copper relative to sulfur-free volatile phase

assemblages. The salinity dependent model is generated by adjusting the partition

coefficients reported by Simon et al. (2006) proportionally to the difference in the

brine/vapor salinity ratio at the conditions of that study to the conditions of the

experiments in this study. A salinity dependent curve can then be generated for $D_{Cu}^{b/v}$

proportionally to the brine/vapor salinity ratio as a function of X_{CO2}. The $D_{Cu}^{b/v}$ at $X_{CO2} =$

0.38 is well above this salinity dependent curve, indicating that the enrichment of sulfur-

bearing magmatic vapors in copper is suppressed by high concentrations of CO_2 (**Figure**

21).
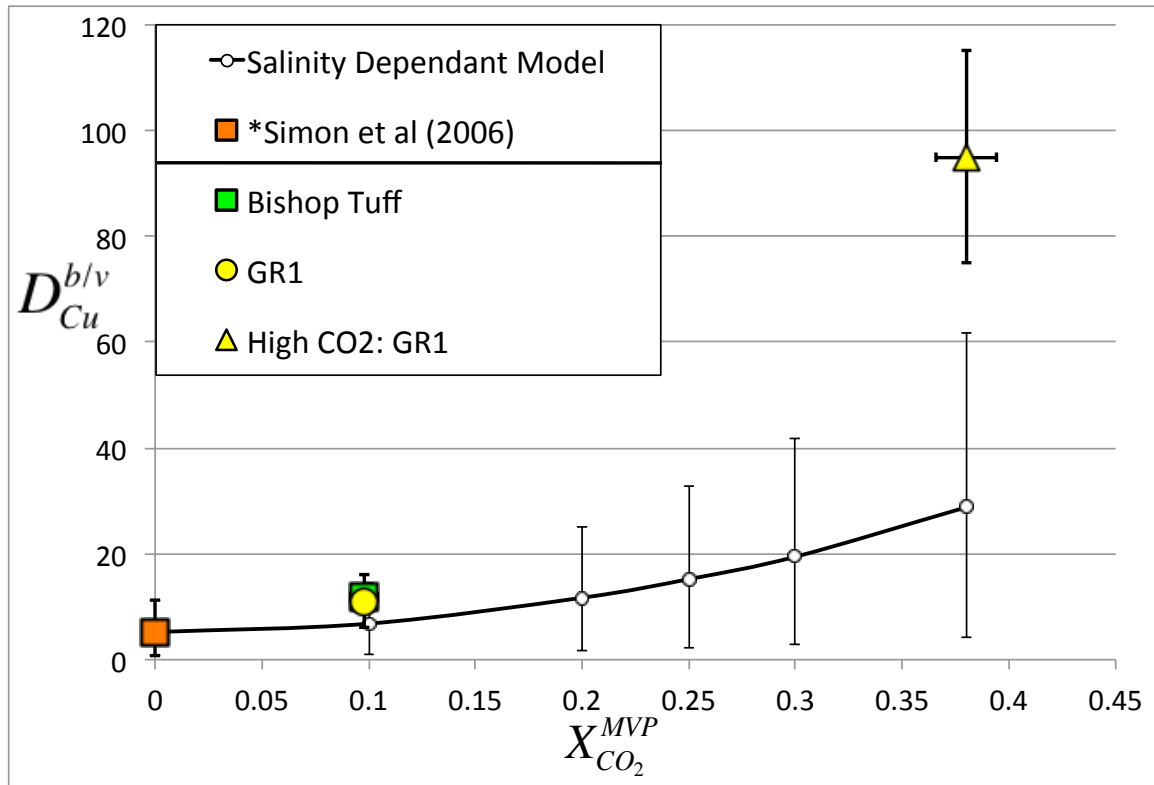
Figure 21: $D_{Cu}^{b/v}$ **plot for CO₂-bearing pyrrhotite-saturated MVP experiments. Bishop Tuff and GR1 experiments at X_{CO2} = 0.10 are the same within analytical uncertainty and are consistent with an enrichment of the magmatic vapor in copper with the addition of sulfur. The low-CO₂ experiments are also consistent with a salinity dependent extrapolation of Simon et al. (2006) data for CO₂-free experiments. GR1 experiments at X_{CO2} = 0.38 do not show an enrichment of copper in the vapor relative to sulfur-free, high-CO₂ experiments described in Chapter 2 and fall above the salinity dependent model.**

172

I consider a number of mechanisms for the suppression of copper enrichment in magmatic vapors with increasing X_{CO2}. These include changes in salinity, changes in relevant fugacities (e.g. fH_2O, fS_2, fH_2S, $fHCl$), or changes in physical characteristics of the magmatic vapor (e.g. polarity, dielectric potential). Zajacz et al. (2011) presents thermodynamic models for the chloride and hydrogen sulfide complexes which are likely stable at magmatic conditions (Table 14).

Chloride
$$CuCl \ < \ HClCuCl \ < \ (Na)^+[CuCl_2^-] \ < \ (K)^+[CuCl_2^-]$$

Bisulfide
$$CuSH \ < \ H_2SCuHS \ < \ (Na)^+[Cu(HS)_2^-] \ < \ (K)^+[Cu(HS)_2^-]$$
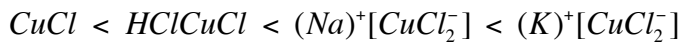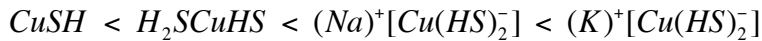
Mixed Chloride – Bisulfide
$$H_2ClCuHS \ < \ (Na)^+[CuHSCl^-] \ < \ (K)^+[CuHSCl^-]$$

Table 14: List of copper complexes predicted by quantum thermodynamic calculations presented by Zajacz et al. (2011). Species in brackets are ion pairs, coordinated with either Na$^+$ or K$^+$ ions to form the stable complex. Each group of complexes is shown in order of increasing predicted stability.

The chloride-only complexes (Table 14) are those that would complex copper at very low fS_2, and their relative stability is a function of the H/Na/K ratio with a maximum near a Na+K/H ratio of 1, in agreement with other magmatic experiments (Simon et al., 2006; Williams et al., 1995). The primary effect of increasing X_{CO2} is a change in the salinity of coexisting vapor and brine, which controls copper partitioning by altering the concentration of these complexes in the MVPs. The presence of sulfur in the magmatic vapor generates a number of stable copper complexes which all include one HS$^-$ ligand and either HCl or H$_2$S, or complexes with either Cl$^-$ or HS$^-$ with a stabilizing Na$^+$ or K$^+$ ion (Table 14). The statistical model presented by Zajacz et al. (2011) notes

that the most stable sulfur-bearing copper complexes are those which include an electrostatically bound Na^+ or K^+ ion.

The reduction in vapor salinity with increasing X_{CO2} is one factor in the suppression of sulfur-bearing copper complexation. The total salinity of the brine-saturated vapor at $X_{CO2} = 0.38$ is ~ 0.15 molar, significantly lower than the range investigated by Zajacz et al. (2011) (0.5 molar). Thus, one explanation for the suppression of sulfur-bearing copper complexation is that the salinity of the high-CO_2 vapors falls below a critical threshold for significant sulfur-bearing copper complexation. The lower $f H_2O$ at $X_{CO2} = 0.38$ will also reduce the $f H_2S$ in the magmatic vapor (Johnson et al., 1992; Ohmoto and Kerrick, 1977). However, no critical threshold for $f H_2S$ is predicted in the statistical model. The agreement between copper partition coefficients for sulfur-free and pyrrhotite-saturated experiments at high-CO_2 points to a suppression of sulfur-bearing copper complexation, rather than simply a decrease in $f H_2S$.

The reduction in salinity and $f H_2S$ will reduce copper complexation, but the consistency of copper partitioning at high X_{CO2} independent of the presence of sulfur suggests that the mechanism for suppression of the sulfur-bearing complexes may also include a fundamental change in magmatic vapor at high X_{CO2}. The most likely candidate for a change to the properties of the magmatic vapor is its polar character. Studies of ore-metal complexing at sub-solidus conditions discuss the effect of polar and non-polar character on the stability of metal complexes (Pokrovski et al., 2008; Pokrovski et al., 2009a; Pokrovski et al., 2009b). The statistical model presented by Zajacz et al. (2011) predicts that the bi-sulfur copper complexes all have a significant deviation in the S-Cu-S

bonding angle from 180°. Combined with the natural polarity of HS^- ligands, the result is that the S-Cu-S complexes will have a strong, complex polar character. The high concentration of non-polar CO_2 at $X_{CO2} = 0.38$ may be sufficient to change the polar character of the magmatic vapor and destabilize the S-Cu-S complexes, which already have a reduced solubility due to low-salinity and fH$_2$S. Unfortunately, without further thermodynamic modeling of both H_2O/CO_2 volatile phase mixtures, and metal complex solubility in those mixtures, the role of each of these causes in the suppression of sulfur-bearing copper complexation remains unclear.

3.5.5   *Copper Removal from the Melt into CO$_2$-Sulfur-Bearing MVPs*

The modified CO_2-MVPart evaluates the effect of CO_2 on the efficiency of removal of copper from the melt into exsolving vapor ± brine in an evolving magma chamber. The model evaluate changes in efficiency of removal of copper into volatile phases via chlorine-complexation, as MVPs exsolve under fixed H_2O/CO_2 ratio conditions. The data presented in this chapter on copper partitioning in CO_2 and sulfur-bearing melt-volatile phase assemblages demonstrates that magmatic sulfur-bearing copper complexation is suppressed by high X_{CO2}. The increased copper partitioning into the magmatic vapor with the addition of sulfur at low X_{CO2} is not observed for high-CO_2 melt-volatile phase assemblages.

The suppression of sulfur complexation at high-X_{CO2} is in contrast to the increase in copper partitioning into the MVPs observed in low-CO_2 melt-volatile phase assemblages. The geologic implications of this contrast will be founded on changes to the predicted efficiency of removal of copper into vapor ± brine. The experiments were conducted at static, sulfide-saturated conditions to fix fS$_2$. However, the variations in the

sulfur concentration of magmatic phases and the budget of sulfur in an evolving magma are quite complex to try and model, and beyond the scope of this study. Accordingly, I will discuss qualitative modifications to the sulfur-free CO_2-MVPart model based upon the copper partition coefficients from pyrrhotite-saturated experiments. These modifications address the impact of variable sulfur complex stability on the efficiency of removal of copper into MVPs in evolving magmas.

The CO_2-MVPart model relies on new functions for water saturation, water fugacity, and coexisting vapor/brine salinities dependent on a fixed X_{CO2} of the magmatic vapor at vapor saturation. The presence of sulfur as a minor component of melt-volatile phase assemblages is not expected to significantly modify the bulk composition or phase relationships. Thus, no modifications should be required for these primary CO_2-sensitive variables of the CO_2-MVPart model. Candela and Piccoli (1998) discuss that the initial water concentration of the melt has a strong influence on the efficiency of removal of copper into exsolved volatile phases. Water-poor melts lose more copper to crystallization, prior to volatile phase saturation, lowering the efficiency of removal of copper into exsolved volatile phases. Melts with high Cl/H_2O ratios have a high potential for deposit formation, and the highest efficiencies of removal of copper into MVPs predicted by the CO_2-MVPart model. Systems with high Cl/H_2O ratios are also predicted to have peak efficiencies of removal of copper into MVPs for low, but non-zero, X_{CO2}, with a sharp decrease in predicted efficiency at high X_{CO2} (Figure 22).

The efficiency of removal of copper into vapor + brine mixtures is increased at low concentrations of CO_2 due to vapor saturation at smaller degrees of crystallization. At high concentrations of CO_2 ($X_{CO2} > 0.24$) the efficiencies of removal of copper into

vapor + brine mixtures are slightly lower. The magmatic vapor alone will have slightly higher efficiency of removal of copper from the melt at low X_{CO2}. At high X_{CO2} the stability of coexisting brine reduces the efficiency of removal of copper into the vapor due to strong partitioning of copper into the high-salinity brine.
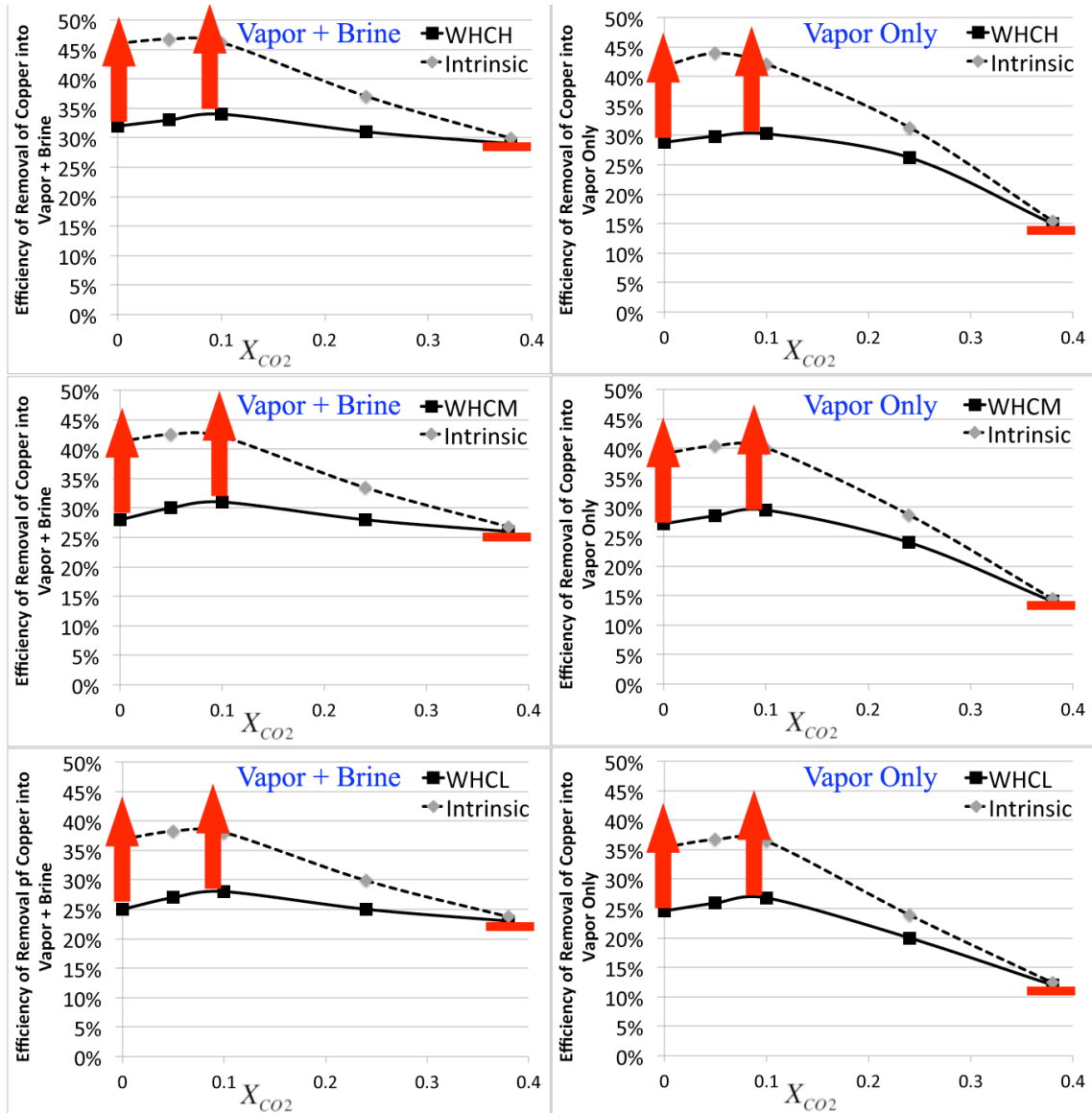

Figure 22: Plots showing results from the CO$_2$-MVPart Model for efficiency of removal of copper into vapor + brine (left), and vapor only (right) and qualitative shifts expected with the addition of sulfur (Red symbols): Model conditions are divided into groups base on water concentration and chlorine concentration; high (H), moderate (M), and low (L) with Cl/H$_2$O ratios shown in parentheses.

The degree of crystallization at volatile phase exsolution will not be affected by the addition of sulfur as a system component. However, the CO_2-MVPart model assumes that the vapor will extract copper proportionally to the partitioning of chlorine with the silicate melt (salinity dependent model). Copper partitioning into the vapor relative to the silicate melt increases ($D_{Cu}^{v/m}$ increases by a factor of 2 to 3) for sulfur-bearing systems, relative to sulfur-free systems. Thus, the efficiency of removal of copper into low-CO_2 sulfur-bearing systems will be higher than predicted for a sulfur-free system (shown by the red arrows at low X_{CO2} in Figure 22). The increase in efficiency of removal of copper into exsolving volatile phase(s) at low X_{CO2} will apply to the vapor, with or without the contribution of any brine exsolved. The change in the value of $D_{Cu}^{v/m}$ is correlated with an increase in the apparent equilibrium constant for the exchange of copper and sodium between the vapor and silicate melt ($K_{Cu,Na}^{v/m}$ increases from 30±19 to 95±40) for metaluminous to peralkaline experiments. The large change in the apparent equilibrium constant supports the conclusion that the change in copper partitioning is a function of a change in complexation. In contrast, no increase in the vapor-melt copper partition coefficient ($D_{Cu}^{v/m}$ = 1.9±0.6 and 2.0±0.8) or the apparent equilibrium constant ($K_{Cu,Na}^{v/m}$ =26±17 and 27±12) was observed with the addition of sulfur for high-CO_2 experiments. This is consistent with the suppression of sulfur-bearing complexing of copper at high X_{CO2}, and minimal chlorine complexing of copper in the low-salinity vapor for sulfur-free or sulfur-bearing systems. Thus, no increase in the efficiency of removal of copper into MVPs is predicted with the addition of sulfur as a component of high-CO_2 melt-volatile phase assemblages (red bar shown in Figure 22). This will exaggerate the

decrease in the efficiency of removal of copper into exsolving magmatic volatile phases for sulfur-bearing systems with increasing X_{CO2}.

The lack of significant sulfur complexing of copper in the vapor (and potentially the brine) will result in low efficiency of removal of copper into high-CO_2 vapor, or vapor + brine mixtures. As a result, the efficiency of removal of copper into sulfur-bearing MVPs is predicted to decrease with increasing X_{CO2} for the exsolution of *either* magmatic vapor only or vapor + brine mixtures. Furthermore, the peak efficiency of removal of copper into sulfur-bearing MVPs at will still occur at low X_{CO2}. The trends for the intrinsic efficiency (E^I) will be affected similarly with the addition of sulfur. The intrinsic efficiency of removal of copper into MVPs will also decrease with increasing X_{CO2} for sulfur-bearing vapors, or vapor + brine mixtures compared to sulfur-free systems.

3.5.6   *Geologic Implications of Copper Removal into Sulfur-CO_2-Bearing MVPs*

The goal of the pyrrhotite-saturated, CO_2-bearing experiments was to evaluate the potential for the formation of porphyry copper deposits as a function of the X_{CO2} of the volatile phase(s) extracting copper from the melt. The data from the sulfur-free experiments allow for expansion of the model for chloride-complexed copper removal from the melt into MVPs during second boiling presented by Candela and Piccoli (1998). The observations from sulfur-bearing experiments include an increase in copper partitioning into the vapor with the addition of sulfur at low X_{CO2} and suppression of sulfur-bearing copper complexation at high X_{CO2}. The increase in the efficiency of removal of copper into MVPs with the addition of sulfur predicted at low X_{CO2} is generally consistent with the results of recent CO_2-free sulfur-bearing experiments (Frank

179

et al., 2011; Lerchbaumer and Audetat, 2009; Simon et al., 2006; Zajacz et al., 2011). The presence of low concentrations of CO_2 in sulfur-bearing systems may also increase the efficiency of removal of copper into exsolved vapor, or vapor ± brine mixtures, relative to CO_2-free volatile phase exsolution. However, the suppression of copper enrichment for sulfur-bearing magmatic vapors at high X_{CO2} suggests a negative influence of high concentrations of CO_2 on the potential for PCD formation.

The exsolution of a high-CO_2 vapor phase will dramatically lower the efficiency of removal of copper into the vapor compared to exsolution of low-CO_2 vapors (> 30% efficiency to as low as 15% efficiency)(Figure 22). Thus, high concentrations of CO_2 will reduce the potential for deposit formation proportionally to the duration of exsolution of high-CO_2 MVP(s). Even in the limiting case where all exsolved brine is ultimately transported and deposited with the copper removed by the vapor phase, the efficiency of removal of copper into sulfur-bearing vapor + brine mixtures is lower at high X_{CO2}. Furthermore, the suppression of sulfur-complexing in high-CO_2 systems suggests that the efficiency of removal of copper into supercritical fluids may also be reduced, corresponding to the X_{CO2} of the exsolved fluid. The modified predictions of the CO_2-MVPart model suggest that the apparent discrepancy between the CO_2 concentration range of porphyry copper deposits ($X_{CO2} = 0$ to 0.10) and the range for arc magmas in general ($X_{CO2} = 0$ to > 0.40) may result from the poisoning effect of high concentrations of CO_2 on efficiency of removal of copper into MVPs. To further address the implications of these results, the various mechanisms for addition of sulfur and CO_2 will be discussed, along with the applicability of these modeling results to the volatile phase exsolution processes likely to obtain in natural shallow arc systems.

Once evolved, arc magmas are emplaced at shallow depth, a strong thermal disequilibrium between magma and country rock is established. As the magma cools and crystallizes, the water concentration increases until volatile phase saturation, or second boiling, occurs. Numerous reviews of porphyry copper deposits support the hypothesis that volatile phases exsolved during second boiling can extract copper from the silicate melt and transport copper from the causative intrusions to the site(s) of ore mineral (e.g Cp, Bn) deposition (John et al., 2010; Sillitoe, 2010; Sinclair, 2007). The CO_2-MVPart model predictions for sulfur-bearing systems highlight the strong influence of CO_2 on the efficiency of removal of copper into these proto-ore fluids.

The presence of CO_2 as a dissolved component of the felsic silicate melt is limited by the initial H_2O/CO_2 ratio of arc magmas, and the limited solubility of CO_2 at shallow depths. The concentration of CO_2 dissolved in the silicate melt is limited to < 1000 ppm and as a result, the exsolution of volatile phases with a high X_{CO2} will quickly deplete the melt in dissolved CO_2. Thus, the lower efficiency of removal of copper into MVPs at high X_{CO2} predicted by the CO_2-MVPart model will only affect the early exsolved fluids in systems with CO_2 dissolved in the shallow felsic melt as the only CO_2 source. However, other sources of CO_2 can buffer the X_{CO2} at elevated levels.

Andesitic melts generated in the lower crust can contain high concentrations of dissolved H_2O and CO_2. Annen et al. (2006) estimate that these deep derived melts can have initial H_2O concentrations between 5 to 15 wt%. The basaltic and andesitic melts in the lower crust are generated by slab derived volatile phase fluxes with X_{CO2} values as high as 20 mol% (Jarrard, 2003). For melts with 2 to 16 wt% H_2O this would translate to approximately 0.8 to 2.4 wt% CO_2. The solubility limit for CO_2 in mafic melts at 1 GPa

is on the order of 1 wt% and as a result, some mafic melts initially emplaced into the lower mantle may exsolve a nearly pure CO_2 (~95 mol% CO_2) volatile phase(s) at depth (Botcharnikov et al., 2005; Lowenstern, 2001). The solubility of CO_2 in andesitic melts generated at ~30 km is significantly lower (maximum ~ 4000 ppm CO_2) than for mafic melts, although the solubility increases by a factor of two (maximum ~ 8000 ppm CO_2) upon ascent to ~15 km (Botcharnikov et al., 2005). The additional CO_2 and sulfur can be added to shallow felsic melts during direct injection of these melts into existing shallow magma chambers, or as CO_2-rich bubbles exsolved from the more mafic melts titrate into shallower parts the system (Annen et al., 2006; Behrens et al., 2004; Botcharnikov et al., 2005; Hattori and Keith, 2001; John et al., 2010; Lowenstern, 2001; Proffett, 2003). Thus, mafic and andesitic magmas, containing up to 8 to 10 times higher concentrations of CO_2 than shallow melts, can greatly increase the budget of CO_2 and sulfur for melt-volatile phase equilibria.

Shallow felsic magmas that are recharged by injection of mafic or andesitic magmas may undergo protracted exsolution of CO_2-rich volatile phases, and as a result would have lower efficiencies of removal of copper into the MVPs. The poisoning effect CO_2 derived from mafic melts is in contrast to the importance of mafic melts in contributing sulfur to previously emplaced felsic melts. Injection of mafic melts may contribute >50% of the ore forming sulfur in some large PCD (Hattori and Keith, 2001; Simon and Ripley, 2011). Thus, models for the effect of mafic recharge must balance the benefit to copper removal at higher fS_2 with the poisoning effect of high X_{CO2}.

Andesitic melts generated at depth may begin ascent at supra-liquidus conditions and resorb entrained sulfur phases (e.g. sulfides or sulfide melts) during ascent (Annen et

al., 2006). Such melts would also exsolve volatile phases with high-sulfur concentrations and/or contribute large amounts of sulfur to existing melts as shallow depths. The exsolution of MVPs from rising andesitic melts will have the same potential drawback to addition of CO_2 as MVPs derived from mafic melts. The sulfur concentration of shallow melts and exsolving MVPs have a strong influence on copper partitioning. As a result, the addition of less evolved melts or associated exsolved volatile phases could either increase or decrease the efficiency of removal of copper into the MVPs. In order for magma recharge to increase potential for formation of PCD, the concentration or rate of addition of CO_2 by magma recharge must remain low.

The strong decrease in the efficiency of removal of copper into sulfur-bearing MVPs at high X_{CO2} supports a causative link between the observations of only low concentrations of CO_2 in porphyry copper deposits. In addition, the range of X_{CO2} at peak efficiency predicted by the CO_2-MVpart model (X_{CO2} = 0 to 0.10) does closely match that observed in porphyry copper deposits. The CO_2-MVPart model does not directly model the evolution of the CO_2 and sulfur concentrations in magmas. However, the sulfur-bearing copper partitioning data and CO_2-MVPart model can predict the general trends for efficiency of removal of copper into the MVPs when comparing exsolution of low-CO_2 and high-CO_2 volatile phases. The presence of sulfur will increase the copper removed by MVPs at low X_{CO2} (0 to 0.10), but the poisoning effect of high concentrations of CO_2 (> 0.24) will hinder copper removal by MVPs, and greatly reduce the potential for the formation of porphyry copper deposits.

Chapter 4: Project Conclusions and Summary

4.1   Experiment Design and Magmatic Vapor Phase Salinity

Understanding the role of CO_2 in the partitioning of copper between melt and volatile phases in both sulfur-free and sulfur-bearing systems is critical to the modeling of copper removal from magmas into proto-ore fluids. New experimental methods, as well as innovations in microthermometry and modeling, were developed and implemented as part of this project to allow for investigating these complex systems. The in-situ fracturing technique of Sterner and Bodnar (1991) allowed for the fracturing of quartz at magmatic conditions during experiments. This ensured that the volatile phases sampled by the fluid inclusions reached fO_2 equilibrium prior to entrapment. In-situ fracturing is crucial for CO_2-bearing experiments that use oxalic acid due to the excess hydrogen generated during oxalic acid decomposition. The addition of CO_2 to the NaCl-H_2O system is modeled to result in an expansion of the vapor-brine solvus with increasing X_{CO2} (Duan et al., 1995). The measured salinity of the brine increased from ~62 wt% to ~71 wt% $NaCl_{eq}$ at X_{CO2} (vapor) = 0.10 and to ~ 80 wt% $NaCl_{eq}$ at X_{CO2} (vapor) = 0.38, consistent with the model presented by Duan et al. (1995) at 800 ^{o}C and 100 MPa.

Trapping the vapor phase with either X_{CO2} = 0.10 or 0.38 resulted in vapor-rich inclusions that nucleate clathrate upon cooling. This prevented accurate determination of salinity from ice melting temperatures (a common method for similar CO_2-free experiments). Calculation of the salinity of the brine-saturated vapor required accurate measurement of fluid inclusion pressure and modeling of the stability boundary of the clathrate that forms from the cooling H_2O-CO_2 ± H_2S liquid-vapor mixture present at

ambient conditions. The calculation of the pressure of vapor-rich fluid inclusions containing CO_2 vapor without CO_2 liquid was imprecise, and was based on observables such as rough estimations of inclusion bubble volume. The method developed by Fall et al. (2011), with my assistance, allows for direct, non-destructive determination of the pressure of fluid inclusions that contain CO_2 vapor (Appendix V). This method for CO_2 pressure determination by Raman Spectroscopy was successfully used to characterize the salinity of a subset of vapor inclusions from all of the sulfur-free experiments presented in this study. The measured salinity of the vapor decreased from ~3.5 wt% $NaCl_{eq}$ to ~1 wt% $NaCl_{eq}$ for $X_{CO2} = 0.10$ and 0.38, respectively, which is also consistent with Duan et al. (1995). However, the presence of H_2S in vapor inclusions from pyrrhotite-saturated experiments requires further modifications to this method for characterizing inclusion salinity.

The presence of H_2S in vapor inclusions from pyrrhotite-saturated experiments results in a significant deviation in the stability of clathrate formed upon cooling. However, the stability of the mixed clathrate formed from CO_2-H_2S mixtures at low X_{H2S} can be approximated by the ideal mixing between the two end-members and the CO_2/H_2S ratio of each inclusion (Diamond, 1994; Sloan and Koh, 2008). A correction factor of 1 ^{o}C ($X_{CO2} = 0.10$) and 0.5 ^{o}C ($X_{CO2} = 0.38$) in the T_m^{Clath} can be used to account for the presence of H_2S in the inclusions formed from the sulfur-bearing experiments described in this study. However, this difference in temperature corresponds to an error in calculated salinity of several weight percent. This would result in errors in calculated partition coefficients ranging from 30 to 50% if the effect of H_2S on the stability of clathrate was ignored.

4.2   Copper Partition Coefficients and Equilibrium Constants

The partitioning of copper among coexisting vapor, brine and silicate melt exerts a significant control on the extraction of copper in systems where magmas exsolve vapor ± brine. Changes in copper partitioning in sulfur-bearing systems with increasing CO_2 were used to evaluate the effect of CO_2 on copper removal from the melt into sulfur-bearing MVPs using the modified CO_2-MVPart model. The shift in the partitioning of copper due to CO_2 that was observed in the case of the sulfur-free experiments is directly proportional to the change in the salinity of the coexisting vapor and brine with increasing X_{CO2}; extrapolation of these results to $X_{CO2} = 0$ yields partition coefficients that are consistent with the CO_2-free, sulfur-free data presented by Simon et al. (2006) (Figure 23). The consistency of the data with the salinity dependent model confirms the hypothesis that the dominant effect of CO_2 on sulfur-free vapor-brine copper partitioning is a change in salinity.
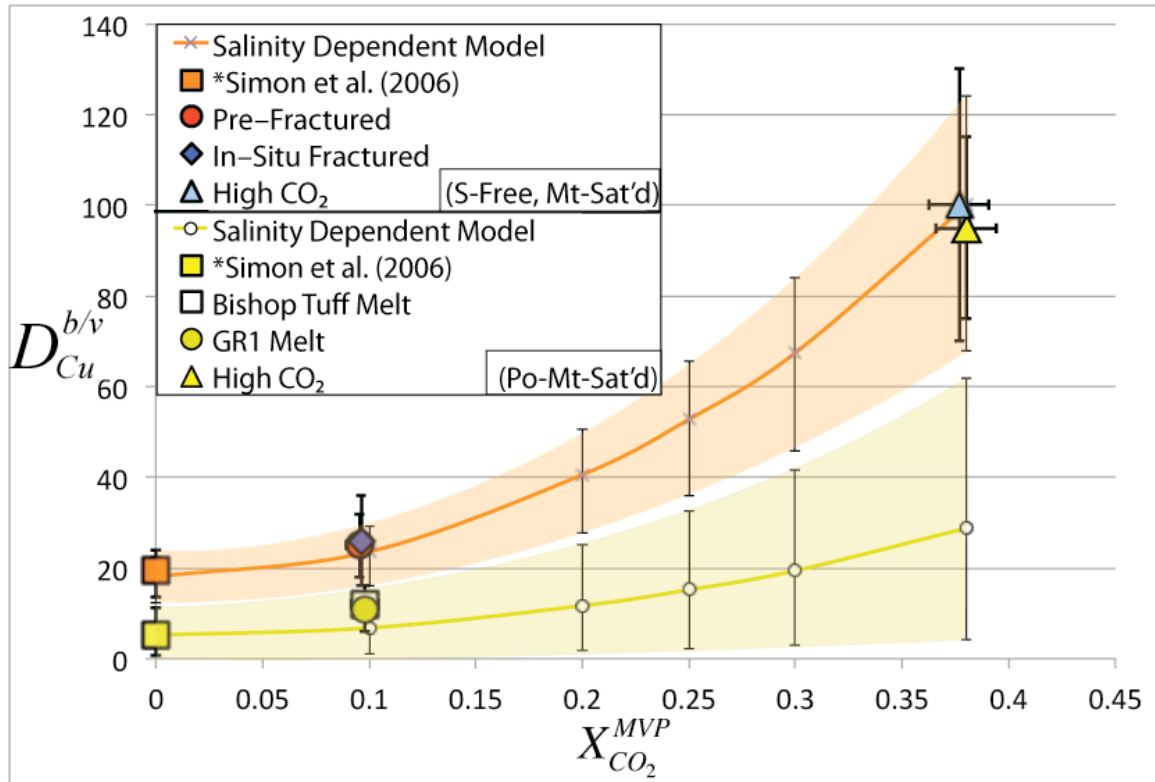
Figure 23: Plot of copper partition coefficients between sulfur-free (orange and blue) and pyrrhotite-saturated (yellow) coexisting brine and vapor as a function of the X_{CO2} in the bulk volatile phase composition. Salinity dependent extrapolation of data presented by Simon et al. (2006) (corrected for differences in vapor-brine solvus at their run pressure of 140 MPa compared to 100 MPa from this study) are shown for sulfur-free and pyrrhotite-saturated conditions. Salinity dependent extrapolation is made based on calculated salinities and model predictions of Duan et al (1995).

The decrease in $D_{Cu}^{b/v}$ for pyrrhotite-saturated experiments at $X_{CO2} = 0.10$

compared to sulfur-free experiments (Figure 23) is primarily a function of an increase in

the copper concentration of the magmatic vapor with the addition of sulfur. This is

confirmed by an increase in copper partitioning into the magmatic vapor relative to the

silicate melt. Sulfur-bearing vapors are enriched in copper by a factor of 2 to 3 relative to

sulfur-free vapors at low X_{CO2}. The copper partition coefficients presented for low-CO_2

experiments are consistent with a salinity-dependent extrapolation of the data presented

by Frank et al. (2011) and Simon et al. (2006) (Figure 23). This comparison demonstrates

that the magnitude of the enrichment of the vapor relative to the brine is also consistent

with pyrrhotite-saturated experiments presented by Simon et al. (2006) compared to sulfur-free experiments from the same study (Figure 23).

In contrast, copper partitioning observed between pyrrhotite-saturated coexisting brine and vapor at $X_{CO2} = 0.38$ is the same as that of sulfur-free experiments. This demonstrates a noted lack of enrichment of the magmatic vapor in copper with the addition of sulfur for high-CO_2 volatile phase assemblages, and a deviation from a salinity dependent enrichment model (Figure 23). The lack of enrichment is also observed in the partitioning of copper between the vapor and silicate melt. The enhancement of copper partitioning into the vapor by sulfur is suppressed for high-CO_2 magmatic volatile phase assemblages. This observed effect is consistent with my general conclusion that the efficiency of removal of copper into magmatic vapor is reduced with increasing X_{CO2}.

No significant variation in Cu-Na exchange between vapor and melt is observed for sulfur-free experiments with increasing X_{CO2} ($K_{Cu,Na}^{v/m}$ = 30 ± 19 and 26 ± 17 at X_{CO2} = 0.10 and 0.38, respectively). This is consistent with salinity dependent variation in vapor-melt copper partitioning as a function of X_{CO2}, which does not affect Cu-Na exchange. However, copper partitioning between the vapor and silicate melt for sulfur-bearing experiments is not simply salinity dependent. The strongest copper partitioning into the vapor relative to the silicate melt is observed for low-CO_2, HCl-bearing, sulfur-bearing experiments ($D_{Cu}^{v/m}$ = 30 ± 11). These experiments also have the highest apparent equilibrium constant for Cu-Na exchange between the vapor and silicate melt ($K_{Cu,Na}^{v/m}$ = 95 ± 40). The concentration of the $CuO_{0.5}$ and Na_2O components of the silicate melt, are not hypothesized to be affected by the presence of sulfur or CO_2. However, the presence

of sulfur-bearing copper complexes in the vapor with sodium (e.g. $Na^+[CuHSCl]^-$,

$Na^+[Cu(HS)_2]^-$), and without sodium (e.g. $CuHClHS$, CuH_2SHS) increases copper

partitioning without a corresponding change in sodium, increasing the $K_{Cu,Na}^{v/m}$. Peralkaline

melts that exsolve fluids at low X_{CO2} will be HCl-free, and should not produce sulfur-

bearing copper complexes stabilized by H^+. However, the presence of additional sodium-

sulfur-bearing complexes and more stable potassium-sulfur complexes will still increase

copper relative to sodium in the vapor relative to sulfur-free conditions, consistent with

the observed Cu-Na exchange constant ($K_{Cu,Na}^{v/m} = 45 \pm 21$).

No increase in copper partitioning into the vapor relative to the silicate melt is

observed for high-CO_2 experiments. The exchange of copper and sodium between the

vapor and melt for sulfur-bearing experiments likewise remains the same as for sulfur-

free experiments at high X_{CO2} ($K_{Cu,Na}^{v/m} = 27 \pm 12$). This variability in the apparent Cu-Na

exchange constant supports the conclusion that sulfur-bearing copper and sodium

complexes will increase efficiency of removal of copper into the MVPs at low X_{CO2},

which will be suppressed at high X_{CO2}. This is in contrast to the increase in copper

partitioning into magmatic vapors otherwise observed with the addition of sulfur (Frank

et al., 2011; Lerchbaumer and Audetat, 2009; Simon et al., 2006; Zajacz et al., 2011).

The presence or suppression of sulfur-bearing copper complexation has important

implications for the results of the CO_2-MVPart model and the potential for the formation

of PCD by CO_2-bearing magmatic volatile phases. In addition to increasing our

understanding of copper in the porphyry environment these experiments are nearly all

saturated with gold. As a result, I will also be able to generate similar data for furutre

publications to address the effect of CO_2 on gold partitioning among vapor, brine and silicate melt.

4.3 Efficiency of Removal of Copper into MVPs and Geologic Implications

The experimental results presented in this study describe the static, equilibrium partitioning of copper in both sulfur-bearing and sulfur-free melt-vapor-brine systems with variable X_{CO2}. Modeling of the exsolution of magmatic volatile phases that incorporate these data allow for the implications of the data for dynamic exsolution of volatile phase(s) to be brought to light. These models describe the possible variations in the efficiency of removal of copper into MVPs as a function of select variables, under conditions similar to those hypothesized for second boiling in shallow arc magmas.

The CO_2-MVPart model predicts a progressive decrease in the efficiency by which copper can be extracted from a crystallizing silicate melt with increasing X_{CO2} for sulfur-free conditions. The decrease in the efficiency of removal of copper into vapor + brine mixtures with increasing X_{CO2} is minor (~5%) for sulfur-free systems. However, as the contribution of the copper removed by the brine decreases, the potential for the formation of PCD will increasingly rely on the efficiency of removal of copper into the vapor alone. The poisoning effect of CO_2 is more pronounced for copper removed by magmatic vapor alone. Lower chlorine partitioning and early brine saturation can both decrease the efficiency of removal of copper into high-CO_2 vapors.

The copper partition coefficients and apparent equilibrium constants for sulfur-bearing experiments demonstrate that the efficiency of removal of copper into sulfur-bearing magmatic volatile phases will not vary simply according to changes in salinity with increasing X_{CO2}. The increase in copper partitioning into the vapor relative to the

silicate melt observed at low X_{CO2} in sulfur-bearing experiments would result in an increase in the efficiency of removal of copper into vapor at low X_{CO2} compared to chlorine-only copper partitioning.

The efficiency of removal of copper into magmatic volatile phases at high X_{CO2} is not predicted to change with the addition of sulfur. The apparent suppression of sulfur-complexing at high concentrations of CO_2 requires that the efficiencies of removal of copper into either the vapor, or vapor + brine mixtures remain low. The incorporation of these adjustments to the CO_2-MVPart model predictions suggests that the high efficiency of removal of copper from the melt into water-rich, chlorine-rich, sulfur-bearing magmatic vapors may be reduced by a factor of three or more for exsolution of vapors at high concentrations of CO_2. Even if the magmatic brine contributes to the copper removal, magmatic volatile phases with high X_{CO2} will have a lower efficiency (up to 10% lower) compared to low-CO_2 systems. Interestingly, the efficiency of removal of copper into exsolving vapor, or vapor + brine mixtures, is highest (i.e. achieves peak efficiency) at X_{CO2} values between 0 and 0.10 for either raw efficiency or intrinsic efficiency; the same as the range observed in PCD. The correlation between these model predictions and the limited range of X_{CO2} observed in natural deposits lends support to the potential poisoning effect of CO_2 on the efficiency of removal of copper into exsolving magmatic volatile phases and the potential for deposit formation.

APPENDICIES

Appendix I.   René Vessel fO_2: CoPd-CoO Sensor

The equilibrium fO_2 of the René 41 vessels used for the CO_2-bearing melt-vapor-brine experiments is used to set the fH_2 in the pressure fluid. Diffusion of H_2 across the Pt and Cu_6Au_{94} capsule walls then controls the fO_2 of the experiment, buffering it to a value near that of the vessel. The René 41 vessels are composed dominantly of Ni metal and thus, the equilibrium between Ni and NiO controls the fO_2 of the vessels once a layer of NiO forms on the inside of the vessels. However, as NiO forms Ni metal is removed from the metal alloy near the inner surface, slightly changing its composition. Over time this results in small changes to the fO_2 of René vessels. In order to characterize the fO_2 of the vessels used for the CO_2-bearing experiments, oxygen sensor experiments were conducted using a Co-Pd alloys similar to the technique described by Taylor et al. (1992). Two vessels were used for the CO_2-bearing experiments and each was tested independently for intrinsic oxygen fugacity.

In both experiments a platinum capsule was first lined with a layer of yttrium-stabilized zirconium oxide paper produced by Zircar Ceramics (ZrO_2 +Yt). A mixture of cobalt metal and palladium metal ($X_{Co} = 0.75$) is then pressed into a small pellet (~ 2mm diameter) and placed inside ZrO_2 lined capsule with a small cap of ZrO_2 (Figure 24). The oxide is stable to high temperatures (>1500 ^{o}C) and ensures that the Co-Pd alloy does not contract the platinum capsule. This mitigates the mixing of the two alloys, which could weaken the capsule integrity. Water is then added to the capsule (~100 µL) to allow for formation of cobalt oxide (CoO) at run temperature. The capsules were run at the same

conditions as the CO_2-bearing experiments (800 °C and 100 MPa) to determine the intrinsic fO_2 of the vessels during the CO_2-bearing experiments.
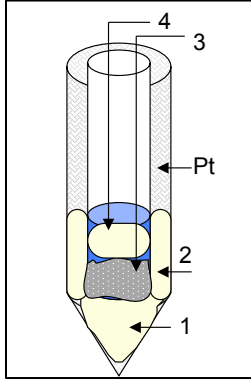

Figure 24: Schematic cross-section of Co-Pd oxygen sensor experiments. A platinum capsule (~ 1.5 mm length) was first lined with yttrium-stabilized ZrO_2 paper (1 and 2). A pellet of cobalt and palladium metal (X_{Co} = 0.75) was then placed in the ZrO_2 "cup" (3). A cap of ZrO_2 paper was then placed on top of the pellet (4) to ensure that the Co-Pd does not contact the platinum capsule. Approximately 100 µL of water was added to the charge before it was sealed to allow for oxidation of the cobalt and fO_2 equilibration.

Oxygen sensor experiments #1 and #2 both produced Co-Pd alloys mixed with large amounts of CoO, and showed no signs of contact between the Co-Pd and the platinum capsule. The metallic portion of the run products were then separated and mounted in epoxy and polished. The compositions of the run product alloys were then characterized by EPMA analysis. Three spots from at least three grains from each experiment were analyzed and then averaged to characterize the equilibrium metallic composition. The X_{Co} of the run products and the run temperature were then input into equation (37) below presented by Taylor et al. (1992) for the fO_2 of Co-Pd alloys in equilibrium with CoO.

$$\log fO_2(Co,Pd) = -2\log X_{Co} - 1/(2.303RT) \cdot$$
$$\left\langle (491649 - 508.527T + 122.6909T \log T - 0.02518T^2) + \right. \tag{37}$$
$$\left. \{2(1-X_{Co})2[-9.76T + 16445(4X_{Co}-1)]\}\right\rangle$$

The run product metal alloys from fO_2 sensor experiments #1 and #2 have average X_{Co} values of 0.270 ± 0.005 and 0.253 ± 0.005, respectively. These values correspond to intrinsic log fO_2 values of -13.70 ± 0.04 and -13.75 ± 0.04 for the two René vessels.

Appendix II.   Diffusion of Hydrogen Through Pt and Au Capsules

The use of oxalic acid to generate CO_2 in sealed hydrothermal experiments requires careful consideration of the impact of hydrogen generation on experiment fO_2 during oxalic acid decomposition. The hydrogen that is generated can produce an internal hydrogen fugacity (fH_2^i) out of equilibrium with the external hydrogen fugacity (fH_2^o) imposed by the vessel. Estimates of the vapor composition of a given experiment were obtained using the model presented by Duan et. al. (1995), which when combined with the mass of H_2 generated by oxalic acid decomposition, can be used to calculated the initial internal fH_2. This calculation utilizes fugacity coefficients based upon the model presented by Churakov et al. (2003). The time required to reach H_2 equilibrium was then estimated using an iterative diffusion calculation detailed below.

An instantaneous diffusion rate for H_2 through a Pt or Au capsule at run P and T, (dH_2/dt), can be obtained using the diffusion model presented by Chou (1987) and by evaluating the gradient between the imposed external fH_2 and an instantaneous internal fH_2. The diffusion equation (38) presented by Chou (1987) shown below

$$\frac{\partial n}{\partial t} = \frac{1}{2} \left\{ \frac{2\pi k l}{\ln\left(r_o / r_i\right)} \right\} \left[\left(\frac{n}{n+m}\right)^{1/2} \left(\Gamma * \gamma * P_T\right)^{1/2} - f_0^{1/2} \right] \tag{38}$$

can be simplified by grouping the material (Pt or Au) diffusion constants

$$\left\{ \frac{2\pi k l}{\ln\left(r_o / r_i\right)} \right\} = D_c \tag{39}$$

$$\left(\Gamma * \gamma * P_T\right) = C_f \tag{40}$$

and then expanded fugacity terms according to equations (39) and (40), respectively. The

material constants account for capsule dimensions (ro/ri = capsule radius [outer/inner], l=

length) and the diffusion constant for either Pt or Au (k = diffusion coefficient [Pt or Au :

temperature dependent]). The expanded fugacity terms (Γ = H_2 fugacity coefficient, γ =

H_2 activity coefficient, P_T = total pressure) are taken to be constant in order to simplify

the diffusion calculations. The fugacity coefficient for H_2, obtained from Churakov et al.

(2003), varies ~ 4% over the range of $f$$H_2$ in these experiments and both other terms

remain the same. The simplifying assumption of setting this coefficient to a constant

value results in a slight under-estimate of diffusion rate and over-estimate of diffusion

time.

 After simplifying the diffusion equation (38) according to equations (39) and (40)

the resulting equation characterizes the diffusion rate of H_2 out of the capsule. The

remaining variables are the external $f$$H_2$ (~ 0.33 MPa ~NNO), number of moles a H_2

remaining inside the capsule (n), and the total moles of the other vapor components (m-

H_2O, CO_2). The instantaneous diffusion rate was then calculated using Equation (41)

$$\frac{\partial n}{\partial t} = \frac{1}{2}\{Dc\}\left[\left(\frac{n}{n+m}\right)^{1/2}(C_f)^{1/2} - f_0^{1/2}\right] \tag{41}$$

to estimate the moles of H_2 lost by the capsule (Δn) during small time steps (e.g. 1 sec).

The new number of moles of H_2 (n) along with (m) were then reentered into the diffusion

equation and the new rate is applied for the next time step. Platinum capsule experiments

were predicted to required ~ 0.5 to 5 hours for the excess hydrogen to diffuse out,

whereas gold capsules would require ~ 4 to 40 hours for experiments with X_{CO2} = 0.10 to

0.38, respectively. These values correspond to > 99% agreement between the predicted

fH$_2$ inside the capsule and the intrinsic fH$_2$ of the René vessel. Copper metal is more permeable to hydrogen at the conditions of the experiments and thus, the Cu$_6$Au$_{94}$ alloy used in the CO$_2$-bearing experiments would likely require slightly less time for diffusion of the excess hydrogen. However, in the absence of an accurate diffusion constant for Cu-Au alloys, the slight over-estimate of diffusion predicted for gold capsules was used to ensure fO$_2$ equilibrium.

Appendix III.   Developing Methods for CO_2-Bearing Experiments

The addition of CO_2 to noble metal capsule experiments required a number of trials and failures before a working method was developed. This first challenge in developing the experiment design was choosing an appropriate CO_2 source. Previous experiments have utilizing oxalic acid and salts of oxalic acid (e.g. silver oxalate) to generate CO_2 (Sterner and Bodnar, 1991). However Kruger and Diamond (2001) discuss that fluid inclusions synthesized using silver oxalate demonstrated strange behavior during microthermometry.

The AgCl component of fluid inclusions must be high if significant mole fractions of CO_2 are desired when using silver oxalate as a CO_2 source. Kruger and Diamond (2001) reported inaccuracies and imprecision when determining clathrate melting temperatures for CO_2-bearing fluid inclusions, which likely resulted from limited solubility of AgCl at low temperatures ($< 10\ ^{o}C$). In order to avoid these problems, my first experiments were run with copper oxalate, because copper chlorides were already present in the starting aqueous solution. However, due to the high concentrations of CO_2 required for the experiments, copper concentrations became too high, affecting the major element (Na, K, Fe) chloride chemistry. The high concentration of copper raised questions of applicability to natural systems and solubility during the runs, and complicated the process of determining salinity from microthermometric measurements. The design of the experiments was then changed to include oxalic acid dihydrate as the CO_2 source.

The use of oxalic acid does not result in the same problems of adding undesired cations to experiments, but instead adds H_2 and H_2O in addition to CO_2 during

decomposition. The H_2O added to my experiments during decomposition did not present any problems due to the range of X_{CO2} examined (X_{CO2} = 0.10 to 0.38). The maximum X_{CO2} achievable using oxalic acid dehydrate is X_{CO2} = 0.5, due to the 1:1 ratio of CO_2 and H_2O produced during decomposition. However, significant adjustments were required to manage the production of H_2 during oxalic acid decomposition. As discussed in Appendix II, the fH_2 inside the noble metal capsule will drop over time to match the fH_2 imposed by the Ni-NiO buffer established by the René vessels. The rate at which the H_2 can diffuse out is a function of the capsule dimensions and material. Platinum capsules were used in early experiments due to the much faster diffusion rate for H_2 compared to gold. However, platinum is less ductile than gold, and at high concentrations of CO_2 the change in capsule volume during the initial heating and pressurization of a capsule often resulted in capsule failure.

When the capsule is sealed, all the CO_2 and a significant portion of the H_2O are present as a solid phase, oxalic acid dihydrate. Thus, prior to oxalic acid decomposition the volume of the starting components is relatively low. If the pressure is raised too high early in the run the capsule will collapse, often tearing along the rigid boundaries of the quartz core or along folds in the metal. As the temperature increases, the oxalic acid undergoes "vigorous decompression" (Sterner and Bodnar, 1991) and the density of the components inside the capsule drops dramatically, which will increasing their volume. If the pressure is too low at this point, the capsule will expand and rupture. In order to produce a successful experiment, the pressure-temperature loading path must be fine-tuned for the particular capsule size and mass of starting materials. This brings us back to the issue of lower ductility for platinum.

Nearly all early experiments with $X_{CO2}= 0.38$ run in platinum capsules failed due to rupturing during decomposition of oxalic acid. This was primarily due to the much larger change in the volume of starting materials during oxalic decomposition. Multiple loading paths were attempted with limited change in success. In addition, early trials of pyrrhotite-saturated experiments run in platinum capsules all resulted in failure, regardless of the mole fraction CO_2. Platinum capsules from the sulfur-bearing experiments were partially sulfidized, producing PtS, and showed signs of embrittlement due to the addition of iron. The compromised integrity of the platinum under sulfur-bearing conditions made it impossible to find a pressure-temperature path that did not result in capsule failure. As a result, the sulfur-bearing experiments could not be run in platinum. Gold capsules were the next logical choice due to limited reactivity with sulfur and minimal solid solution with iron. However, copper has a high solubility in metallic gold and experimental trials that included metallic gold demonstrated evidence for variable and decreasing concentrations of copper as a function of run duration.

Experiments run in platinum capsules that contained flakes of gold produced fluid inclusions trapped in pre-fractured quartz with highly variable copper concentrations. In-situ fracturing did provide a means to trap equilibrated fluids, but the equilibrium concentration of copper in the magmatic phases was generally so low that it could not be detected in the low-salinity vapor inclusions or glass. Fortunately, work by post-doctoral researcher Zoltan Zajacz was underway that allowed for pre-alloying gold capsule material with copper (presented in Zajacz et al. 2011). This technique provided the means to create capsules that were relatively unaffected by sulfur or iron, and which buffered the activity of copper rather than absorbing it from the magmatic phases. The H_2

generated during oxalic acid decomposition results in a lower fO_2 that persists much longer in gold capsules (Appendix II). However, by adjusting run duration, timing of in-situ fracturing, and capsule size, a Cu_6Au_{94} capsule composition ultimately allowed for successful runs at $X_{CO2} = 0.10$ and 0.38, with and without sulfur, that produced fluid inclusions and glass with measurable copper concentrations.

Appendix IV.   Mixed CO₂-H₂S Clathrate Stability Model

The model for mixed CO_2-H_2S clathrates relies upon ideal mixing of the end-member clathrate stability boundaries. The pure CO_2 clathrate stability boundary was calculated using the model presented by Duan and Sun (2006). This model also allows for the calculation of the clathrate stability boundary as a function of salinity. The boundary predicted by the model was fitted by an exponential function shown as Equation (42) below.

$$P_{CSB} = (4.57x10^{-16})e^{-0.1302 \cdot T_m^{Clath}} \tag{42}$$

This function correlates the pressure at the clathrate stability boundary (P_{CSB}) with the temperature of clathrate melting (T) and fits the model data with an R^2 value of 0.99699. The model also fits experimental data presented by Adasiamoto et al. (1991) with an R^2 value > 0.99.

The data on pure H_2S clathrate stability is more limited. Selleck et al. (1952) presented data on H_2S-clathrate stability for H_2S vapor clathrate equilibrium. The model for the pure H_2S clathrate was generated by fitting the presented by to an exponential function shown as Equation (43) below.

$$P_{CSB} = (2.99x10^{-14})e^{-0.1054 \cdot T_m^{Clath}} \tag{43}$$

This equation fits the existing data with an R^2 value of 0.999, and is used along with Equation (42) to generate the mixed clathrate stability boundary. The X_{CO2} of the gas mixture is then used to generate a proportional mixing model between these two equations two generate the exponential function that defines the clathrate stability boundary for any X_{CO2}. However, as discussed in chapter 3, the ideal mixing of the two

end-member clathrates only represents a proxy for predicting the mixed clathrate melting behavior at high X_{CO2} (>0.9). The same procedure was used to generate the line defined by the loci of Q_2 points predicted to exist by the behavior of mixed CO_2-H_2S clathrates (Diamond, 1994). This line defines the intersection between the vapor-clathrate boundary and the boiling curve for the CO_2-H_2S mixture at any X_{CO2}. Clathrate melting in CO_2-rich experiments occurs along the boiling curve and thus, the Q_2 points are also critical in characterizing inclusion salinity.

Appendix V.   Raman Spectroscopy: CO_2 Fermi-diad splitting

The advent of small-diameter Raman spectroscopy systems can now allow for the characterization of phases inside an inclusion as small as 5-10 μm in diameter. In addition to vapor phase characterization I will discuss work in which I participated designed to determine the CO_2 density in low-density vapor inclusions via Raman measurements. Raman analyses were conducted at Virginia Tech using a JY Horiba LabRam HR (800 mm) spectrometer and a 514.53 nm Laser Physics 100S-514 Ar^+ Laser with the assistance of technician Charles Farley. The first goal in using Raman spectroscopy was to characterize the carbon speciation in synthetic CO_2-bearing vapor inclusions, specifically ruling out the formation of CO or CH_4 during the decomposition of oxalic acid. Wide passes over wavenumbers from 800-3000 cm^{-1} and 600 grooves/mm grating were run to confirm the presence or absence of CO_2, CO, or CH_4. The observation of CO_2 without other C-O or C-H scattering confirms the absence of CO or CH4, as CO and CH_4 signals are 2 to 7 times more intense than CO_2. Once CO_2 is confirmed as the only carbon species present, the spectrometer is focused on 1200 to 1500 cm^{-1} with high resolution 2400 grooves/mm grating to observe the Fermi-diad peaks characteristic of Raman scattering by CO_2.

The presence of H_2S in pyrrhotite-saturated experiments required an adjustment to this procedure to characterize H_2S-bearing vapor inclusions. Vapor inclusions with both CO_2 and H_2S were characterized by using 600 grooves/mm grating and an analysis window from 1100 to 2800 cm^{-1} in order to measure the two CO_2 peaks (~1286 and ~1389 cm^{-1}) and H_2S peak (~2611 cm^{-1}) in a single analysis (Figure 25).
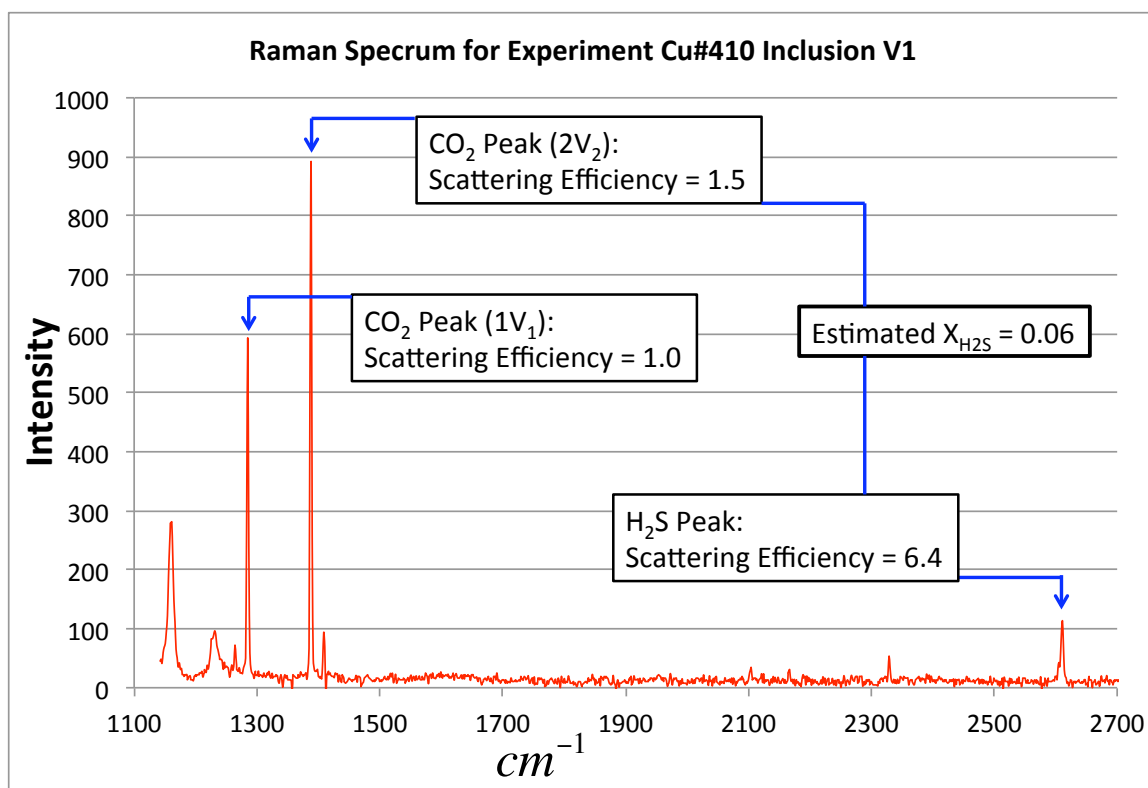
Figure 25: An example of a Raman spectrum from Experiment Cu#410.

The area under each peak is proportional to the mole fraction of CO_2 and H_2S in the vapor bubble, adjusted for the relative scattering efficiency of each vibrational mode. The peak area from each CO_2-H_2S analysis was measured directly by integrating the raw Raman intensity data. Thus, peak areas from one of the CO_2 peaks and the H_2S peak from each analysis were used to estimate the CO_2/H_2S ratio in the vapor inclusions for use in the mixed clathrate stability model.

i. Fermi-diad and CO_2 Vibrational Spectroscopy:

The structure of the CO_2 molecule allows for three basic types of vibrations or modes, which are capable of IR absorption. The vibrations are described as a symmetric stretch (v_1), asymmetric stretch (v_3), and 2 bending modes combined to form (v_2). The symmetric stretch (v_1) is Raman active and IR absorption inactive as these two interaction types are mutually exclusive for a given vibrational mode. The asymmetric stretch (v_3), and 2 bending modes (v_2), are IR active and Raman inactive. However, the

energy of the second excitation of the (v_2) bending vibrations, identified as ($2v_2$), has nearly the same energy as the (v_1) mode. Part of the ($2v_2$) vibrational mode also shares a symmetry type with the (v_1) mode, which combined with the energy match, allows the vibrations to interact via Fermi-resonance (Kawakami et al. 2003). The result is the two Raman peaks observed for CO_2 rather than just one for (v_1) alone, owing to the scattering being dominantly caused by either the (v_1) or ($2v_2$) vibrations (Rosso and Bodnar 1995). The two peaks are observed at ~1286 and 1388 cm^{-1} with increasing density increasing the peak splitting (Figure 26).

Cu#321 Inclusion VR1 Raman CO$_2$ Signal
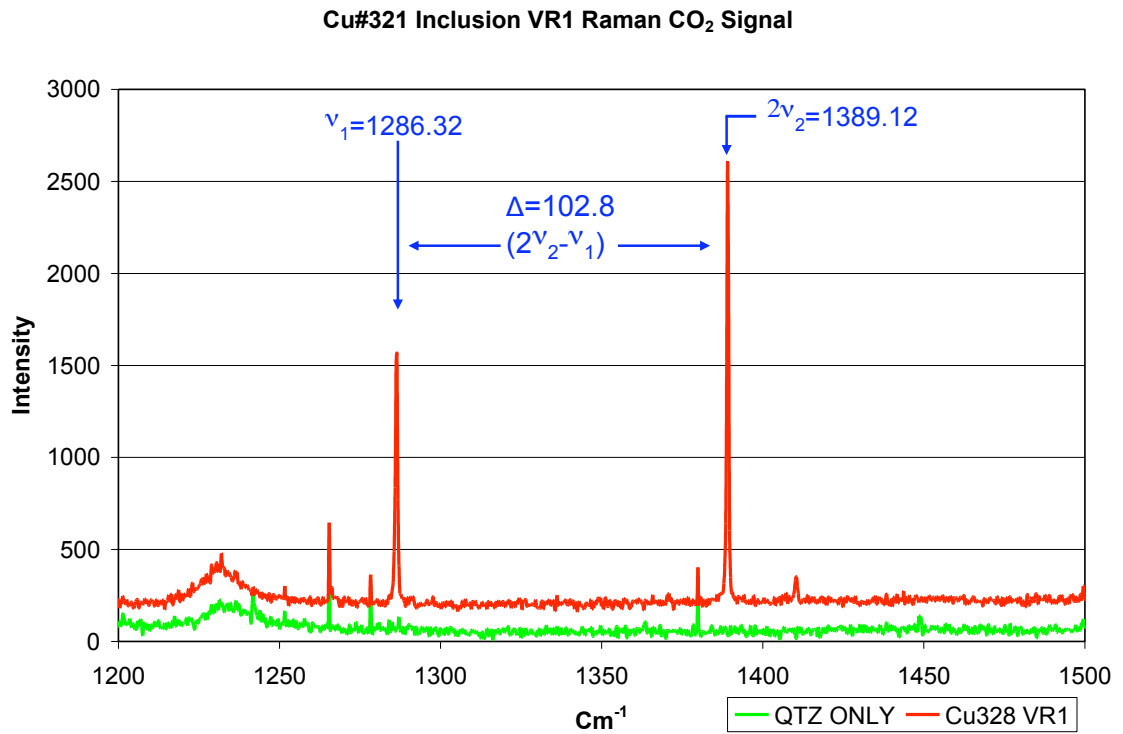
Figure 26: [red] Raman IR absorption spectrum for vapor-rich inclusion Cu321-VR1 showing the two Fermi-diad peaks (v_1 dominant & $2v_2$ dominant) for CO$_2$. The split between the peaks (Δ) is used to calculate the CO$_2$ density of the inclusion. [green] Absorption spectrum for the host quartz showing the peaks not relevant to the inclusion (intensity offset by 100 to remove overlap)

The recent work presented by Fall et al. (2011) characterized the correlation between the Fermi-diad splitting (Δ) and the density of CO_2 near the boiling curve for CO_2 at ambient temperatures. A custom designed transparent sample cell was filled with

pure CO_2 at pressures ranging from 0.5 to 30 MPa. Raman splitting measurements were then made at pressure intervals of 0.5 MPa to 5 MPa across this range. Equation (7) was generated by the best fit of these data, correlating the density of CO_2 with Δ. I contributed to this work by examining the Fermi-diad splitting of vapor inclusions generated in sulfur-free, low-CO_2, experiments. These synthetic inclusions, along with others synthesized by the collaborators, confirmed that the CO_2 density predicted by Raman spectroscopy matched observed phase relations for vapor, vapor + liquid, and liquid CO_2 inclusions. In addition, the inclusions confirmed that the Δ and clathrate melting temperature (Tm^{Clath}) can be used to estimate inclusion salinity. The calculated salinities were consistent both the model predictions for the $NaCl-H_2O-CO_2$ system (Duan et al., 1995) and the predicted phase assemblage based upon experiment starting material compositions.

Appendix VI.   CO$_2$-MVPart Model: X$_{CO2}$ Dependent Variables

The modified CO$_2$-MVPart model was created by replacing several fixed variables in the original MVPart model with functions to account for the presence of CO$_2$. These include the melt water concentration at volatile phase saturation, the fH$_2$O in the exsolved vapor, and the salinity of the brine-saturated vapor and vapor-saturated brine. The melt water concentration ($[H_2O]^{melt}$) at volatile phase saturation was determined at intervals of 5 to 10 mol% CO$_2$ using the VolatileCalc model presented by Newman and Lowenstern (2002)(Figure 27).
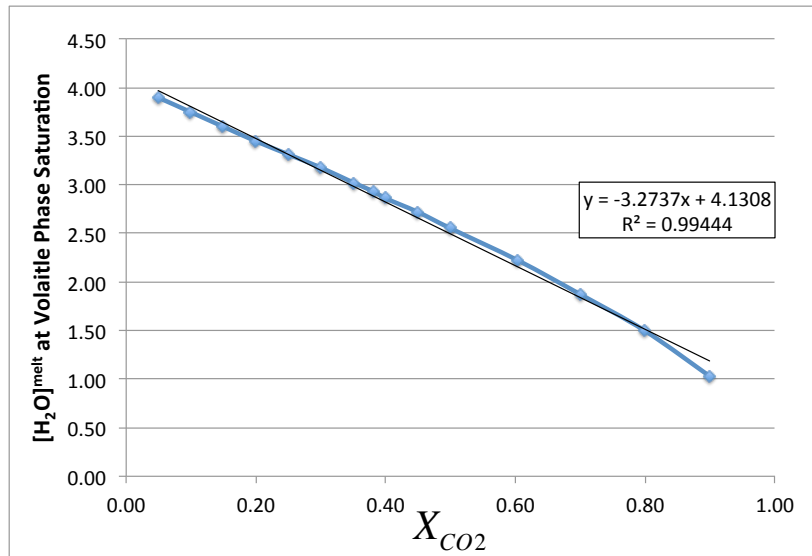
Figure 27: Plot of the correlation between the water concentration required for volatile phase saturation of a felsic silicate melt and the X$_{CO2}$ of the exsolved vapor. Data were generated using the VolatileCalc program presented by Newman and Lowenstern (2002).

The fH$_2$O is the exsolved volatile phase was determined at similar intervals using the theoretical model presented by Churakov et al. (2003) (Figure 28).
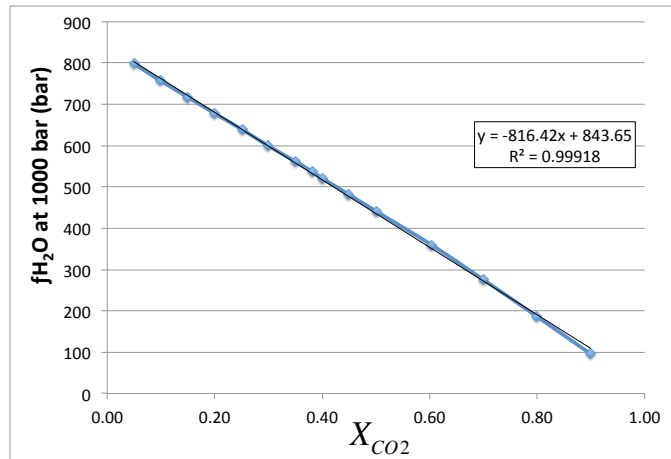
Figure 28: Plot of ƒH2O in the magmatic vapor phase at 1000 bar (100 MPa) as a function of X_{CO2}.

This model accounts for non-ideal mixing between CO_2 and H_2O in the magmatic vapor. Using an adjusted ƒH_2O ensures that melt-volatile phase equilibria (e.g. iron speciation) are modeled accurately for the CO_2-bearing system.

The salinity of the coexisting vapor and brine were determined using a combination of microthermometric data and model results from Duan et al. (1995). Measured vapor and brine salinities were used for X_{CO2} = 0.10 and 0.38 and model results were used to fill in the gaps. The salinity of the two phases was calculated in mol/kg because these were the units used in the original MVPart model (Figure 29).
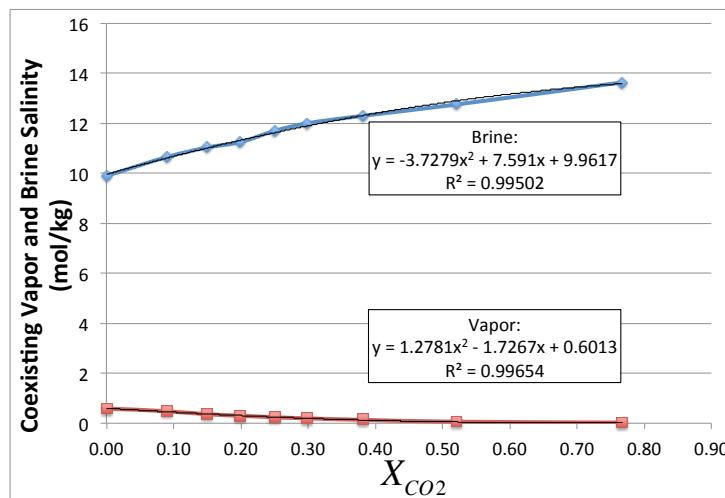
Figure 29: Coexisting vapor and brine salinities determined using microthermometry and model results from Duan et al. (1995).

Appendix VII.   LA-ICPMS Parameters

Fluid inclusion analyses were conducted at Virginia Tech using an Agilent 7500ce

ICPMS and GeoLas 193nm Eximer Laser. The suite of elements analyzed was reduced

throughout the course of the project in order to improve detection of vital elements (Cu,

Au) and remove elements not present at concentrations detectable above the gas

background (e.g. Ti, Zn, Mn). A complete list of the isotopes measured for each element

analyzed includes, ^{23}Na, ^{25}Mg, ^{27}Al, ^{28}Si, ^{39}K, ^{40}Ca, ^{49}Ti, ^{55}Mn, ^{56}Fe, ^{59}Co, ^{63}Cu, ^{66}Zn,

^{195}Pt, and ^{197}Au. Dwell time for each isotope was 10 ms except for Cu and Au, which

both had dwell times of 40 ms. A sensitivity test was run during analysis of fluid

inclusions from Cu330 in which both ^{63}Cu and ^{65}Cu were measured. No discrepancy in

measured Cu abundance was discernable within the analytical uncertainty when

comparing the two isotopes of copper. The instrument conditions for the laser and mass

spectrometer are shown below in Figure 30.

Laser:	*ICPMS: Quadrupole*
193 nm wavelength	(Figure from Agillent)
7-10 J/cm^2 energy density	Torch:
5 Hz firing rate	27.12 MHz Rf coil
4-60 μm beam size (160 μm max)	He-Argon torch gas

Figure 30: Instrument conditions for LA-ICPMS analysis of fluid inclusions using an Agilent 7500ce ICPMS and GeoLas 193nm Eximer Laser.

Appendix VII: Data Tables for Brine Inclusions, Vapor Inclusions, Pyrrhotite and Glass

LA-ICPMS Analysis of Brine Inclusions						
Brine: X_{CO2}=0.10 S-Free (ppm) LOD = Average Limit of Detection (ppm)						
Cu320	Na	K	Ca	Fe	Cu	Au
LOD	400	830	290	61	130	16
Cu320aB25.txt	150000	200000	6100	3500	2000	23
Cu320aB25b.txt	150000	180000	9900	5400	4100	68
Cu320aB26.txt	150000	200000	6200	3600	2200	68
Cu320aB24.txt	150000	210000	15000	2100	8200	110
Cu320aBL3.txt	150000	260000	4600	3700	4800	52
Cu320aB18b.txt	150000	140000	1900	1000	1300	-
Cu320bB1c.txt	150000	200000	7800	14000	3900	150
Cu320bB3.txt	150000	270000	6700	14000	3800	100
Cu320bB6.txt	150000	200000	8200	14000	3700	100
Cu320bB8.txt	150000	200000	8100	15000	3700	100
Cu320bB8b.txt	150000	210000	8400	14000	3700	74
Cu320bB8c.txt	150000	200000	8400	15000	4100	99
Cu320bB18.txt	150000	200000	8000	15000	4000	140
Cu320bB19.txt	150000	200000	8500	15000	3900	150
Cu320bB22.txt	150000	200000	7000	12000	2800	140
Cu320bB22b.txt	150000	200000	7600	14000	3700	150
Cu320bB26.txt	150000	200000	8000	14000	3800	130
Cu320bB27.txt	150000	200000	8100	15000	3900	140
Cu320bBL1.txt	150000	200000	8100	15000	3800	120
Cu320bBL3.txt	150000	200000	8200	15000	3800	160
Cu320aB28.txt	110000	200000	4700	3900	4100	-
Cu320aB25b.txt	130000	170000	6700	14000	3300	120
Cu320bBL2.txt	120000	190000	4700	11000	3600	140
Cu321						
LOD	1200	2700	1100	200	510	61
Cu321B17.txt	140000	200000	4000	1900	48000	20
Cu321B21.txt	140000	180000	4700	2900	65000	19
Cu321BL21.txt	140000	170000	2300	3500	48000	13
Cu321BL22.txt	140000	180000	1800	1900	50000	-
Cu321BL23.txt	140000	190000	1000	2000	60000	-
Cu321BL25.txt	140000	200000	4500	2400	51000	27
Cu321B23.txt	150000	200000	4200	2000	49000	25
Cu321BL26.txt	130000	86000	-	9800	60000	-

Cu326	Na	K	Ca	Fe	Cu	Au
LOD	370	840	330	59	150	19
Cu326B17.txt	150000	190000	5500	7200	2700	37
Cu326B18.txt	150000	190000	5800	7400	2600	20
Cu326B19.txt	150000	190000	5500	7800	3200	25
Cu326B21.txt	150000	190000	6000	8100	2900	30
Cu326BL21.txt	150000	190000	5700	7000	2100	-
Cu326BL22.txt	150000	190000	5600	7800	2600	26
Cu326BL23.txt	150000	200000	5700	4600	2200	-
Cu326B16.txt	86000	210000	5100	6500	2700	24
Cu351						
LOD	480	1100	420	79	90	12
Cu351B1-3a.txt	110000	170000	-	42000	9200	-
Cu351B1-3b.txt	110000	170000	-	42000	9200	-
Cu351B1-3c.txt	120000	160000	-	44000	9500	-
Cu351B7-8a.txt	110000	170000	-	42000	9700	-
Cu351B20-21.txt	110000	160000	-	44000	9400	-
Cu351B22-26a.txt	100000	170000	-	48000	11000	-
Cu351B22-26b.txt	110000	160000	-	48000	9800	-
Cu351B27-28a.txt	110000	150000	-	53000	9500	-
Cu351B27-28b.txt	140000	110000	-	58000	11000	-
Cu351B29-30a.txt	110000	170000	1000	42000	9200	-
Cu351B29-30b.txt	130000	140000	8000	39000	8800	-
Cu351B31-32a.txt	120000	160000	-	38000	8200	-
Cu351B31-32b.txt	130000	150000	-	45000	8000	-
Cu351B70-71a.txt	120000	93000	-	43000	7600	-
Cu351B70-71b.txt	120000	160000	97	46000	8300	8.6
Cu330						
LOD	370	890	330	57	120	9.3
Cu330B2-3-4.txt	140000	200000	5000	1900	2000	-
Cu330B2-3-4.txt	140000	200000	5900	2200	2600	-
Cu330B30.txt	140000	190000	5600	2700	2600	-
Cu330B31.txt	140000	180000	5500	2600	2600	-
Cu330B32.txt	140000	190000	5100	2400	2300	-
Cu330B33.txt	140000	190000	5800	2800	2800	-
Cu330B34.txt	140000	200000	5700	2800	2700	-
Cu330B35.txt	140000	200000	5700	2900	2200	-
Cu330B36.txt	140000	200000	4900	3400	2500	-
Cu330B38.txt	140000	210000	6300	1700	3000	-
Cu330B39.txt	110000	170000	24000	4100	2100	-

Cu332	Na	K	Ca	Fe	Cu	Au
LOD	560	1200	440	76	140	12
Cu332B3.txt	140000	190000	4400	1200	2500	-
Cu332B4.txt	140000	200000	4600	1200	2100	-
Cu332B5.txt	140000	190000	6300	1500	2600	-
Cu332B39.txt	140000	210000	28000	1400	2400	-
Cu332B80.txt	140000	170000	5800	1300	2500	-
Cu332B30.txt	92000	230000	3600	930	2800	-
Cu332B6.txt	130000	180000	4100	1100	2700	-

Brine: X_{CO2}=0.38 S-Free (ppm)   LOD = Average Limit of Detection (ppm)

Cu500	Na	K	Ca	Fe	Cu	Au
LOD	210	220	-	160	13	17
Cu500B10-11.txt	170000	180000	-	-	1900	-
Cu500B12-13.txt	160000	190000	-	-	1700	-
Cu500B12-13.txt	160000	190000	-	-	1700	-
Cu500B12-13.txt	160000	200000	-	-	1900	-
Cu500B20-22.txt	160000	190000	-	-	1700	-
Cu500B20-22.txt	160000	190000	120	-	1700	-
<u>Cu502</u>						
LOD	1300	2300	-	770	150	180
Cu502B1-2.txt	160000	190000	-	470	3800	-
Cu502B1-2.txt	120000	250000	-	870	5000	-
Cu502B2-3.txt	94000	280000	-	-	3800	-
Cu502B2-3.txt	120000	240000	-	-	3000	-
Cu502B3-5.txt	160000	190000	150	450	4300	-
Cu502B3-5.txt	160000	190000	420	500	6800	-
Cu502B4.txt	160000	190000	-	490	4500	-
Cu502BL2-3.txt	99000	280000	-	-	4600	-
Cu502BL2-3.txt	130000	240000	-	-	3700	-
Cu502BL4.txt	160000	190000	-	550	5800	-
Cu502B4_2.txt	160000	190000	-	550	5800	-
<u>Cu503</u>						
LOD	170	350	200	29	34	3.2
Cu503B1.txt	150000	190000	-	24000	9800	-
Cu503B-2.txt	140000	190000	390	26000	11000	-
Cu503B21.txt	100000	180000	-	68000	9200	-
Cu504B4.txt	140000	190000	-	18000	9000	14
Cu504B5.txt	140000	190000	-	16000	9400	14
Cu503B3.txt	140000	190000	-	23000	7700	-
Cu503B13.txt	140000	200000	-	28000	8200	4
Cu503B11-12.txt	110000	180000	-	61000	9800	-
Cu503B11-12.txt	110000	180000	-	61000	9800	-

Cu504	Na	K	Ca	Fe	Cu	Au
LOD	360	600	190	42	48	6
Cu504B1.txt	140000	190000	-	18000	9000	14
Cu504B2.txt	140000	190000	-	16000	9400	14
Cu504B3.txt	140000	190000	210	18000	8700	11
Cu504B5.txt	140000	190000	-	18000	9000	5
Cu504B6.txt	150000	180000	-	19000	9300	8
Cu504B10-11.txt	140000	190000	-	18000	9100	12
Cu504B12-13.txt	150000	180000	-	18000	8900	9
Cu504B10-11.txt	150000	190000	-	17000	8100	9
Cu504B12-13.txt	170000	160000	-	17000	8600	-
Cu505						
LOD	300	710	330	54	59	5.8
Cu505_I_B1.txt	150000	190000	1300	23000	2000	-
Cu505_I_B3-5.txt	140000	200000	300	24000	2600	-
Cu505_I_B4-6.txt	180000	150000	3100	21000	2100	-
Cu505_I_B4-6.txt	130000	220000	-	19000	2700	-
Cu505_I_B12-14.txt	150000	190000	-	26000	2500	-
Cu505_I_B40.txt	150000	200000	-	17000	2900	-
Cu505_P_B5-7.txt	160000	180000	-	24000	2500	3
Cu505_P_B10-11.txt	160000	180000	-	24000	2400	-
Cu505_P_B12-14.txt	160000	180000	-	24000	2500	3
Cu505_P_B12-14.txt	150000	180000	130	24000	2500	2
Cu505_P_B12-14.txt	160000	170000	-	25000	2500	-
Cu505_P_B20-21.txt	160000	180000	320	23000	2600	49
Cu505_P_B20-21.txt	160000	180000	-	24000	2500	3
Cu505_P_B22-23.txt	160000	180000	120	23000	2500	-
Cu505_P_B22-23.txt	160000	180000	-	23000	2600	-
Cu505_P_B24.txt	150000	180000	110	27000	2800	-
Cu505_P_B30-31.txt	160000	180000	-	25000	2600	4
Cu505_P_B30-31.txt	160000	180000	-	24000	2500	3
Cu505_PB1-3.txt	160000	170000	-	22000	2800	-
Cu505_PB1-3.txt	150000	200000	-	16000	3000	-
Cu505_PB1-3.txt	150000	190000	-	26000	3000	3

Brine: X_{CO_2}=0.10 Po-Saturated (ppm)   LOD = Average Limit of Detection (ppm)

Cu402	Na	K	Ca	Fe	Cu	Au
LOD	150	320	130	26	29	3.7
Cu402B21-20b.txt	140000	200000	930	42000	2000	62
Cu402B23-22.txt	140000	200000	940	44000	1900	72
Cu402B40-41.txt	120000	170000	960	42000	1800	54
Cu402B42-43a.txt	120000	160000	1200	44000	1600	43
Cu402B42-43b.txt	100000	180000	820	49000	2100	52

Cu402	Na	K	Ca	Fe	Cu	Au
Cu402B50-51a.txt	120000	170000	900	40000	1800	59
Cu402B50-51b.txt	120000	170000	830	33000	1800	87
Cu402xB1.txt	110000	190000	940	31000	2100	110
Cu402xB3-4-2a.txt	110000	190000	360	22000	2100	140
Cu402xB3-4-2b.txt	120000	170000	780	30000	1700	79
Cu402xB3-4-2c.txt	120000	160000	780	36000	1800	66
Cu402xB5.txt	140000	190000	1100	48000	1800	69
Cu402xB6-7.txt	140000	180000	750	33000	1800	94
Cu404						
LOD	150	300	190	27	29	2.8
Cu404_I_B1-2.txt	130000	170000	-	28000	1600	20
Cu404_I_B1-2.txt	130000	160000	-	27000	1500	15
Cu404_I_B1-3.txt	130000	150000	110	37000	1900	39
Cu404_I_B1-3.txt	120000	160000	79	46000	1900	38
Cu404_I_B1-3.txt	120000	160000	140	40000	2000	36
Cu404_I_B3-6.txt	130000	160000	-	28000	1500	22
Cu404_I_B3-6.txt	130000	160000	230	29000	1700	21
Cu404_I_B3-6.txt	120000	170000	480	29000	1600	27
Cu404_I_B3-6.txt	120000	170000	-	33000	1900	17
Cu404_I_B10-11.txt	130000	170000	240	27000	1600	20
Cu404_I2_B1-2.txt	130000	170000	230	26000	1400	19
Cu404_I2_B1-2.txt	130000	170000	240	27000	1500	21
Cu404_I2_B10-11.txt	130000	160000	290	28000	1500	19
Cu404_I2_B10-11.txt	130000	160000	-	29000	1500	20
Cu404_P_B20-23.txt	130000	170000	-	19000	1600	26
Cu404_P_B13-15.txt	91000	180000	-	60000	1700	55
Cu405						
LOD	160	400	160	31	34	3.3
Cu405_I_B1.txt	120000	160000	-	46000	3000	55
Cu405_I_B2.txt	150000	140000	-	32000	2200	51
Cu405_I_B4-4b.txt	120000	150000	-	49000	2900	68
Cu405_I_B4-4b.txt	120000	150000	160	50000	3300	65
Cu405_I_B10-11.txt	120000	150000	-	52000	3600	63
Cu405_I_B10-11.txt	130000	160000	-	30000	2500	64
Cu405_I_B50-51.txt	100000	150000	-	71000	2400	51
Cu405_I_B50-51.txt	110000	150000	-	70000	2200	53
Cu405_I_B52-53.txt	120000	150000	-	51000	2200	120
Cu405_I_B52-53.txt	120000	160000	120	48000	2600	34
Cu405_P_B1-2.txt	120000	150000	75	48000	3100	66
Cu405_P_B3-6.txt	120000	150000	120	48000	3100	66
Cu405_P_B3-6.txt	120000	150000	110	49000	3300	62
Cu405_P_B3-6.txt	120000	150000	-	48000	3000	68

Cu405	Na	K	Ca	Fe	Cu	Au
Cu405_P_B10-11.txt	110000	150000	210	57000	2900	66
Cu405_P_B10-11.txt	120000	150000	-	49000	3200	68
Cu405_P_B20-21.txt	120000	150000	75	49000	3300	72
Cu405_P_B20-21.txt	120000	150000	-	49000	3400	70
Cu405_P_B30-31.txt	110000	170000	220	48000	3600	72
Cu405_P_B30-31.txt	120000	160000	130	46000	3200	65
Cu405_P_B40-42.txt	120000	150000	120	48000	2900	62
Cu405_P_B40-42.txt	120000	150000	100	47000	3100	68
Cu405_P_B40-42.txt	120000	150000	-	51000	3300	74
Cu405_P_B70-71.txt	120000	160000	400	48000	3100	62
Cu405_P_B72-73.txt	120000	160000	120	48000	3200	71
Cu410						
LOD	100	170	-	18	16	1.2
CU410B3-5.txt	100000	160000	-	56000	5000	74
CU410B3-5.txt	100000	160000	-	55000	5100	73
CU410B8-9.txt	110000	150000	-	60000	5100	82
CU410B8-9.txt	100000	160000	-	59000	5000	84
CU410B10-12.txt	100000	150000	-	61000	4900	93
CU410B10-12.txt	87000	170000	-	67000	5000	57
CU410B10-12.txt	88000	170000	-	65000	4900	59
CU410B20-22.txt	100000	160000	-	62000	5300	76
CU410B50.txt	100000	160000	-	60000	5200	80
CU410B51-52.txt	87000	150000	-	85000	5100	54
CU410B70.txt	91000	160000	-	73000	4700	67
CU410B71-72.txt	93000	140000	-	83000	5100	63
CU410B80.txt	100000	160000	-	59000	4600	87
Cu411						
LOD	170	290	-	34	26	2.1
CU411B1-2.txt	99000	160000	-	67000	4600	83
CU411B1-2.txt	99000	150000	-	69000	4100	49
CU411B20-21.txt	96000	160000	-	69000	4900	89
CU411B20-21.txt	100000	160000	-	64000	4200	75
CU411B23-24.txt	100000	160000	-	62000	4400	76
CU411B23-24.txt	100000	150000	-	65000	4600	85
CU411B30.txt	100000	160000	-	64000	4400	71

Brine: X_{CO_2}=0.38 Po-Saturated (ppm)   LOD = Average Limit of Detection (ppm)

Cu601	Na	K	Ca	Fe	Cu	Au
LOD	260	280	-	31	26	1.8
CU601B1-3.txt	140000	190000	-	31000	4000	84
CU601B1-3.txt	140000	190000	-	29000	3800	87
CU601B1-3.txt	150000	190000	-	28000	3500	80

Cu601	Na	K	Ca	Fe	Cu	Au
CU601B10-11.txt	150000	190000	-	24000	3700	82
CU601B10-11.txt	150000	180000	-	31000	4000	77
CU601B12.txt	140000	190000	-	29000	4400	110
CU601B30-31.txt	140000	190000	-	29000	4600	90
CU601B30-31.txt	140000	190000	-	29000	4500	70
CU601B32-33.txt	140000	190000	-	32000	4600	85
CU601B32-33.txt	160000	170000	-	24000	3900	85
Cu606						
LOD	260	420	-	92	42	3.1
CU606B20-21.txt	140000	190000	-	38000	4400	110
CU606B20-21.txt	140000	180000	-	36000	4500	110
CU606B30-33.txt	140000	180000	-	35000	3900	110
CU606B30-33.txt	140000	190000	-	35000	4700	110
CU606B30-33.txt	140000	190000	-	35000	4300	110
CU606B30-33.txt	140000	180000	-	33000	4800	100
CU606B40.txt	140000	190000	-	34000	4500	100
CU606B41.txt	140000	180000	-	37000	4700	110
CU606B50-51.txt	140000	180000	-	37000	5000	130
CU606B52.txt	140000	180000	-	32000	5300	110
CU606B60.txt	140000	180000	-	34000	4800	100
CU606B61.txt	140000	190000	-	37000	4500	100
CU606B70-71.txt	140000	190000	-	34000	5200	110
Cu607						
LOD	310	310	-	23	31	2.2
CU607B1-2.txt	140000	190000	-	37000	3400	53
CU607B4.txt	140000	190000	-	34000	3900	97
CU607B5.txt	140000	200000	-	26000	3300	98
CU607B10-11.txt	140000	190000	-	32000	3200	97
CU607B10-11.txt	150000	180000	-	34000	3700	120
CU607B20-22.txt	140000	190000	-	35000	3600	96
CU607B20-22.txt	140000	180000	-	36000	3700	88
CU607B50-51.txt	140000	190000	-	32000	3500	98
CU607B50-51.txt	140000	200000	-	28000	2800	160
CU607B60-61.txt	140000	190000	-	35000	2900	93
CU607B60-61.txt	140000	190000	-	28000	3500	110

LA-ICPMS Analysis of Vapor Inclusions

Vapor: X_{CO2}=0.10 S-Free (ppm)   LOD = Average Limit of Detection (ppm)

Cu320	Na	K	Ca	Fe	Cu	Au
LOD	250	620	220	42	110	12
Cu320aV1.txt	6900	11000	310	150	100	15
Cu320aV6.txt	6900	14000	250	140	88	34
Cu320aVL1.txt	6900	13000	520	450	210	-
Cu320aV7.txt	4900	5800	-	110	150	39
Cu320aV12.txt	4100	8300	660	120	150	-
Cu320aVL3.txt	4300	6900	710	340	140	24
Cu321						
LOD	220	480	180	35	80	10
Cu321V1.txt	4900	8100	-	210	3600	-
Cu321V2.txt	10000	12000	610	250	3100	10
Cu321V3.txt	6900	9800	-	290	2800	-
Cu321V6.txt	6900	9600	120	250	2500	-
Cu321VL2.txt	6900	9400	180	120	2600	-
Cu321VL22.txt	6900	10000	-	380	3200	-
Cu321VL23.txt	6900	9200	210	380	2600	-
Cu321VL25.txt	6900	9400	280	350	2400	-
Cu321VL26.txt	6900	9300	-	110	2500	-
Cu321VL27.txt	6900	9700	270	300	2200	-
Cu321VL28.txt	6900	9500	200	190	2500	-
Cu326						
LOD	260	630	220	41	110	13
Cu326V1.txt	7900	7700		290	140	-
Cu326V2.txt	7900	11000	280	400	82	-
Cu326V3.txt	6900	13000	520	450	210	-
Cu320aVL3.txt	4300	6900	710	340	140	24
Cu351						
LOD	370	860	290	63	71	7.7
Cu351V20-22a.txt	5900	8600	840	1800	490	-
Cu351V20-22b.txt	5900	8000	-	1100	290	-
Cu351V20-22c.txt	5900	8200	-	1200	410	-
Cu351V25-26a.txt	5700	5700	-	1600	310	-
Cu351V25-26b.txt	5900	5800	-	1400	310	-
Cu351V30-33.txt	5900	7300	190	1300	350	-
Cu351V40-42a.txt	5900	7700	-	1500	300	-
Cu351V40-42b.txt	5900	7400	-	1600	340	-
Cu351V46-50.txt	5900	7200	-	1200	310	-
Cu351V60-61.txt	5900	8100	-	1400	390	-

Cu351	Na	K	Ca	Fe	Cu	Au
Cu351V70.txt	5900	10000	-	1400	390	-
Cu330						
LOD	120	270	110	18	31	2.6
Cu330V4.txt	5900	12000	-	54	110	-
Cu330V10.txt	5900	8300	270	88	150	-
Cu330V11.txt	5900	5700	340	57	130	-
Cu330V12.txt	5900	3800	280	73	83	-
Cu330V40-42.txt	5900	7900	-	68	150	-
Cu330V41.txt	5900	8000	260	74	170	-
Cu330V43.txt	5900	8300	330	110	130	-
Cu330V45.txt	5900	7900	210	62	120	-
Cu330V14.txt	5900	8200	170	120	96	-
Cu332						
LOD	180	440	160	25	40	3.8
Cu332V2.txt	5900	5200	-	-	80	-
Cu332V3-4.txt	5900	6900	-	41	84	-
Cu332V5.txt	5900	4800	200	67	100	-
Cu332V6.txt	5900	5300	220	17	170	-
Cu332V10-9.txt	5900	9000	150	21	100	-
Cu332V13-12.txt	5900	7200	-	-	110	-
Cu332V10-9.txt	7300	5300	400	49	84	-
Cu332V13-12.txt	7400	5700	-	-	110	-

Vapor: X_{CO2}=0.38 S-Free (ppm)   LOD = Average Limit of Detection (ppm)

Cu500	Na	K	Ca	Fe	Cu	Au
LOD	49	97	32	6.7	7.6	1
Cu500V1-2.txt	2300	2000	110	8.5	28	-
Cu500V1-2.txt	2300	2000	120	7.5	27	-
Cu500V1-2.txt	2300	1800	200	-	25	-
Cu500V10-11.txt	2300	1900	140	-	26	-
Cu500V12-13.txt	2600	1600	83	13	32	1
Cu500V12-13.txt	2500	1900	-	-	19	-
Cu500V14-15.txt	2000	1800	460	7.4	30	-
Cu500V10-11.txt	2400	1700	150	11	49	-
Cu502						
LOD	130	230	78	15	18	2.3
Cu502V1-4.txt	2100	2300	-	-	110	-
Cu502V7.txt	1700	2600	-	36	110	-
Cu502V8-10.txt	2100	2300	-	19	92	-
Cu502V8-10.txt	2200	2100	-	19	93	-
Cu502V11-12.txt	2000	2500	-	13	82	-
Cu502V11-12.txt	2100	2300	-	-	100	-

Cu502	Na	K	Ca	Fe	Cu	Au
Cu502V8-10.txt	2100	2300	-	25	98	-
Cu503						
LOD	210	320	-	98	22	24
Cu503V1.txt	1700	1700	-	1000	110	-
Cu503V2.txt	1400	2000	220	800	83	-
Cu503V4.txt	1400	2100	110	820	120	-
Cu503V5.txt	1400	2200	-	830	130	-
Cu503V6.txt	1800	1900	-	680	65	-
Cu503V7.txt	1600	2000	58	820	60	-
Cu503V10.txt	1400	2700	82	420	83	-
Cu503V11-14.txt	1700	2400	-	390	110	-
Cu503V20.txt	1700	2400	-	400	66	-
Cu503V21.txt	1500	2000	160	800	62	-
Cu503V28-30-31.txt	2000	1500	-	750	86	-
Cu504						
LOD	150	260	77	16	19	2.3
Cu504V1-4.txt	1800	2300	-	340	130	-
Cu504V15.txt	1800	2100	-	580	76	-
Cu504V10-15.txt	1400	2200	52	910	72	2
Cu504V2.txt	1400	2000	220	800	83	-
Cu504V10.txt	1400	2700	82	420	83	-
Cu504V12.txt	2000	1500	-	750	86	-
Cu504V1-4.txt	1300	2700	100	450	65	-
Cu504V1-4.txt	1800	2300	-	360	120	-
Cu504V10-15.txt	1400	2100	-	940	69	-
Cu505						
LOD	55	150	58	11	12	1.2
Cu505_I_V20-21.txt	2100	2200	-	170	28	-
Cu505_I_V22-24.txt	2200	2200	-	67	26	-
Cu505_I_V30-31.txt	1000	3500	24	320	28	-
Cu505_I_V30-33.txt	2100	1800	-	550	24	-
Cu505_I_V30-33.txt	2000	2000	-	440	26	-
Cu505_P_V7-8.txt	2000	2200	-	330	31	-
Cu505_P_V20-21.txt	2200	1400	310	330	28	-
Cu505_P_V24-26.txt	2200	1800	-	440	24	-
Cu505_P_V24-26.txt	2100	1900	-	370	35	-
Cu505_P_V27-28.txt	2000	2100	-	360	30	-
Cu505_P_V30-32.txt	2000	2000	150	300	28	-
Cu505_P_V33.txt	1900	2100	-	450	28	-
Cu505_P_V50-51.txt	1800	2100	-	560	27	-
Cu505_P_V50-51.txt	2000	2100	-	380	29	-
Cu505_P_V52-53.txt	1900	2200	-	410	24	-

Vapor: X_{CO_2}=0.10 Po-Saturated (ppm)   LOD = Average Limit of Detection (ppm)

Cu402	Na	K	Ca	Fe	Cu	Au
LOD	67	150	59	12	14	1.7
Cu402xV70-72.txt	5900	7800	45	3200	91	3
Cu402xV70-72.txt	5900	7700	65	2200	87	3
Cu402V20-21.txt	5900	8300	46	7400	97	3
Cu402V20-21.txt	5900	7000	-	2400	110	3
Cu401V2-1.txt	5900	8000	-	1700	100	4
Cu401V3.txt	5900	8400	-	6000	180	4
Cu401V21-20.txt	5900	7000	94	1700	130	7
Cu401V21-20b.txt	5900	8100	540	7900	92	3
Cu404						
LOD	100	240	100	18	22	2.2
Cu404_I_V1-2.txt	6900	8100	-	2200	100	-
Cu404_I_V1-2.txt	6900	5300	3400	1200	97	8
Cu404_I_V1-4.txt	6900	8000	290	2500	180	-
Cu404_I_V1-4.txt	6900	7800	-	3900	180	-
Cu404_I_V10-12.txt	6900	8400	-	8000	140	4
Cu404_I_V10-12.txt	6900	8900	-	-	94	2
Cu404_I2_V1-4.txt	6900	9400	2200	-	89	2
Cu404_I2_V1-4.txt	6900	8400	1900	-	86	2
Cu404_I2_V2-3.txt	6900	8800	310	-	88	1
Cu405						
LOD	99	250	110	19	22	2.3
Cu405_I_V3-4.txt	6900	7000	-	6100	340	-
Cu405_I_V3-4.txt	6900	5800	-	3100	160	-
Cu405_I_V5-6.txt	6900	8800	-	3300	180	3.5
Cu405_I_V5-6.txt	6900	8700	-	3900	180	3.3
Cu405_I_V10-11.txt	6900	8500	-	4000	190	2.5
Cu405_I_V30-31.txt	6900	8400	-	6100	190	-
Cu405_I_V30-31.txt	6900	9000	-	3100	210	3.3
Cu405_P_V1-3.txt	6900	7000	-	2500	210	4
Cu405_P_V1-3.txt	6900	6700	-	2400	200	3.4
Cu405_P_V1-3.txt	6900	8000	-	3900	200	2.1
Cu405_P_V4.txt	6900	6600	-	1700	210	3.1
Cu405_P_V5-6.txt	6900	7700	-	3200	210	4.3
Cu405_P_V5-6.txt	6900	7900	-	8000	290	2.6
Cu410						
LOD	40	61	-	4.6	6.6	0.47
CU410V13.txt	6900	9500	-	1800	400	6
CU410V30-31.txt	6900	11000	-	3300	410	4
CU410V30-31.txt	6900	11000	-	4900	360	5

Cu410	Na	K	Ca	Fe	Cu	Au
CU410V75.txt	6900	11000	-	3700	440	6
CU410V10-11.txt	6900	11000	-	4800	340	5
Cu411						
LOD	150	260	-	18	26	2.1
CU411V1-2.txt	6900	11000	-	4600	380	12
CU411V1-2.txt	6900	12000	-	4000	300	-
CU411V4.txt	6900	11000	-	2800	320	7
CU411V6-7.txt	6900	11000	-	5200	330	6
CU411V10-11.txt	6900	10000	-	5200	410	7
CU411V12-13.txt	6900	11000	-	4500	330	4
CU411V15-16.txt	6900	11000	-	4100	320	5
CU411V15-16.txt	6900	11000	-	4600	310	5
CU411V20.txt	6900	11000	-	5000	320	7
CU411V30-32.txt	6900	12000	-	5000	300	4
CU411V30-32.txt	6900	13000	-	6100	270	5
CU411V40-41.txt	6900	11000	-	5400	280	7
CU411V40-42.txt	6900	8400	-	2700	320	-
CU411V45-46.txt	6900	11000	-	4900	280	4

Vapor: X_{CO2}=0.38 Po-Saturated (ppm)   LOD = Average Limit of Detection (ppm)

Cu601	Na	K	Ca	Fe	Cu	Au
LOD	55	72	-	4.8	6.7	0.43
CU601V1.txt	2200	1700	-	420	58	1
CU601V4.txt	1900	2300	-	310	62	1
CU601V5-6.txt	1700	2300	-	490	53	1
CU601V9-10.txt	2000	2200	-	310	56	1
CU601V9-10.txt	1700	2400	-	460	44	0.5
CU601V11.txt	2100	1900	-	410	46	0.8
CU601V13.txt	2000	2400	-	130	57	-
CU601V16-17.txt	2100	1800	-	500	50	-
CU601V16-17.txt	2000	3000	-	1200	42	0.9
CU601V20-21.txt	1800	2300	-	450	50	1
CU601V20-21.txt	1700	2400	-	460	45	0.9
CU601V22-23.txt	1800	2300	-	420	51	1
CU601V22-23.txt	1700	2500	-	360	54	1
CU601V40.txt	1800	2400	-	400	51	1
Cu606						
LOD	43	83	-	6.1	8.5	0.63
CU606V1-3.txt	1900	2300	-	290	56	-
CU606V1-3.txt	1700	2600	-	290	41	-
CU606V4-6.txt	1800	2500	-	260	48	-
CU606V7-8.txt	1800	2400	-	290	52	-

Cu606	Na	K	Ca	Fe	Cu	Au
CU606V9-10.txt	1800	2400	-	350	45	-
CU606V20-21.txt	1700	2400	-	410	54	2
CU606V30.txt	1800	2300	-	460	57	2
Cu607						
LOD	23	38	-	2.7	3.5	0.3
CU607V2-3-1.txt	1400	2300	-	900	36	0
CU607V4-5.txt	1600	2200	-	760	33	2
CU607V4-5.txt	1300	2300	-	960	38	1
CU607V6.txt	1500	2300	-	790	32	1
CU607V44.txt	1500	2300	-	700	35	1

LA-ICPMS Analysis of Run Product Glasses

Glass: X$_{CO2}$=0.10 S-Free (ppm)   LOD = Average Limit of Detection (ppm)

Cu320	Na	Al	Si	K	Ca	Fe	Cu	Au
LOD	4.6	5.8	25	9.7	3.9	0.7	1.8	0.22
Cu320GLS10.txt	22000	79000	350000	57000	230	230	12	1
Cu320GLS11.txt	21000	79000	350000	54000	220	370	19	4
Cu320GLS2.txt	21000	77000	350000	56000	220	250	7.2	0
Cu320GLS3.txt	22000	78000	350000	59000	240	350	14	11
Cu320GLS6.txt	21000	75000	360000	57000	180	210	10	-
Cu321								
LOD	5.4	6.8	30	11	4.5	0.82	2.1	0.26
Cu321GLS2.txt	21000	77000	350000	56000	210	250	6.5	-
Cu321GLS1.txt	21000	78000	350000	56000	220	280	10	1
Cu321GLS3.txt	22000	78000	350000	59000	240	350	14	11
Cu321GLS5.txt	21000	75000	360000	57000	180	210	10	-
Cu321GLS10.txt	22000	78000	350000	58000	220	220	6.7	1
Cu321GLS11.txt	21000	81000	350000	56000	230	250	10	1
Cu326								
LOD	2.5	3.2	13	5.1	1.9	0.37	1	0.11
Cu328GLS1.txt	21000	84000	340000	77000	450	430	15	0.2
Cu328GLS2.txt	21000	75000	350000	61000	200	330	20	-
Cu328GLS3.txt	20000	70000	360000	57000	160	230	11	0.2
Cu328GLS4.txt	20000	70000	360000	59000	190	300	15	-
Cu328GLS7.txt	20000	70000	360000	59000	140	250	11	-
Cu351								
LOD	3.2	4.5	21	7.8	2.9	0.54	0.68	0.09
Glass351ax3.txt	22000	52000	360000	54000	16	22000	41	-
Glass351ax3.txt	22000	54000	360000	55000	16	19000	32	-
Glass351ax3.txt	23000	56000	360000	55000	18	18000	21	-
Glass351bx3.txt	23000	62000	350000	61000	18	16000	22	-
Glass351bx3.txt	22000	66000	360000	61000	35	7400	31	-
Cu330								
LOD	2	2.7	11	4.6	1.9	0.34	0.43	0.048
Cu330glass1.txt	20000	75000	350000	62000	140	250	14	-
Cu330glass3.txt	20000	76000	350000	62000	140	210	12	-
Cu330glass4.txt	20000	77000	350000	61000	150	220	14	-
Cu332								
LOD	4.1	3.4	20	5.6	3.8	0.42	0.55	0.055
Cu332glass1.txt	31000	300000	1900000	1700000	240	6300	88	-
Cu332glass2.txt	61000	540000	7600000	11000000	1600	540	26	-
Cu332glass3.txt	520000	2800000	3800000	2500000	560	1	15	-

Cu332	Na	Al	Si	K	Ca	Fe	Cu	Au
Cu332glass4.txt	26000	410000	550000	4300000	160	5400	5.1	-
Cu332glass5.txt	65000	7300000	18000000	11000000	1300	5700	160	-
Cu332glass6.txt	43000	820000	1300000	720000	650	2300	19	-

Glass: X_{CO_2}=0.38 S-Free (ppm)   LOD = Average Limit of Detection (ppm)

Cu500	Na	Al	Si	K	Ca	Fe	Cu	Au
LOD	6.1	7.3	50	15	6	1	1.3	0.15
Cu500glass1-5.txt	24000	76000	350000	59000	34	42	7.9	-
Cu500glass1-5.txt	21000	95000	320000	89000	45	27	15	-
Cu500glass1-5.txt	17000	40000	400000	35000	120	35	13	-
Cu500glass1-5.txt	24000	67000	360000	52000	37	36	9.8	-
Cu502								
LOD	7.3	8.2	56	16	6.4	1.2	1.4	0.16
Cu502glass1-5.txt	29000	72000	350000	61000	110	35	56	-
Cu502glass1-5.txt	25000	79000	350000	61000	50	28	14	-
Cu502glass1-5.txt	41000	61000	350000	63000	200	43	52	-
Cu502glass1-5.txt	24000	71000	360000	51000	40	72	17	-
Cu503								
LOD	68	130	310	55	-	5.3	0.33	-
Au06c01_AMS.txt	26000	63000	350000	62000	23000	23	24	-
Au06c02_AMS.txt	27000	59000	340000	69000	24000	24	26	-
Au06c04_AMS.txt	21000	58000	340000	85000	19000	64	67	-
Au06c05_AMS.txt	25000	60000	350000	68000	21000	66	72	-
Au06c03_AMS.txt	29000	62000	340000	80000	18000	65	69	-
Cu504								
LOD	290	590	1100	230	-	-	1.4	-
Au06c010_AMS.txt	23000	60000	360000	59000	11000	49	51	-
Au06c013_AMS.txt	24000	62000	360000	59000	11000	41	40	-
Au06c012_AMS.txt	22000	59000	360000	59000	11000	53	48	-
Au06c010_AMS.txt	23000	57000	360000	57000	11000	68	82	-
Cu505								
LOD	3.3	4.2	31	8.2	3.2	0.6	0.76	0.082
Cu505glass1-6.txt	22000	62000	360000	52000	30	14000	8	-
Cu505glass1-6.txt	21000	69000	350000	62000	33	12000	8.3	-
Cu505glass1-6.txt	21000	60000	360000	53000	34	14000	8.1	-
Cu505glass1-6.txt	22000	61000	360000	52000	33	14000	6.6	-
Cu505glass1-6.txt	21000	58000	360000	52000	39	15000	14	2.4
Cu505glass7-13.txt	21000	58000	370000	52000	40	15000	9.4	4.5
Cu505glass7-13.txt	21000	59000	370000	51000	30	11000	15	-
Cu505glass7-13.txt	21000	59000	360000	52000	37	15000	14	2.2
Cu505glass7-13.txt	20000	59000	360000	52000	110	15000	9.8	0.3
Cu505glass7-13.txt	20000	60000	360000	55000	39	15000	8.7	0.5

Cu505	Na	Al	Si	K	Ca	Fe	Cu	Au
Cu505glass7-13.txt	21000	60000	370000	51000	29	11000	17	-
Cu505glass7-13.txt	21000	58000	370000	52000	40	15000	8.1	2.5
Cu505glass20-26.txt	20000	60000	360000	53000	28	13000	7.8	-
Cu505glass20-26.txt	21000	59000	360000	52000	40	15000	16	3.8
Cu505glass20-26.txt	21000	63000	360000	54000	25	8900	16	0.6
Cu505glass20-26.txt	21000	63000	360000	54000	24	8900	10	0.6
Cu505glass20-26.txt	21000	64000	360000	55000	25	9300	12	2.9

Glass: X_{CO2}=0.10 Po-Saturated (ppm)   LOD = Average Limit of Detection (ppm)

Cu402	Na	Al	Si	K	Ca	Fe	Cu	Au
LOD	0.9	1.3	6.8	2.3	0.81	0.21	0.19	0.024
Glass402_90m.txt	27000	42000	350000	57000	600	46000	12	0.4
Glass402ax3.txt	26000	41000	350000	56000	620	48000	12	0.2
Glass402ax3.txt	26000	39000	360000	55000	620	48000	13	0.3
Glass402ax3.txt	25000	38000	360000	53000	560	44000	12	0.9
Glass402bx3.txt	23000	41000	360000	53000	430	36000	9.6	1
Glass402bx3.txt	23000	40000	360000	53000	450	38000	9.4	1.1
Glass402bx3.txt	24000	40000	360000	53000	550	43000	12	0.3
Cu404								
LOD	1.8	2.3	16	7.4	1.6	0.32	0.4	0.043
Cu404glass1-7.txt	23000	48000	360000	51000	210	38000	9.3	0.7
Cu404glass1-7.txt	23000	47000	360000	53000	200	39000	11	8
Cu404glass1-7.txt	23000	46000	360000	52000	200	39000	9.7	10.6
Cu404glass1-7.txt	24000	48000	360000	54000	200	37000	16	2
Cu404glass1-7.txt	23000	47000	360000	54000	190	37000	10	0.9
Cu404glass8-12.txt	24000	53000	350000	55000	190	34000	12	0.8
Cu404glass8-12.txt	23000	62000	340000	65000	160	35000	15	0.5
Cu404glass8-12.txt	26000	57000	350000	56000	77	30000	13	0.2
Cu404glass8-12.txt	25000	53000	350000	55000	78	32000	14	0.3
Cu405								
LOD	0.34	0.42	2.9	1	0.32	0.069	0.075	0.0082
Cu405glass1-6.txt	25000	54000	350000	56000	84	33000	14	0.6
Cu405glass1-6.txt	26000	57000	350000	56000	77	30000	13	0.1
Cu405glass1-6.txt	25000	53000	350000	55000	78	32000	14	0.3
Cu405glass1-6.txt	26000	57000	350000	57000	79	30000	13	13.3
Cu405glass1-6.txt	25000	53000	350000	56000	84	34000	14	17.3
Cu405glass1-6.txt	25000	51000	350000	55000	81	34000	14	1.2
Cu405glass7-12.txt	24000	52000	350000	56000	88	36000	15	14.4
Cu405glass7-12.txt	24000	50000	360000	54000	86	37000	14	0.9
Cu405glass7-12.txt	25000	52000	350000	55000	89	35000	15	0.2
Cu405glass7-12.txt	26000	59000	350000	59000	82	30000	13	6

Cu410	Na	Al	Si	K	Ca	Fe	Cu	Au
LOD	1.3	1.4	7	13	2.5	0.2	0.24	0.021
CU410GLASS1.txt	23000	62000	360000	150	60000	12000	13	4.3
CU410GLASS1b.txt	23000	66000	350000	220	63000	11000	18	13.3
CU410GLASS2-3.txt	25000	66000	350000	190	62000	12000	12	0.9
CU410GLASS2-3.txt	25000	66000	350000	170	62000	13000	13	0.2
CU410GLASS4-5.txt	22000	70000	360000	100	60000	3500	17	12
CU410GLASS4-5.txt	23000	62000	360000	150	60000	12000	13	4.2
Cu411								
LOD	0.87	0.84	4.3	4.9	1.6	0.12	0.16	0.012
CU411GLASS1-2.txt	23000	63000	360000	190	59000	12000	12	4.4
CU411GLASS1-2.txt	25000	67000	350000	230	61000	15000	12	0.2
CU411GLASS3.txt	25000	69000	350000	220	62000	11000	13	24
CU411GLASS3b.txt	25000	69000	350000	210	61000	11000	9.8	0
CU411GLASS4.txt	25000	66000	350000	170	62000	13000	13	0.2
CU411GLASS4b.txt	25000	66000	350000	190	62000	12000	12	0.9
CU411GLASSc.txt	24000	71000	350000	-	62000	14000	10	-

Glass: X_{CO_2}=0.38 Po-Saturated (ppm)   LOD = Average Limit of Detection (ppm)

Cu601	Na	Al	Si	K	Ca	Fe	Cu	Au
LOD	1.5	1.6	7.5	13	2.2	0.25	0.23	0.015
CU601GLASS1-4.txt	22000	50000	360000	210	58000	29000	26	0.1
CU601GLASS1-4.txt	22000	50000	360000	-	58000	29000	20	0.1
CU601GLASS1-4.txt	22000	50000	360000	190	61000	28000	21	0.2
CU601GLASS1-4.txt	22000	45000	360000	190	57000	32000	34	0.2
Cu606								
LOD	2.2	2.1	10	22	4.3	0.32	0.44	0.034
CU606GLASS1-4.txt	19000	51000	370000	120	52000	16000	26	0.1
CU606GLASS1-4.txt	23000	59000	360000	100	59000	18000	15	0
CU606GLASS1-4.txt	21000	49000	360000	210	55000	30000	19	0.1
CU606GLASS1-4.txt	21000	50000	360000	120	55000	25000	19	0
Cu607								
LOD	1.2	1.3	5.5	12	2.4	0.18	0.23	0.02
CU607GLASS1-2.txt	20000	47000	360000	190	58000	31000	22	0.3
CU607GLASS1-2.txt	20000	47000	360000	160	57000	30000	15	0.1
CU607GLASS3-4.txt	22000	48000	360000	180	58000	29000	18	0.2
CU607GLASS3-4.txt	23000	52000	360000	140	62000	27000	19	0.3

EPMA Analysis of Run-Product Pyrrhotite (wt%)
LOD = Average Limit of Detection (wt%)

Cu402	Fe	S	Cu	Total	
LOD	0.0085	0.0054	0.012		
Po402g1pt1	59.3	38.2	3.14	100.6	
Po402g1pt2	59.7	38.1	2.8	100.6	
Po402g1pt3	59.2	38.2	3.81	101.2	
Po402g1pt4	59.2	38.2	3.63	101.1	
Po402g2pt5	59.5	38.3	3.53	101.3	
Po402g2pt6	59.3	38.2	3.18	100.7	
Po402g2pt7	58.9	38.2	3.57	100.7	
Po402g2pt8	59.2	38	3.51	100.7	
Po402g2pt9	59.2	37.9	3.45	100.6	
Po402g3pt1	60.1	38.1	2.5	100.6	
Po402g3pt2	60	38.1	2.59	100.6	
Po402g3pt3	59.7	37.9	2.62	100.3	
Po402g3pt4	59.4	38.2	3.26	100.9	
Po402g3pt5	59.6	38.3	3.07	101	
Po402g3pt6	59.6	38.2	2.94	100.7	
Po402g4pt1	59.4	38	3.39	100.8	
Po402g4pt2	59.7	38.3	3.02	101.1	
Po402g4pt3	58.5	38.3	4.43	101.2	
Po402g4pt4	60	38.1	2.75	100.9	
Po402g5pt1	59	38.1	3.79	100.9	
Po402g5pt2	59.1	38.3	3.71	101.2	
Po402g5pt3	59.3	38.2	3.45	101	
Po402g6pt1	59.3	38.6	3.64	101.5	
Po402g6pt2	59.8	38.3	2.99	101.1	
Po402g6pt3	60	38.6	2.82	101.4	
Po402g7pt1	59.9	38.7	2.79	101.4	
Po402g7pt2	59.3	38.5	3.01	100.8	
Po402g7pt3	59.3	38.6	3.08	101	
Cu404	Fe	S	Cu	Au	Total
LOD	0.0039	0.0091	0.013	0.048	
Cu404-Po-1-3	59.9	38.5	2	0.0091	100.4
Cu404-Po-1-4	58.7	38.5	3.47	0.0056	100.6
Cu404-Po-1-6	59.4	38.4	2.99	-	100.8
Cu404-Po-1-7	59.3	38.1	3.13	0.0063	100.5
Cu404-Po-1-9	58.4	38.2	3.97	-	100.6
Cu404-Po-1-10	58.7	38.4	3.84	-	100.9
Cu404-Po-1-11	59.7	38.6	2.86	0.0159	101.2
Cu404-Po-2-1	58.7	38.5	3.47	0.0156	100.7
Cu404-Po-2-2	59.7	38.5	2.85	-	101

Cu404	Fe	S	Cu	Au	Total
Cu404-Po-2-3	59	38.3	3.6	0.0094	101
Cu404-Po-2-4	60.3	38.7	2.37	-	101.3
Cu404-Po-2-5	59.4	38.4	2.76	0.0058	100.6
Cu404-Po-2-6	60	38.4	2.65	-	101.1
Cu404-Po-2-7	59.6	38.7	2.88	0.0077	101.1
Cu404-Po-2-8	60.1	39	2.45	0.0184	101.5
Cu405					
Cu405-Po-1-1	59.7	38.4	2.62	-	100.7
Cu405-Po-1-2	60.2	38.3	2.13	-	100.6
Cu405-Po-1-3	59.6	38.5	2.86	-	101
Cu405-Po-1-4	59.3	38.3	2.64	-	100.3
Cu405-Po-1-5	58.7	38.1	2.76	0.0133	99.6
Cu405-Po-1-6	59.7	38.6	2.19	-	100.5
Cu405-Po-2-1	56.9	37.8	6.34	-	101
Cu405-Po-2-2	57.8	38	5.11	-	100.9
Cu405-Po-2-3	59.5	37.8	2.58	-	99.9
Cu405-Po-2-4	59.5	38.7	2.8	-	101
Cu405-Po-2-5	59.9	38	2.28	-	100.2
Cu405-Po-2-6	58.9	38.1	2.99	0.0166	100
Cu405-Po-2-7	59.4	38.2	3.16	0.0026	100.7
Cu405-Po-2-8	59.2	38.2	3.2	0.0016	100.7
Cu405-Po-2-9	59.8	38.3	2.67	0.0197	100.8
Cu405-Po-3-1	57.3	38.4	5.45	-	101.1
Cu405-Po-3-2	58.8	38.2	3.8	0.0023	100.8
Cu405-Po-3-3	60.1	38.2	2.11	-	100.4
Cu405-Po-3-4	58.9	38.7	3.34	-	100.9
Cu405-Po-3-5	59	38.8	3.15	-	100.9
Cu405-Po-3-6	59.6	38.4	2.75	-	100.7
Cu405-Po-3-7	59.7	38.5	2.54	0.0189	100.8
Cu405-Po-3-8	58.4	38.1	4.15	-	100.7
Cu410					
Cu410-Po-1-2	59.8	38.3	2.44	-	100.6
Cu410-Po-1-3	59.5	37.6	2.57	-	99.7
Cu410-Po-1-4	58.8	38	3.13	-	99.9
Cu410-Po-1-5	59.8	38.4	2.51	-	100.7
Cu410-Po-1-6	59	38	3.27	-	100.3
Cu410-Po-2-1	57.7	38	4.8	0.0094	100.5
Cu410-Po-2-2	60.2	38.3	2	-	100.5
Cu410-Po-2-3	59.8	38	2.73	-	100.5
Cu410-Po-2-4	59.1	37.8	3.2	-	100.2
Cu410-Po-2-5	58.3	38.1	4.24	-	100.7
Cu410-Po-2-6	59.5	38.2	2.66	-	100.4

Cu410	Fe	S	Cu	Au	Total
Cu410-Po-2-7	59.4	37.8	3.06	-	100.3
Cu410-Po-3-1	57.4	38	5.65	-	101.1
Cu410-Po-3-2	58.4	38.6	3.91	-	100.9
Cu410-Po-3-3	60.3	38.4	1.97	0.013	100.7
Cu410-Po-3-4	58.8	38.2	3.36	-	100.4
Cu410-Po-3-5	59.3	38.2	3.34	0.0079	100.8
Cu410-Po-3-6	59.5	38.6	2.98	0.0054	101.1
Cu410-Po-3-7	59.4	37.8	3.02	0.0077	100.2
Cu410-Po-3-8	59.7	38.4	2.65	-	100.7
Cu411					
Cu411-Po1-1	59.9	38.2	2.56	-	100.6
Cu411-Po1-2	59.2	38	3.5	0.0132	100.7
Cu411-Po1-3	59.8	37.9	2.72	-	100.4
Cu411-Po1-4	59.9	38.2	2.54	0.0242	100.7
Cu411-Po1-6	58.5	37.5	3.7	-	99.7
Cu411-Po2-1	59.5	38.6	3.02	0.0031	101.1
Cu411-Po2-2	59.5	38.2	2.84	-	100.5
Cu411-Po2-3	59.6	38.1	2.9	-	100.5
Cu411-Po2-4	59.2	38.1	3.43	-	100.7
Cu411-Po3-1	59.2	38.3	3.17	0.0129	100.8
Cu411-Po3-2	58.4	38.1	4.56	-	101.1
Cu411-Po3-4	58.5	37.7	4.28	0.0052	100.6
Cu411-Po3-5	58.8	38.4	3.84	0.0012	101
Cu411-Po3-6	58.4	37.6	3.5	-	99.4
Cu411-Po4-1	57.6	37.5	5.06	-	100.1
Cu411-Po4-2	60.7	37.8	1.61	-	100.1
Cu411-Po4-3	58.4	37.3	3.72	0.0012	99.4
Cu411-Po4-4	59.2	37.9	3.39	0.0066	100.5
Cu411-Po4-5	59.6	37.8	2.92	-	100.3
Cu411-Po4-6	59.5	38	3.19	-	100.7
Cu601					
Cu601-Po-1-1	60.5	38.4	1.88	-	100.8
Cu601-Po-1-2	60.6	38.5	2.01	0.0346	101.1
Cu601-Po-1-3	60.2	38.7	2.14	-	101.1
Cu601-Po-1-4	60.7	38.6	1.87	-	101.2
Cu601-Po-1-5	60.4	38.4	2.19	0.0121	101
Cu601-Po-1-6	60.5	38.5	1.86	-	100.9
Cu601-Po-1-7	60.7	38.4	2.06	0.0346	101.3
Cu601-Po-2-1	60.2	38.6	2.53	-	101.3
Cu601-Po-2-2	59.6	38	2.48	-	100.1
Cu601-Po-2-3	60.3	38.2	1.74	-	100.3
Cu601-Po-2-4	60.4	38.4	2.51	-	101.3

Cu601	Fe	S	Cu	Au	Total
Cu601-Po-2-5	60.1	38.5	2.22	0.0102	100.8
Cu601-Po-2-6	60.1	38.4	2.13	-	100.6
Cu601-Po-3-1	60	38.6	2.66	-	101.3
Cu601-Po-3-2	60.2	38.7	2.67	-	101.6
Cu601-Po-3-3	60.4	38.2	2.3	-	101
Cu601-Po-3-4	59.8	38.2	2.24	-	100.2
Cu601-Po-3-5	60	38.3	2.37	-	100.6
Cu601-Po-3-6	60	38.7	2.58	-	101.3
Cu601-Po-3-7	60.4	38.7	2.34	-	101.4
Cu601-Po-3-8	60.2	38.7	2.28	0.0018	101.1
Cu601-Po-3-9	59.7	37.7	2.26	0.0037	99.7
Cu601-Po-3-10	59.9	38.5	2.7	-	101.1
Cu606					
Cu606-Po-1-1	59.8	38.5	2.49	0.0023	100.8
Cu606-Po-1-2	59.7	38.4	2.66	-	100.8
Cu606-Po-1-3	60.1	38.9	2.47	-	101.5
Cu606-Po-1-4	60.1	38.5	2.6	-	101.2
Cu606-Po-1-5	60.4	39.1	2.79	-	102.3
Cu606-Po-1-6	60.4	38.7	2.08	-	101.1
Cu606-Po-1-7	60.1	38.7	2.45	-	101.3
Cu606-Po-1-8	60.2	38.7	2.42	-	101.4
Cu606-Po-1-9	59.7	38.6	2.52	-	100.9
Cu606-Po-1-10	59.6	38.3	2.22	-	100.1
Cu606-Po-2-1	59.6	38.8	2.35	-	100.8
Cu606-Po-2-2	60.1	38.7	2.3	-	101
Cu606-Po-2-3	59.5	38.7	2.42	-	100.7
Cu606-Po-2-4	60	38.8	2.26	0.0079	101.1
Cu606-Po-2-5	59.8	38.6	2.22	0.015	100.7
Cu606-Po-2-6	59.8	38.8	2.09	0.0079	100.7
Cu606-Po-2-7	60.3	38.7	1.76	-	100.7
Cu606-Po-2-8	60.2	38.7	1.74	-	100.6
Cu606-Po-2-9	59.9	39	2	-	100.9
Cu606-Po-3-1	59.2	38.2	3.1	-	100.5
Cu606-Po-3-2	59.2	38.1	2.93	-	100.2
Cu606-Po-3-3	59.5	38.2	3.08	-	100.8
Cu606-Po-3-4	58.3	38.4	3.37	0.043	100.1
Cu606-Po-3-5	60.1	38.4	2.3	-	100.8
Cu606-Po-3-6	59.5	38.3	3.1	0.0257	100.9
Cu606-Po-3-7	59.7	38.3	3.19	0.0146	101.2
Cu606-Po-3-8	60	38.4	2.73	-	101.1
Cu606-Po-3-9	59.7	38	2.87	-	100.6

Cu607	Fe	S	Cu	Au	Total
Cu607-Po-1-1	59.7	38.2	2.5	-	100.4
Cu607-Po-1-2	59.6	38.2	2.64	-	100.4
Cu607-Po-1-3	59.7	38.3	2.48	-	100.4
Cu607-Po-1-4	59.3	37.9	3.29	0.0185	100.6
Cu607-Po-1-5	60	38	2.14	-	100.2
Cu607-Po-1-6	59.8	38	2.54	-	100.3
Cu607-Po-2-1	60.7	38	1.65	-	100.4
Cu607-Po-2-2	59.7	38.1	2.79	-	100.6
Cu607-Po-2-3	55.8	37.6	6.63	0.0103	100
Cu607-Po-2-4	59.5	38.1	2.79	-	100.4
Cu607-Po-2-5	59.8	38.4	2.23	-	100.5
Cu607-Po-2-6	59.1	38.2	2.73	-	100
Cu607-Po-2-7	59.4	38.3	2.71	-	100.4
Cu607-Po-2-8	59.6	38.4	2.57	0.024	100.5
Cu607-Po-2-9	59.6	38.3	2.7	0.0179	100.6
Cu607-Po-2-10	59.4	37.7	2.73	0.0028	99.9
Cu607-Po-2-11	58.8	37.9	3.26	-	99.9
Cu607-Po-2-12	59.3	38.1	2.93	-	100.3
Cu607-Po-3-1	59.4	38.2	2.77	-	100.4
Cu607-Po-3-2	59.6	38.3	2.4	-	100.4
Cu607-Po-3-3	59.8	38.3	2.38	0.0056	100.5
Cu607-PoCp-1-1	60	38.1	2.5	-	100.6
Cu607-PoCp-1-2	60.2	38.7	2	-	100.9
Cu607-PoCp-1-3	60.2	38	2.07	-	100.2
Cu607-PoCp-1-4	60.5	38.1	1.6	0.0012	100.2
Cu607-PoCp-1-5	42.3	35.2	21.5	-	99
Cu607-PoCp-1-6	42.2	35.3	21.6	-	99.1
Cu607-PoCp-1-7	42.2	35.2	21.5	-	99
Cu607-PoCp-1-8	42	35.1	21.5	0.0155	98.7
Cu606					
Cu606-Po-1-1	59.8	38.5	2.49	0.0023	100.8
Cu606-Po-1-2	59.7	38.4	2.66	-	100.8
Cu606-Po-1-3	60.1	38.9	2.47	-	101.5
Cu606-Po-1-4	60.1	38.5	2.6	-	101.2
Cu606-Po-1-5	60.4	39.1	2.79	-	102.3
Cu606-Po-1-6	60.4	38.7	2.08	-	101.1
Cu606-Po-1-7	60.1	38.7	2.45	-	101.3
Cu606-Po-1-8	60.2	38.7	2.42	-	101.4
Cu606-Po-1-9	59.7	38.6	2.52	-	100.9
Cu606-Po-1-10	59.6	38.3	2.22	-	100.1
Cu606-Po-2-1	59.6	38.8	2.35	-	100.8
Cu606-Po-2-2	60.1	38.7	2.3	-	101

Cu606	Fe	S	Cu	Au	Total
Cu606-Po-2-3	59.5	38.7	2.42	-	100.7
Cu606-Po-2-4	60	38.8	2.26	0.0079	101.1
Cu606-Po-2-5	59.8	38.6	2.22	0.015	100.7
Cu606-Po-2-6	59.8	38.8	2.09	0.0079	100.7
Cu606-Po-2-7	60.3	38.7	1.76	-	100.7
Cu606-Po-2-8	60.2	38.7	1.74	-	100.6
Cu606-Po-2-9	59.9	39	2	-	100.9
Cu606-Po-3-1	59.2	38.2	3.1	-	100.5
Cu606-Po-3-2	59.2	38.1	2.93	-	100.2
Cu606-Po-3-3	59.5	38.2	3.08	-	100.8
Cu606-Po-3-4	58.3	38.4	3.37	0.043	100.1
Cu606-Po-3-5	60.1	38.4	2.3	-	100.8
Cu606-Po-3-6	59.5	38.3	3.1	0.0257	100.9
Cu606-Po-3-7	59.7	38.3	3.19	0.0146	101.2
Cu606-Po-3-8	60	38.4	2.73	-	101.1
Cu606-Po-3-9	59.7	38	2.87	-	100.6

EMPA Analysis of Run Product Glasses (wt%) LOD = Average Limit of Detection (wt%)

Cu320	Na$_2$O	K$_2$O	MgO	FeO	SiO$_2$	CaO	Al$_2$O$_3$	SO$_3$	Total
LOD	0.025	0.014	0.01	0.04	0.043	0.012	0.029	0.016	
33	2.9	6.4	0.03	0.04	73.4	0.03	12.8	0.01	95.5
34	2.7	6.4	0	-	73	0.03	12.4	0.03	94.6
35	2.7	6.5	0.02	0.04	72.9	0.02	12.5	-	94.7
36	2.9	6.4	0.02	-	72.5	0.02	12.7	0.01	94.6
37	2.9	6.6	0.03	0.03	73.1	0.03	12.7	0.01	95.4
38	2.8	6.4	-	-	73.7	0.03	12.5	0.02	95.4
39	2.8	6.3	0.03	-	73.3	0.03	12.5	-	95
40	2.6	6.4	0.01	0.04	72.4	0.04	12.1	-	93.6
41	2.6	6.3	0.02	0.04	72.9	0.03	11.8	-	93.7
43	2.8	6.5	0.02	0.05	73.1	0.02	12.5	0.02	94.9
44	2.4	6.4	0	0.08	72.6	0.01	12.3	-	93.9
Cu321									
10	2.4	6.9	-	0.03	72.9	0.02	11.9	0.05	94.2
11	2.4	6.8	0.03	0.02	72.4	0.02	11.9	-	93.6
12	2.5	6.8	0.01	0.02	73.1	0.01	11.8	-	94.3
13	2.2	7.7	0.02	-	72.3	0.01	13	-	95.3
15	2.5	6.6	0.02	0.03	73.2	0.03	11.8	0.01	94.2
16	2.4	6.8	0.03	0.03	72	0.02	12	0.02	93.3
17	2.3	6.8	0.05	-	73.4	0.02	12.1	-	94.6
18	2.5	7.4	0.01	-	72.3	0.01	12.6	-	94.8
19	2.2	6.9	0.03	0.06	72.3	0	11.6	0	93.1
Cu326									
20	2.4	6.9	0.01	0.04	73.2	0	11.9	0.02	94.5
21	2.1	8.1	0.04	0.06	71.8	0.02	12.9	0.01	95
22	2.4	6.9	0.02	-	72.8	-	11.8	0.04	93.9
23	2.5	6.8	0.02	0.07	73	0.02	12.3	-	94.8
27	2.2	6.7	-	-	72.6	0.02	12.1	0.05	93.7
28	2.2	6.9	0.02	0	73.3	0.01	11.4	0.03	93.9
29	2.7	6.7	0.01	0.03	73.4	0.03	11.9	0.01	94.8
30	2.2	7.3	0.01	0.04	71.9	0.01	12.2	-	93.6
31	2.4	6.8	0.01	0.03	73.3	0.01	11.8	-	94.2
32	2.3	8	0	-	71.9	0	12.7	-	95

Cu330	Na$_2$O	Cl	Al$_2$O$_3$	FeO	SiO$_2$	K$_2$O	CaO	SO$_3$	Total
LOD	0.025	0.0072	0.029	0.04	0.043	0.014	0.012	0.016	
30	2.1	0.2	11.6	0.07	74.8	6.2	0.01	-	95
31	2.3	0.15	12.4	0.01	72.8	7.1	0.01	0.01	94.8
32	2.4	0.21	11.9	-	73.6	6.3	0.02	0.01	94.4
33	2.3	0.24	11.9	-	73.7	6.2	0.01	0.02	94.4
35	2.2	0.21	12.2	0.02	72.8	6.7	0.01	-	94.1

Cu330	Na$_2$O	Cl	Al$_2$O$_3$	FeO	SiO$_2$	K$_2$O	CaO	SO$_3$	Total
36	2.3	0.21	11.7	0.04	74	6.5	0.03	-	94.6
37	2.1	0.21	11.7	0.04	73.3	6.1	0.02	0.01	93.4
39	2.2	0.19	11.2	-	73.9	6	0.03	0.03	93.6
Cu332									
40	2.3	0.21	11.8	-	72.8	6.5	0.03	-	93.6
41	2.3	0.19	12.2	-	72.6	6.9	0.04	-	94.2
42	2.2	0.19	11.5	-	72.5	6.3	0.01	-	92.6
43	2.2	0.2	11.9	0.02	73	6.2	-	0.01	93.6
44	2.4	0.19	11.7	0.02	73.7	6.4	-	0.02	94.3
46	2.3	0.2	12	0.03	73.4	6.4	0.02	0.02	94.2
47	2.4	0.26	11.6	-	73.1	6.5	0.01	0.01	93.8
48	2.4	0.32	11.2	0.01	73.7	6.1	0.03	-	93.7
49	2.2	0.22	11.7	0.01	72.4	6.5	0.02	-	92.9
Cu402									
20	2.2	0.55	7	5.8	72	4.2	0.09	0.06	91.8
21	2.3	0.61	7	5.88	71.7	4.1	0.09	0.02	91.6
22	2.4	0.57	7.6	5.35	71.9	4.4	0.08	0.01	92.1
23	1.8	0.42	6.2	3.97	74.5	4.1	0.06	-	91
24	1.7	0.37	7.2	3.91	73.7	3.8	0.03	0.02	90.7
25	2.1	0.4	8.3	3.3	74.2	5	0.05	0.03	93.3
26	2.4	0.24	10.1	1.24	74.1	5.6	0.01	-	93.7
27	2.4	0.35	9.9	2.77	72.6	5.3	0.03	-	93.3
28	2.3	0.39	9	3.49	72.9	5	0.02	-	93

Cu500	Na$_2$O	Cl	K$_2$O	FeO	SiO$_2$	Al$_2$O$_3$	Total
LOD	0.02	0.0084	0.023	0.04	0.042	0.015	
93	2.8	0.16	5.7	-	76	10.1	94.8
94	2.7	0.16	5.7	-	74.9	10.1	93.5
95	2.6	0.15	5.7	-	73.5	9.9	91.8
96	3.3	0.19	6.4	-	72.9	11.6	94.4
97	2.9	0.17	6.1	-	74.5	10.7	94.4
98	3.3	0.19	6.4	-	72.9	11.8	94.6
99	2.6	0.15	5.5	-	75	9.7	92.9
100	3.2	0.18	6.6	-	72.3	11.8	94.1
101	2.5	0.14	5.7	-	76	9.7	94
102	3.2	0.19	6.2	-	72.1	11.8	93.5
Cu502							
83	2.3	0.26	6	2.7	74.9	9.3	95.6
84	2.3	0.25	5.7	2.9	75.1	9.2	95.4
85	2.3	0.26	5.9	3	75.7	8.8	96
86	2.3	0.28	6	2.9	74.9	9.3	95.6
87	2.5	0.6	6.1	2.8	73.7	8.8	94.4
88	2.3	0.25	5.8	2.2	75.6	9	95.1

Cu502	Na$_2$O	Cl	K$_2$O	FeO	SiO$_2$	Al$_2$O$_3$	Total
90	2	0.32	5.7	3	73.7	8.6	93.4
91	1.8	0.29	5.1	3.1	73.7	8.6	92.6
92	1.9	0.26	4.9	3	73.3	8.8	92
Cu503							
22	2.3	0.26	6	2.3	73.9	9.4	94.2
23	2.3	0.26	6.2	2.3	74.3	9.1	94.3
24	2.3	0.23	7.3	2.2	72.6	10.7	95.3
25	2.3	0.24	8	2.5	71.3	11.5	95.7
26	2.3	0.22	6.2	2.4	74.6	9.3	95
27	2.5	0.24	6.3	2.5	73.6	9.4	94.4
28	2.5	0.25	6.1	2.7	74	9.1	94.6
29	2.5	0.28	6.2	2.5	74	9.7	95.1
32	2.3	0.27	6.1	2.5	73.9	9.2	94.3
33	2.3	0.23	6.1	2.4	74.3	9.6	94.8
34	2.4	0.28	6.1	2.7	74.1	9.4	94.9
Cu504							
6	3	0.34	6.4	2.6	71.6	10.9	94.8
7	2.9	0.33	6.6	2.5	71.8	11.2	95.2
8	3	0.32	6.6	2.5	71.5	11.2	94.9
9	2.9	0.3	6.4	2.6	72	10.6	94.7
10	2.9	0.32	6.5	2.4	72	10.9	94.9
11	2.6	0.3	6.1	2.9	72.6	9.7	94.2
12	2.6	0.34	6.3	2.9	73.2	10	95.2
13	2.5	0.33	6.4	3	72.7	9.9	94.7
14	2.9	0.35	6.3	2.7	72.1	10.2	94.5
15	3.1	0.32	6.8	2.2	70.5	11.9	94.8
16	3.4	0.35	6.9	2	70.5	12.6	95.6
17	2.5	0.28	6.1	2.7	74.1	9.7	95.2
18	2.5	0.28	6	2.6	74.4	9.6	95.2
Cu505							
35	2.5	0.25	5.9	1.8	75.3	9.5	95.3
36	2.5	0.25	5.9	1.9	74.8	9.7	95.1
38	2.2	0.27	5.6	1.9	74.8	9	93.7
39	2.3	0.23	5.8	1.9	74.8	9.1	94
40	2.4	0.24	5.9	2.1	75.1	9.7	95.4
41	2.5	0.26	5.9	2	74.8	9.4	94.8
42	2.5	0.24	6.1	1.2	75.2	10	95.2
43	2.3	0.25	6	1.6	74.8	9.7	94.6
44	2.5	0.22	6.1	0.9	75.1	10.3	95
45	2.5	0.2	6	0.9	76.6	9.8	95.9
47	2.5	0.25	5.9	1.6	74.9	9.7	94.8
48	2.4	0.27	6.1	1.5	74.9	10.2	95.2

Cu505	Na$_2$O	Cl	K$_2$O	FeO	SiO$_2$	Al$_2$O$_3$	Total
50	2.5	0.23	6.1	1.3	75.4	9.9	95.4
Cu404							
68	1.9	0.43	4.4	5.3	72.7	7.5	92.1
69	2.1	0.4	4.8	5.4	73	7.6	93.2
70	2.2	0.46	4.8	5.3	72.9	7.8	93.3
71	2.1	0.47	4.6	5.6	72.5	7.4	92.5
72	2	0.43	4.4	5.3	72.6	7.5	92.2
73	2.1	0.43	4.9	5.1	72.5	7.9	92.8
74	2.3	0.4	5.1	4.5	71.9	8.8	92.9
75	2.2	0.4	5.2	4.3	72.2	8.4	92.5
76	2.2	0.39	5.1	4.2	71.8	8.6	92.1
77	2.3	0.42	5.2	4.8	71.8	8.3	92.8
78	2	0.46	5.1	5.6	72.8	7.5	93.4
79	2	0.45	5.1	5.5	72.2	7.9	93.1
81	2.1	0.39	4.5	4.8	71.9	8.3	92
82	1.9	0.43	4.1	5.7	73	7.1	92.2
Cu405							
51	2.4	0.49	4.9	4.7	72.2	8.8	93.5
52	2.5	0.44	5.6	4.5	72.3	8.8	94.1
53	2.5	0.43	5.6	4.3	72.4	8.7	93.9
54	2.5	0.46	5.2	4.8	73.1	8.5	94.4
55	2.5	0.45	5.6	4.4	71.7	9.3	93.9
56	2.4	0.45	5.4	4.8	72.5	8.6	94.1
57	2.2	0.52	5	5.3	72.4	7.6	93
58	2	0.49	4.7	5.4	72.4	7.6	92.5
59	2	0.48	4.8	5.4	73	7.7	93.3
60	2.4	0.47	5.4	4.6	72.2	8.6	93.5
61	2.4	0.44	5.3	4.8	71.7	8.6	93.1
62	2.6	0.4	6.1	3.5	70.9	10.5	93.9
63	2.4	0.45	5.8	4.2	71.4	9.8	93.9
64	2.4	0.5	5.2	5.2	73	8.3	94.5
65	2.4	0.48	5.4	5	72.5	8.6	94.2
66	2.3	0.48	5	5.1	72.1	8.3	93.1
67	2.4	0.47	5.5	4.5	72.1	8.8	93.7
Cu410							
9	2.8	6.5	1.1	72.3	0.1	11.7	94.4
10	2.7	6.5	1.5	72.1	0.07	11.3	94.2
11	2.9	6.5	0.8	71.8	0.09	11.5	93.6
12	2.5	6.3	0.6	72.9	0.05	11.7	94.1
13	2.8	6.6	1	72.4	0.08	11.5	94.4
14	2.8	6.8	1.2	71.9	0.05	11.4	94.1
15	2.9	6.7	0.6	72.8	0.06	11.7	94.9

Cu410	Na$_2$O	Cl	K$_2$O	FeO	SiO$_2$	Al$_2$O$_3$	Total
16	2.7	6.8	1	71.8	0.06	11.8	94.1
Cu411							
1	3	6.5	1.6	72.5	0.09	10.7	94.3
2	3	6.7	2	71	0.13	11.1	93.8
3	3.1	6.9	1.3	71.6	0.09	11.4	94.4
4	3	6.6	1.9	71.4	0.09	10.6	93.7
5	2.8	6.4	0.5	72.9	0.08	12	94.7
6	2.6	6.3	2.4	72.3	0.1	9.9	93.5
7	2.9	6.9	2.1	71.4	0.09	10.9	94.3
8	2.8	6.5	1.5	71.2	0.1	11.2	93.3
Cu601							
25	2.6	6.2	3.6	72.4	0.02	8.4	93.2
26	2.5	6.1	1.2	73.8	0.03	9.3	93
27	2.4	6.1	0.3	75.2	0.01	10	94
29	3	6.6	1.3	71.3	0.01	11.1	93.3
31	2.3	6.1	0.2	74.8	0.02	9.6	93
32	2.4	6	0.2	74.4	0.01	9.5	92.5
33	2.8	6.7	1.3	70.9	0.01	10.5	92.5
Cu606							
44	2.4	5.6	1.3	75.4	0.01	9.8	93.8
45	2.5	6	2.4	73	0.01	9.2	93.1
46	2.6	6	1.3	74.1	0.01	9.4	93.5
47	2.3	5.8	1.9	74	-	9.4	93.3
48	2.4	5.8	2.5	73.6	-	8.8	93.1
49	2.7	6	2.3	74.4	0.01	9.1	94.5
50	2.4	5.8	2.7	73.1	-	8.6	92.6
Cu607							
17	2.5	6.2	3.1	72.7	-	8.3	93.3
18	2.6	6.3	3.6	72.6	0.01	8.4	93.5
19	2.8	6.3	2.7	70.6	-	10.4	93.3
20	2.7	6.5	2.9	71.5	-	9.4	93.1
21	2.6	6	3.8	72.3	0.01	7.7	92.6
22	2.8	6.4	2.9	71.4	-	9.5	93.1
23	2.7	6.2	3.3	73.4	0.02	8.5	94.2
24	2.2	6.3	2.6	70.4	0.02	9.9	92

References

Alletti, M., Baker, D. R., Scaillet, B., Aiuppa, A., Moretti, R., Ottolini, L., 2009. Chlorine partitioning between a basaltic melt and H_2O-CO_2 fluids at Mount Etna. Chemical Geology, 263(1-4): 37-50.

Anderson, A.T., Newman, S., Williams, S. N., Druitt, T. H., Skirius, C., Stolper, E., 1989. H_2O, CO_2, Cl, and gas in plinian and ash-flow bishop rhyolite. Geology, 17(3): 221-225.

Annen, C., Blundy, J.D., Sparks, R.S.J., 2006. The genesis of intermediate and silicic magmas in deep crustal hot zones. Journal of Petrology, 47(3): 505-539.

Audetat, A., Dolejs, D., Lowenstern, J.B., 2011. Molybdenite Saturation in Silicic Magmas: Occurrence and Petrological Implications. Journal of Petrology, 52(5): 891-904.

Audetat, A., Gunther, D., Heinrich, C.A., 1998. Formation of a magmatic-hydrothermal ore deposit: Insights with LA-ICP-MS analysis of fluid inclusions. Science, 279(5359): 2091-2094.

Audetat, A., Pettke, T., Heinrich, C.A., Bodnar, R.J., 2008. The Composition of Magmatic-Hydrothermal Fluids in Barren and Mineralized Intrusions. Economic Geology, 103(5): 877-908.

Avlonitis, D., 2005. An investigation of gas hydrates formation energetics. Aiche Journal, 51(4): 1258-1273.

Azbej, T., Severs, M.J., Rusk, B.G., Bodnar, R.J., 2007. In situ quantitative analysis of individual H_2O-CO_2 fluid inclusions by laser Raman spectroscopy. Chemical Geology, 237(3-4): 255-263.

Baker, D.R., Balcone-Boissard, H., 2009. Halogen diffusion in magmatic systems: Our current state of knowledge. Chemical Geology, 263(1-4): 82-88.

Bakker, R.J., 2003. Package FLUIDS 1. Computer programs for analysis of fluid inclusion data and for modelling bulk fluid properties. Chemical Geology, 194(1-3): 3-23.

Bakker, R.J., Brown, P.E., 2003. Computer modeling in fluid inclusion research. Fluid inclusions analysis and interpretation: Mineralogical Association of Canada: Short Course V.32(Ch. 7): 175-212.

Bakker, R.J., Diamond, L.W., 2000. Determination of the composition and molar volume of H_2O-CO_2 fluid inclusions by microthermometry. Geochimica et Cosmochimica Acta, 64(10): 1753-1764.

Behrens, H., Gaillard, F., 2006. Geochemical aspects of melts: Volatiles and redox behavior. Elements, 2(5): 275-280.

Behrens, H., Ohlhorst, S., Holtz, F., Champenois, M., 2004. CO_2 solubility in dacitic melts equilibrated with H_2O-CO_2 fluids: Implications for modeling the solubility of CO2 in silicic melts. Geochimica et Cosmochimica Acta, 68(22): 4687-4703.

Bierlein, J.A., Kay, W.B., 1953. Phase-equilibrium properties of the system carbon dioxide-hydrogen sulfide. Industrial and Engineering Chemistry, 45(3): 618-624.

Bodnar, R.J., 1995. Fluid inclusion evidence for a magmatic source for metals in porphyry copper deposits. Magmas, Fluids and Ore Deposits. Thompson JFH (ed) Mineralogical Association of Canada Short Course, 23: 139-152.

Bodnar, R.J., Burnham, C.W., Sterner, S.M., 1985. Synthetic fluid inclusions in natural quartz. 3.Determination of phase-equilibrium properties in the system H_2O-NaCl to 1000 ^{o}C and 1500 bars. Geochimica et Cosmochimica Acta, 49(9): 1861-1873.

Bodnar, R.J., Sterner, S.M., 1985. Synthetic fluid inclusions in natural quartz. II. Application to PVT studies. Geochimica et Cosmochimica Acta, 49(9): 1855-1859.

Bond, D.C., Russell, N.B., 1949. Effect of antifreeze agents on the formation of hydrogen sulphide hydrate. Transactions of the American Institute of Mining and Metallurgical Engineers, 179: 192-198.

Botcharnikov, R., Freise, M., Holtz, F., Behrens, H., 2005. Solubility of C-O-H mixtures in natural melts: new experimental data and application range of recent models. Annals of Geophysics, 48(4-5): 633-646.

Candela, P.A., Holland, H.D., 1984. The partitioning of copper and molybdenum between silicate melts and aqueous fluids. Geochimica et Cosmochimica Acta, 48(2): 373-380.

Candela, P.A., Piccoli, P.M., 2005. Magmatic processes in the development of porphyry-type ore systems. Economic Geology, 100th Anniversary Volume: 25-38.

Candela, P.M., Piccoli, P.M., 1998. Magmatic contributions to hydrothermal ore deposits: An algorithm (MVPart) for calculating the composition of the magmatic volatile phase. Techniques in Hydrothermal Ore Deposits Geology, 10: 97-108.

Candela, P.A., Piccoli, P.M., 1995. An experimental-theoretical model of brine-vapor-silicate melt equilibria with applications to geothermal and ore-forming systems. Magmas, Fluids and Ore Deposits, Thompson, J.F.H. (ed.). Mineralogical Association of Canada Short Course, 23: 101-127.

Chou, I.M., 1987. Oxygen buffer and hydrogen sensor techniques at elevated pressures and temperatures. Hydrothermal Experimental Techniques. Ch. 3: 61-98.

Churakov, S.V., Gottschalk, M., 2003. Perturbation theory based equation of state for polar molecular fluids: II. Fluid mixtures. Geochimica et Cosmochimica Acta, 67(13): 2415-2425.

Clemente, B., Scaillet, B., Pichavant, M., 2004. The solubility of sulphur in hydrous rhyolitic melts. Journal of Petrology, 45(11): 2171-2196.

de Leeuw, G.A.M., Hilton, D.R., Fischer, T.P., Walker, J.A., 2007. The He-CO_2 isotope and relative abundance characteristics of geothermal fluids in El Salvador and Honduras: New constraints on volatile mass balance of the Central American Volcanic Arc. Earth and Planetary Science Letters, 258(1-2): 132-146.

Deubener, J., Muller, R., Behrens, H., Heide, G., 2003. Water and the glass transition temperature of silicate melts. Journal of Non-Crystalline Solids, 330(1-3): 268-273.

Diamond, L.W., 1994. Salinity of multivolatile fluid inclusions determined from clathrate hydrate stability. Geochimica et Cosmochimica Acta, 58(1): 19-41.

Diamond, L.W., 2003. Introduction to gas-bearing, aqueous fluid inclusions. Mineralogical Association of Canada, Short Course 32: Fluid Inclusions, Analysis and Interpretation: 101-158.

Dilles, J.H., Solomon, G.C., Taylor, H.P., Einaudi, M.T., 1992. Oxygen and hydrogen isotope characteristics of hydrothermal alteration at the Ann-Mason porphyry copper-deposit, Yerrigton, Nevada. Economic Geology, 87(1): 44-63.

Duan, Z.H., Moller, N., Weare, J.H., 1995. Equation of state for the NaCl-H_2O-CO_2 system - Prediction of phase-equilibria and volumetric properties. Geochimica et Cosmochimica Acta, 59(14): 2869-2882.

Duan, Z.H., Sun, R., 2003. An improved model calculating CO_2 solubility in pure water and aqueous NaCl solutions from 273 to 533 K and from 0 to 2000 bar. Chemical Geology, 193(3-4): 257-271.

Duan, Z.H., Sun, R., 2006. A model to predict phase equilibrium of CH_4 and CO_2 clathrate hydrate in aqueous electrolyte solutions. American Mineralogist, 91(8-9): 1346-1354.

Duan, Z.H., Sun, R., Zhu, C., Chou, I.M., 2006. An improved model for the calculation of CO_2 solubility in aqueous solutions containing Na^+, K^+, Ca^{2+}, Mg^{2+}, Cl^-, and $SO_4^{(-2)}$. Marine Chemistry, 98(2-4): 131-139.

Eugster, H.P., Baumgartner, L., 1987. Mineral solubilities and speciation in supercritical metamorphic fluids. Reviews in Mineralogy, 17: 367-403.

Fall, A., Tattitch, B., Bodnar, R.J., 2011. Combined microthermometric and Raman spectroscopic technique to determine the salinity of H_2O-CO_2-NaCl fluid inclusions based on clathrate melting. Geochimica et Cosmochimica Acta, 75(4): 951-964.

Field, C.W., Zhang, L., Dilles, J.H., Rye, R.O., Reed, M.H., 2005. Sulfur and oxygen isotopic record in sulfate and sulfide minerals of early, deep, pre-Main Stage porphyry Cu-Mo and late Main Stage base-metal mineral deposits, Butte district, Montana. Chemical Geology, 215(1-4): 61-93.

Fischer, T.P., 2008. Fluxes of volatiles (H_2O, CO_2, N_2, Cl, F) from arc volcanoes. Geochemical Journal, 42(1): 21-38.

Frank, M.R., 2001. An experimental investigation of ore metals in silicate melt-volatile phase systems. Ph.D. dissertation, University of Maryland.

Frank, M.R., Candela, P.A., Piccoli, P.M., 2003. Alkali exchange equilibria between a silicate melt and coexisting magmatic volatile phase: An experimental study at 800 ^{o}C and 100 MPa. Geochimica et Cosmochimica Acta, 67(7): 1415-1427.

Frank, M.R., Simon, A.C., Pettke, T., Candela, P.A., Piccoli, P.M., 2011. Gold and copper partitioning in magmatic-hydrothermal systems at 800 ^{o}C and 100 MPa. Geochimica et Cosmochimica Acta, 75(9): 2470-2482.

Geiger, S., Driesner, T., Heinrich, C.A., Matthai, S.K., 2005. On the dynamics of NaCl-H_2O fluid convection in the Earth's crust. Journal of Geophysical Research-Solid Earth, 110(B7).

Gunther, D., Audetat, A., Frischknecht, R., Heinrich, C.A., 1998. Quantitative analysis of major, minor and trace elements in fluid inclusions using laser ablation inductively coupled plasma mass spectrometry. Journal of Analytical Atomic Spectrometry, 13(4): 263-270.

Halter, W., Heinrich, C., Pettke, T., 2005. Magma evolution and the formation of porphyry Cu-Au ore fluids: evidence from silicate and sulfide melt inclusions. Mineralium Deposita, 39(8): 845-863.

Halter, W.E. et al., 2004. From andesitic volcanism to the formation of a porphyry Cu-Au mineralizing magma chamber: the Farallon Negro Volcanic Complex, northwestern Argentina. Journal of Volcanology and Geothermal Research, 136(1-2): 1-30.

Harris, A.C., Golding, S.D., White, N.C., 2005. Bajo de la Alumbrera copper-gold deposit: Stable isotope evidence for a porphyry-related hydrothermal system dominated by magmatic aqueous fluids. Economic Geology, 100(5): 863-886.

Hattori, K.H., Keith, J.D., 2001. Contribution of mafic melt to porphyry copper mineralization: evidence from Mount Pinatubo, Philippines, and Bingham Canyon, Utah, USA. Mineralium Deposita, 36(8): 799-806.

Hedenquist, J.W., Lowenstern, J.B., 1994. The role of magmas in the formation of hydrothermal ore-deposits. Nature, 370(6490): 519-527.

Heinrich, C., 2005. The physical and chemical evolution of low-salinity magmatic fluids at the porphyry to epithermal transition: a thermodynamic study. Mineralium Deposita, 39(8): 864-889.

Heinrich, C.A., Driesner, T., Landtwing, M.R., 2004. Boiling, condensation and vapour contraction in magmatic-hydrothermal Cu-Au ore systems. Geochimica et Cosmochimica Acta, 68(11): A295-A295.

Heinrich, C.A., Gunther, D., Audetat, A., Ulrich, T., Frischknecht, R., 1999. Metal fractionation between magmatic brine and vapor, determined by microanalysis of fluid inclusions. Geology, 27(8): 755-758.

Heinrich, C.A. et al., 2003. Quantitative multi-element analysis of minerals, fluid and melt inclusions by laser-ablation inductively-coupled-plasma mass-spectrometry. Geochimica et Cosmochimica Acta, 67(18): 3473-3497.

Heinrich, C.A., Ryan, C.G., Mernagh, T.P., Eadington, P.J., 1992. Segregation of ore metals between magmatic brine and vapor - A fluid inclusion study using PIXE microanalysis. Economic Geology, 87(6): 1566-1583.

Herri, J.M. et al., 2011. Gas hydrate equilibria for CO_2-N_2 and CO_2-CH_4 gas mixtures-Experimental studies and thermodynamic modelling. Fluid Phase Equilibria, 301(2): 171-190.

Higgins, J., Zhou, X.F., Liu, R.F., Huang, T.T.S., 1997. Theoretical study of thermal decomposition mechanism of oxalic acid. Journal of Physical Chemistry A, 101(14): 2702-2708.

Hildreth, W., Wilson, C.J.N., 2007. Compositional zoning of the Bishop Tuff. Journal of Petrology, 48(5): 951-999.

Holland, H.D., 1965. Some applications of thermochemical data to problems of ore deposits; [Part] 2, Mineral assemblages and the composition of ore forming fluids Economic Geology 60: 1101-1166.

Holland, H.D., 1972. Granites, solutions, and base metal deposits. Economic Geology, 67(3): 281-301.

Holtz, F., Behrens, H., Dingwell, D.B., Johannes, W., 1995. H_2O solubility in haplogranite melts - compositional, pressure, and temperature-dependence. American Mineralogist, 80(1-2): 94-108.

Imai, A., 2000. Mineral paragenesis, fluid inclusions and sulfur isotope systematics of the Lepanto Far Southeast porphyry Cu-Au deposit, Mankayan, Philippines. Resource Geology, 50(3): 151-168.

Jarrard, R.D., 2003. Subduction fluxes of water, carbon dioxide, chlorine, and potassium. Geochemistry Geophysics Geosystems, 4(5): 1-50.

John, D.A. et al., 2010. Porphyry copper deposit model, chap. B of Mineral deposit models for resource assessment. U.S. Geological Survey Scientific Investigations Report 2010–5070–B: 1-169.

Johnson, J.W., Oelkers, E.H., Helgeson, H.C., 1992. SUPCRT92 - A software package for calculating the standard molal thermodynamic properties of minerals, gases, aqueous species, and reactions from 1-bar to 5000 bar and 0 $^{\circ}$C to 1000 $^{\circ}$C. Computers & Geosciences, 18(7): 899-947.

Jugo, P.J., Candela, P.A., Piccoli, P.M., 1999. Magmatic sulfides and Au : Cu ratios in porphyry deposits: an experimental study of copper and gold partitioning at 850 $^{\circ}$C, 100 MPa in a haplogranitic melt pyrrhotite intermediate solid solution gold metal assemblage, at gas saturation. Lithos, 46(3): 573-589.

Kawakami, Y., Yamamoto, J., Kagi, H., 2003. Micro-raman densimeter for CO_2 inclusions in mantle-derived minerals. Applied Spectroscopy, 57(11): 1333-1339.

Kodera, P., Murphy, P.J., Rankin, A.H., 2003. Retrograde mineral reactions in saline fluid inclusions: The transformation ferropyrosmalite <-> clinopyroxene. American Mineralogist, 88(1): 151-158.

Kruger, Y., Diamond, L.W., 2001. Unexpected behaviour of fluid inclusions synthesized from silver oxalate and an aqueous NaCl solution. Chemical Geology, 173(1-3): 159-177.

Leeman, W.P., Carr, M.J., Morris, J.D., 1994. Boron geochemistry of the Central-American volcanic arc - Constraints on the genesis of subduction-related magmas. Geochimica et Cosmochimica Acta, 58(1): 149-168.

Lemmon, E.W., McLinden, M.O., Friend, D.G., 2012. "Thermophysical Properties of Fluid Systems" in NIST Chemistry WebBook, NIST Standard Reference Database Number 69, Eds. P.J. Linstrom and W.G. Mallard. National Institute of Standards and Technology, Gaithersburg MD, 20899.

Lerchbaumer, L., Audetat, A., 2009. Partitioning of Cu between vapor and brine - An experimental study based on LA-ICP-MS analysis of synthetic fluid inclusions. Geochimica et Cosmochimica Acta, 73(13): A744-A744.

Li, H.L., Jakobsen, J.P., Wilhelmsen, O., Yan, J.Y., 2011. PVTxy properties of CO_2 mixtures relevant for CO_2 capture, transport and storage: Review of available experimental data and theoretical models. Applied Energy, 88(11): 3567-3579.

Liu, Y., Zhang, Y.X., Behrens, H., 2005. Solubility of H_2O in rhyolitic melts at low pressures and a new empirical model for mixed H_2O-CO_2 solubility in rhyolitic melts. Journal of Volcanology and Geothermal Research, 143(1-3): 219-235.

Lowenstern, J.B., 1994. Dissolved volatile concentrations in an ore-forming magma. Geology, 22(10): 893-896.

Lowenstern, J.B., 2000. A review of the contrasting behavior of two magmatic volatiles: chlorine and carbon dioxide. Journal of Geochemical Exploration, 69: 287-290.

Lowenstern, J.B., 2001. Carbon dioxide in magmas and implications for hydrothermal systems. Mineralium Deposita, 36(6): 490-502.

Lynton, S.J., Candela, P.A., Piccoli, P.M., 1993. An experimental-study of the partitioning on copper between pyrrhotite and a high-silica rhyolitic melt. Economic Geology, 88(4): 901-915.

Mengason, M.J., 2007. Experimental study of the partitioning of copper, silver, gold, molybdenum, and tungsten among pyrrhotite and immiscible iron-sulfur-oxygen

and silicate melts. M.S. dissertation, University of Maryland, College Park, United States - Maryland.: 113 pages

Mengason, M.J., Piccoli, P.M., Candela, P., 2010. An evaluation of the effect of copper on the estimation of sulfur fugacity (f(S_2)) from pyrrhotite composition. Economic Geology, 105(6): 1163-1169.

Mengason, M.J., Piccoli, P.M., Candela, P.A., 2008. Impact of sulfide separation on Ag and Mo budgets in arc magmas. Geochimica et Cosmochimica Acta, 72(12): A620-A620.

Morizet, Y., Brooker, R.A., Kohn, S.C., 2002. CO_2 in haplo-phonolite Melt: Solubility, speciation and carbonate complexation. Geochimica et Cosmochimica Acta, 66(10): 1809-1820.

Murakami, H., Seo, J.H., Heinrich, C.A., 2010. The relation between Cu/Au ratio and formation depth of porphyry-style Cu-Au +/- Mo deposits. Mineralium Deposita, 45(1): 11-21.

Mutchler, S., Fedele, L., Bodnar, R., 2008. Analysis Management System (AMS) for reduction of laser ablation ICPMS data. Laser-Ablation-ICPMS in the Earth Sciences: Current Practices and Outstanding Issues (P. Sylvester, ed.) Mineralogical Association of Canada Short Course Series, 40: 318-327.

Nagaseki, H., Hayashi, K., 2008. Experimental study of the behavior of copper and zinc in a boiling hydrothermal system. Geology, 36(1): 27-30.

Nagaseki, H., Hayashi, K., Iida, A., 2006. Quantitative analysis of fluid inclusions by synchrotron X-ray fluorescence: calibration of Cu and Zn in synthetic quartz inclusions. European Journal of Mineralogy, 18(3): 309-318.

Newman, S., Lowenstern, J.B., 2002. VOLATILECALC: a silicate melt-H_2O-CO_2 solution model written in Visual Basic for excel. Computers & Geosciences, 28(5): 597-604.

Nowak, M., Behrens, H., 1995. The speciation of water in haplogranite glasses and melts determined by in-situ near-infrared spectroscopy. Geochimica et Cosmochimica Acta, 59(16): 3445-3450.

Ohmoto, H., Kerrick, D., 1977. Devolatilization equilibria in graphitic systems. American Journal of Science, 277(8): 1013-1044.

O'Neill, H.S., 1988. Systems Fe-O and Cu-O - Thermodynamic data for the equilibria Fe-FeO, Fe-Fe_3O_4, FeO-Fe_3O_4, Fe_3O_4, Fe_2O_3, Cu-Cu_2O, and Cu_2O-CuO from EMF-measurements. American Mineralogist, 73(5-6): 470-486.

Pasteris, J.D., Kuehn, C.A., Bodnar, R.J., 1986. Applications of the laser Raman microprobe Ramanor U-1000 to hydrothermal ore-deposits - Carlin as an example. Economic Geology, 81(4): 915-930.

Pettke, T., Oberli, F., Heinrich, C.A., 2010. The magma and metal source of giant porphyry-type ore deposits, based on lead isotope microanalysis of individual fluid inclusions. Earth and Planetary Science Letters, 296(3-4): 267-277.

Pokrovski, G.S., Borisova, A.Y., Harrichoury, J.C., 2008. The effect of sulfur on vapor-liquid fractionation of metals in hydrothermal systems. Earth and Planetary Science Letters, 266(3-4): 345-362.

Pokrovski, G.S., Dubrovinsky, L.S., 2011. The S_3(-) Ion Is Stable in Geological Fluids at Elevated Temperatures and Pressures. Science, 331(6020): 1052-1054.

Pokrovski, G.S., Roux, J., Harrichoury, J.C., 2005. Fluid density control on vapor-liquid partitioning of metals in hydrothermal systems. Geology, 33(8): 657-660.

Pokrovski, G.S. et al., 2009a. An in situ X-ray absorption spectroscopy study of gold-chloride complexing in hydrothermal fluids. Chemical Geology, 259(1-2): 17-29.

Pokrovski, G.S., Tagirov, B.R., Schott, J., Hazemann, J.L., Proux, O., 2009b. A new view on gold speciation in sulfur-bearing hydrothermal fluids from in situ X-ray absorption spectroscopy and quantum-chemical modeling. Geochimica et Cosmochimica Acta, 73(18): 5406-5427.

Proffett, J.M., 2003. Geology of the Bajo de la Alumbrera porphyry copper-gold deposit, Argentina. Economic Geology, 98(8): 1535.

Redmond, P.B., Einaudi, M.T., Inan, E.E., Landtwing, M.R., Heinrich, C.A., 2004. Copper deposition by fluid cooling in intrusion-centered systems: New insights from the Bingham porphyry ore deposit, Utah. Geology, 32(3): 217-220.

Roedder, E., 1971. Fluid inclusion studies on porphyry-type ore deposits at Bignham, Utah, Butte, Montana, and Climax, Colorado. Economic Geology, 66(1): 98-120.

Rudnick, R.L., Gao, S., 2004. Composition of the Continental Crust. In: Treatise on Geochemistry. Holland, H.D. and Turekian, K.K> (Editors), Elsevier, Amsterdam(3): 1-64.

Rusk, B.G., Reed, M.H., Dilles, J.H., 2008. Fluid inclusion evidence for magmatic-hydrothermal fluid evolution in the porphyry copper-molybdenum deposit at Butte, Montana. Economic Geology, 103(2): 307-334.

Rusk, B.G., Reed, M.H., Dilles, J.H., Klemm, L.M., Heinrich, C.A., 2004. Compositions of magmatic hydrothermal fluids determined by LA-ICP-MS of fluid inclusions from the porphyry copper-molybdenum deposit at Butte, MT. Chemical Geology, 210(1-4): 173-199.

Sano, Y., Williams, S.N., 1996. Fluxes of mantle and subducted carbon along convergent plate boundaries. Geophysical Research Letters, 23(20): 2749-2752.

Schmidt, C., Bodnar, R.J., 2000. Synthetic fluid inclusions: XVI. PVTX properties in the system H_2O-NaCl-CO_2 at elevated temperatures, pressures, and salinities. Geochimica et Cosmochimica Acta, 64(22): 3853-3869.

Seo, J.H., Guillong, M., Heinrich, C.A., 2009. Role of sulfur in hydrothermal metal fractionation and the formation of porphyry-type ore deposits. Geochimica et Cosmochimica Acta, 73(13): A1197-A1197.

Shand, S.J., 1949. Eruptive Rocks. Their genesis, composition, classification and their relation to ore deposits. Thomas Murby and Co., London: 488p.

Shinohara, H., 1994. Exsolution of immiscible vapor and liquid-phases from a crystallizing silicate melt - Implications for chlorine and metal transport. Geochimica et Cosmochimica Acta, 58(23): 5215-5221.

Sillitoe, R.H., 2010. Porphyry Copper Systems. Economic Geology, 105(1): 3-41.

Simon, A.C., Ripley, E.M., 2011. The Role of Magmatic Sulfur in the Formation of Ore Deposits. In: Behrens, H., Webster, J.D. (Eds.), Sulfur in Magmas and Melts: Its Importance for Natural and Technical Processes. Reviews in Mineralogy & Geochemistry, pp. 513-578.

Simon, A.C., Candela, P.A., Piccoli, P.M., Mengason, M., Englander, L., 2008a. The effect of crystal-melt partitioning on the budgets of Cu, An, and Ag. American Mineralogist, 93(8-9): 1437-1448.

Simon, A.C., Pettke, T., Candela, P.A., Piccoli, P.M., 2008b. The partitioning behavior of silver in a vapor-brine-rhyolite melt assemblage. Geochimica et Cosmochimica Acta, 72(6): 1638-1659.

Simon, A.C., Pettke, T., Candela, P.A., Piccoli, P.M., Heinrich, C.A., 2007. The partitioning behavior of As and Au in S-free and S-bearing magmatic assemblages. Geochimica et Cosmochimica Acta, 71(7): 1764-1782.

Simon, A.C., Pettke, T., Candela, P.A., Piccoli, P.M., Heinrich, C.A., 2006. Copper partitioning in a melt-vapor-brine-magnetite-pyrrhotite assemblage. Geochimica et Cosmochimica Acta, 70(22): 5583-5600.

Simon, A.C. et al., 2005. Gold partitioning in melt-vapor-brine systems. Geochimica et Cosmochimica Acta, 69(13): 3321-3335.

Sinclair, W.D., 2007. Porphyry deposits, in Goodfellow, W.D., ed., Mineral Deposits of Canada: A Synthesis of Major Deposit-Types, District Metallogeny, the Evolution of Geological Provinces, and Exploration Methods. Geological Association of Canada, Mineral Deposits Division, Special Publication, No. 5: 223-243.

Sloan, E.D., Koh, C.A., 2008. Clathrate hydrates of natural gases. CRC Press.

Sobocinski, D.P., Kurata, F., 1959. Heterogeneous phase equilibria of the hydrogen sulfide-carbon dioxide system. Aiche Journal, 5(4): 545-551.

Soloviev, S.G., 2011. Geology, Mineralization, and Fluid Inclusion Characteristics of the Kensu W-Mo Skarn and Mo-W-Cu-Au Alkalic Porphyry Deposit, Tien Shan, Kyrgyzstan. Economic Geology, 106(2): 193-222.

Sterner, S.M., Bodnar, R.J., 1991. Synthetic fluid inclusions .10. Experimental-determination of P-V-T-X properties in the CO_2-H_2O system to 6-kb and 700-degrees-C. American Journal of Science, 291(1): 1-54.

Stouffer, C.E. et al., 2001. Densities of carbon dioxide plus hydrogen sulfide mixtures from 220 K to 450 K at pressures up to 25 MPa. Journal of Chemical and Engineering Data, 46(5): 1309-1318.

Taylor, J.R., Wall, V.J., Pownceby, M.I., 1992. The calibration and application of accurate redox sensors. American Mineralogist, 77(3-4): 284-295.

Tohidi, B., Danesh, A., Todd, A.C., Burgass, R.W., 1997. Hydrate-free zone for synthetic and real reservoir fluids in the presence of saline water. Chemical Engineering Science, 52(19): 3257-3263.

Toulmin, P., Barton, P.B., 1964. A thermodynamic study of pyrite and pyrrhotite. Geochimica et Cosmochimica Acta, 28: 641-671.

Ulrich, T., Gunther, D., Heinrich, C.A., 1999. Gold concentrations of magmatic brines and the metal budget of porphyry copper deposits. Nature, 399(6737): 676-679.

Ulrich, T., Mavrogenes, J., 2008. An experimental study of the solubility of molybdenum in H_2O and KCl-H_2O solutions from 500 degrees C to 800 degrees C, and 150 to 300 MPa. Geochimica et Cosmochimica Acta, 72(9): 2316-2330.

Wallace, P.J., 2005. Volatiles in subduction zone magmas: concentrations and fluxes based on melt inclusion and volcanic gas data. Journal of Volcanology and Geothermal Research, 140(1-3): 217-240.

Webster, J.D., Goldoff, B., Shimizu, N., 2011. C-O-H-S fluids and granitic magma: how S partitions and modifies CO_2 concentrations of fluid-saturated felsic melt at 200 MPa. Contributions to Mineralogy and Petrology, 162(4): 849-865.

Webster, J.D., Holloway, J.R., 1988. Experimental constraints on the partitioning of Cl between topaz rhyoltite melt and H_2O and $H_2O + CO_2$ fluids - New implications for granitic differentiation and ore deposition. Geochimica et Cosmochimica Acta, 52(8): 2091-2105.

Whitney, J.A., 1984. Fugacities of sulfurous gases in pyrrhotite-bearing silicic magmas. American Mineralogist, 69(1-2): 69-78.

Whitney, J.A., 1988. Composition and activity of sulfurous species in quenched magmatic gases associated with pyrrhotite-bearing silicic systems. Economic Geology, 83(1): 86-92.

Williams, T.J., Candela, P.A., Piccoli, P.M., 1995. The partitioning of copper between silicate melts and 2-phase aqueous fluids - An experimental investigation at 1-kbar, 800-degrees-C and 0.5-kbar, 850 ^{o}C. Contributions to Mineralogy and Petrology, 121(4): 388-399.

Williams, T.J., Candela, P.A., Piccoli, P.M., 1997. Hydrogen-alkali exchange between silicate melts and two-phase aqueous mixtures: an experimental investigation. Contributions to Mineralogy and Petrology, 128(2-3): 114-126.

Wilson, A.J., Cooke, D.R., Harper, B.L., 2003. The ridgeway gold-copper deposit: A high-grade alkalic porpbyry deposit in the Lachlan fold belt, New South Wales, Australia. Economic Geology, 98(8): 1637-1666.

Wilson, C.J.N., Hildreth, W., 1997. The Bishop Tuff: New insights from eruptive stratigraphy. Journal of Geology, 105(4): 407-439.

Zajacz, Z., Hanley, J., Heinrich, C.A., Halter, W.E., Guillong, M., 2009. Diffusive reequilibration of quartz hosted silicate melt and fluid inclusions: Are all metal concentrations unmodified? Geochimica et Cosmochimica Acta, 73(13): A1496

Zajacz, Z., Seo, J.H., Candela, P.A., Piccoli, P.M., Heinrich, C.A., 2010a. The effect of magma composition on the genesis of hydrothermal gold and copper ore deposits. Geochimica et Cosmochimica Acta, 74(12): A1196-A1196.

Zajacz, Z. et al., 2010b. Alkali metals control the release of gold from volatile-rich magmas. Earth and Planetary Science Letters, 297(1-2): 50-56.

Zajacz, Z., Seo, J.H., Candela, P.A., Piccoli, P.M., Tossell, J.A., 2011. The solubility of copper in high-temperature magmatic vapors: A quest for the significance of various chloride and sulfide complexes. Geochimica et Cosmochimica Acta, 75(10): 2811-2827.

Zhang, Y.X., Ni, H.W., Chen, Y., 2010. Diffusion Data in Silicate Melts. Diffusion in Minerals and Melts, 72: 311-408.